Spectroscopy and photochemistry of astrophysically-relevant molecules of the cyanoactylene family

Urszula Szczepaniak

NNT : 2017SACLS128

THESE DE DOCTORAT
DE
L'INSTITUT DE CHIMIE PHYSIQUE
DE L'ACADEMIE POLONAISE DES SCIENCES
ET DE
L'UNIVERSITE PARIS-SACLAY
PREPAREE A
L'UNIVERSITE PARIS-SUD

ECOLE DOCTORALE N° 572
Ondes et matière

Spécialité de doctorat : Milieux dilués et optique fondamentale

Par

Mme Urszula Szczepaniak

Spectroscopy and photochemistry of astrophysically-relevant molecules of the cyanoacetylene family

Thèse présentée et soutenue à Varsovie, le 27 juin 2017 :

Composition du Jury :

M. Herbich, Jerzy, Professeur, Institut de Chimie Physique, Académie Polonaise des Sciences, Président
Mme Wierzejewska, Maria, Professeur, University of Wroclaw, Rapporteur
M. Nowak, Maciej, Professeur, Institut de Physique, Académie Polonaise des Sciences, Rapporteur
Mme Sadlej, Joanna, Professeur, Université de Varsovie, Examinatrice
Mme Boyé-Péronne, Séverine, Maître de Conférence, Université Paris-Sud, Examinatrice
M. Kolos, Robert, Professeur, Institut de Chimie Physique, Académie Polonaise des Sciences, Directeur de thèse
Mme Crépin-Gilbert, Claudine, Directrice de Recherche, Université Paris-Sud, Directrice de thèse

Rodzicom

ACKNOWLEDGMENTS

I would like to express my gratitude to my supervisors Prof. Robert Kołos and Prof. Claudine Crépin-Gilbert who trusted that even without proper background knowledge I would be able to work in the field of spectroscopy and matrix isolation, for the guidance, support, and all the lessons I learnt (and those that I refused to learn), for being helpful and friendly (not only when it comes to science, but also in other areas of life), and for many hours spent on helping me present the obtained results in a better way (until the very end of the writing process).

A group of people invested their time in reading the manuscript and helping me improve it, to whom I am thankful: my Supervisors, Tom, Marcin, Natalia, Asia, Michèle, and Krzysiek. Thank you for all the contributions to removing the mistakes, suggested additions and refinements of the text that improved it immeasurably.

I cannot imagine this work to be completed without help of a whole group of scientists to whom I owe a debt of gratitude. I would like to thank Jean-Claude Guillemin for the syntheses of chemical compounds that I used, Marcin Gronowski – for the quantum computations without which I could not support the presented identifications and for the help with the computations I did, Michał Turowski – for the guidance in the lab work, help in analyses, and the theoretical predictions that backed my first experiments with long chains formation, Thomas Custer – for help both in the lab and with analyses, the data for preparing graphs and for corrections of both language and content of this Thesis. I would also like to thank all colleagues from ISMO (Equipe D) for being very welcoming, patient, and helpful, especially: Michèle Chevalier and Alejandro Gutiérrez-Quintanilla, with whom I worked directly, and Catherine Le Bris and Thierry Chamaillé for the help with lasers.

I would also like to thank people whose presence in my life encouraged me to pursue scientific path in the direction of physical chemistry, starting from Christian Jungnickel and Wojciech Chrzanowski who have successfully encouraged me to continue my education after undergraduate studies. I owe a debt of gratitude to Gyorgyi Remenyi and Mark E. Casida, who offered me patience and kindness and who also took the effort of putting something into my head. Gentlemen, one of you taught me about cryogenics, the other about spectroscopy. Look what that led to! I learnt a lot from Stéphane Douin who introduced me to the technique of CRDS (that unfortunately didn't find its place in this thesis). Thank you for that. I am also thankful to Tomonari Wakabayashi, for the discussions at conferences and after them, for letting me use the original data from his article in this Thesis, as well as for the quizzes and insight to Japanese culture.

I am deeply indebted to all the people from administration division, both in IPC PAS and in ISMO, especially Danuta Dudek, Joanna Wiszniowska, Joanna Pińkowska, Jadwiga Skrzecz, Magdalena Szustak, Martine Basset, Marie-Claire Paul, Bernadette Rome, Audrey Colin and Annie Le Gal. Thanks to you my studies and travels between laboratories were as smooth as they could be.

There is a big group of people that I am thankful to for their support, encouragement and good words in times of frustration, but also for the distraction that they were able to provide letting me get some rest and perspective when it was needed. Thank you for your patience in this intense time. That is mainly addressed to my parents, who always granted me support and guidance from the very beginning of my life, and who taught me things that made me want explore the world. I am also thankful to my friends, Mariola, Michał Ś., Artur, Ali, Michał Ż., Karolina, Gosia, and Rafał for being there for me, and to all the wonderful people that I was lucky to meet during my PhD studies. Natalia, Krzysztof R. K., Krzysztof S., Tom, Ania, Lek, Valerii, Ephriem, Ivan A., Feriel, Felipe, Cristiano, Gabriela, Ariel, Ivan C., Rolando, Thejus, Gerard, Nina, Martin, Mathieu, Themis, Odélie, people from CCOF, and many more: thank you all for the discussions, whether they were on spectroscopy, general science or topography and metro system of Paris, Madrid or Havana. Thank you for letting me learn a new perspective, for sharing nice moments, introducing me to didgeridoo, trips we made, coffee we drank, movies we watched (or made), things we explored, and songs we sang, for being helpful and welcoming. Even though I was away from home, thanks to you it felt like home, anyway. Thank you for that.

Finally, I am also thankful to brothers Y. for helping me reduce the pressure to the right amount, as well as to all the (unnamed here) superheroes and gods that helped me survive every day.

This work was financially supported by:

- the French Government scholarship *Bourse Eiffel*, managed by Campus France;
- Polish National Science Centre, project No. 2011/03/B/ST4/02763;
- PICS (Programmes Internationaux de la Coopération Scientifique): PAN-CNRS (2014-2016);
- French–Polish Partenariat Hubert-Curien Polonium project (2012-2013 and 2015-2016) of scientific cooperation;
- the project "Scholarships for PhD students of Podlaskie Voivodeship"; the project was co-financed by the European Social Fund, Polish Government and Podlaskie Voivodeship[*];
- Polish National Science Centre, project No. 2015/17/B/ST4/03875.

[*]Autorka pracy doktorskiej była uczestniczką projektu „Stypendia dla doktorantów województwa podlaskiego" współfinansowanego ze środków Europejskiego Funduszu Społecznego, środków budżetu państwa oraz ze środków budżetu Województwa Podlaskiego. Projekt był realizowany na podstawie Umowy o dofinansowanie projektu Instytucji Pośredniczącej w ramach Programu Operacyjnego Kapitał ludzki 2007 – 2013, nr POKL.08.02.02-20-002/12. Działanie 8.2.Transfer wiedzy, Poddziałanie 8.2.2. Regionalne Strategie Innowacji.

TABLE OF CONTENTS

GLOSSARY

CCD – Charged Coupled Device

CCSD – coupled-cluster singles-and-doubles

CNRS – Centre National de la Recherche Scientifique

EOM-CCSD – equation of motion CCSD

IPC PAS – Institute of Physical Chemistry of Polish Academy of Sciences

IR – Infrared

ISMO – Institut des Sciences Moléculaires d'Orsay

MP2 – second order Møller-Plesset perturbation theory

n/a – not available

PMT – Photomultiplier Tube

RCCSD(T) – restricted CCSD with approximate triples correction

S/N – signal-to-noise ratio

UV-Vis – Ultraviolet-Visible

VUV – Vacuum Ultraviolet

ABSTRACT

This work is devoted to spectroscopic characterization and photochemical studies of several astrochemically interesting molecules of the cyanoacetylene family. The cryogenic rare-gas matrix isolation technique was employed for the preparation of most of the samples. Although rare gas matrices are not direct astrochemical analogues, they are transparent and non-reactive media that enable to study the interesting species.

Some of the molecules investigated, including CH_3C_3N (and some of its isomers), CH_3C_5N, and HC_5N, were available *via* preparative organic chemical synthesis. Others appeared as the products of photochemical reactions run mostly in solid Kr in which the technique of UV-stimulated cryogenic elongation of unsaturated carbon-nitrogen chains was used to produce longer species. This approach led to successful preparation of HC_9N, starting from $C_4H_2 + HC_5N$, and $C_{10}N_2$, starting from either $C_4H_2 + HC_5N$ or $HC_5N + HC_5N$. The method was further extended to the synthesis of methylated compounds with formation of CH_3C_5N from $CH_3C_2H + HC_3N$, and CH_3C_7N from $CH_3C_2H + HC_5N$. In addition, photochemical experiments using HC_5N-containing matrices led to the detection of HC_7N and of the C_5N^- anion. A general scheme describing the chain elongation processes was formulated.

Two isomeric products of the UV photolysis of Ar matrix isolated CH_3C_3N were identified based on measured IR absorption spectra of pure compounds and on available theoretical predictions. The photochemical processes leading to their production have been described in terms of the precursor molecule being converted into propargyl cyanide, with allenyl cyanide formed as an intermediate.

A thorough spectroscopic characterization of gaseous, solid, and cryogenic matrix-isolated CH_3C_5N was performed with the combined use of IR absorption, Raman scattering, electronic absorption, and electronic luminescence measurements. Phosphorescence of the related molecule, HC_5N, was revisited, and several new spectral assignments were reported.

Detection of CH_3C_5N, CH_3C_7N, HC_9N, $C_{10}N_2$ and C_5N^- as a result of UV-assisted chain elongation would not have been possible without these molecules possessing strong electronic phosphorescence, that was observed here for the first time. The vibronic structure of their emission and excitation was analysed, allowing characterization of several of their electronic states.

Similarities, differences, and patterns in selection rules, vibronic spacings, electronic transition energies, and phosphorescence decay times were examined for the homologous series $HC_{2n+1}N$, $NC_{2n}N$ and $CH_3C_{2n+1}N$. Within each of these series, the $\tilde{a}$-$\tilde{X}$ vibrationless origin wavelengths were found to linearly correlate with the lengths of unsaturated carbon-nitrogen backbones. Extrapolation allows estimation of the $\tilde{a}$-$\tilde{X}$ vibrationless origin wavelength to currently unexplored cyanopolyynes.

1 INTRODUCTION

The Universe has always been a source of wonder and the object of studies. Throughout the ages humanity has studied space. At first, these were naked eye observations of stars. Later, more and more technologically advanced instruments were used, some of them even being sent outside of the Earth entirely. Together with the discovery of thousands of galaxies, stars, planets and smaller bodies, our understanding of their nature has also improved. In spite of the enormous amounts of data that have been acquired, we still barely understand the composition of the Universe. Not only because only a small fraction of its mass is matter as we know it – mostly in the form of stars and interstellar gas and dust (while the remaining part is deduced to be hidden in the form of dark matter and dark energy), but also because we still do not know the exact composition of the observable fraction.

Stars, planets, comets and other cosmic bodies form from gas and dust spreading over vast areas (up to several hundreds of light years across) of the Universe. This gas and dust, known as the interstellar medium, provide not only matter for the formation of various bodies, but they also define the conditions for such processes. Understanding the composition, structure and evolution of the interstellar medium is "one of the most significant challenges in modern astrophysics" (as stated by Louis Allamandola [1]).

The goal of this study is the spectroscopic characterization of some astrophysically-relevant molecules – species already detected or postulated to be present in the interstellar medium. Selected molecules belong to the cyanoacetylene family. Although the experiments described here are mainly dealing with rare gas cryogenic matrices, and therefore cannot be treated as a direct reflection of astrochemical processes, nonetheless they may give some insight into possible UV-stimulated reactions occurring between interstellar molecules. Data acquired with rare gas matrix experiments might serve as a starting point for experiments with more realistic interstellar solids including water or carbon monoxide which are abundant in interstellar ices. The results obtained also provide data that might be of relevance for future astrochemical detection involving the techniques other than microwave spectroscopy (currently the most popular in the field).

This Introduction explains what astrophysically-relevant molecules are, with particular attention being given to interstellar nitriles and especially cyano(poly)ynes. A literature review on the spectroscopy and photochemistry of cyano(poly)ynes is provided together with a justification of the species selected for this study. At the end of Introduction, the main focus for the research in this work is presented in addition to a short description of contents of the following chapters.

1.1 Astrophysically-relevant molecules and processes

Understanding processes occurring in the interstellar medium aids in understanding the formation of various astronomical objects. The substances present in the interstellar medium might also be responsible for seeding life on cosmic bodies: either by delivering organisms

in form of spores [2] or by delivering organic matter from which molecules leading to creation of life might have been synthesized. A simplified cycle of matter in the Universe and how it may be delivered to planets is depicted in Figure 1.

Although 'astrochemistry' might be considered as part of 'astrophysics', the first term is deliberately used here to stress the importance of chemical processes.

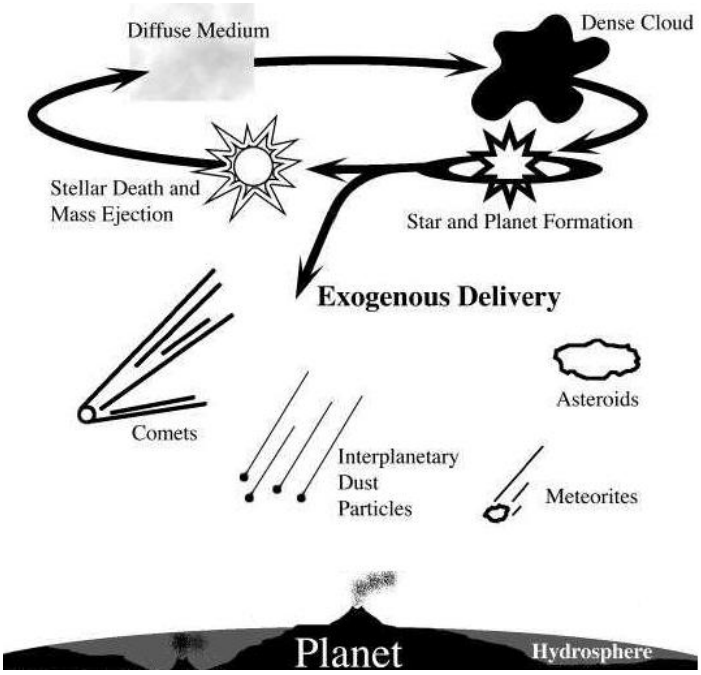

Figure 1. A simplified cycle of the processing of matter in Space, depicting a path by which it can be delivered to a planetary surface. (Adapted from Ref. [3].)

Chemistry in space is very often much different than the chemistry as we know it on Earth (where vast amount of reactions takes place in liquid solutions). The synthesis of relatively small and simple interstellar molecules (for example, methanol) have still not been explained. Hydrogen appears very often as an atomic species, not as a diatomic molecule. Chemistry takes place under specific conditions. The matter is extremely highly diluted (on the order of 10^4-10^6 atoms/molecules[1] per cm^3 in "dense" clouds). Most reactions occur in the gas phase or on the surface of dust particles. Due to very high dilutions (and thus low collision rates) and low temperatures (up to 100 K), the reactions in gas clouds are mainly exothermic. In these reactions, excess energy is released mostly as the kinetic energy of products. In the case of surface reactions, dust grains serve as an energy sink. Reactions with activation barriers normally slow down or stop at such low temperatures – that they nevertheless proceed can, however, be explained by invoking enhancement of quantum mechanical tunnelling through their energetic barrier [4].

This work is devoted, not only to the studies of spectroscopic properties of chosen molecules, but also to the studies of several reactions involving them and, as such, falls within the astrochemistry rubric. While the reactions studied here do not directly resemble

[1] Neutral or ionic.

the ones occurring in space, they nevertheless unveil crucial chemical properties of the investigated molecules.

There are a variety of chemical species which have been identified in space ranging from atoms to complicated carbon-based molecules. H and He make approximately 98 % of the mass of the observable Universe (mostly as nuclei) and, together with Li nuclei, were formed in the Big Bang. Some of the most abundant elements, namely C, N, and O originate from nucleosynthesis within stars. Once formed, these elements undergo a variety of processes to eventually form diverse molecules. So far, almost 200 molecules have been observed in the interstellar medium (Table 1), many of which are unstable species under terrestrial conditions (like radicals and ions). Apart from fullerenes, they are usually small molecules of up to 12 atoms ($HC_{11}N$ detection is considered tentative). These molecules have mainly been identified through use of rotational spectroscopy. Molecules possessing no permanent dipole moment can only be observed *via* other methods (*e.g.* dicarbon, C_2, and acetylene were detected with electronic and infrared spectroscopy, respectively).

Several molecules in Table 1 are marked with colours. They show a homologous series of chemicals which are the main focus of this work. These are families of molecules capped with the –CN group. They are characterized by the alignment of π-orbitals and alternating single and triple bonds. The family members differ among one another by the number of –C≡C– units: monocyanopolyynes (blue), methylcyanopolyynes (yellow) and cyanopolyyne anions (green). The molecules of particular interest here are either linear or belong to the symmetric-top (C_{3v}) group (by addition of methyl group to a linear structure).

Monocyanopolyynes ($HC_{2n+1}N$) constitute the most prominent homologous series of astrochemically-relevant molecules. They have been detected *via* microwave rotational transitions in many extraterrestrial sources with chain lengths up to $n = 5$ (*e.g.* [5–7]). Their further growth may lead to formation of large carbon structures.

Cyanoacetylene, HC_3N, the smallest neutral molecule possessing both –C≡C– and –C≡N, was first observed in a star-forming region of Sagittarius (Sgr B2(N)) [8] – one of the most heavily studied regions, because of its position close to the Galaxy centre and because of its richness in molecules. Cyanoacetylene was then observed in other Galactic radio sources [9–11], as well as extragalactic ones, *i.e.* in the NGC 253 (“Silver Coin”) galaxy [12]. The $C_2H_2 + CN$ reaction was suggested to be responsible for its formation both in low-mass and high-mass star-forming regions based on observations of three ^{13}C isotopologues [13]. It has also been observed in Titan’s atmosphere [14,15] and in the atmosphere of the Hale-Bopp comet [16], revealing its importance to both planetology and cometary studies. Due to its seeming prevalence in the universe as well as its ease of synthesis in the laboratory, this astrochemical molecule and many of its isomers have been the subject of intense study. Such studies have led to detection of its isomers, HCCNC [17] and HNCCC [18] in the dense interstellar Taurus Molecular Cloud (TMC-1). Other isomers have also been postulated: CC(H)CN [19,20] and HCNCC [21], although they have not yet been detected in space.

Cyanoacetylene also has potential prebiotic significance and is thought to be one precursor for pyrimidines – nucleic acid bases – and, in particular, appears as a reaction intermediate in the synthesis of cytosine and/or uracil [22–29]. Polymerization of HCN, a smaller analogue of cyanoacetylene, also leads to formation of purines. These factors make the cyanoacetylene family an important class of interstellar molecules.

Along with the shorter cyanoacetylene molecule, longer chain $HC_{2n+1}N$ (n = 2, 3) molecules were also detected in several molecular clouds, *e.g.* in the clouds within the constellation of Taurus [30]. HC_9N was first observed in 1978, at millimetre wavelengths in the dense interstellar cloud HCl-2 [31] and then in two expanding circumstellar envelopes: of IRC +10216 (the most often observed carbon star) [32,33] and of CRL 2688 (known as Egg Nebula) [33]. The molecule $HC_{11}N$ was first reported in IRC +10216 [5], although this was later shown to be an erroneous identification. Subsequently it was reported to be present in TMC-1 [6], although this claim has also been recently called into question [34]. Loomis *et al.* [34] suggests cyclization reactions as being responsible for non-detection of longer monocyanopolyynes. Cyanopolyynes have mostly been observed in millimetre wavelengths although infrared detection has been gaining in importance. The number of detections using IR wavelengths (*e.g.* [35]), might increase in the near future thanks to development of advanced multichannel detectors and deployment of modern spectrometers beyond the Earth's atmosphere, as for example Spitzer Space Telescope.

The astrochemical synthesis of monocyanopolyynes probably involves the reactions of $CN^{\bullet}$ or $C_{2n+1}N^{\bullet}$ radicals with polyynic hydrocarbons $HC_{2m}H$ (n, m being natural numbers). Cherchneff *et al.* propose following pathway for formation of monocyanopolyynes in the circumstellar gas cloud IRC + 10216: $HC_2H + C_{2n+1}N^{\bullet} \rightarrow HC_{2n+3}N + H^{\bullet}$ [36,37].

Methylated compounds of the type $CH_3(CC)_nCN$ are also of astrochemical interest. Molecules with $n \in \{0, 1, 2\}$ have already been confirmed in the interstellar medium [38–44]. The presence of larger ones, as $CH_3(CC)_3CN$, is postulated, as they appear in the chemical models of interstellar medium (*e.g.* Refs. [45–48]).

Methylated cyanoacetylene, CH_3C_3N, was identified in TMC-1 [42] and more recently in SgrB2 [49]. It was also searched for, but not found, in the Westbrook Nebula (CRL 618) [50]. It is also predicted to be present in Titan's atmosphere [51]. Although data from Huygens probe did not confirm it [52], data from the Cassini probe found signatures of its existence [53,54]. Its structural isomer, allenyl cyanide (CH_2CCHCN) [55], has also been detected in the interstellar medium (in TMC-1). Its formation was proposed *e.g.* in a barrierless synthesis from smaller molecules [56]. Other isomers also seem to be plausible interstellar species, in particular propargyl cyanide ($HC{\equiv}C–CH_2CN$), whose rotational spectroscopy is available [57–60] to support its possible future identification in galactic gas clouds.

Table 1. List of detected interstellar molecules grouped by the number of atoms (on the basis of Ref. [61], as accessed in January, 2017). Formulas in *italics* refer to tentative detections. Colours mark three cyanopolyynic series of molecules (see text).

2	3	4	5	6	7	8	9	10
H_2	C_3	*c*-C_3H	C_5	C_5H	C_6H	CH_3C_3N	CH_3C_4H	CH_3C_5N
AlF	C_2H	*l*-C_3H	C_4H	*l*-H_2C_4	CH_2CHCN	$HC(O)OCH_3$	CH_3CH_2CN	$(CH_3)_2CO$
AlCl	C_2O	C_3N	C_4Si	C_2H_4	CH_3C_2H	CH_3COOH	$(CH_3)_2O$	$(CH_2OH)_2$
C_2	C_2S	C_3O	*l*-C_3H_2	CH_3CN	HC_5N	C_7H	CH_3CH_2OH	CH_3CH_2CHO
CH	CH_2	C_3S	*c*-C_3H_2	CH_3NC	CH_3CHO	C_6H_2	HC_7N	CH_3CHCH_2O
CH^+	HCN	C_2H_2	H_2CCN	CH_3OH	CH_3NH_2	CH_2OHCHO	C_8H	
CN	HCO	NH_3	CH_4	CH_3SH	*c*-C_2H_4O	*l*-HC_6H	$CH_3C(O)NH_2$	
CO	HCO^+	HCCN	HC_3N	HC_3NH^+	H_2CCHOH	*CH_2CHCHO*	C_8H^-	
CO^+	HCS^+	$HCNH^+$	HC_2NC	HC_2CHO	C_6H^-	CH_2CCHCN	C_3H_6	
CP	HOC^+	HNCO	HCOOH	NH_2CHO	CH_3NCO	H_2NCH_2CN	*CH_3CH_2SH*	
SiC	H_2O	HNCS	H_2CNH	C_5N		CH_3CHNH		
HCl	H_2S	$HOCO^+$	H_2C_2O	*l*-HC_4H				**11**
KCl	HNC	H_2CO	H_2NCN	*l*-HC_4N				HC_9N
NH	HNO	H_2CN	HNC_3	*c*-H_2C_3O				CH_3C_6H
NO	MgCN	H_2CS	SiH_4	*H_2CCNH*				C_2H_5OCHO
NS	MgNC	H_3O^+	H_2COH	C_5N^-				$CH_3OC(O)CH_3$
NaCl	N_2H^+	*c*-SiC_3	C_4H^-	HNCHCN				
OH	N_2O	CH_3	HC(O)CN					**12**
PN	NaCN	C_3N^-	HNCNH					*c*-C_6H_6
SO	OCS	PH_3	CH_3O					*n*-C_3H_7CN
SO^+	SO_2	HCNO	NH_4^+					*i*-C_3H_7CN
SiN	*c*-SiC_2	HOCN	*H_2NCO^+*					*$C_2H_5OCH_3$*
SiO	CO_2	HSCN	$NCCNH^+$					
SiS	NH_2	H_2O_2						**13**
CS	H_3^+	C_3H^+						*$HC_{11}N$*
HF	SiCN	HMgNC						
HD	AlCN	HCCO						**60**
FeO	SiNC							C_{60}
O_2	HCP							C_{60}^+
CF^+	CCP							
SiH	AlOH							**70**
PO	H_2O^+							C_{70}
AlO	H_2Cl^+							
OH^+	KCN							
CN^-	FeCN							
SH^+	HO_2							
SH	TiO_2							
HCl^+	C_2N							
TiO	Si_2C							
ArH^+								
N_2								
NO^+								

The presence of methylcyanodiacetylene, CH_3C_5N, in the interstellar medium was postulated on the basis of radioastronomical observations [43] and more than 20 years later it was confirmed in TMC-1 [44]. This compound appears in astrochemical kinetic models (*e.g.* [45,62,63]) and, according to Markwick *et al.* [62], it is probably synthesized from HC_5N through a reaction with $CH_3OH_2^+$. From an experimental perspective, it was reported that photolysis of small gaseous acetylenic compounds of astrophysical importance leads to formation of this molecule [64].

Dinitriles of the form, ($NC_{2n}N$), have not, as yet, been observed in interstellar space[1]. However, the presence of the n = 2 compound in the atmosphere of Titan has been tentatively established [65]. It has been postulated that monocyanopolyynes formed in Titan's atmosphere polymerize to form larger dicyanopolyynes. Titan, Saturn's moon, appears as an orange body. Whatever molecules are responsible for this haze absorb in the visible region. This opens a path to laboratory investigations of the visible spectroscopy of potential atmospheric constitutents including dinitriles and other potential polymerization products. Part of this Thesis is devoted to studying how acetylenic cyanides might evolve towards longer, CN-capped chains by exposing either acetylenic cyanides alone or mixed with (poly)yne molecules to UV radiation.

So far, two of the smallest $C_{2n+1}N^-$ anions (n = 1, 2) have been identified in the interstellar medium, both around the carbon star IRC +10216 [66,67]. A search for C_3N^- was also conducted in the dense interstellar cloud TMC-1, although the anion was not detected. For the C_5N^-, detection was based on *ab initio* quantum chemical calculations, as no laboratory data were available for comparison. Quantum chemical calculations and comparison with abundances of other species suggest difficulties with the detection of longer interstellar anions of this family using the current generation of radio telescopes [68].

Although the question of formation of longer carbon-nitrogen chains is motivated here by its importance for understanding astrochemical processes, it might be also important from technological point of view. Very long carbon chains, or nanowires, are currently an important area of research. Studies on $C_{16}N_2$ have shown that due to π-electron localization and the acetylenic character of the chain (bond-length alternation), a nanowire with a terminating N-atom will be semiconducting [69]. Such nanowires might be bound to surfaces with the use of numerous compounds. For example, nitrogen lone pair from pyridine base can be used as a molecular "alligator clip" binding the chain to Au surface [70]. Modifications of the endings (capping) might lead to various functionalities. Whatever the motivation behind undertaking these studies, the long carbon-nitrogen chains are interesting molecules having symmetry that is unusual for organic molecules and there is still a lot to learn about them.

An appropriate technique to study the spectroscopy of reactive species is cryogenic matrix isolation [1]. The data from such experiments are close to those of the gas phase and can serve as the first step in identification of new molecules in space. Matrix isolation will be described in more detail in Chapter 2.1.

[1] Lack of dipole moment makes them invisible to microwave spectroscopy.

1.2 Cyanoacetylene family – cyano(poly)ynes spectroscopy and cryogenic synthesis of carbon-nitrogen chains

The title compounds are conjugated unsaturated carbon chains capped with –CN at one end. Depending on the termination of the other end, such compounds can be divided into: monocyanopolyynes (–H), methylcyanopolyynes (–CH_3) and dicyanopolyynes (–CN). Monocyanopolyyne anions ($C_{2n+1}N^-$) are a fourth related family that is of interest for this Thesis.

Cyanoacetylene, even though it is not formally a *poly*ynic compound, can be regarded as the first member of the monocyanopolyyne series. Several literature entries are devoted to this molecule, including spectroscopic reports (*e.g.* [71–73]). Studies on its photochemistry [74–77] show that the main gas-phase photodissociation channel is H-detachment ($HC_3N \rightarrow H^\bullet + C_3N^\bullet$). Clarke and Ferris [78] reported the wavelength threshold for this process as 240 nm. Seki *et al.* [76] proposed a second channel: $HC_3N \rightarrow HC_2^\bullet + CN^\bullet$, where the dissociation energy is 9.41 eV (131.8 nm) [74]. However, both products were observed in experiments involving lower energy photolyses (193 nm and 212 nm) [77]. Additionally, upon 193 nm photolysis of gas-phase HC_3N, the formation of HCN, C_2H_2, C_4N_2, HC_5N, C_6N_2 were all observed [77]. The first two products were also formed as a result of photolysis at 248 nm [76]. These collected observations led to the hypothesis of electronically excited HC_3N reaction with other HC_3N molecules, instead simple photodissociation. However, it was reported that such a reaction leads mainly to polymerization. It was also tentatively connected with the 'foggy' atmosphere of Titan. C_6N_2 is supposed to form from either two $C_3N^\bullet$ radicals or from $C_3N^\bullet$ radical reacting with HC_3N. In Silva *et al.* [77], a variety of isomerisation or dissociation products of HC_3N were also investigated using quantum chemistry calculations. These products included HCN, HC_3N isomers (including cyclic ones), and radicals.

Various isomers of cyanoacetylene (CCCNH [79], HCCNC [80,81], HNCCC [81,82], HCNCC [81,83]) have been produced and identified experimentally in cryogenic matrices, with the use of either UV-irradiation or the cold-window-radial-discharge (CWRD) [84] technique. Reported photolysis products included: CN^-, C_2N^-, $C_2NC^\bullet$, C_2NC^- [81,83], C_3N^- [85,86], HC_3N^+ [87], and, tentatively $C_3N^\bullet$ [81]. Formation of H-Kr-C_3N and H-Xe-C_3N was observed [81] upon 193 nm laser photolysis of HC_3N isolated in cryogenic Kr and Xe. Noteworthy, while HC_3N does not exhibit any luminescence in cryogenic matrices, the isoelectronic C_3N^- [86] anion and C_2N_2 dinitrile [88,89] do.

Cyanodiacetylene, HC_5N, spectroscopic properties were calculated *e.g.* by Botschwina [90]. Its electronic emission and absorption were studied both in the gas phase and in cryogenic matrix by Turowski *et al.* [91], and the Raman spectra of a cryogenic sample were also reported [92]. Gas phase HC_5N photolysis was described by Guillemin *et al.* who also detailed the preparatory synthesis of this species [93]. Upon far-UV photolysis (achieved with H_2 or Xe discharge lamps) in cryogenic matrices, HC_5N can yield HC_4NC, C_5N^-, HNC_5 and C_4HCN [94], as well as inclusion species of type H-Rg-C_5N (Rg denoting Kr or Xe) [95] although such inclusion species are difficult to form and observe. Quantum chemical predictions can greatly aid in the identification of isomers formed through

photolysis and other processes. For example, Gronowski and Kołos theoretically predicted certain HC_5N isomers [96,97] that were subsequently spectroscopically detected [94,97].

Some longer monocyanopolyynes $HC_{2n+1}CN$ (n = 3-6) were obtained by laser ablation of graphite in liquid acetonitrile followed by chromatographic purification and characterized with UV absorption and NMR spectroscopy [98]. Isotopic experiments proved that carbon atoms of the chains come both from graphite and the solvent. Devienne *et al.* [99], in an experimental work on the synthesis of biological compounds in interstellar-like conditions, refers to previous work in which graphite bombardment with high energy H_2 and N_2 beams resulted in production of monocyanopolyynes up to HC_9N. Gas-phase spectroscopic studies of HC_9N are limited to microwave measurements, which relied on the transient formation of minute amounts in discharge plasma using acetylene and cyanoethylene [100] or dicyanoacetylene and cyanoacetylene [101] as seed gases. These measurements allowed the geometry of HC_9N to be determined. Other experimental studies reporting electronic absorption of monocyanopolyynes are available, *e.g.* [98,102–105]. This family has also been the subject of calculations at various levels of theory. Calculations of HC_9N in particular are well represented *e.g.* Refs. [106–109]. Density functional theory (B3LYP) investigations [110] suggested that $HC_{2n+1}N$ compounds should be linear and polyynic (considering the bond lengths and bond orders along the carbon chain) at least up to n = 8. In Vichietti and Haiduke [111,112], the IR intensity of the vibrational modes in long cyanopolyynes and isocyanopolyynes was analysed, pointing to the central triple CC bond stretching as producing the strongest band.

The study of a VUV spectroscopy of a series of molecules, HC_3N, C_2N_2, C_4N_2, C_6N_2 showed some trends in the series. $n - \pi^*$ transitions for these species were concluded to fall in approximately the same region (58 000 – 62 000 cm^{-1}), while $\pi - \pi^*$ transitions tended to have lower energy in longer chains. [113]

Apart from C_2N_2 [88,89], luminescence has also been observed for other molecules in the dicyanopolyyne family (C_4N_2 [114], C_6N_2 [115], C_8N_2 [116]). For all of them, the emission is characterized by at least one prominent vibronic with a spacing of 2000 – 2200 cm^{-1}, characteristic of CC or CN triple bond stretching modes. Also dicyanopolyyne cations showed luminescence in cryogenic Ne matrices ($C_4N_2^+$ [117], $C_6N_2^+$, $C_8N_2^+$ [118]). Especially interesting for this Thesis are studies concerning $C_{10}N_2$. Electronic absorption spectra were reported for solutions of this chemical in organic solvents [103–105]. Schermann *et al.* [104] used toluene to extract $C_{2n}N_2$ (n = 4-9) compounds from solid residues produced by the vaporization of graphite in the presence of cyanogen; not only UV absorption and NMR spectra of liquid solutions were published, but also the IR absorption of solid substance. No luminescence of this compound has yet been reported. Dicyanopolyynes appear also in theoretical studies as astrochemically-interesting molecules, *e.g.* in Ref. [106].

Addition of a methyl group to a chain changes its physical properties. For example, it was reported [64] that thermal decomposition (without melting) of HC_5N is observed at -40°C[1],

[1] In the experiments described here, slight decomposition was observed even at -78°C, see Chapter 2.3.

while its methylated analogue, CH_3C_5N is stable until it starts to melt at 92°C. The same trend, although less pronounced, was also observed for a shorter pair of substances: HC_3N/CH_3C_3N. At room temperature, the latter is stable while the former decomposes and has to be kept in the freezer.

The smallest of the methylcyanopolyynes, CH_3C_3N, has been the subject of several studies. Data on its rotational [119–122], vibrational [123–127], and electronic [128] spectroscopy are available. Some of these reports were supported with calculations of its thermodynamic or spectroscopic properties. Purely theoretical studies are also available and provide rotational constants [129] or vibrational energy levels [130]. Photoelectron spectra were measured by Bieri *et al.* [131]. Its excited electronic structure was also recently measured by VUV FT absorption spectroscopy [132]. However, little is known about its photochemical transformations. A related compound, CH_3CN, produced H_2CNC [133] and H_2CCNH [134] upon photolysis. Similar observations have been made concerning the photolysis of HC_3N which forms C_3NH and HCCNC. Using these species as a template, it is reasonable to expect formation of CH_3CCNC (whose gas phase IR absorption spectrum is available [135]) and/or $H_2CCCCNH$ upon UV photolysis of CH_3C_3N.

One of CH_3C_3N isomers that is synthetically available in its pure form is propargyl cyanide, $HCCCH_2CN$. Formally, this chemical is a result of hydrogen atom migration along the CH_3C_3N chain. At this point in time, propargyl cyanide has not yet been characterized due to the difficult synthesis and demanding storage conditions of the pure substance[1]. No infrared spectroscopic studies of the pure compound, either gas or solid, have been reported although the IR spectrum in a solution of CCl_4 is known [136]. It has also been discussed in several theoretical studies in which a number of properties, including polarizability, electric dipole moment [106], enthalpy of formation [137,138], and adiabatic ionization energies [138] have been reported. The chemistry of this species in solution has been described in Haruki *et al.* [139] where it was used as a precursor to synthesize some substituted heterocyclic compounds. No photochemical studies have yet been performed.

Another stable C_4H_3N isomer is allenyl cyanide, CH_2CCHCN. It has been the subject of several theoretical and experimental studies. For example, in a quantum chemical and spectroscopic study [56], full vibrational analysis and a proposed path to its interstellar formation are reported. Its microwave spectroscopy is also known [140]. Isocyano isomers of both allenyl and propargyl cyanides have been measured with microwave [59,141] and infrared spectroscopy (in the gas phase) [142].

For a longer representative of $CH_3C_{2n+1}N$ family, CH_3C_5N, various studies [45,106,143,144] have provided MP2, DFT or CCSD(T) predictions of a variety of parameters including structure, rotational constants, electric dipole moment and polarizability. From an experimental standpoint, rotational transitions [145,146] and the gas-phase infrared absorption [144] have been reported. The latter study on CH_3C_5N, investigated along with

[1] One report [136] claims to have stored this chemical for ten months in a sealed vial at room temperature with no decomposition – presumably as solution in CCl_4. In the experiments described here, propargyl cyanide was found to spontaneously transform into allenyl cyanide while stored at dry ice temperature (-78°C), in a matter of weeks.

BrC_5N, was published very recently, coincident with the experiments described in the Chapter 3.2 ("Spectroscopy of methylcyanodiacetylene, CH_3C_5N").

The first report to mention CH_3C_7N discusses its synthesis, along with infrared and UV absorption spectra in ether solution [147]. Arnau *et al.* [148] provides calculated rotational constants. Another theoretical investigation by Woon and Herbst [106] provides molecular geometry, polarizability, and electric dipole moment, although no experimental data exist with which to compare these predictions. A report on the radio spectroscopy of CH_3C_7N was published in Thaddeus *et al.* [7], and provided a group of rotational transitions that are of interest for astronomers. Microwave spectra were measured and rotational transitions published in Chen *et al.* [146] and McCarthy *et al.* [149]. Kerisit *et al.* suggests that it may be formed *via* photochemical reactions of smaller organic compounds: CH_3C_4H (1,3-pentadiyne) with HC_3N [150]. However, this is based on a ^1H NMR spectrum peak whose attribution to this molecule needs to be confirmed.

Laboratory experiments on astrophysical cyano(poly)yne anions C_3N^- and C_5N^-, include infrared absorption and electronic spectroscopy of matrix-isolated species [81,83,85,86,94,151] and infrared photodissociation spectroscopy [152] studies that reveal several additional (weaker) transitions. Photoelectron spectroscopy of both anions was also studied yielding adiabatic electron affinities: 4.305 ± 0.001 (C_3N) and 4.45 ± 0.03 (C_5N) eV [153]. The resulting radicals formed upon electron detachment are also astrophysically relevant. Some astrochemical reactions involving these anions have also been studied both experimentally and theoretically. These studies suggest that reactions between the anions and HC_3N results in chain growth. At first, the ions form clusters, being solvated by one or several HC_3N molecules: $(HC_3N)_x \cdot C_{2n+1}N^-$. Then, chain growth is observed within those clusters: $(HC_3N)_{x-1} \cdot C_{2n+3}N^-$. Such a mechanism is faster than the one involving bare anion + HC_3N reactions (which also lead to anionic chain elongation). [154] This contrasts with the encounters of isolated C_3N^- and HC_3N species, for which the only deduced reaction channel was the proton transfer [155].

One of the challenges in studying such molecules is their instability under standard laboratory conditions. They require vacuum and low temperature when stored and special handling when working with them. Specific experimental techniques also greatly aid their study. Cryogenic matrix isolation is one technique that involves isolation of unstable molecules in a non-reactive environment, allowing their observation for extended periods of time. Rare-gas matrices are transparent in the IR and UV facilitating astrochemical studies in these wavelength ranges. Isolation of exotic species in a rare gas matrix also aids in studying photochemical reactions where, unlike in the gas phase, the matrix *cage* effect might favour creation of isomers (*e.g.* Ref. [96]) or other metastable species including radicals or ions. Matrix isolation is also useful for *in situ* formation of longer cyanopolyynes from shorter precursors. This has been demonstrated starting from HC_5N [115,156], and later HC_7N [157], C_6N_2 [115], C_8N_2 [116]. HC_5N appeared in UV-irradiated Ar solids doped with HC_3N/C_2H_2 mixtures [156]. HC_5N together with C_2N_2, C_4N_2, C_6N_2 were observed in UV-photolysed (193 nm) Ar, Kr and N_2 solids containing HC_3N alone [115]. HC_7N was detected in solid Ar doped with HC_5N/C_2H_2 [157]. This last study provided insight into the electronic spectroscopy (as well as IR absorption spectroscopy) of

cyanotriyne, the longest monocyanopolyyne obtained thus far under such conditions. C_8N_2 (reportedly the longest dicyanopolyyne formed in cryogenic matrices) was observed in a solid Kr/HC_3N mixture subjected to electric discharges before solidification [116]. In all of these low temperature experiments, produced mono- or dicyanopolyynes were found to emit strong phosphorescence, which proved to be the best method for their detection. No studies devoted to cryogenic formation of methylated cyanopolyynes could be found.

The molecules of interest were also subject to several other studies, exploiting several techniques, such as crossed molecular beams ([158]), gas kinetics at very low temperatures (CRESU – reaction kinetics in uniform supersonic flow, [159]) or cavity ring-down spectroscopy (CRDS, *e.g.* [160]), that are not directly relevant here.

1.3 The goal: spectroscopy of available and newly-created molecules

The aim of this Thesis is to report the spectroscopic characterization and the exploration of the associated photochemistry of several poorly characterized molecules belonging or closely related to the cyanoacetylene family. These are C_4H_3N isomers and several cyanopolyynes. The objects of the studies were chosen based on:

- astrophysical relevance, *i.e.* their possible role in chemical reactions in the interstellar medium;
- the need and feasibility of gaining or extending knowledge of their spectroscopy and/or photochemistry;
- ease of their synthesis or the good prospects for their UV-induced cryogenic formation from smaller, readily available precursors.

Within this framework, there are several specific goals:

1. Create the molecules of interest *via* UV-stimulated cryogenic synthesis, whenever the standard organic-chemical route was unavailable. While several astrophysically-relevant molecules of the cyanopolyyne family have already been synthesized and spectroscopically characterized in inert gas matrices, no traditional pathway to synthesis of analogous longer chain species has been found. Here, the intention was to go beyond what was reachable using standard synthetic techniques or previous cryogenic studies within the families of monocyanopolyynes and dicyanopolyynes and to study HC_9N and $C_{10}N_2$. These chains are the longest reachable due to limits in the size and high reactivity of available precursors. The longest monocyanopolyyne available through preparatory organic synthesis is HC_5N. Polyynes available in pure form are as big as C_6H_2 and C_8H_2 [161,162]. However, these are highly unstable (explosive) substances. Because of this, C_4H_2 was used as a safer alternative. Combinations of C_4H_2 and HC_5N lead to HC_9N and $C_{10}N_2$ as the largest mono- and dicyanopolyyne achievable in a bimolecular reaction. An additional objective was to check the applicability of the analogous approach to the synthesis of methylated cyanopolyynes, CH_3C_5N and CH_3C_7N.
2. Compare the spectroscopy of $HC_{2n+1}N$ and $CH_3C_{2n+1}N$ compounds.
3. Investigate the effect of chain elongation on the spectroscopy of the cyanopolyyne family.

4. Test the validity of the previously proposed mechanisms [115,157] for the synthesis of cyano- and dicyanopolyynes in rare gas matrices.
5. Investigate photolysis pathways for CH_3C_3N using all synthetically available C_4H_3N isomers or theoretical predictions.

The results of such investigations are likely to assist in further, gas-phase studies, eventually promoting future interstellar detections or helping in the interpretation of existing observational data. Apart from the astronomical context, the elucidation of processes occurring in matrices may uncover unusual reaction mechanisms that are also of pure chemical interest.

The choice of the principal experimental method – cryogenic matrix isolation, was justified by the results of previous, closely related research (as described earlier). Quantum chemical methods (mostly the density functional theory, yielding electronic and vibrational energy levels for isolated, gas-phase molecules) applied were assumed to be sufficiently precise to aid in spectroscopic identification of photolysis products generated in solid rare gas hosts.

The main potential problems and constraints were the following:

- The formation of relatively large products *via* coupling of smaller precursors involves certain rearrangements within an otherwise fairly rigid cryogenic matrix. The geometry of precursor molecules (their length and the possible presence of a terminating methyl group) introduces non-negligible spatial constraints. Positions of many rare gas atoms have to be altered and precursor species (or the products of their primary photolysis) have to shift and turn considerably to form a longer chain. This shifting requires additional energy, apart from that necessary to excite or photolyze precursor molecules. Energy delivered to such a system should not destroy the products. Such processes are not straightforward and may not be possible at all.
- Not all the molecules are trapped in the matrix cage of the same type and size and that can affect the spectra. In particular, dissimilar microenvironments, so-called *matrix sites* will result in the appearance of additional spectral features. These features might hinder identification of intermolecular complexes or isotopologue bands.
- Even when rare gases are used, the inertness of the host is not always satisfied. For the details on cryogenic matrix isolation, see Chapter 2.1.
- Technical/organizational constraints, as *e.g.* limited time allocated for the measurements requiring a tunable laser (OPO) system, hence non-uniform spectral ranges explored in consecutive experiments.

This dissertation is organized in the following way. The next chapter describes materials, techniques and methods that were used in the course of this work, and includes a list of chemical species used and a brief comment on the quantum chemical calculations that assisted in the interpretation of experimental results. The two following chapters are devoted to results of experiments. Chapter 3 describes spectroscopy and photochemistry of methylated cyano(poly)ynes that were available by preparatory organic synthesis: UV-

induced isomerization of CH_3C_3N and thorough spectroscopic characterization of CH_3C_5N. Chapter 4 describes the UV-stimulated synthesis and subsequent characterization of cyanopolyynes in cryogenic matrices. Chapter 5 contains summary of the presented work and an outlook for possible future research. Additional sections include literature references, appendices with the revision of HC_5N electronic spectroscopy and the visualization of vibrational modes, a list of figures, a list of tables, as well as abstracts in Polish and in French.

Unless otherwise stated, all equations in this dissertation employ SI units. Abbreviations are listed in the “Glossary” (p. ix) preceding this chapter.

2 MATERIALS, TECHNIQUES AND METHODS

Following the goals formulated in Chapter 1.3, most of this Thesis describes cryogenic experiments, performed at temperatures on the order of 10 K. Solid Ar or Kr matrices were typically used and UV radiation from excimer lasers was employed in photolysis experiments. Products were identified with vibrational and electronic spectroscopy. Quantum chemical calculations assisted in the identification of features in the resulting spectra.

The first part of the research (Chapter 3.1) was devoted mainly to CH_3C_3N isomerization upon UV-irradiation. Product identification was accomplished based on the available IR absorption spectra of pure substances and on quantum chemical calculations. These experiments were performed in IPC PAS.

Thorough characterization of cryogenic matrix-isolated, gaseous and solid CH_3C_5N (Chapter 3.2) involved IR absorption and Raman scattering measurements, as well as UV-Vis absorption and luminescence spectroscopy. The experiments were performed in IPC PAS (gas phase, pure solid, and matrices: Ar, Kr, Xe, N_2) and ISMO (matrices: Ne and *p*-H_2).

The method of choice for studies of UV-induced formation of longer chains from smaller, specially selected molecules in cryogenic matrices (Chapter 4) was luminescence spectroscopy. This was possible because the targeted products were found to phosphoresce. These experiments were performed in ISMO.

Technical aspects of the research are described in subsequent sections. At first, the technique of matrix isolation fundamental to most of the experimental work described here – is briefly explained. This is followed by two sections dealing with vibrational and electronic spectroscopy that stress some of their characteristic features when applied to cryogenic samples. Later on, chemicals used in the experiments are listed and the sample preparation and deposition are explained. Further on, technical details concerning cryostats, and some aspects of gas phase and photochemical experiments are provided, followed by the details of spectroscopic measurements and description of experimental set-up. The last part of this chapter presents a brief summary of the theoretical methods behind the reported calculation results.

2.1 Providing stability: cryogenic matrix isolation

Matrix isolation is a technique that involves trapping chemical species known as *guest* molecules or atoms in an unreactive solid matrix, called the *host*. The easiest way to do this, is to freeze a previously prepared solution of a chemical under investigation. At the inception of the matrix isolation technique, molecules were generally frozen in transparent organic glasses, often a mixture of ethyl ether, isopentane, and ethyl alcohol [163], known as EPA), that is still popular today. Thanks to further developments, mainly by George C. Pimentel [164], who used rare gases instead of organic liquids, the technique has its modern

look, where frozen inert gases are often used as host materials for molecules under study. The choice of the host (*e.g.* organic glass, polymer or rare gas) depends on experimental needs. Here, mainly rare gases (and nitrogen) were used, as they are inert and transparent media in the spectral range of interest. In order to study isolated molecules, highly diluted gas mixtures have to be used.

When a gas mixture is cooled sufficiently, it forms a solid matrix in which the guest molecules are embedded. When sufficiently diluted, one guest molecule is isolated from another by rare gas atoms and interactions between the guest species are minimized. High dilutions also help decrease the possibility of forming intermolecular complexes or larger molecular aggregates between multiple guest molecules. For well isolated guest molecules, the energies of vibrational, electronic or vibronic transitions tend to be similar to those observed for free, gas-phase molecules, and the usual[1] lack of molecular rotations contributes to a relative ease of spectral assignments. However, this ideal[2] isolation is difficult to achieve, since guest-guest interactions (*e.g.* hydrogen bonding) which are always present can sometimes be substantial and may cause formation of intermolecular complexes or aggregates in a gas mixture prior to or during matrix solidification process.

With the exception of very small species such as hydrogen atoms, once guest molecules are trapped inside a rigid, inert matrix, they cannot diffuse. This means, there is no possibility of contact between the guest molecules that would lead to reactions as might happen for example in a liquid. Individual molecules, surrounded by rare gas atoms, occupy certain positions often referred to as *cages*. Mobility of guest molecules in a matrix can be restored by elevating the temperature or absorption of radiation. After absorption of one or more photons, a guest molecule may reach an excited state. The excited molecule may then relax *via* energy transfer to the matrix, photon emission or dissociation (or all of these). The first of these possibilities results in the excitation of phonons or local heating, possibly rearranging host lattice atoms allowing the guest molecule limited mobility. The matrix may therefore play the role of energy sink/reservoir. When dissociation of the guest molecule occurs, the excess energy released can take the form of kinetic energy of the resultant fragments. Such fragments, if small (*e.g.* atomic) and energetic enough, may migrate, possibly taking part in chemical reactions themselves. Alternatively, when the fragments remain in the native cage, they may recombine and recreate the original species or produce an isomer. The cage effect favours isomerization in comparison with gas and liquid phases.

The main advantages of using the matrix isolation technique are:

- isolation of molecules and inertness of the host leading to:
    - a convenient approximation of the gas phase and insight to intrinsic molecular properties;
    - the possibility of tracking intermediate products of photochemical reactions

[1] More or less hindered rotations can be observed for diatomic hydrides. Other small (mostly diatomic) molecules may exhibit a restricted motion (frustrated rotation), known as *libration*.

[2] Ideal for the purposes of this research. Other studies might deliberately increase concentration of the guest in order to study molecular interactions. Sometimes higher concentrations are also needed to acquire a sufficient S/N, *e.g.* for Raman spectroscopy.

(free radicals, ions, high energy isomers), as even small energy barriers are likely to prevent any structural changes, including those towards more thermodynamically stable structural and conformational isomers [165];
    - very small solvent-shifts (see section 2.2.1), as compared to those observed for traditional solvents;
    - easy observation of long lifetime emissions (see section 2.2.2);
- samples are transparent in a wide spectral range, including 400 – 53 000 cm^{-1}, which is of interest in this study;
- spectra are simplified due to the relative lack of molecular rotations (also a disadvantage, see points below) – sharp bands are typically observed instead of rotational branches;
- spectra often do not exhibit features originating in excited vibrational states (*hot bands*);
- matrices are a first approximation for astrophysically-relevant ices made up *e.g.* of water or carbon monoxide although direct analogues of cryogenic rare gas matrices are not expected in interstellar environments;
- low temperature spectroscopy is expected to be directly relevant to astrochemistry, given that low rotational temperatures have been found for many interstellar molecules (*e.g.* HC_5N rotational temperatures are 28 K, 5.5 K, and 13 K in the interstellar sources Sgr B2(N), TMC-1, and IRC +10216, respectively [166]).

The main disadvantages are:

- no precise insight to molecular geometry *via* the derivation of rotational constants from rotational spectra (nevertheless, vibrational spectroscopy, possibly combined with isotopic substitution studies and with quantum chemical predictions, still permits for the elucidation of geometry);
- complications due to non-identical matrix microenvironments, *i.e.* the *site effect* (see section 2.2.1);
- necessity of high vacuum to prevent the trapping of atmospheric gases.

A more elaborate description of matrix isolation can be found in the books on which this section was largely based: *Matrix-Isolation Techniques. A Practical Approach*, by Dunkin [167] and *Physics and Chemistry at Low Temperatures*, edited by Khriachtchev [168].

2.2 Spectroscopy

2.2.1 Vibrational spectroscopy

Vibrational spectra are fingerprints of the molecules, usually allowing for their unambiguous identification. In general, there are numerous spectroscopic techniques that can provide information about vibrational energy levels. In this subsection, the application of IR absorption and Raman scattering measurements in matrix isolation studies is highlighted.

The two spectroscopic techniques are complementary due to different selection rules. To be spectroscopically active, a vibration must lead to a non-zero derivative of the electric dipole moment (IR) or polarizability (Raman) at the equilibrium geometry. Thus, some vibrations

might appear stronger or weaker depending on the technique used (vibrations might also be absent as in the case of centrosymmetric molecules, where the mutual exclusion rule applies). IR absorption spectra show the absorption of photons leading to excitation of a given vibrational level. The Raman technique is based on inelastic scattering where photons excite a molecule to a state (virtual) higher than the initial vibrational state. The excited molecule may then relax to a vibrational state higher than the original one, scattering the light of a smaller energy (for the *Stokes scattering* case) than that used for the excitation. The energy difference corresponds to the spacing between vibrational levels.

Positions of vibrational bands of matrix-isolated molecules tend to be shifted when compared to gas-phase spectra. Usually, positions of vibrational bands in matrices are lower in wavenumber (‘red shifts’) than those in the gas phase. This stems from attractive interactions present in the matrices such as van der Waals forces. A typical gas-to-matrix shift is on the order of few cm^{-1}. Usually, it does not exceed 1 % for solid Ar, the most popular matrix host. This shift is much smaller than for other commonly used cryogenic matrices (such as polycyclic aromatic hydrocarbons, also referred to as Shpolskii matrices). These shifts depend on the type of vibrational mode (stretching/bending) and on the host (usually increasing with the host atom mass). However, if there are repulsive interactions, shifts towards higher wavenumber (‘blue shifts’) may also be observed. These shifts are due to changes in molecular potential energy surfaces, that get flattened and lowered in the presence of attractive forces, and behave in the opposite way when repulsion is dominant.

With the exception of the smallest molecules (footnote p. 16), bands observed in the spectra of matrix-isolated molecules do not possess rotational structures as rotational motions are blocked. Thanks to this, matrix spectra are often simpler and have narrower bands.

On the other hand, there are several effects that complicate the vibrational spectra of matrix-isolated molecules. The most often observed are listed below.

1. Matrix sites (or "site bands"). Some bands, in both vibrational and electronic spectra, can appear as multiplets with components typically separated in IR by a few cm^{-1}. The multiplet structure stems from guest molecules trapped in a particular host microenvironment (*site*) where the guest must adopt a particular geometrical arrangement with respect to the host. Multiple sites are, in principle, possible and it is the arrangement of the host that defines the nature and potential occupancy of a given site. By changing host gas, these microenvironments also change, allowing them to be identified. Heating a matrix without desorbing the host can lead to relaxation of guest molecules, allowing them to take “more comfortable” (stable) positions in their respective microenvironments. Thus, thermal annealing can also be used to identify site bands, and often to reduce their number, simplifying the spectra.
2. Degeneracy can be removed. Degenerate vibrations, appearing as one band in the spectra of gaseous substance, might appear as multiplets in matrix spectra, when site symmetry (point group) of the guest molecule in a matrix is lower than that of unconstrained species.
3. Presence of phonons, especially vibration-phonon coupling. Vibrational, translational (depending on mass) and rotational (depending on moment of inertia)

motions of the guest molecule may couple with lattice vibrations of the host. The wavenumbers of phonons (usually not higher than 200 cm^{-1} [169]) and intensity of corresponding bands depends on temperature [170] and pressure [171].

4. Anharmonic interactions in a molecule, such as Fermi-type resonances. Although such interactions are a property of the guest molecule itself, they may be influenced by a matrix
5. Interactions between two or more guest molecules. These can usually be identified by performing experiments at various dilution ratios.
6. Interactions of guest molecules with impurities (*e.g.* atmospheric) or other molecules created in the matrix, especially during photolysis.

2.2.2 Electronic spectroscopy

Electronic energy levels may be probed (disregarding more exotic approaches) either by UV-Vis absorption or by luminescence measurements. Insight to the energetics of these levels may also be offered by studying the luminescence intensity as the function of excitation energy (so-called luminescence excitation spectroscopy).

The use of matrices can modify electronic spectra in ways that may or may not be useful depending on what information is required. For these experiments, use of matrices is mostly beneficial. In the case of luminescence, cold and weakly emitting molecules are concentrated in an inert matrix having a small, well-defined area. Luminescence signals are more easily observable than for gas phase samples where the emitters tend to disperse. Matrices also prevent the diffusional deactivation of triplet states that could otherwise occur following collision with a phosphorescence quencher such as another excited molecule (triplet-triplet annihilation), paramagnetic impurities (*e.g.* dioxygen) or a boundary wall (window). An important difference between electronic spectra of matrix-isolated and gaseous species, is that some electronic states might become available more easily in matrices than in the gas phase if a (slight) symmetry break in the guest molecule is induced by its microenvironment. Comparisons between the UV absorption of a gaseous substance with the corresponding UV absorption (or luminescence excitation) of a cryogenic matrix may assist in the recognition of hot bands. Identification of hot bands can lead to the determination of a vibrationless origin wavenumber (when selections rules prohibit the appearance of a '*0-0*' band). Furthermore, the use of various matrix hosts can sometimes allow (by studying the host-induced wavenumber shifts) for separation of the bands coming from different electronic systems of a given compound.

Electronic spectroscopy may provide information not only on the electronic energy levels of the molecule, but also on vibrational excitations in various electronic states. The basic principles, of particular importance in this work, are briefly presented below.

1. All compounds for which phosphorescence has been observed here, have singlet electronic ground states (S_0). After excitation to one of the higher singlet states S_n, and following internal conversion processes accompanied with vibrational relaxation, some of the molecules can undergo intersystem crossing to a lowest energy triplet state (T_1). A rare gas matrix may promote this process due to large

spin-orbit coupling between a molecule and a host atom (the so-called *external heavy atom effect*[1], observed mainly in Xe and Kr matrices), and may also increase the $S_0 \leftarrow T_1$ phosphorescence rate [172]. Before the final relaxation to S_0 occurs, the molecule reaches the lowest vibrational level of the triplet. The matrix environment can aid in collecting the excess energy that needs to be dispersed during this process. The process is very efficient due to high vibrational energy level density and possible coupling with matrix phonons. It is completed on the time scale of ps (compared to triplet-state lifetimes on the order of μs or ms). Depending on Franck-Condon factors (overlap of lower- and upper-state vibrational wavefunctions for a given geometry), the $S_0 \leftarrow T_1$ transition leads, with dissimilar probabilities, to certain vibrational levels of the ground electronic state. A number of vibronic bands are consequently observed, reflecting the vibrational energy levels of the ground electronic state.

2. Information on vibrational energy levels in excited electronic states S_n can be extracted from the observed transitions to these levels originating, typically, in a vibrationally relaxed S_0 state. Which vibronic bands are observed again depends on relevant Franck-Condon factors (thus, on molecular change accompanying the electronic transition).

2.3 Chemicals

Table 2 lists the chemical compounds, available through preparatory organic synthesis, that were studied spectroscopically (compounds *1-6*) or were used as precursors (compounds *7-10*) leading to formation of HC_7N, HC_9N, $C_{10}N_2$ or CH_3C_7N. The listed compounds (apart from molecules *9-10*), were obtained in the framework of a collaboration with Jean-Claude Guillemin (Ecole Nationale Supérieure de Chimie de Rennes, France) and were synthesized either in IPC PAS or in Rennes. The author of this Thesis participated in the preparation of species *1-3* and *6*.

The storage of several of these substances is demanding. They were kept in glass tubes, at low temperatures. Chemicals *1*, *6*, and *9*, were stored in a standard freezer capable of reaching -20°C. Chemicals *3-5*, *7*, and *8*, were stored at -78°C (dry ice). Chemical *2*, even while kept at -78°C, converted into species *4*. Thus, to assure its purity and hinder such a transformation, the sample tube was stored inside a Dewar vessel filled with liquid nitrogen (-196°C). Chemical *9* was commercially available (AirLiquide). Chemical *10*, gaseous acetylene (AirGas, Inc.) was stored and used as provided by the manufacturer.

[1] The effect is dependent on spin-orbit coupling between the molecule of interest and surrounding, perturbing matrix atoms. This coupling is proportional to Z^4/n^3, Z being the nuclear charge of a matrix atom, and n – its principal quantum number [172], thus it is stronger for heavier atoms.

Table 2. List of the molecules used in the experiments described in the Thesis. Literature references correspond to the used synthesis methods.

No.	Chemical		Systematic name	Used name[a]	Ref.
1	CH_3C_3N	$H_3C–C≡C–C≡N$	2-butynenitrile	methylcyanoacetylene	[173]
2	HC_3H_2CN	$HC≡C–CH_2–C≡N$	3-butynenitrile	propargyl cyanide	[174]
3	HC_3H_2NC	$HC≡C–CH_2–N≡C$	3-isocyanoprop-1-yne	propargyl isocyanide	[174]
4	CH_2CCHCN	$H_2C=C=CH–C≡N$	buta-2,3-dienenitrile	allenyl cyanide	[174]
5	CH_2CCHNC	$H_2C=C=CH–N≡C$	1-isocyano-1,2-propadiene	allenyl isocyanide	[141]
6	CH_3C_5N	$H_3C–C≡C–C≡C–C≡N$	2,4-hexadiynenitrile	methylcyanodiacetylene	[150]
7	HC_5N	$H–C≡C–C≡C–C≡N$	2,4-pentadiynenitrile	cyanodiacetylene	[175]
8	C_4H_2	$H–C≡C–C≡C–H$	1,3-butadiyne	diacetylene	[176]
9	CH_3C_2H	$H_3C–C≡C–H$	1-propyne	propyne	-[b]
10	C_2H_2	$HC≡CH$	ethyne	acetylene	-[b]

[a] The molecules are referred to by this name in the text.

[b] Products commercially available.

In all of the experiments, the purity of the substances was checked using IR absorption spectroscopy. As most of the chemicals were stored in dry ice, the most common impurity was CO_2. Before every use, substances were purified either by freeze-pump-thaw cycles, provided that all three phases could be reached without chemical decomposition, or by pumping at a sufficiently low temperature. Liquid nitrogen, a cooled ethanol bath or dry ice were used as freezing agents. The purification procedure was as follows. The sample kept at low temperature was opened to a vacuum line (also referred to as a "manifold") and any volatile species were pumped away immediately. Then, the cooling agent was removed and a pressure rise was observed. For a short time (on the order of several seconds) this first volatile fraction was removed, assuming a higher content of volatile impurities in it, such as carbon dioxide. The pumping was stopped, sample cooled down, and the cycle was repeated for 2-3 times. Only then, the fraction of the chemical that evaporated filling the vacuum line was taken for use in the experiments (see next section). The substance filling the space between the tube and the manifold was recovered by cold pumping (liquid nitrogen was used to force the condensation of the sample back into the tube).

It was impossible to measure the substance temperature at the moment of its evaporation to the manifold (after sample preparation was completed, the gas was kept at room temperature). Only the lowest temperature of purification was known. For molecules *1-6* and *8-9* it was the freezing temperature of freeze-pump-thaw cycles, namely that of dry ice or liquid nitrogen (for molecule *2*, dry ice only). Only pumping at low temperature, rather than freeze-pump-thaw cycling, was used for HC_5N, *7*, (-78 to -55°C), since that compound sublimated or polymerized easily upon heating (the white substance turned pink), resulting in an inaccessible 'thaw' part of the cycle. There was also no need for freeze-pump-thaw cycling in the case of CH_3C_5N, *6*, a substance that was solid at room temperature (and yet sufficiently volatile for the adopted standard sample preparation method; see next section). For all applied chemicals, the first purification pumping was performed at the temperature of liquid nitrogen.

The gases used in the experiments performed in IPC PAS were: Ar (5.0 Multax s.c.), Kr (5.0 Messer Austria GmbH), Xe (4.5 Messer Austria GmbH), N_2 (Multax s.c.). In experiments performed in ISMO, the following gases were used: Ar (6.0 Messer), Kr (4.0 Messer), Ne (5.0 Messer) and H_2 (5.5 Messer). All gases, except N_2, were used as provided by the manufacturer. In case of N_2, the first matrix spectra showed intense CO_2 and H_2O bands and purification of the host gas was needed. For this reason, nitrogen line was passed through a liquid nitrogen bath to freeze out the impurities.

Most of the experiments devoted to photochemical syntheses (described in Chapter 4) were performed with the use of Kr. This choice was made based on two factors. Firstly, previous studies showed that higher quality spectra were obtained for solid Kr than for Ar matrices. Secondly, there was the hope to promote the heavy atom effect. The use of Xe would enhance this effect even more, but Xe has a high polarizability and often participates in strong host-guest interactions, complicating spectra. Additionally, Xe is much more expensive than Kr. Another particular gas used here is parahydrogen (p-H_2). It forms soft (in comparison with other gases) matrices that permit for rotation of small embedded molecules to a larger extent than any other solid host. This softness also minimizes site effects.

2.4 Sample preparation

The purified sample was transferred from the glass tube to a stainless steel manifold (pumped off to a residual pressure of not more than 4×10^{-6} mbar), where a highly diluted mixture with a host gas was prepared[1]. Standard manometric methods were applied, with the use of capacitance pressure gauges. In experiments aimed at studying UV-induced bimolecular reactions, the involved chemicals were first combined in the manifold, and then an inert gas was added. This guaranteed the uniform mixing of gaseous components[2]. The host gas purity was at least 99.99 % to minimize the contaminations.

In the experiments described here, the host:guest ratio was at least 200, and usually on the order of 500-1000. However, in certain cases, due to the adsorption of chemicals onto manifold walls[3], the actual matrix ratios could only be estimated.

The gas transfer, either to a manifold or to a cryostat, was through stainless steel or, in the case of inert gases, copper pipes. Once ready for deposition, a mixture was directed to a <5 mm diameter nozzle whose end was ~2 cm away from a cold window or, for Raman scattering spectroscopy experiments, a gold-plated-copper cold substrate. Deposition rate, controlled by a "variable leak" valve (Granville-Phillips, 203 series), did not exceed few mmol/h.

Both the rate of deposition of a gas mixture and the temperature of the substrate influence the light scattering by a sample. The deposition window (1-2 cm in diameter) has to be

[1] Parahydrogen sample preparation was different and is described in section 2.9.

[2] In other laboratories, there are also set-ups in which the molecules are codeposited (twin jet), so they have no contact prior to the deposition. Here, such a contact is appreciated, as the goal was to promote reactions between molecules.

[3] It was observed in the described experiments, especially for HC_5N and CH_3C_5N, as pressure decrease inside the manifold filled with a chemical. No quantitative studies of this effect have been performed.

cooled down to a temperature, at which the deposited sample pressure does not spoil the vacuum (*i.e.* does not exceed ~10^{-7} – 10^{-6} mbar). In the case of Ar, the deposition was usually performed at 22-23 K. In case of Kr, the deposition temperature was usually 28-30 K. Xe deposition started at 100 K, and then the temperature was gradually lowered, down to 33 K. For IR absorption studies, N_2 was deposited at 15 K, while for UV-Vis studies, where the transparency of sample is particularly fragile to the phenomenon of radiation scattering, the highest optical quality was obtained when the substrate window was at first cooled down to the lowest achievable temperature and then it was reheated to ~60 K. The deposition started at this elevated temperature and continued when the heater was turned off. Ne and *p*-H_2 needed lower solidification temperatures, in the range 3-4 K. In the case of CH_3C_5N, also the pure solid substance was studied, and its deposition was performed either at 190 K, to obtain a sample of high optical quality, desirable for electronic spectroscopy, or 6.5 K, for an amorphous sample used in vibrational spectroscopy measurements (several tests were performed to find these conditions).

2.5 Cryostat

The low temperature experiments were conducted with closed-cycle helium-cooled refrigerators (cryostats) that achieve temperatures low enough for standard rare gas matrix isolation work and that are able to sustain those temperatures in a stable operation mode for long time.[1]

Cryostats used in the course of this work are of the Gifford-McMahon (GM) type. The main cooling step is the isentropic expansion of high pressure helium gas into a chamber. The gas already present in that chamber is also pushed out. The expanding gas cools to a lower temperature, also cooling the sample attached to the "cold finger" (see Figure 2). Then, through a low pressure path, the gas circulates back to a secondary (external) refrigerator (or regenerating material), returning to ambient temperature. It is then compressed again and moved to the regenerator, from which it restarts the cycle [177].

For most of the closed-cycle cryostats used in this work, temperatures below 10 K could be obtained. More advanced systems, such as the one used here for Ne and *p*-H_2 experiments, can achieve temperatures of 3 K and less. Thus, the pressure in the cryostat vacuum chamber must be sufficiently low (typically 10^{-7} – 10^{-6} mbar) to ensure the proper thermal insulation and to eliminate the condensation of atmospheric gases. Once temperature and pressure conditions are fulfilled, the previously prepared gas mixture can be directed onto a cold substrate (transparent window or metal plate). Deposition window holders are typically made of high-purity copper, as it has very good thermal conductivity at low temperatures, is versatile (small elements, like screws, can be machined), and relatively cheap.

[1] Open-cycle solutions also exist that employ an external supply of liquid He. While these refrigerators can access lower temperatures than closed-cycle refrigerators and are subject to fewer mechanical vibrations that might affect a measurement, they are in principle not capable of maintaining low temperatures over long time and have high costs associated with consumption of liquid He.

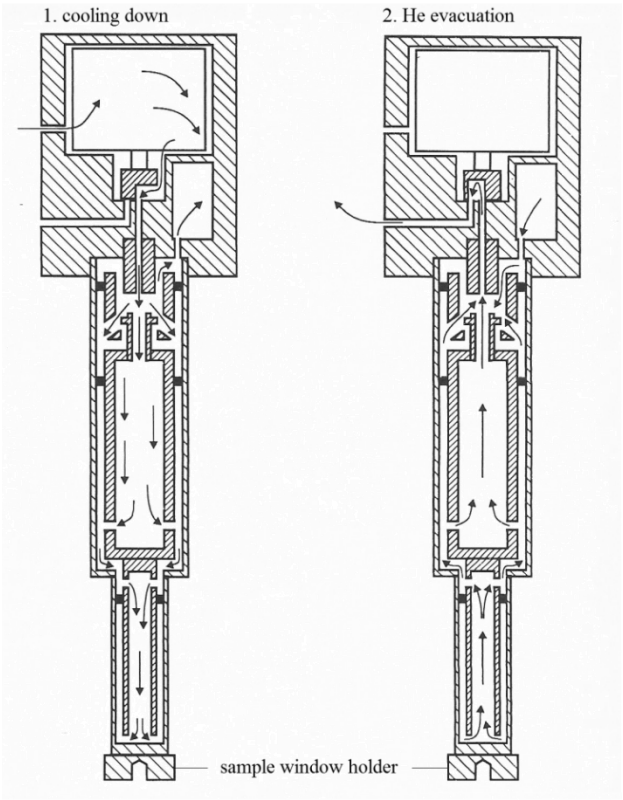

Figure 2. Closed-cycle helium refrigeration. Schematics depict a cryostat head featuring two stages of expansion. Arrows show the directions of He flow in the two consecutive phases: cooling down (left), and evacuation of the heated He (right). The bottommost part, to which the sample substrate is attached, is usually referred to as *cold finger*. Figure adapted from Ref. [167].

The cryostats used in IPC PAS were *Displex* 1RO2W-H (Air Products, Inc., capable of reaching the temperature of 15 K) and DE-202SE (Advanced Research Systems; 5.5 K). In ISMO, these were *Displex* DE202FF (Air Products, Inc.; 7 K) and ICES3731 (ICEoxford Ltd.; 3 K). The latter one was employed in *p*-H_2 and Ne experiments only. Hydrogen *ortho-para* conversion was based on *Displex* DE202FF or DE-202SE (7 K or 17 K, respectively) cryostats. Temperature of cold fingers was monitored and stabilized by Lake Shore Cryotronics, Inc. temperature controllers.

2.6 Gas-phase experiments

For one of the compounds investigated here (CH_3C_5N), spectroscopic measurements were carried out not only for cryogenic samples, but also for the gaseous ones. This was accomplished with the use of 10 cm long gas cells equipped with either quartz or KBr windows, for transparency in UV-Vis or IR ranges, respectively. These experiments were performed in IPC PAS.

2.7 Photochemical experiments

In order to induce photochemical reactions, a sufficient excitation of the molecule is needed, possibly leading to the dissociation. To provide sufficient energy, UV sources are necessary (as shown in Chapter 1). One powerful and effective source is an excimer laser. In both laboratories (IPC PAS, ISMO), the Coherent *Compex Pro* UV excimer lasers were used. Depending on the gas mixture inside the laser, photons of various energy could be

produced. With an ArF mixture, the one mostly used here, the pulse wavelength is 193 nm (6.42 eV, 51 800 cm^{-1}), while with a KrF mixture, it is 248 nm (5.00 eV, 40 300 cm^{-1}). The energy delivered to samples was ~5 mJ/cm^2 per pulse, with a repetition rate of 10 Hz. In the case of CH_3C_3N photolysis, the ArF pulse energy was around four times lower.

In cases where unstable products (such as C_5N^- or high energy isomers from C_4H_3N family) were studied, the irradiation and spectroscopic characterization were done at constant temperature. When the aim was to induce reactions, the cryogenic matrices subjected to the laser radiation were usually subsequently heated up by 10-20 K to facilitate the mobility of formed species. They were then re-cooled for spectroscopic studies. For such studies, the matrix could also be irradiated at an elevated temperature (around 30 K for $Kr/C_4H_2/HC_5N$ mixtures) to promote reactions during irradiation.

2.8 Spectroscopic measurements

In order to enable spectroscopic measurements, optics transparent in the spectral regions of interest were needed. The optics used for these experiments are presented in Table 3.

Table 3. Applied optical windows and their spectral transparency ranges [178,179].

	CsI	CaF_2	Sapphire	Quartz	KBr	Diamond
Transparency range [cm^{-1}]	150 – 33000	1000 [a] – 66000	1600 [a] – 66000	3000 – 55600	400 – 33000	10 – 45000
Application	external and deposition windows (IPC PAS cryostats)	external windows (ISMO cryostat)	deposition window (ISMO and IPC PAS cryostats)	external windows (IPC PAS gas cell and cryostats)	external windows (IPC PAS gas cell)	deposition window for *p*-H_2 and Ne experiments (ISMO cryostat)

[a] Values corrected accordingly to the obtained experimental results.

2.8.1 Infrared absorption spectroscopy measurements

The main technique used here for studying vibrational spectroscopy is that of infrared absorption. For these experiments Fourier transform (FT) spectrometers were employed. Briefly, use of an FT instrument allows for an acquisition of a spectrum without scanning the wavelength of the light, which results in higher S/N than in conventional (dispersive) instruments. The maximum resolution of a Fourier transform measurement depends on the distance travelled by the moving mirror of the interferometer; better resolution necessitates a longer distance, and therefore a longer acquisition time. Other factors also influence the resolution, such as the speed of mirror displacement, detector response time, and divergence of the IR beam.

In IPC PAS, infrared absorption was measured with the use of Bruker VERTEX 70 spectrometer, equipped with a KBr beamsplitter and liquid nitrogen-cooled wide range HgCdTe or sandwich InSb + HgCdTe detector. The measured range was confined to the region between 400 – 6000 cm^{-1} with a maximum resolution of 0.16 cm^{-1}. Often, lower resolution was used to strike a balance between acquisition time and obtained S/N. It was verified that the use of lower resolution (*i.e.* 1 cm^{-1} for gaseous CH_3C_5N) did not noticeably

spoil the resolution of the spectral features observed Typically, several hundreds of spectra were registered (and averaged). A miscalibration of the spectrometer was found by the end of this doctoral work, with an error reaching +0.3 cm^{-1} in the 2300 cm^{-1} region. The problem has not been fully addressed yet and the data reported here are not corrected.

In ISMO, IR absorption spectra were registered using a Fourier transform Nicolet *Nexus* 670/870 IR spectrometer equipped with a liquid nitrogen-cooled HgCdTe detector and KBr beamsplitter. Spectra were recorded between 950 and 4500 cm^{-1}, as necessitated by the cryostat optics with a spectral resolution that varied between 0.125 and 0.5 cm^{-1}.

2.8.2 Raman scattering spectroscopy measurements

Raman scattering experiments were performed for Ar matrix-isolated and pure solid CH_3C_5N samples, using a Renishaw *inVia* Raman spectrometer (IPC PAS).

The main advantage of using the Raman instrumentation here was the access to data complementary to the IR absorption studies. However, analyte concentrations higher than in IR measurements were necessary and several-hour scans (resulting in several hundreds of spectra) had to be performed to obtain satisfactory S/N. Due to constant excitation using a powerful laser during Raman scattering measurements, the sample had to be controlled for possible losses or destruction.

The Raman spectrometer (or, more exactly: Raman microscope) was equipped with a 30 mm or 60 mm objective lens (Leica) and a monochromator featuring a 1200 or 1800 groove/mm diffraction grating. The laser-illuminated sample area was ~20 μm in diameter. Typically, an Ar ion laser (Modu-Laser, Stellar-REN, operating at 514 nm) was used. The 785 nm line of a Renishaw HPNIR785 diode laser was used for some measurements of pure solid samples, allowing for the identification of artifact bands that change their position upon variation of the excitation wavelength. The detection was performed with a CCD camera. The relative wavenumber range of the Raman spectrum was 100 – 3400 cm^{-1}. Achieved resolution was not worse than 6 cm^{-1}.

The observed Raman intensity is proportional to $\frac{(\nu_0-\nu_i)^4}{\nu_i}\frac{S_i}{1-\exp\left(\frac{-h\nu_i c}{kT}\right)}$, where ν_0 is the wavenumber of the excitation laser, ν_i and S_i are the wavenumber and Raman activity of the *i*-th vibrational mode, *T* is temperature, and *h, c,* and *k,* are Planck constant, speed of light, and Boltzmann constant, respectively. Raman activity values can be computed on theoretical grounds, the above formula is therefore useful for predicting the Raman spectrum intensity patterns for a given excitation laser and temperature.

2.8.3 Electronic spectroscopy measurements

In the work described here, the data on electronic spectroscopy came from three sources:

1. UV-Vis absorption spectra.

Measurements were performed in IPC PAS for gaseous and cryogenic matrix-isolated CH_3C_5N, using UV-3100 and UV-2700 Shimadzu Scientific Instruments dual-beam

spectrophotometers equipped with grating monochromators. Instrumental resolution was set to 0.5 nm and up to 100 scans were typically averaged to achieve satisfactory S/N. While increasing the resolution to 0.2 nm resulted in a narrowing of the observed absorption bands, it did not influence the ability to resolve them for the chemicals tested here. Measurements of gaseous samples were accomplished with an evacuated cell (identical to that containing the measured substance) inserted to the reference beam of the spectrophotometer, otherwise the reference channel was left empty. The shortest accessible wavelength was ~195 nm while the longest one was in the IR range, 2.7 μm or 3.1 μm, for the respective spectrometers.

2. Dispersed phosphorescence spectra.

The majority of luminescence studies were performed in ISMO. The emission from matrices containing species of interest was registered with the use of an Andor *iStar* DH720 CCD camera coupled with a 0.3 m Acton SpectraPro 2300i (Princeton Instruments) grating monochromator (1200 grooves/mm, resolution of ~0.08 nm) or with a 0.6 m Jobin-Yvon grating monochromator (1200 grooves/mm, resolution of ~0.04 nm). The Jobin-Yvon monochromator was also connected to a photomultiplier (Hamamatsu H3177-50 PMT). The maximal detection range was between 200 – 850 nm.

The use of a time-gated camera allowed for the separation of long-lived emission bands (phosphorescence) from the initial laser pulse and from any possible short-lifetime bands. It could also allow differentiate bands coming from various emitters. The time range of measurements was 10^{-7} – 10^{-2} s, with a minimum gate opening time of 2 ns.

PMT measurements were used mainly to observe phosphorescence decay, as they were free of ~1s limitation for maximal half-life as compared to the CCD. It was also used to measure C_5N^- phosphorescence excitation spectrum. In parallel to the phosphorescence intensity measurements, the excitation laser intensity was monitored with a photodiode.

The electronic luminescence of CH_3C_5N was partly studied in IPC PAS with an FS 900 (Edinburgh Instruments Ltd., U.K.) spectrofluorimeter. It was equipped with a high-pressure xenon lamp (450 W), excitation and detection monochromators featuring 1800 grooves/mm gratings, and a photon-counting Hamamatsu R-955 system. Resolution used for dispersed phosphorescence and phosphorescence excitation measurements was in the range between 0.1 nm and 0.5 nm. Luminescence lifetime was studied with an FL 900 (Edinburgh Instruments Ltd., U.K.) time-resolved fluorimeter, capable of measuring half-lives from ~1μs to 1 s. It was equipped with a pulsed microsecond nitrogen discharge lamp.

3. Phosphorescence excitation spectra.

In IPC PAS: FS 900 spectrofluorimeter (as above).

In ISMO: Luminescence was selectively excited with tunable sources. First experiments were performed using a dye laser (Lambda Physik LPD3000); Coumarine 540A was used as a dye and a XeCl excimer laser (Lumonics) for pumping. The 520-570 nm range was mostly explored, where the majority of detected compounds could be studied. Further experiments

were performed in a wider spectral range with the use of *Surelite II – Horizon* (Continuum) optical parametric oscillator (OPO) system. In OPO systems, *signal* and *idler* are two output waves that are generated in a nonlinear crystal from the input laser wave (*pump*). Signal is the one of a higher frequency. All three (signal, idler and pump) might be mixed together. Because of the internal configuration of crystals inside the OPO laser, it could operate continuously in the following ranges of interest: 192 – 208 nm (doubled signal), 208 – 400 nm (doubled and mixed signal), 400 – 500 nm (pure signal). Typically, the laser operated in the 192-400 nm range. Within the 208 – 400 nm range, there are two wavelengths, where the crystal used for the frequency doubling was changed, at around 234 nm and 292 nm. Therefore, spectra had corresponding "holes" at these wavelengths. Another technical difficulty found when using this system was that even if calibrated, the crystals did not always reach the requested positions in the requested time, resulting in intensity variations of the output beam and a consequent increase in the S/N of collected luminescence signals. Synchronization of the excitation pulses, either from the excimer laser or tunable (dye or OPO) laser, with the detection of the luminescence signal was accomplished with the custom-made (ISMO) hardware and software. Signal acquisition (either from a PM or photodiode) was performed with the use of a PCIe-6251 card (National Instruments) supported with *LabView 8.5* to ensure communication with other software. Monochromator scanning was controlled by *LabView*-based software, created at ISMO.

Coupling of a CCD camera with a tunable laser allowed for simultaneous observation of luminescence emitted by multiple chemical species and for the recognition of excitation patterns characterizing these emissions. This was analysed with the help of two-dimensional emission-excitation mapping, which allowed pinpointing of the excitation wavelengths suitable in the detailed analysis of the dispersed luminescence spectra.

2.9 Experimental set-up

The experimental set-up used in ISMO is schematically presented in Figure 3. Firstly, the gas mixture containing the molecules of interest (propyne and cyanodiacetylene are presented as an example) diluted in the host gas is deposited onto a cold sapphire substrate to form a cryogenic matrix. This cryostat head, together with the substrate window, can be rotated around a vertical axis, to optimize its angle either for the deposition or for subsequent spectroscopic studies. Following deposition, the composition of the matrix is verified using IR spectroscopy. Next, the matrix sample of a satisfactory quality is irradiated in the UV using an excimer laser, typically for several hours, to induce photochemical transformations. Finally, the products are analysed with electronic emission spectroscopy, employing a tuneable laser as the excitation source. IR spectroscopy is used to monitor the consumption of precursor species and/or the formation of new products, whenever possible.

Ne and *p*-H_2 experiments did not involve photochemistry and did not employ the excimer laser. For *p*-H_2, there were two more technical details specific to this measurement. First, two cryostats were used, as described in [180]. Normal hydrogen, containing both *ortho* and *para* spin isomers, was converted to pure *para* form in the primary cryostat using the catalyst Fe_2O_3, kept at 17-20 K. The second difference, is that no gas mixture preparation was performed prior to the deposition. Instead, parahydrogen was passed over a compound

to be studied and mixed with its vapours just prior to reaching the cold window for deposition.

For experiments performed in IPC PAS, the set-up was similar, though the cryostats were moveable. This mobility allowed for use of diverse measurement equipment including a UV-Vis absorption spectrophotometer for direct absorption studies and a spectrofluorimeter for emission studies. Similarly as in ISMO, IR absorption was probed using an FTIR spectrometer.

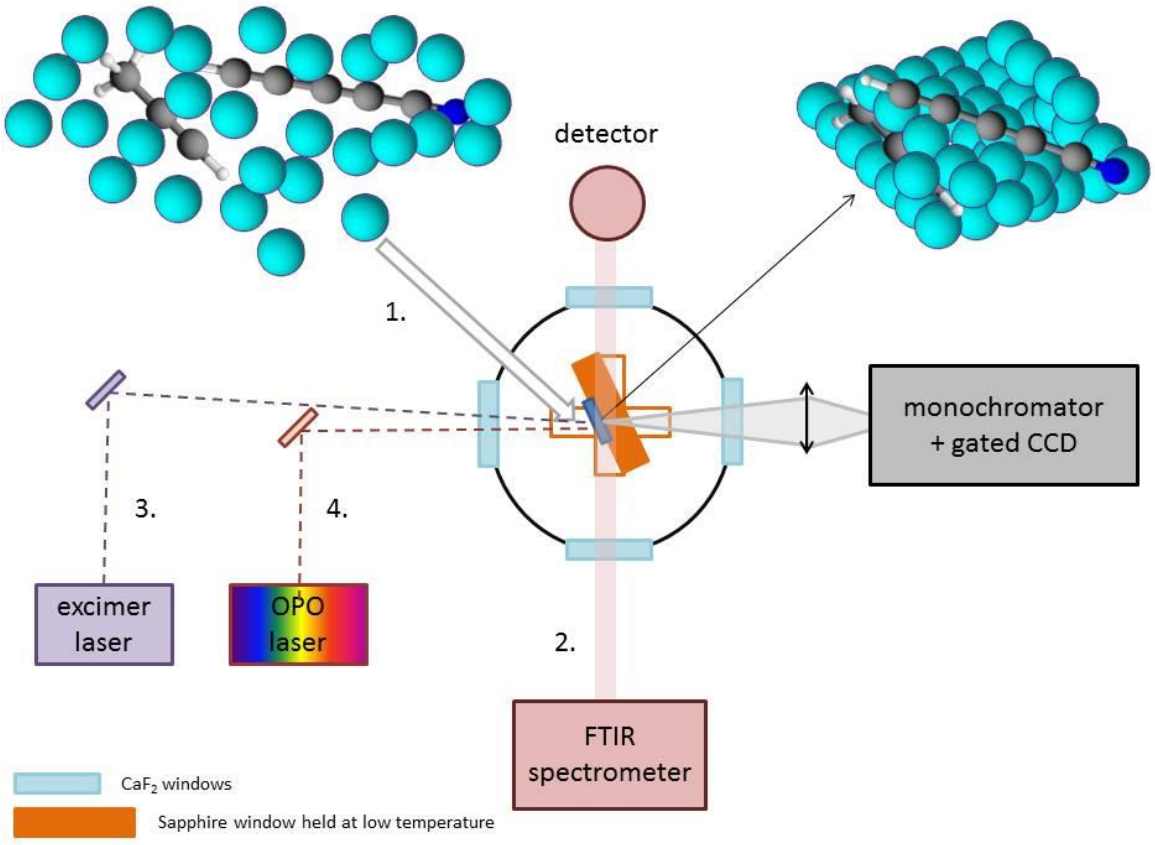

Figure 3. Scheme of the experimental set-up used in ISMO.

2.10 Quantum chemical computations

To interpret the experimental results, the quantum chemical calculations were necessary. Most of the calculations reported here were performed with Density Functional Theory (DFT) [181] using hybrid functionals: Becke's three parameter correlation functional [182] incorporating the expressions by Lee, Yang and Parr [183] (B3LYP) or by Perdew and Wang [184,185] (B3PW91). Their use proved to be time-economic and accurate enough for previous studies of similar species. Excited singlet electronic states were calculated with TD-DFT (time-dependent) approach.

Dunning-type correlation-consistent (cc) [186] polarized basis sets were used, involving polarization and diffuse functions, usually aug-cc-pVTZ (VTZ denoting triple splitting of the valence shells) [186,187]. The calculations were performed in a harmonic approximation and the anharmonicity was accounted for by applying a scaling factor of 0.96 (this factor

was used also to account for other inaccuracies, coming from approximations assumed in a computational method or from the finite sizes of basis sets). The validity of such an approach has been confirmed for cyano(poly)ynes in several works, *e.g.* Refs. [82,96,188,189].

The calculations of various C_4H_3N isomers were performed at B3LYP/aug-cc-pVTZ level of theory. For other neutral molecules (CH_3C_5N and other cyanoacetylenes), B3PW91/aug-cc-pVTZ calculations were performed. In both cases, the calculations provided data on several parameters of the molecules of interest. Of use for this work were mainly: molecular geometry, thermodynamic stability, vibrational energy levels, IR absorption intensity, Raman scattering activity, polarizability, singlet-triplet splitting, singlet-singlet vertical and vibrationless transition energy, and respective oscillator strengths.

The calculations regarding anions were focused mainly on singlet-triplet splittings. Also of interest were the vibrational energy levels of the C_5N^- anion. These calculations were performed at CAM-B3LYP/aug-cc-pVTZ[1] (CAM stands for Coulomb-attenuating method) [190] level of theory, which modifies the B3LYP functional with long-range corrections as proposed in Tawada *et al.* [191]. The same method was applied for the calculations of intermolecular complexes.

The majority of the quantum chemical calculations cited here were performed by Dr. Marcin Gronowski and have not yet been published. They are reported here with Dr. Gronowski's consent [192]. The author of the Thesis partly performed the computations for C_3N^-, C_5N^- and C_7N^- anions. They are of use in Chapter 4, devoted to the photochemical synthesis of long carbon-nitrogen chains. The author took also part in a theoretical study of C_4H_3N isomers [193], by performing calculations of several cyclic (4-member and 5-member rings) compounds, an imine isomer (the results are not presented in this Thesis), and of propargyl cyanide (see Chapter 3.1).

All the calculations were carried out with the Gaussian 09 software package [194].

In several cases, apparently trustworthy theoretical results are available in the literature (as cited in Chapter 1.2) but were not of use in the present study. This applies, for instance, to vibrational energy levels previously obtained with B3LYP/aug-cc-pVTZ [157] and CCSD(T)/cc-pVTZ [195] approaches for the ground electronic state of HC_7N. In this work, calculational results at a uniform level of theory were necessary for the ground and the excited electronic states. Thus, a report on a HC_7N ground-state B3PW91/aug-cc-pVTZ [192] was used and cited, since the excited-state calculations were performed at that same level.

[1] In one case (C_5N^-), an even larger basis set, aug-cc-pVQZ was applied for the excited electronic states.

3 METHYLATED CYANO(POLY)YNES

The first section of this chapter concerns the UV-induced isomerization of CH_3C_3N. While the spectroscopy of this molecule is known (see Chapter 1.2), its photochemistry is largely unexplored. Several C_4H_3N-stoichiometry isomers are available in pure form and their IR absorption spectra serve as references for identification of expected isomerization products formed upon irradiation of CH_3C_3N. More postulated products were searched for based on quantum chemical predictions and published literature.

The second section is devoted to CH_3C_5N, the longest methylated cyanopolyyne so far detected in interstellar space. The IR absorption, Raman scattering and UV-Vis spectroscopy (in particular, phosphorescence) of the matrix-isolated, solid and gaseous compounds are described. Electronic spectroscopy data were measured directly by UV-Vis absorption or derived from phosphorescence excitation and dispersed phosphorescence. Vibronic spacings measured in phosphorescence spectra provided additional insight into ground-state vibrational energy levels previously investigated with IR absorption and Raman scattering spectroscopy. Various cryogenic matrices were used including neon, argon, krypton, xenon, nitrogen, and parahydrogen. The IR absorption spectroscopy of gaseous CH_3C_5N has already been described in the literature [144,145]. These data were revisited and revised in Szczepaniak *et al.* [196]. Conversely, no measurements concerning the electronic spectroscopy of CH_3C_5N were available prior to Turowski *et al.* [197], to which the present work contributed.

The discussion is provided along with the obtained results.

3.1 Photochemistry of methylcyanoacetylene, CH_3C_3N

193 nm (ArF) and 248 nm (KrF) laser photolysis of CH_3C_3N (Figure 4) was studied here in solid Ar. From more than fifty isomers of CH_3C_3N explored by DFT calculations [193] the most stable ones are presented in Figure 5. Among the probable photolysis products were the lowest energy isomers, especially: allenyl cyanide, propargyl cyanide, and an imine CH_2CCCNH. Literature reports on the photochemistry of two similar compounds, namely HC_3N [79,81] and CH_3CN [133,134], could suggest the CH_3CCNC isonitrile as one of possible photoproducts, along with CH_2CCCNH imine.

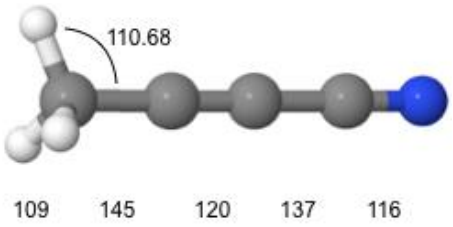

Figure 4. Geometry of methylcyanoacetylene, as derived at the B3LYP/aug/cc-pVTZ level of theory [193]. Distances in pm, angle in degrees.

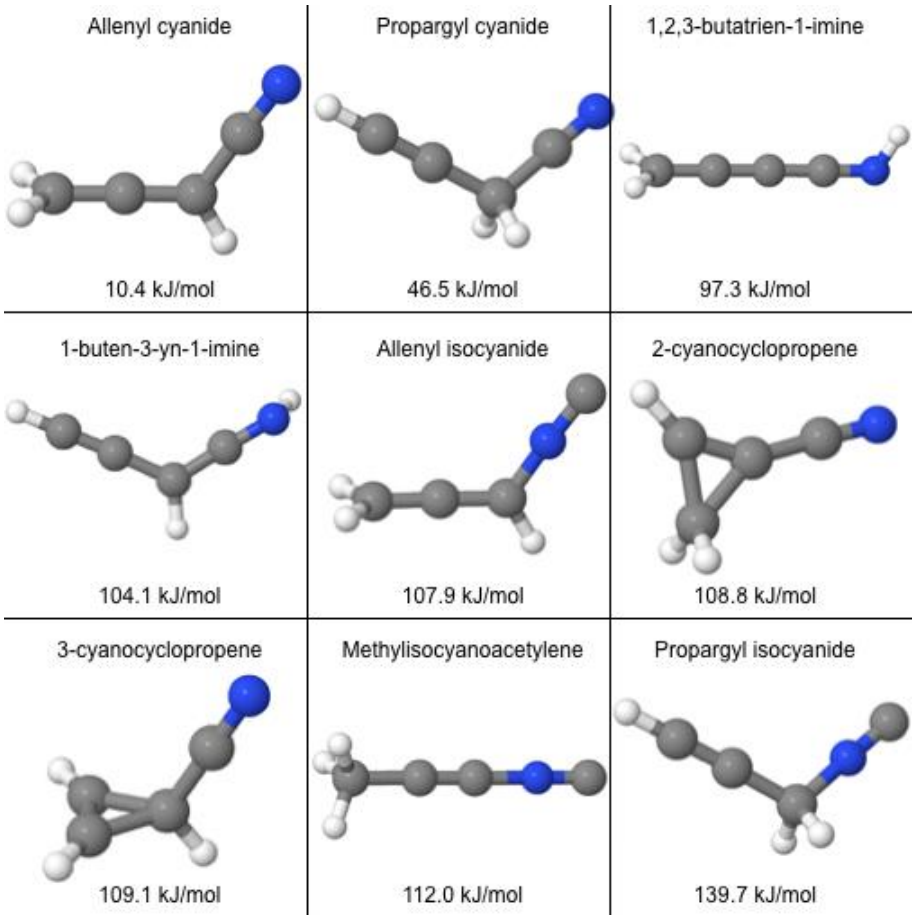

Figure 5. The most stable isomers of methylcyanoacetylene. Electronic energy, predicted at the B3LYP/aug/cc-pVTZ level of theory [193] is given relative to that of CH_3C_3N. Adapted from Ref. [193].

There exist preparatory organic chemical synthesis routes for at least four CH_3C_3N isomers: allenyl cyanide, propargyl cyanide, and their respective isocyanides. These have been obtained in pure form (see Chapter 2.4), and the IR absorption of Ar-matrix isolated compounds was measured for comparison with the spectra produced following CH_3C_3N photolysis. Such a comparison was not possible for CH_2CCCNH, CH_3CCNC, or any other C_4H_3N species. In these cases, the search must be performed based solely on DFT calculations and on experiments involving the ^{15}N-labelled precursor molecule.

3.1.1 Allenyl cyanide, propargyl cyanide, and respective isocyanides

IR absorption spectra of the four title compounds were interpreted based on quantum chemical computations concerning their vibrational spectroscopy [193]. The most intense predicted and experimentally observed bands are listed in Table 4.

Table 4. Theoretical and experimental (for Ar solids) wavenumber ($\bar{\nu}$ in cm^{-1}) and IR absorption intensity values for the strongest (predicted intensity higher than 20 km/mol) vibrational transitions of selected C_4H_3N isomers. Calculated absolute IR absorption intensities in km/mol, as derived with the harmonic approximation.

Mode	B3LYP/aug/cc-pVTZ [193]			Experiment	
	$\bar{\nu}$		IR intensity [km/mol]	$\bar{\nu}$	IR intensity [b]
	harmonic [a]	anharmonic			
allenyl cyanide (CH_2CCHCN)					
ν_3	2241	2303	23	2227.3, ~2244	m
ν_4	1959	2013	92	1982.6, 1978.1	s
ν_9	862	877	46	858.1	s
ν_{15}	840	854	23	834.1	s
propargyl cyanide ($HCCCH_2CN$) [c]					
ν_1	3329	3342	70	3319.0	vs
ν_9	680	692	38	662.5	vs
ν_{16}	664	674	44	645.2, 649.3	vs
allenyl isocyanide (CH_2CCHNC)					
ν_3	2110	2164	193	2129.8	vs
ν_8	929	956	26	951.2	s
ν_9	880	898	40	875.9	vs
ν_{15}	838	845	21	826.5	s
propargyl isocyanide ($HCCCH_2NC$)					
ν_1	3329	3340	67	3318.0	w
ν_4	2139	2190	170	~2148 [d]	m
ν_6	1321	1348	46	1345.5	w
ν_7	955	975	29	983.6	w
ν_9	691	704	35	672.9	w
ν_{16}	657	668	45	640.8, 644.9	w

[a] Scaled by 0.96.

[b] Rough estimates; s – strong, m – medium, w – weak, v – very.

[c] Calculations carried out by the author of the Thesis.

[d] Maximum of a broad, structured band.

Allenyl cyanide formation was observed (Figure 6) following the 248 nm laser photolysis of CH_3C_3N isolated in solid Ar. Only the minute traces of that molecule were found among the products of 193 nm laser irradiations. Propargyl cyanide was detected as the product of both 193 nm and 248 nm irradiations (Figure 7).

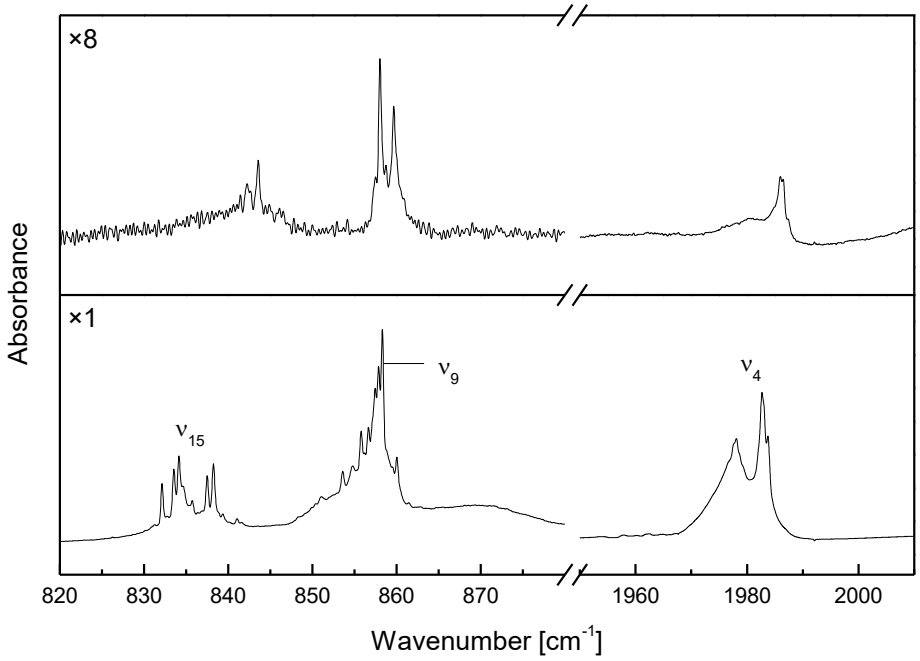

Figure 6. Net 248 nm (KrF, top) photolysis effects observed *via* IR absorption for CH_3C_3N isolated (at the dilution of 1:1000) in solid argon (difference spectrum: after - before irradiation), compared to the spectrum of pure allenyl cyanide isolated in solid Ar with the dilution of 1:1000 (bottom). Vertical purple bar corresponds, in both spectra, to the same change of optical density.

IR bands of both photolytically formed compounds were slightly shifted (by less than 10 cm^{-1}) and featured different site-splitting when compared to the matrix spectra of pure substances. This indicates the sensitivity of vibrational energy levels of these molecules to the presence of precursor species in their close vicinity, along with other photoproducts. Good mutual correlations have been found [198] for the strongest bands depicted in Figure 6 and Figure 7, separately for each of the identified isomers.

Neither allenyl isocyanide nor propargyl isocyanide was observed following the irradiation of CH_3C_3N with either of the two lasers.

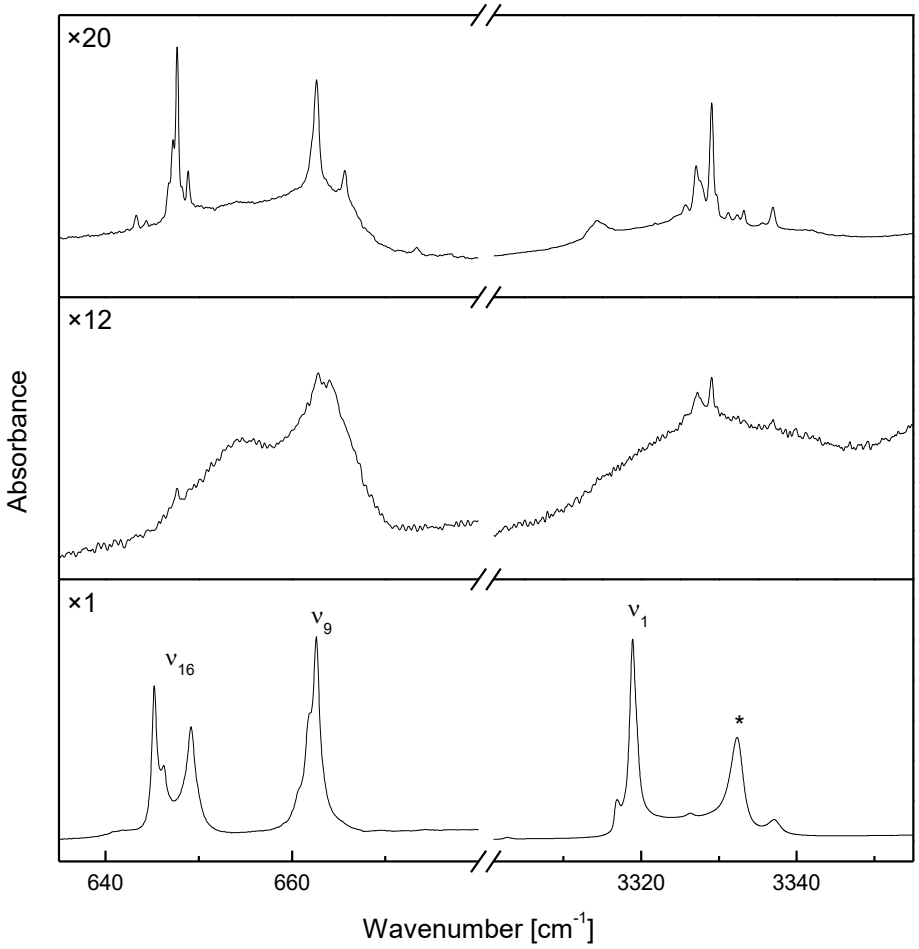

Figure 7. Net effects of 193 nm (ArF, top) and 248 nm (KrF, middle) photolyses, observed *via* IR absorption for CH_3C_3N isolated (at the dilution of 1:1000) in solid argon (difference spectrum: after - before irradiation), compared to the spectrum of pure propargyl cyanide isolated in solid Ar with the dilution of 1:1000 (bottom). Asterisked band remains unassigned.

The photoproduct evolution was traced during the 248 nm laser irradiation of CH_3C_3N isolated in solid Ar. The analysis of such growth curves (unpublished results of Custer *et al.* [198]) reveals differences in photoproduct formation kinetics (see Figure 8). Allenyl cyanide grows swiftly at first and then plateaus at long times and is likely a primary photolysis product. Propargyl cyanide grows steadily throughout and is likely a secondary product formed from allenyl cyanide.

The following process, involving two consecutive migrations of hydrogen atoms, can therefore be proposed:

$$H_3C–C{\equiv}C–C{\equiv}N \xrightarrow{h\nu} H_2C{=}C{=}CH–C{\equiv}N \xrightarrow{h\nu} HC{\equiv}C–CH_2–C{\equiv}N, \qquad \text{(R1)}$$

with allenyl cyanide playing the role of an intermediate species. Indeed, preliminary experiments with the photolysis of allenyl cyanide (not described here), have shown the transformation of that compound to propargyl cyanide. A thermal reaction (Chapter 2.3) observed during the storage of propargyl cyanide, proceeds in the opposite direction, as the compound transforms into allenyl cyanide (*i.e.* into a more stable isomer).

As already mentioned, only traces of allenyl cyanide could be observed following 193 nm irradiation, suggesting that the highly energetic photons kept its steady-state concentration near the detection limit. In other words, one may presume that allenyl cyanide to propargyl cyanide conversion (R1) was efficient enough to prevent ready observation of the allenyl cyanide intermediate.

Recent, unpublished results of Piétri *et al.* (CNRS and Aix-Marseille Université) [199] also support the idea of allenyl cyanide being an intermediate along the way to propargyl cyanide. Their experiments involved 121.6 nm (Ly α) irradiation of solid argon-isolated CH_3C_3N. The allenyl cyanide concentration reached a maximum and then dropped, while propargyl cyanide continued to grow.

The similarity of photoproducts observed with drastically different irradiation wavelengths, 121.6 and 248 nm for a H_2 discharge lamp and laser, respectively, suggests the importance of a 2-photon processes in the case of the 248 nm laser irradiation. If this is so, the same may also be happening during 193 nm laser photolysis. Obviously, a doubled 193 nm quantum supplies more energy to the precursor molecule than a single photon from the Ly α lamp or two KrF laser photons, which may explain differences in the photolysis products. This point deserves further systematic studies.

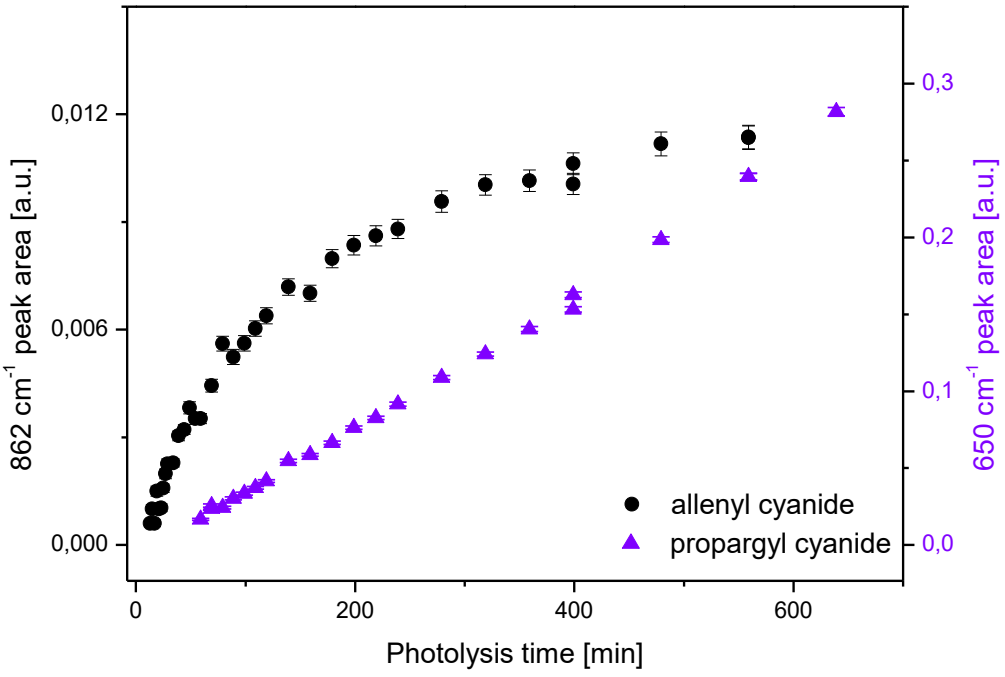

Figure 8. Kinetics of allenyl cyanide and propargyl cyanide formation in the photolysed CH_3C_3N isolated in solid Ar. Photolysis with 248 nm laser. Common beginning of the *y* axis, different, arbitrary, scales.

3.1.2 Search for an imine and for methylisocyanoacetylene

Theoretical predictions from Ref. [193] served as a roadmap for the search of other low energy C_4H_3N isomers (see Figure 5). However, none of these could be detected in the experiments described here. Especially important was the lack of two anticipated compounds: CH_2CCCNH imine and methylisocyanoacetylene.

The chemical 1,2,3-butatrien-1-imine, CH_2CCCNH, which has so far not been reported in the literature, is one possible CH_3C_3N photolysis product. Theoretical predictions for its ^{14}N and ^{15}N isotopologues are presented in Table 5. According to harmonic DFT calculations, the most intense IR band should be observed around 2160 cm^{-1} (or 50 cm^{-1} towards higher wavenumbers in an anharmonic approximation), and should feature an isotopic ^{14}N-^{15}N shift of 3 cm^{-1}.

The 193 nm photolysis of argon matrix-isolated $CH_3C_3{}^{14}N$ led to the appearance of an IR absorption band at 2160.6 cm^{-1}, which could be considered as a signature of the imine in question. However, the photolysis of $CH_3C_3{}^{15}N$ resulted in a band shifted to 2122.0 cm^{-1}, *i.e.* by 38.6 cm^{-1}, an order of magnitude larger than predicted. Similar results were obtained using 248 nm photolysis, although the strength of the bands in question was much lower. The presumption that CH_2CCCNH is the carrier of either absorption was therefore rejected. No other candidate bands were found in the region where the strongest imine absorption feature was expected. The 2160.6/2122.0 cm^{-1} feature remains unassigned.

Table 5. B3LYP/aug-cc-pVTZ-derived predictions of vibrational wavenumbers ($\bar{\nu}$ in cm^{-1}) and of IR intensity in km/mol for ^{14}N and ^{15}N isotopologues of the CH_2CCCNH imine [193].

Mode	$\bar{\nu}$				IR intensity [b]
	harmonic [a]			anharmonic	
	^{14}N	^{15}N	^{14}N-^{15}N shift		
A' symmetry					
ν_1	3342	3334	7.6	3305	45
ν_2	3008	3008	0	3020	5
ν_3	2162	2159	2.7	2214	1444
ν_4	1933	1925	8.1	1988	20
ν_5	1448	1442	6.1	1483	100
ν_6	1313	1309	4	1341	16
ν_7	941	935	5.7	938	435
ν_8	757	757	0	770	66
ν_9	732	724	8	742	0
ν_{10}	471	471	0	487	0
ν_{11}	410	408	1.3	426	17
ν_{12}	123	122	0.7	123	4
A" symmetry					
ν_{13}	3080	3080	0	3062	0
ν_{14}	949	949	0	969	0
ν_{15}	695	693	2	707	59
ν_{16}	561	559	1.3	588	1
ν_{17}	366	366	0.2	404	0
ν_{18}	137	136	1	162	1

[a] Scaled by 0.96.

[b] For the ^{14}N-isotopologue. Harmonic approximation.

No evidence for the formation of CH_2CCCNH suggests that the following process:

$$H_3C–C{\equiv}C–C{\equiv}N \xrightarrow{h\nu} H_2C{=}C{=}CH–C{\equiv}N \xrightarrow{h\nu} H_2C{=}C{=}C{=}C–NH \qquad \text{(R2)}$$

is much less probable than (R1) proposed earlier. The intermediate allenyl cyanide molecule is more likely to detach an H atom connected to the terminal carbon and transfer it to the

carbon adjacent to the cyano group, than to create the more energetic imine using the nearest available hydrogen atom.

Considering the order of thermodynamic stabilities (see Figure 5), together with the fact that 1,2,3-butatrien-1-imine and allenyl isocyanide were not observed in the described experiments, the lack of signal for an even more energetic isomer, methylisocyanoacetylene, comes as no surprise. Indeed, the search for that molecule, based on the theoretical predictions (Table 6), did not provide any proof of its formation from matrix-isolated, UV-photolysed CH_3C_3N.

Table 6. B3LYP/aug-cc-pVTZ-derived predictions of vibrational wavenumbers ($\bar{\nu}$ in cm^{-1}) and of IR intensity in km/mol for ^{14}N and ^{15}N isotopologues of methylisocyanoacetylene (CH_3CCNC) [193].

Mode	$\bar{\nu}$				IR intensity [b]
	harmonic [a]			anharmonic	
	^{14}N	^{15}N	^{14}N-^{15}N shift		
A_1 symmetry					
ν_1	2907	2907	0	2830	12
ν_2	2285	2280	5	2267	1
ν_3	2060	2025	35	2109	134
ν_4	1360	1360	0	1345	2
ν_5	1165	1164	2	1159	3
ν_6	667	663	4	695	0
E symmetry					
ν_7	2963	2963	0	2942, 2866	3
ν_8	1415	1415	0	1450, 1384	9
ν_9	1010	1010	0	990, 978	1
ν_{10}	451	446	4	451, 441	0
ν_{11}	305	302	3	317, 262	5
ν_{12}	148	148	0	113, 51	0

[a] Scaled by 0.96.

[b] For the ^{14}N-isotopologue. Harmonic approximation.

The anticipated observation of CH_3C_2NC amongst CH_3C_3N photolysis products was based on the theoretically derived isocyano-cyano energy difference. Very similar energetic separations were calculated for the related isomeric pairs HC_2NC/HC_3N and HC_4NC/HC_5N [96,200], and the two isonitriles appeared as the most prominent products of respective nitrile photolyses [80,97]. However, in both these cases the isonitrile is the lowest-energy isomeric modification of the original nitrile. This is not true for CH_3C_3N in which various H atom migration processes seem much more plausible than CN group flipping. Obviously, thermodynamic stabilities are by far not the only factors shaping the range of photoproduced isomers. Any reliable theoretical description of photochemical processes following the absorption of UV radiation should incorporate the transformations occurring within the potential energy surface of an excited electronic state.

Some of the observed CH_3C_3N photolysis products could not be identified basing on available or theoretically predicted IR spectra of C_4H_3N isomers, or on the known spectra of other, related molecules. This line of research is currently continuing in the framework of a cooperation between IPC PAS and *Physique des Interactions Ioniques et Moléculaires* Laboratory (CNRS and Aix-Marseille Université).

3.2 Spectroscopy of methylcyanodiacetylene, CH_3C_5N

Compared to its H-terminal analogue HC_5N, little is known about the spectroscopy of CH_3C_5N. Both molecules feature almost identical C_5N backbones whose corresponding interatomic distances (see Figure 9) do not differ by more than 0.3 pm. A similar observation holds for comparison of their respective excited singlet electronic states. These similarities suggest that there should also be similarities in the energetics of the vibrational modes of HC_5N and CH_3C_5N, in spite of having different molecular symmetries.

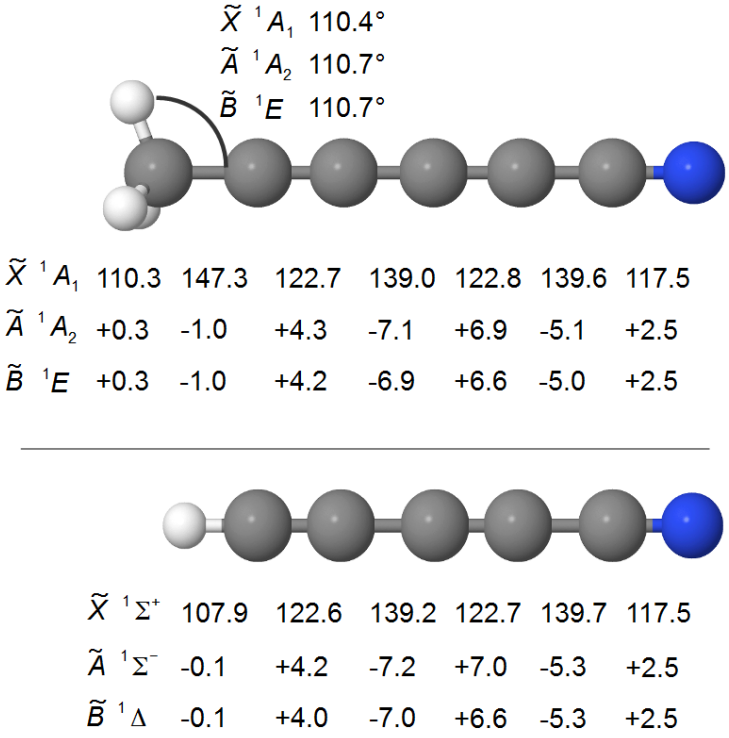

Figure 9. Geometry of CH_3C_5N and HC_5N in the ground and first excited singlet electronic states, as derived with CCSD/cc-pVDZ (ground state) or EOM-CCSD/ccpVDZ (excited states) levels of theory (adapted from [197]).

Large dissimilarities are however predicted for the lowest triplet electronic states of the two molecules (see Figure 10). The C_5N backbone, practically linear for the methylated compound, features a clear banana-like curvature in the H-terminated analogue. This distortion is much less severe than for the C_3N backbone in the triplet state of the homologous species, HC_3N [192].

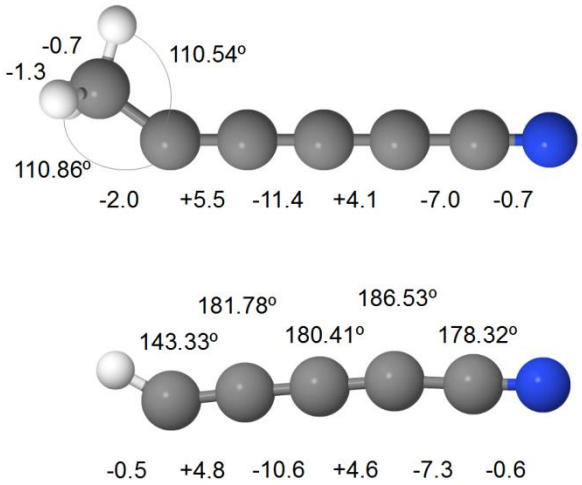

Figure 10. Geometry of CH_3C_5N and HC_5N in the triplet $\tilde{a}$ electronic states, as derived with CAM-B3LYP/cc-pVDZ level of theory ([192], adapted from [197]). Distances [pm] as relative to the geometry in the respective ground electronic states.

Thanks to additional data acquired and analyses thereof, the spectral assignments proposed previously [196,197] could be revisited and reviewed. All changes are indicated in the text.

3.2.1 Vibrational spectroscopy

3.2.1.1 Theoretial predictions and previous works

Table 7 presents the quantum chemical predictions for the vibrational spectroscopy of HC_5N [188] and CH_3C_5N [196], together with experimental data coming from IR absorption measurements of a gaseous CH_3C_5N sample recently reported in Montero-Campillo *et al.* [144][1]. These served as the basis for the proposed spectral assignments.

Compared to the interpretation proposed in Montero-Campillo *et al.* [144] for the gas-phase IR absorption spectrum of CH_3C_5N, the present work extends the analysis of the ν_2-ν_3 region, changes the spectral assignments of several fundamentals (ν_7, ν_9, ν_{12}), adds the identification of ν_6, and provides an in-depth examination of three perpendicular modes (ν_9, ν_{10}, ν_{11}).

[1] Montero-Campillo *et al.* [144] reports the serious problem of CH_3C_5N pressure decrease during the gas-phase IR absorption measurements (adsorption on cell walls). Here, the problem was overcome by putting a small amount of bulk substance inside the cell, *i.e.* by using the saturated vapour pressure, 0.5 mbar at (21 ± 1) °C.

Table 7. Wavenumbers ($\bar{\nu}$ [cm^{-1}]) for the fundamental vibrational modes of HC_5N and CH_3C_5N, theoretically predicted and gas-phase experimental results [144] for CH_3C_5N. Vibrational modes of HC_5N and CH_3C_5N characterized by similar displacements of atoms share common rows.

HC_5N			CH_3C_5N				
Main molecular fragment involved (dominant movement) [c]	Mode	Theory [a] $\bar{\nu}$	Mode	Theory [b] $\bar{\nu}$	Theory [b] IR intensity [%]	Theory [b] Raman Activity [%] (Raman Intensity [d] [%])	gas phase IR absorption [144] $\bar{\nu}$
stretching	σ symmetry		a_1 symmetry				
CH	ν_1	3321	ν_1	2912	2	19 (10)	2935
symmetric, central C≡C and C≡N	ν_2	2256	ν_2	2258	100	100 (100)	2262
asymmetric triple bond, CN	ν_3	2192	ν_3	2246	33	33 (34)	2248
asymmetric triple bond	ν_4	2061	ν_4	2126	1	2 (2)	2121
			ν_5	1347	1	2 (7)	1381
asymmetric single CC bond	ν_5	1153	ν_6	1270	0.1	0.3 (1)	-
			ν_7	912	1	0.02 (0.2)	918
symmetric chain	ν_6	603	ν_8	499.8	0.2	0.1 (3)	-
bending	π symmetry		e symmetry				
			ν_9	2978	0.6	7 (4)	2864
CH	ν_7	653	ν_{10}	1398	8	1 (2)	1412, 1451
			ν_{11}	992.7	2	0.2 (1)	1019, 1045
symmetric zig-zag	ν_8	545	ν_{12}	540	2	1 (21)	541[e], 547[e]
zig-zag, about single CC bonds	ν_9	485	ν_{13}	488.1	2	0.04 (1)	n/a
			ν_{14}	342.7	0.04	0.05 (3)	n/a
asymmetric skeleton	ν_{10}	272	ν_{15}	195	5	0.03 (6)	n/a
banana	ν_{11}	108	ν_{16}	75.8	0	0 (4)	n/a

[a] B3LYP/aug-cc-pVTZ, from Ref. [188]. Wavenumbers scaled by 0.96.

[b] B3PW91/aug-cc-pVTZ from Ref. [196]. Wavenumbers scaled by 0.96. 100 % corresponds to IR intensity of 277 km/mol and Raman activity of 3887 Å^4/amu.

[c] Symmetric/asymmetric notation is an approximation, referring to the nearest centrosymmetric species. Formally, it corresponds to pseudosymmetric and non symmetric vibrations.

[d] Raman intensity prediction refers to T = 15 K and the excitation wavelength of 514 nm.

[e] Tentative.

3.2.1.2 Vibrational spectra – an overview

IR absorption spectra for gaseous, solid, and Ar matrix-isolated CH_3C_5N are presented in Figure 11. The most straightforward assignments were those for vibrational transitions observed in the Ar matrix. Figure 12 presents the corresponding IR absorption and Raman scattering spectroscopy results. The four selected spectral ranges allow all identified fundamental vibrational bands to be displayed in one plot. These served as reference points for other cryogenic matrices.

Several bands exhibit large wavenumber shifts between matrix-isolated and pure solid (probably amorphous) samples (see Figure 11) and the solid-phase spectrum is characterized by relatively broad bands. The shifts for ν_1, ν_3, ν_9, ν_{10}, and ν_{12} are clearly visible. For a crystalline HC_5N sample, the biggest differences between pure solid and matrix isolated samples were reported for the modes representing mainly H atom stretching and bending (ν_1 and ν_7, corresponding here to ν_1 and ν_9, respectively) [92]. Here, however, the differences cannot be explained simply by the interaction between H atom(s) of a given molecule and the N atom of a neighbour, in the pure solid sample.

Almost all fundamental modes could be identified, with two exceptions: ν_8 and ν_{16}. The ν_8 band could not be directly observed in any medium other than Ar and the previous [196] tentative identification was not confirmed. Band ν_{16} is expected at ~76 cm^{-1}, *i.e.* outside of FTIR detection range accessible here, and at the very edge of sensitivity specified for the Raman spectrometer. The Raman spectrum featured some weak bands in the ν_{16} overtone region, but no conclusive assignment was possible. However, the mode could be identified by analysing the vibronic combination bands appearing in the phosphorescence spectra (see next section, “Electronic spectroscopy”, p. 55).

In general, good agreement was observed between the experimental findings (Table 8) and the theoretical predictions (Table 7). With the exception of ν_1 and ν_5, agreement between theoretical predictions and experimental values for the gaseous sample is on the order of ± 10 cm^{-1} and ± 40 cm^{-1} for a_1- and e-symmetry modes, respectively. The values for matrix samples are close to the gas-phase ones, taking into account the presence of gas-to-matrix shifts. Similar to what was observed for HC_5N [156], IR and Raman intensity values agree only qualitatively.

Solid Ne hosts are expected to have the smallest interactions with guest molecules and a spectrum in solid Ne should closely reproduce what is observed in a gaseous sample. This was not the case for these measurements. Even at a guest:host dilution of 1:1100, bands were broad, presumably due to the aggregation of molecules. Data coming from a nitrogen matrix showed the most complicated vibrational band structure, probably coming from dissimilar matrix sites. For Kr and Xe solids, spectra were generally similar to Ar ones, with unavoidably larger gas-to-matrix shifts. Interestingly, bands corresponding to the main matrix sites were especially narrow for the Xe host.

Table 8. Wavenumber values [cm^{-1}] of fundamental vibrational bands, as measured in IR absorption ($\bar{\nu}$) and Raman scattering ($\bar{\nu}_R$) spectra of CH_3C_5N.

Mode	Gas	Cryogenic matrices							Pure solid	
		Ne [a]	*p*-H_2 [a]	Ar		N_2 [a]	Kr [a]	Xe [a]		
	$\bar{\nu}$	$\bar{\nu}$	$\bar{\nu}$	$\bar{\nu}$	$\bar{\nu}_R$	$\bar{\nu}$	$\bar{\nu}$	$\bar{\nu}$	$\bar{\nu}$	$\bar{\nu}_R$
a_1 symmetry										
ν_1	2932.2 (P) 2939.4 (R)	2940, 2947.2	2930	2930.9, 2932.4	2933	2931.2, 2933.5	2919.6, 2920.8	2909-2917	2916.8	2920.0
ν_2 [b]	2265	2263.8	2261.6	2261.2	2263	2258.5	2255.8	2251.2	2260.7	2259.5
- [b]	2255.3	2253.3	2250.9	2253.0	2254	2250.1, 2248.3	2247.9	2242.6	2249	2248
ν_3 [b]	2246	2241, 2239.5	2238.0	2240.9	2242	2236.6, 2237.9	2236.5	2231.5	2233.9	2238
ν_4	2118 (P) 2123 (R)	2123.2	2121.4	2121.8	2123	2119	2117.3	2113.2	2114	2118
ν_5	1379.5	1383	1380	1377.6	1379	1380.4	1376.4	1373.1	1376	1372
ν_6	1282.1	-	-	1280.4	1281	1276.3	1277.3	1274.8	1281	1285
ν_7	908 (P) 913.3 (R)	n/a	n/a	913.0	-	910.6	910.5	908	912.8	914
ν_8	-	n/a	n/a	-	-	-	-	-	-	-
e symmetry										
ν_9	2982.4 ±0.1 [c]	2985.5	2983-2986 [d]	2982.1	2983	2982.2, 2981.1, 2980.3	~2970	2960.4, 2958.2, 2956.5	2971.2	2975
ν_{10}	1443 ±0.3 [c]	1441	1433-1446 [e]	1434.0	1434	1434.6 [f]	1430.5 [f]	~1420-1435 [e]	1424.5	1424
ν_{11}	1027.56 ±0.05 [c]	1027	1025.6	1022.5	1023	1023	1021	1019.8	1021	1022
ν_{12}	500.0	n/a	n/a	498.6	501	499.5, 500.3	497.9	496.4, 497.3	496.3	497.1
ν_{13}	463.4	n/a	n/a	465.8	467	466.4	465.6	464.5	467	467
ν_{14}	n/a	n/a	n/a	n/a	336	n/a	n/a	n/a	n/a	341.5
ν_{15}	n/a	n/a	n/a	n/a	200	n/a	n/a	n/a	n/a	200

[a] This work, unpublished results.

[b] Bands in anharmonic interaction (see text).

[c] Band origin estimated from the positions of rovibrational branches.

[d] Broad band that may hide a structure between 2974-2990 cm^{-1}.

[e] A well-defined multiplet. Partial overlap with water bands.

[f] Partial overlap with water bands.

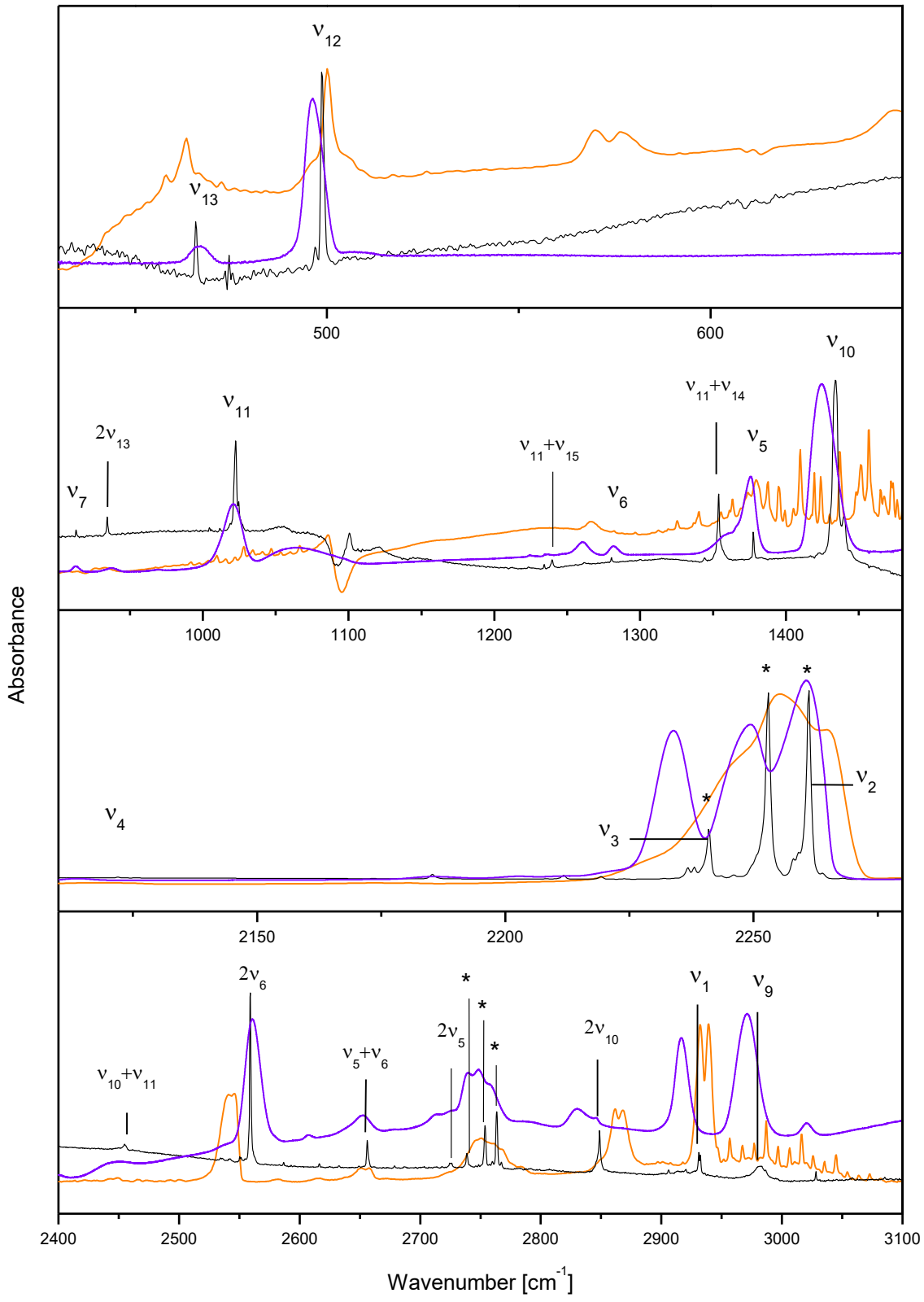

Figure 11. Vibrational spectra of solid Ar-isolated (black), pure solid (purple), and gaseous (orange) CH_3C_5N, as measured with IR absorption spectroscopy. Absorbance axes were magnified, in individual panels, by arbitrarily chosen factors, to optimize the visibility of spectral features. Asterisks denote recognized systems of anharmonically interacting modes (see text). Vibrational mode labels refer to Ar-matrix bands assignments.

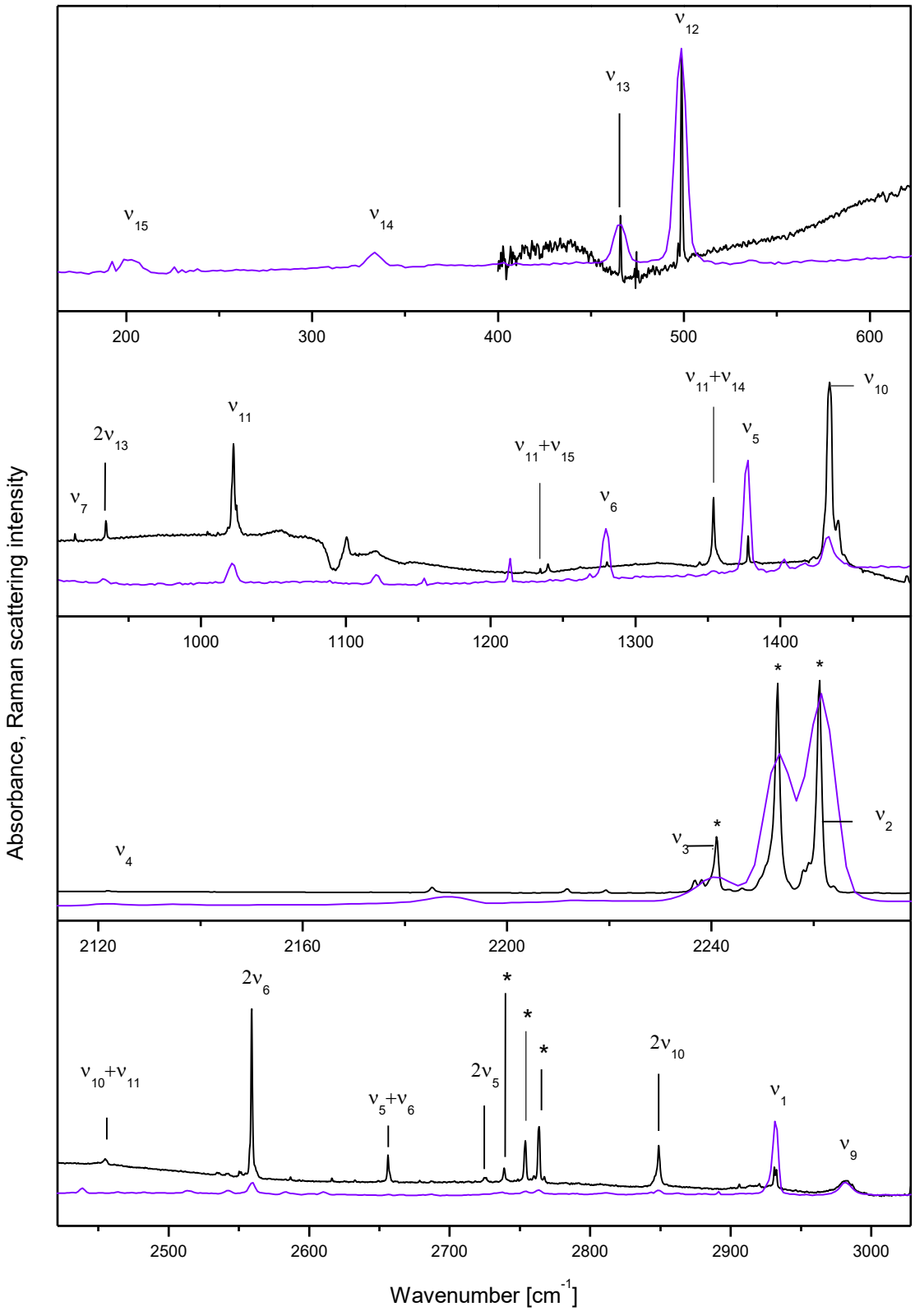

Figure 12. Vibrational spectra of solid Ar-isolated CH_3C_5N, as measured with IR absorption (black) or Raman scattering (purple) spectroscopy. Absorbance axes were magnified, in individual panels, by arbitrarily chosen factors, to optimize the visibility of spectral features. Asterisks denote recognized systems of anharmonically interacting modes (see text).

3.2.1.3 The most intense spectral features

There were several challenges with the assignment of bands, starting with the most intense spectral features, *i.e.* those appearing in the ν_2, ν_3 region. Quantum chemical calculations of vibrational transitions performed using the harmonic approximation (Table 7), predict ν_2 to be the most intense feature, while ν_3 should be several times weaker. However, around 2250 cm^{-1}, in all experimental spectra (including the gas-phase, where there is a partial overlap of rotational envelopes), two very intense bands were detected along with a third, less intense one (see the asterisked features in Figure 12 and Figure 13). The relative intensities of these "triplet" components change from matrix to matrix (compare the IR absorption of *p*-H_2 and Ar-samples; Figure 13). IR absorption and Raman scattering spectra are also distinctly different in this region, a fact that can best be seen in the different intensity patterns of the two most intense bands (Figure 12). Because of these differences, one can conclude that the two bands do not share a common origin.

In solid nitrogen, the weakest (and lowest wavenumber) component of the discussed triplet shows the same doublet sub-structure (probably coming from a site-splitting) as the mid-intensity band (Figure 13), suggesting a common origin of the two. Such similarities are not present for Ne and *p*-H_2 samples, where a complex site-splitting pattern was found exclusively for the weakest band.

Anharmonic DFT (B3PW91) calculations suggested a resonance of the combination band $\nu_5 + \nu_7$ with either ν_3 or ν_2. A mutual interaction of all three, namely ν_2, ν_3, and a combination mode, may explain the observations, along with the band intensity patterns. The combination mode is currently interpreted as $\nu_5 + \nu_7$ (see Table 12, p. 54, for the assignment of combination bands observed here). Other possibilities, mentioned in Ref. [196] include: $\nu_6 + \nu_7$ (preferred, based on VPT2-MP2/cc-pVTZ anharmonic calculations), $\nu_6 + 2\nu_{12}$, $\nu_6 + 2\nu_8$, and $\nu_6 + 2\nu_{13}$. The presence of similar patterns can be traced around 2760 cm^{-1}, 3150 cm^{-1}, 3200 cm^{-1}, and 4500 cm^{-1}, reflecting the possibility of coupling the above discussed modes to ν_{12}, ν_7, $2\nu_{12}$, and ν_2/ν_3, respectively. There are no similarities to HC_5N or CH_3C_3N that could help in this interpretation, as both these molecules feature a different type of resonance in this region, namely the interaction of a triple-bond stretching with a stretching overtone.

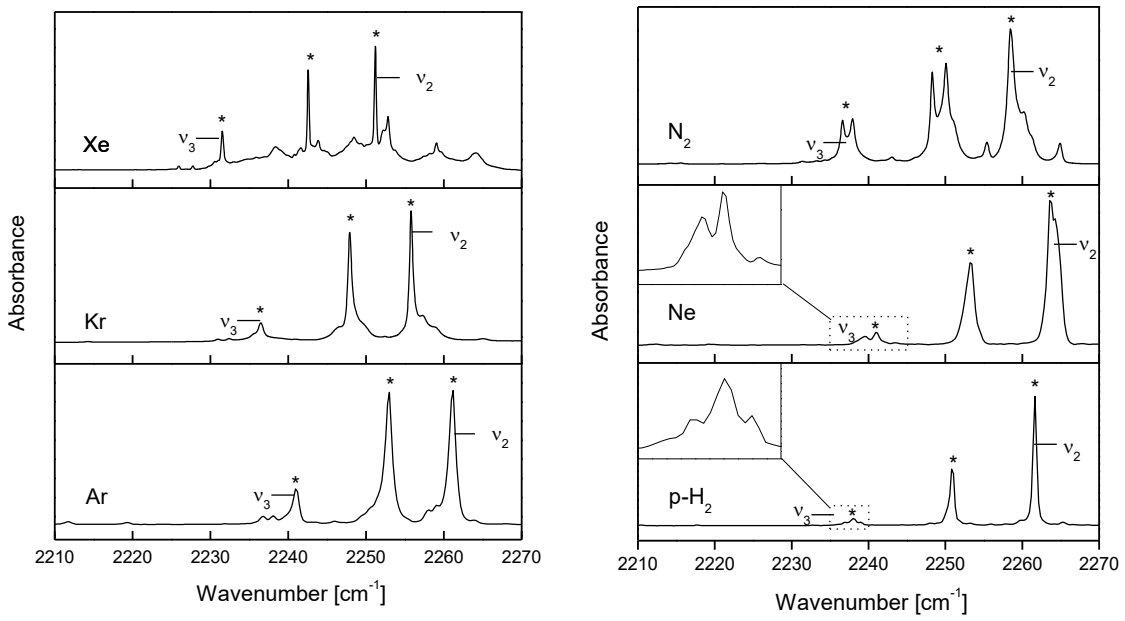

Figure 13. The ν_2, ν_3 region in IR absorption spectra of CH_3C_5N isolated in various cryogenic hosts. Asterisks mark three bands presumably coupled by an anharmonic interaction (the middle one likely comes from $\nu_5+\nu_7$). Absorbance scales differ to increase the visibility of the detected spectral features.

Several weak features around 2210 – 2240 cm^{-1}, most easily observed in the IR absorption spectra of Ar matrix-isolated CH_3C_5N (see Figure 13 and Figure 14), are assigned here to the ν_3 band of diverse ^{13}C-isotopologues of CH_3C_5N, as proposed in Table 9. Indeed, site-splitting patterns observed for ν_3 were mimicked in a given host by those weak bands (particularly well distinguished for solid N_2). To test these assignments, isotopic shifts (*vs.* the all-^{12}C molecule) were theoretically derived for ^{13}C-isotopologues. Together with experimental positions of the respective bands, they served to predict, case by case, the wavenumber of the all-^{12}C band. Resultant values were all reasonably close to the observed location of the main ν_3 band (see Table 9, column: $\bar{\nu}_{exp} - \bar{\nu}_{shift}$), adding to the credibility of original assumptions. Better match was not expected, given the anticipated anharmonic interactions (isotopologue-dependent) involving the ν_3 mode, difficult to reproduce at the applied level of theory. The region around two other strong bands (~2250-2260 cm^{-1}) is too crowded to discern analogous isotopic bands (they could also fall beneath the main spectral features).

Table 9. Experimental ($\bar{\nu}_{exp}$) and theoretical ($\bar{\nu}_{calc}$) wavenumber values [cm^{-1}] with tentative assignments of the bands marked in Figure 14.

Band	$\bar{\nu}_{exp}$	Proposed assignment	Theory [a]			$\bar{\nu}_{exp} - \bar{\nu}_{shift}$
			$\bar{\nu}_{cal}$	$\bar{\nu}_{shift}$	IR intensity change	
I	2211.8	$CH_3C^{13}CCCCN$	2210.8	-35.2	+40	2247.1
II	2219.2	$CH_3CCCC^{13}CN$	2219.3	-26.7	-50	2245.9
III	2236.7	$CH_3CC^{13}CCCN$	2232.9	-13.1	+240	2249.8
IV	2238.1	$CH_3CCC^{13}CCN$	2235.7	-10.3	+280	2248.4

[a] B3PW91/aug-cc-pVTZ, after Ref. [196]. Isotopic shift ($\bar{\nu}_{shift}$) with respect to the wavenumber of 2246 cm^{-1}, calculated for the ν_3 mode of the all-^{12}C molecule. Percent IR intensity change given with respect to ν_3 intensity of 33 km/mol, predicted for the all-^{12}C molecule.

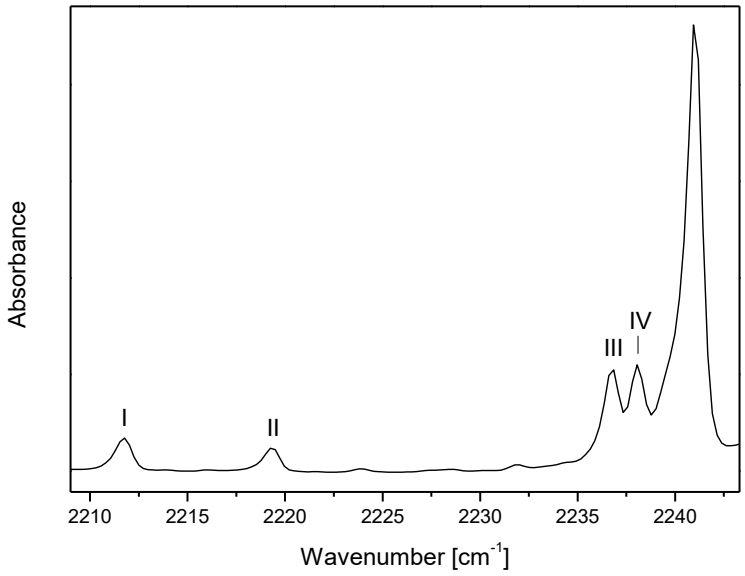

Figure 14. IR absorption spectrum of Ar matrix-isolated CH_3C_5N, depicting multiple ν_3 bands due to ^{13}C-isotopologues.

3.2.1.4 Perpendicular bands with rovibrational structure

Being a symmetric top molecule, CH_3C_5N has two unequal rotational constants, *A* and *B*, corresponding to the rotations about two mutually perpendicular axes, with *A* belonging to the principal axis of rotation. The *K* quantum number, referring to the rotation about principal axis, is present in the selection rules. For perpendicular transitions (*i.e*. those originating in vibrations which change the electric dipole moment along a direction perpendicular to the principal axis of rotation), these are: $\Delta K = \pm 1$ and $\Delta J = 0, \pm 1$. Respective rovibrational bands can therefore be more complex than the parallel bands, for which no change of *K* is permitted. The Q branches of perpendicular bands are separated by approximately $2(A–B)$, where *A* and *B* correspond to an excited vibrational state. With inclusion of the Coriolis coupling constant ζ_i (for the *i*-th mode), the above formula reads: $2[A(1–\zeta_i)–B]$. Coriolis constants (ζ_i) calculated for the modes involving mainly CH vibrations, *i.e*. ν_9, ν_{10}, and ν_{11} (Table 10) are much different than 1, unlike for other perpendicular modes [192]. That makes the separation between Q branches large enough to be distinguished (given small *B*) only for these three modes.

Table 10. Coriolis coupling constants (ξ_i), as predicted and derived experimentally [196].

Mode	ξ_i	
	B3PW91/aug-cc-pVTZ	Experiment
ν_9	0.05	0.0742 ± 0.0012
ν_{10}	-0.3	-0.349 ± 0.011
ν_{11}	0.4	0.4013 ± 0.0006

Indeed, ν_9, ν_{10}, and ν_{11} produced a series of Q branches (Table 11) featuring the intensity alternation pattern *strong-weak-weak-strong* (Figure 15) typical for C_{3v} symmetry species. Dependence of the Coriolis constant on the mode explains the observed differences in the spacing of Q branches, observed for disparate perpendicular bands of a symmetric top

molecule. Figure 15 shows a series of ν_9-band Q branches in the IR absorption spectrum of gaseous CH_3C_5N. The branches are spaced by ~10 cm^{-1}. Indeed, available values of molecular constants (A=160.7 GHz (5.36 cm^{-1}) [144], B=0.8 GHz (0.03 cm^{-1}) [44]) and ζ_9 = 0.05 (DFT prediction) lead to a Q-branch spacing of 10.1 cm^{-1}.[1] Corresponding features, similarly spaced, were also observed in this spectral region for other C_{3v}-symmetry molecules, including acetonitrile [201] (centered at 3027 cm^{-1}) and cyanopropyne [123] (centered at ~2980 cm^{-1}). Q branches similar to those associated with ν_{10} were reported for CH_3C_3N [123] (1453.8 cm^{-1}), CH_3CN [201] (1447.9 cm^{-1}) and CH_3C_2H [202] (1450.3 cm^{-1}).

Coriolis coupling constants experimentally derived for the modes ν_9, ν_{10}, and ν_{11} [196] (see Table 10) are in reasonable agreement with theoretical predictions. The values are similar to those experimentally found for the analogous modes of a shorter, but similar molecule, CH_3C_3N, *i.e.* 0.047 for ν_7 (CH_3 asymmetric stretching), -0.370 for ν_8 (CH_3 asymmetric bending), and 0.408 for ν_9 (CH_3 rocking), respectively [123].

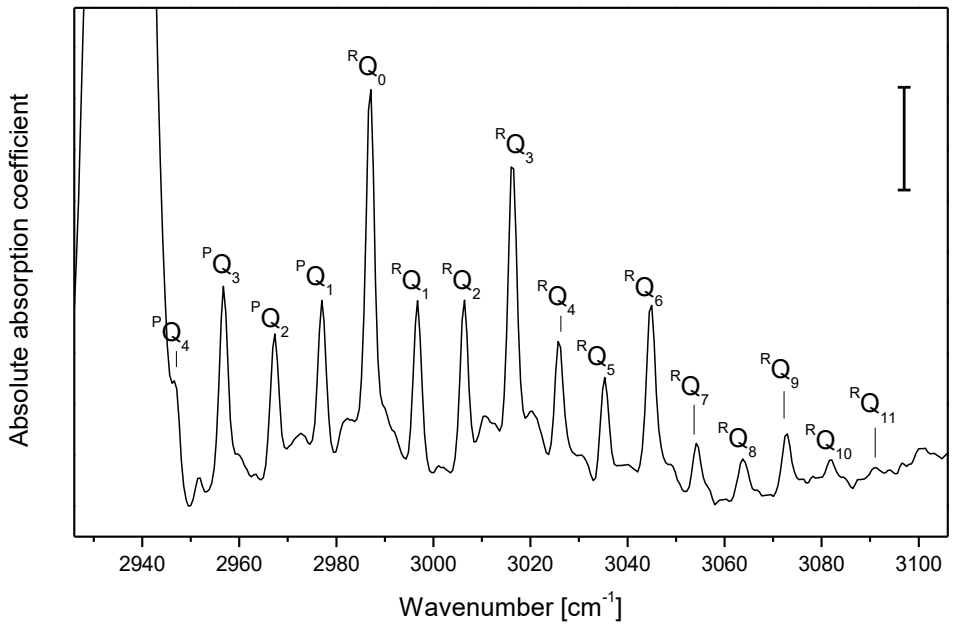

Figure 15. The rovibrational structure of ν_9 in the IR absorption spectrum of gaseous CH_3C_5N. The strong leftmost feature is due to ν_1. Vertical bar corresponds to the absolute absorption coefficient change equal to 0.1 cm^{-1} atm^{-1}, as calculated for 294 K, at base *e*.

[1] *A* and *B* represent ground-state rotational constants. Formally, constants describing the excited vibrational state geometry should be used; the respective difference is however negligible for the purposes of this discussion.

Table 11. Rovibrational Q branches for the IR absorption bands ν_9, ν_{10}, and ν_{11} of gaseous CH_3C_5N. Wavenumbers in cm^{-1}.

	ν_9		ν_{10}		ν_{11}	
K	^PQ_K	^RQ_K	^PQ_K	^RQ_K	^PQ_K	^RQ_K
0		2987.1		1451.5		1028.5
1	2977.0	2996.8	1437.9 [b]	1467.6	1022.5	1034.7
2	2967.4	3006.4	1424.1	1481.0	1016.2	1041.0
3	2956.7	3016.3	1409.8	1495.0	1010.1	1047.3
4	2946.6	3025.7	1395.6	1509.5	1004.1	1053.7
5	- [a]	3035.3		1525.2 [b]	998.2	1060.0
6	- [a]	3045.0			992.4	1066.8
7	2917.7	3054.1			986.7 [c]	1073.0
8	2907.6	3063.8				1079.6
9	2897.0	3073.0				1086.2
10	2887.8 [c]	3082.1				1093.5 [c]
11		3091.3				
12		3100.9				

[a] Coincident with the strong ν_1 band.

[b] Coincident with H_2O bands (atmospheric).

[c] Tentative.

Characteristic rovibrational features, expected for the gas-phase perpendicular bands ν_9, ν_{10} and ν_{11}, helped in the identification of these three transitions in the spectrum of the gaseous sample, and subsequently, in cryogenic matrix spectra (see p. 51).

3.2.1.5 Other fundamentals

Another challenging spectral region was that near the predicted positions of the ν_8, ν_{12} and ν_{13} bands (499.8, 540, and 488.1 cm^{-1} respectively; Table 7). Theory predicted the following patterns of IR and Raman intensities: $I_{IR}(\nu_{12}) = I_{IR}(\nu_{13}) \approx 10\ I_{IR}(\nu_8)$ for IR and $I_R(\nu_{12}) > I_R(\nu_8) > I_R(\nu_{13})$ for Raman. However, both IR absorption and Raman spectra show only two distinct bands attributable to any of these modes: one around 470 cm^{-1} and another around 500 cm^{-1} (a medium intensity IR band at ~474 cm^{-1} in Figure 12 is identified as an artifact). The first band (the least energetic of the three), is assigned to ν_{13}. The next one, to ν_{12}, based on analogy with a similar band appearing in the IR spectrum of HC_5N (comparison of corresponding displacement vectors). That results in $I_{IR}(\nu_{12}) > I_{IR}(\nu_{13})$ relation (not agreeing with DFT, but matching with what is predicted using CCSD [196]) and $I_R(\nu_{12}) > I_R(\nu_{13})$, in agreement with theoretical results. In the IR absorption spectrum of the Ar matrix-isolated compound (*e.g.* Figure 12), there is a weak feature very close to ν_{12}, previously ([196]) assigned to the fundamental mode ν_8. This assignment has been rejected, since the feature was not observed in other cryogenic solids or in the gas phase.

Several other assignments were also based on theoretically predicted band intensities. For example, the ν_7 mode was assigned to the band observed around 913 cm^{-1} (on the basis of comparison with the IR intensity of ν_4 and low Raman activity) and the other band of this region, at 934.4 cm^{-1} was assigned to $2\nu_{13}$. This assignment is in agreement with the results

of anharmonic DFT calculations [196]. Another such case was the assignment of a band at ~1280 cm^{-1} to ν_6 (based on the intensity comparison, both IR and Raman, of ν_6 and ν_{12}).

Other assignments proved quite straightforward, *e.g.* ν_1 was identified as the strongest band in the C-H stretching region. The identified fundamental modes are listed in Table 8 with the corresponding spectra presented in Figure 17 and Figure 18.

Perpendicular ($e \leftarrow a_1$) bands ν_9, ν_{10}, and ν_{11}, easily recognized in the gas phase (see p. 49), show some remnants of rovibrational structure in solid *p*-H_2 (Figure 16). Evidently, molecular rotation around the main axis (equivalent to methyl group rotation) is still possible in that host, and the rotational constant *A* (see p. 48) still has a sizable value there, permitting for some separation of the resultant Q branches. Such structured bands were observed for the analogous vibrational modes of another C_{3v} molecule, propyne, isolated in solid *p*-H_2 [203]. More surprisingly, some possibly associated structure also seem to be observable for CH_3C_5N molecules isolated in solid Xe, which could possibly be explained by their libration in a large matrix cage. It is however difficult to tell the difference between these spectral features and those coming from unique matrix microenvironments.[1] Such similarities between *p*-H_2 and Xe with regard to complicated structures accompanying perpendicular bands, were also observed in the ν_9 and ν_{11} regions.

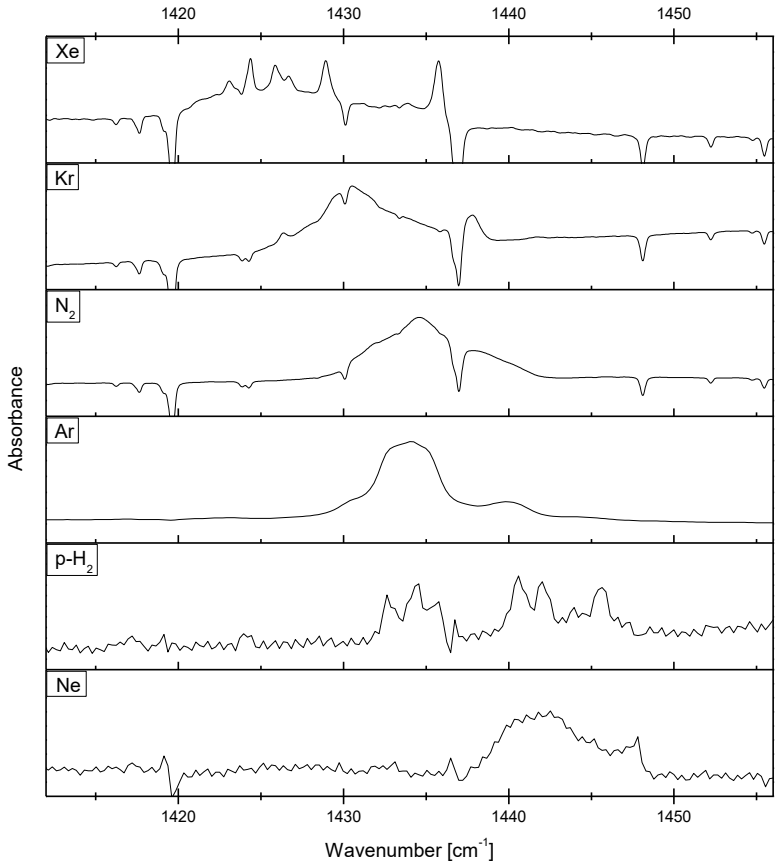

Figure 16. Spectral region of the ν_{10} vibrational mode, for CH_3C_5N and in several cryogenic matrices. Peaks pointing downwards come from the uncompensated atmospheric (water) lines.

[1] Noteworthy, similar substructure was not observed for an analogous smaller molecule, CH_3CN, isolated in solid Xe [204].

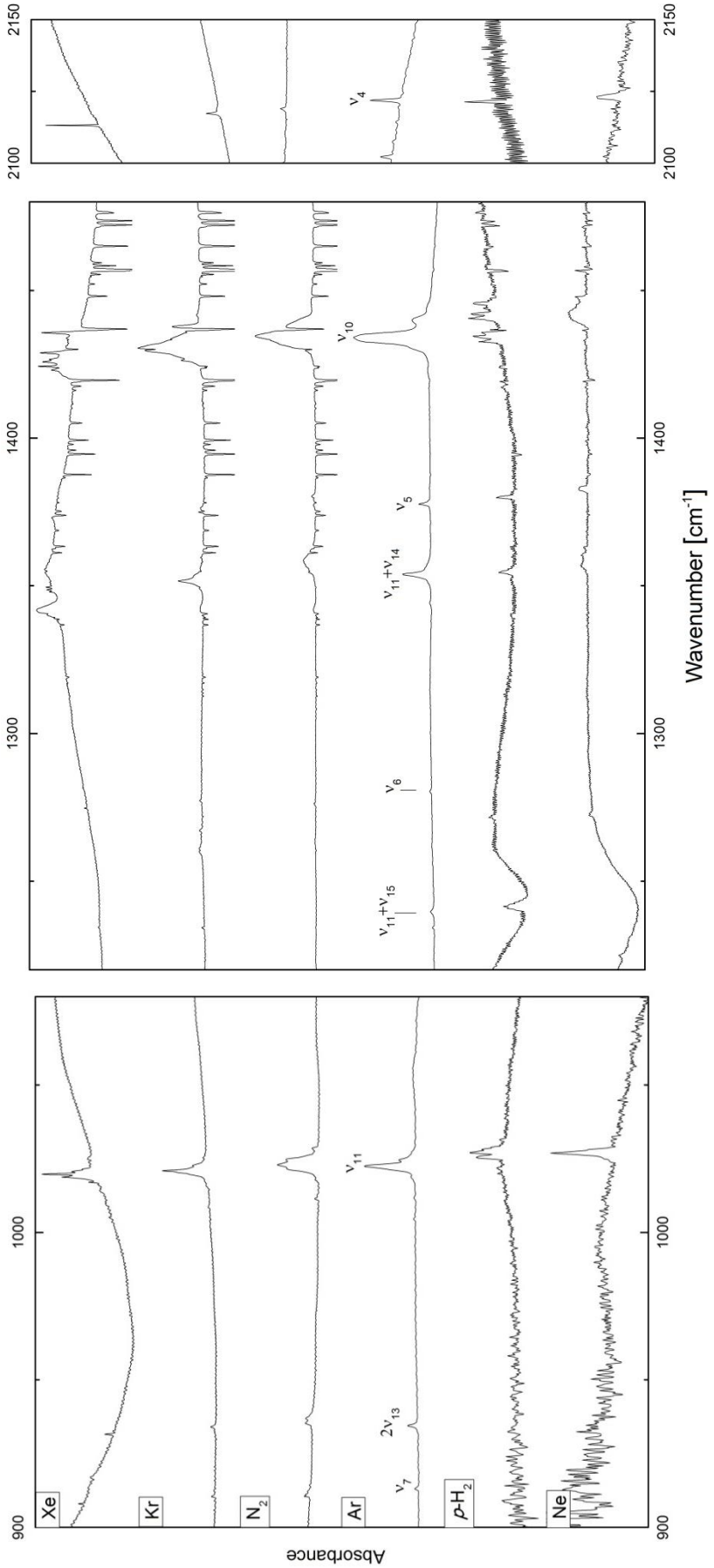

Figure 17. IR absorption spectra of CH_3C_5N isolated in cryogenic solids. Traces are ordered (bottom to top) according to the increase of host polarizability. Fragments shown in the leftmost panel are vertically expanded by the factors of 20 (Ar and *p*-H_2) or 40 (other hosts) with respect to the corresponding spectra in Figure 13. In the middle panel, the analoguous expansion factors are: 20, 40, 20, 15, 20, 10 for Xe, Kr, N_2, Ar, *p*-H_2 and Ne, respectively, and 100 for all traces in the panel on the right. Downward-pointing features are due to atmospheric gases.

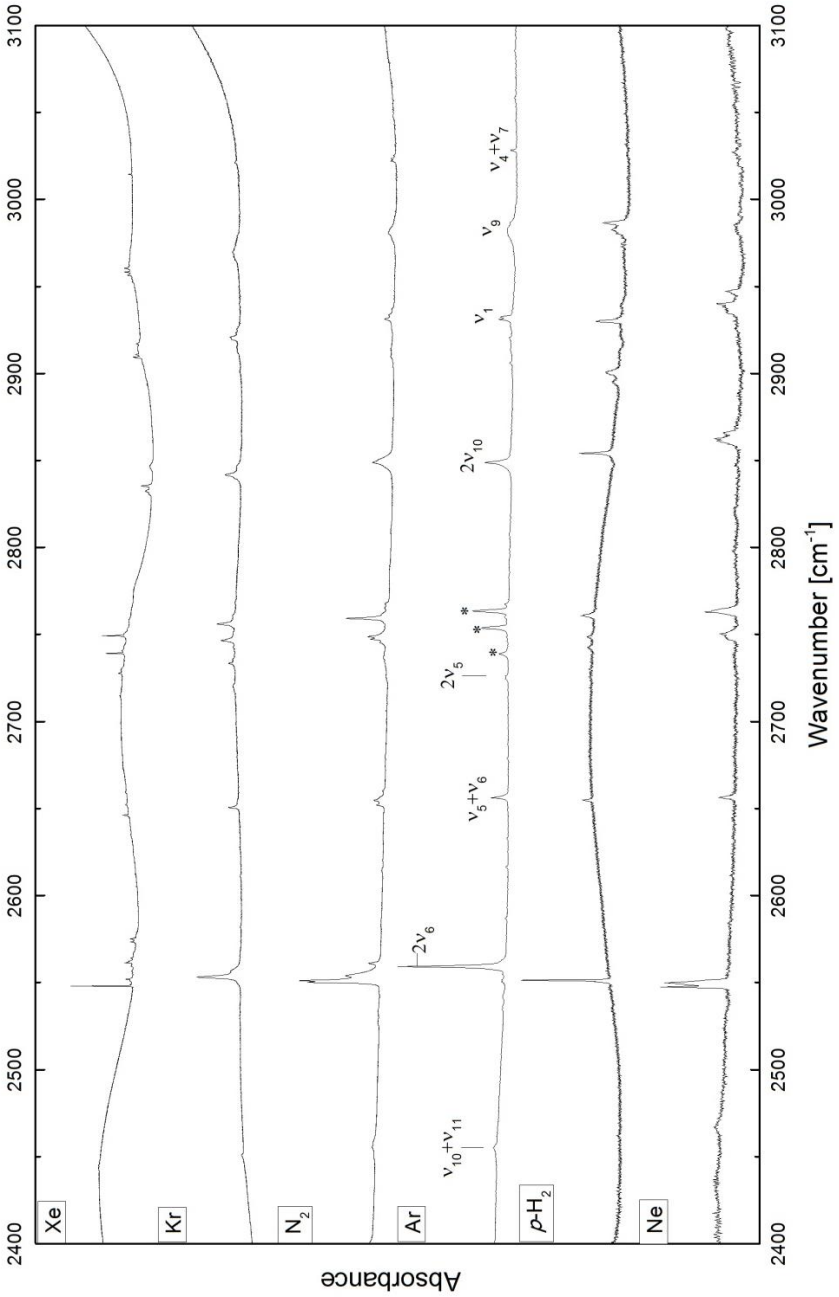

Figure 18. Continuation of Figure 17. Traces are vertically expanded by the factors of 20 (Xe, Ar and *p*-H_2) or 40 (other hosts) with respect to the corresponding spectra in Figure 13.

3.2.1.6 Other combination bands

Apart from the fundamental vibrations, combination and overtone modes of CH_3C_5N were also identified, based on quantum chemical predictions of anharmonic vibrational frequencies. Still, a number of them remain unassigned and further progress in that direction would require an isotopic labelling study. Table 12 lists the bands interpreted as due to combination and overtone vibrational modes, observed in cryogenic matrices. The Ne and *p*-H_2 samples were characterized by CH_3C_5N absorption too weak to permit for the measurement of less intense bands. Additionally, absorption of the *p*-H_2 host prevents any spectral measurement around 4500 cm^{-1}.

In general, the observed positions of combination and overtone bands follow the usual trend observed for fundamental modes: host materials with higher polarizability produce

bathochromic ("red") shifts. However, hypsochromic shifts (the opposite of bathochromic) could also be observed *e.g.* for $\nu_{10}+\nu_{11}$ in N_2 matrices, or for $\nu_5+2\nu_7$ and its further combinations in *p*-H_2 matrices. These can be understood in terms of a repulsion existing between the molecule and host atoms, for a given arrangement.

Compared to the spectral attributions given in Szczepaniak *et al.* [196], those presented in Table 12 include several improvements, in particular the change of the $\nu_6 + \nu_7$ combination to $\nu_5 + \nu_7$, assignment of a different band to $\nu_6 + \nu_7$, and the replacement of contributions from ν_8 to those from ν_{12}.

Table 12. Wavenumber values in cm^{-1} of the identified combination and overtone vibrational modes of cryogenic matrix-isolated CH_3C_5N.

Mode [a]	Ne [b]	*p*-H_2 [b]	Ar	N_2 [b]	Kr [b]	Xe [b]
$\nu_{12}+\nu_{14}$	n/a	n/a	797.1 [c]	800.9	796.5	794.1
$2\nu_{13}$	-	-	934.5	935.3, 937.0	934.1	931.6
$\nu_{11}+\nu_{14}$	1357, 1360.5	1354.6	1354	1358.2 [d]	1351.7	1341.8 [d]
$2\nu_{11}$	2044.4	2039.6	2035.1	2037.9, 2032.9	2030.8	2027.8
$\nu_6+\nu_7$	2180.4	2180.5	2185.3	2179.7	2179.8	2175
$\nu_5+\nu_7$	2253.3	2250.9	2253.0	2250.1, 2248.3	2247.9	2242.6
$\nu_5+\nu_{11}$	~2290	2286.4	2288.9 2284.1 2291.6	2287.4 [d]	2283.7?	2278.8?
$\nu_{10}+\nu_{11}$	2466.8	2462	2454.8	2458.2, 2455.4	2450.8	2443.5, 2444.9, 2447
$2\nu_6$	2547.4, 2548.8	2551.3	2559.1	2551.1, 2550.2	2553.1	2547.9
$\nu_5+\nu_6$	2656.3	2654.7	2656.2	2654.7, 2652	2650.6	2646.1
$2\nu_5$	2729 [e]	2725.5	2724.6, 2726.0	~2727, 2706.1 [d]	2720.3	2714.8
$\nu_3+\nu_{12}$ *	2737.4	2742.7	2738.8	~2737	2733.4	2727.7
$\nu_5+\nu_7+\nu_{12}$ *	2750.3	2748.8	2753.7	2748.7, 2747.3	2746.5	2739.2
$\nu_2+\nu_{12}$ *	2763.1	2760.9	2763.4 (2760.0)	2759.2	2756	2749.3
$2\nu_{10}$	2862.6, 2865.8	2854.2	2848.7	2848.8	2841.7	2835.4
$\nu_4+\nu_7$	3027.1	3024	3028.2	3023.3, 3022.1	3021.3	3014.4
$\nu_5+2\nu_7$*	3146.2	3141.8	3146.2	3143.4, 3141.2	3140.3	3132
$\nu_2+\nu_7$*	3159.9	3157.1	3160.2	3155.6, 3153.3	3152.8	3145.2
$\nu_2+2\nu_{13}$	-	3191	3185.5	-	-	-
$\nu_5+\nu_7+2\nu_{12}$*	-	-	3196.3	-	-	-
$\nu_2+2\nu_{12}$*	-	-	3204.1	3202.6, 3200.3	3197.8	-
$\nu_4+\nu_6$	3391.5, 3393.3	3392.5	3397.5	3390.3, 3389.3	3389.8	3382.9
$\nu_1+\nu_{11}$	-	-	3945.4	-	-	-
$2\nu_4$	4237	4234.2	4235.3	4229.2, 4228.2	4225.9	4217.7
$\nu_5+\nu_9$	~4370	-	4349.2	4357.4	?	?
$\nu_9+\nu_{10}$	~4415	-	4400.9	~4405	~4387 [d]	4372.2
$2\nu_3$ *	-	-	4481.9	4475.8	-	4462.9
$\nu_2+\nu_3$ / $\nu_2+\nu_5+\nu_7$ *	-	-	4504.6	~4499	-	4485
$2\nu_2$ *	~4512 [d]	-	4521.5	~4517	~4494 [d]	4502.2
$2\nu_1$ [b]	n/a	n/a	5754.5	-	-	-
$\nu_9+\nu_1$ [b]	n/a	n/a	5799.7	-	-	-
$2\nu_9$ [b]	n/a	n/a	5915.2	-	-	-

[a] Modes marked with * produce triplets analogous to the three dominant spectral features observed around 2250 cm^{-1}. Assignments are tentative.

[b] This work, unpublished results.

[c] Not reported in [196].

[d] Broad and/or weak, wavenumber less certain.

[e] Tentative.

3.2.2 Electronic spectroscopy

3.2.2.1 Theoretical predictions and an overview

DFT predictions for electronic transitions and the corresponding experimental results are summed up in Table 13.[1] Predicted values of singlet-triplet splitting are similar for CH_3C_5N and HC_5N, although their calculated geometries in their lowest triplet states differ significantly (see Figure 10). Phosphorescence measurements performed for the Ar-matrix isolated compound have confirmed that similarity, yielding 2.92 eV [91] and 2.94 eV for the $\tilde{a}$-$\tilde{X}$ vibrationless origins of HC_5N and CH_3C_5N, respectively.

Table 13. Energy [eV] of vibrationless electronic transitions from the ground to selected excited electronic states, as theoretically predicted (B3PW91/aug-cc-pVTZ [197]) and experimentally observed for CH_3C_5N and HC_5N.

State	Theory	Experiment						
		Gas phase	Ne [a]	*p*-H_2 [a]	Ar	N_2	Kr	Xe
CH_3C_5N								
$\tilde{A}\ ^1A_2$ [b]	3.38	4.03	4.01	3.97	3.93	3.95	3.91	3.89
$\tilde{B}\ ^1E$ [c]	3.58	4.33	4.31	4.27	4.23	4.24	4.21	4.19
$\tilde{a}\ ^3A'$	2.74	-	2.98	2.96	2.94	2.94	2.92	2.92
HC_5N [d]								
$\tilde{A}\ ^1\Sigma$	3.45	4.041	-	-	3.983	-	3.968	3.927
$\tilde{B}\ ^1\Delta$	3.64	4.389	-	-	4.316	-	4.298	4.274
$\tilde{a}\ ^3A'$	3.00	-	-	-	2.919	-	2.911	2.882

[a] This work, unpublished results.

[b] Estimated, based on ν_{12} calculated wavenumber (see further in the text). Thus, with higher uncertainty of experimental values, estimated to be ± 0.03 eV.

[c] Estimated, based on ν_{12} wavenumber in the gas-phase spectrum (see further in the text).

[d] Experimental values after Ref. [91].

The transitions observed here are: $\tilde{A} - \tilde{X}$, formally forbidden due to orbital symmetry reasons, $\tilde{B} - \tilde{X}$, formally allowed, but in practice needing the excitation of an e-symmetry vibrational mode (for the discussion of such couplings, occurring in a C_{3v} molecule, see section 3.2.2.3 or Chapter 4.2.3), as well as $\tilde{a} - \tilde{X}$, forbidden due to spin change (singlet-triplet) reasons.

3.2.2.2 Phosphorescence

The most prominent feature of the CH_3C_5N phosphorescence spectrum is a progression of bands spaced by 2200-2300 cm^{-1} (see Figure 19). The observation of a vibronic progression involving a specific mode is related to the geometry change between the states involved in the electronic transition. In general, the vibrational motion in this mode tends to reflect the molecular distortion induced by the electronic excitation. Here, this mode is interpreted as ν_2. All vibronic bands presently identified in that emission are listed in Table 14 (only the strongest feature is given whenever the splitting, referred to on p. 59, occurred). These spectral assignments were assisted mainly with quantum chemical calculations and by

[1] The author of this Thesis did not participate in the detailed analysis of $\tilde{A}$-$\tilde{X}$ and $\tilde{B}$-$\tilde{X}$ transitions, reported in Ref. [197].

analogy to well characterized HC_5N spectroscopy, a comparison justified by the common C_5N chromophore.

The most complicated sub-structures of electronic spectra were observed for the Xe matrix, indicating strong interactions with the host atoms. In nitrogen, the breadth of the bands prevents the separation of disparate vibronic features. The best separation of bands was achieved with Kr and *p*-H_2 matrices.

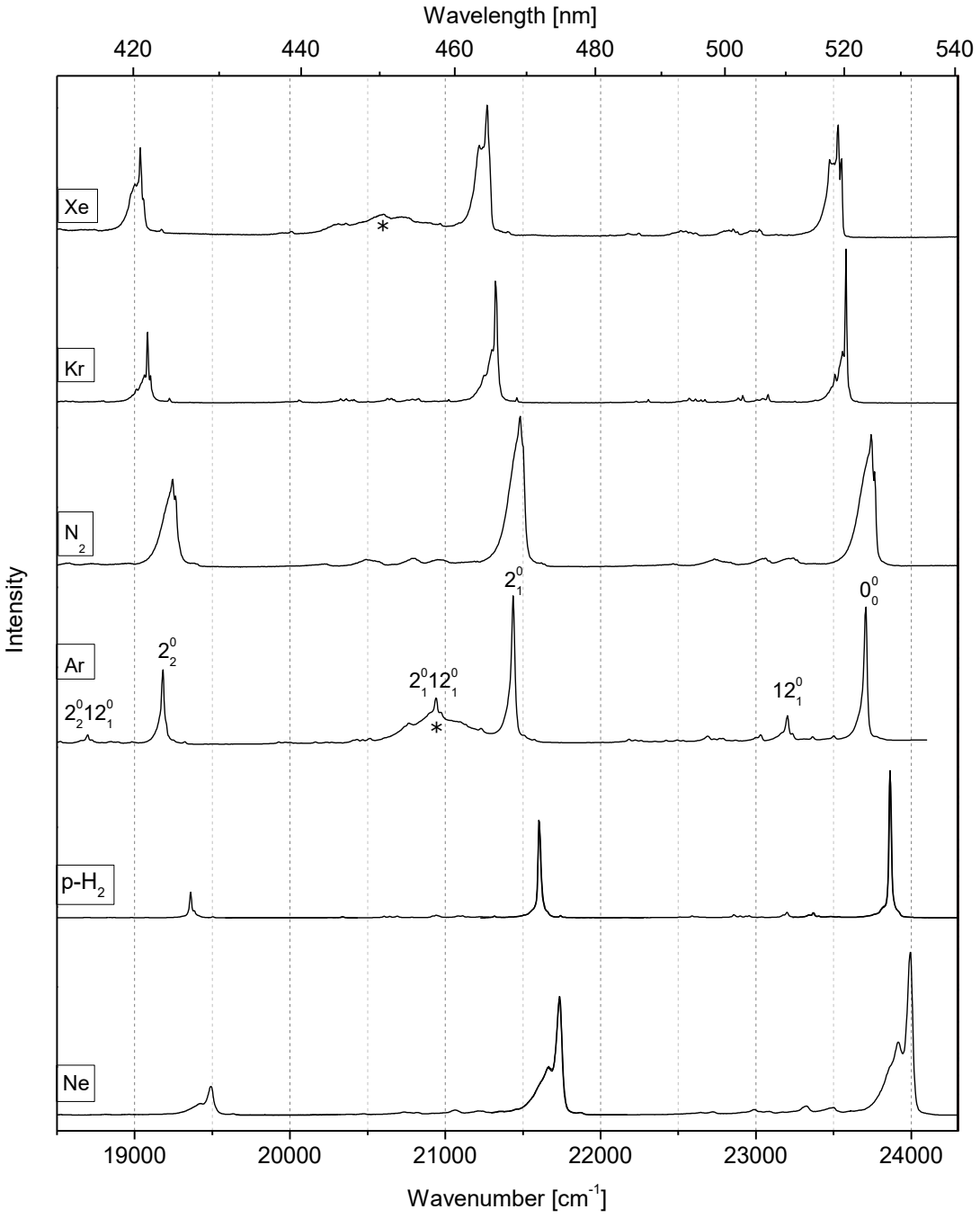

Figure 19. Phosphorescence of matrix-isolated CH_3C_5N, emitted following the excitation of $\widetilde{B}$-$\widetilde{X}$ 12_0^1 band. Vibronic assignments are given for the most intense bands observed for solid Ar-isolated compound.

All $\tilde{a}$-$\tilde{X}$ vibronic assignments are based on phosphorescence spectra excited at the maximal absorption, *i.e.* corresponding to the 12_0^1 band of the $\tilde{B}$-$\tilde{X}$ system (see p. 62). Compared to the attributions reported in Ref. [197], several changes, prompted by additional experiments, are proposed here. The main differences include:

- new assignments for the modes previously assigned as ν_5 and ν_{11} and their relevant combinations – while other fundamental vibrational modes are in very good agreement with the vibrational spectroscopy measurements, disagreement for these two modes was substantial;
- additional assignment of a band observed around 660-680 cm^{-1} as $2\nu_{14}$ – while this spectral feature is easily detected, neither ν_{13} nor ν_{15} were found in Ne matrices; an analogous mode, active in vibronic progressions, was observed for HC_5N [91];

assignment of a previously unassigned band at ~3511 cm^{-1} to $2\nu_6 + 2\nu_{12}$.

Table 14. Vibronic bands in $\tilde{a}$-$\tilde{X}$ phosphorescence of CH_3C_5N isolated in various cryogenic solids. Numerical entries correspond to relative wavenumber values [cm^{-1}], calculated with respect to vibrationless (*0-0*) $\tilde{a}$-$\tilde{X}$ origins at 23 994 cm^{-1} (Ne), 23 863 cm^{-1} (*p*-H_2), 23 708 cm^{-1} (Ar), 23 742 cm^{-1} (N_2), 23 580 cm^{-1} (Kr), and 23 530 cm^{-1} (Xe). Values for Ar differ from those in [197] due to improved calibration.

Relative wavenumber						Intensity [b]	Assignment
Ne [a]	*p*-H_2 [a]	Ar	N_2	Kr	Xe		
0	0	0	0	0	0	vs	0_0^0
	189	200		196		m	15_1^0
326	330	337		329	317	m	14_1^0
385	379		361, 372	400	368, 400	vw	15_2^0
	461	466	475	463		m	13_1^0
498	496	499	502	500	509	m	12_1^0
	522	537 [c]	534 [c]	536	541	vw	$13_1^0 16_1^0$ [c] / $14_1^0 15_1^0$
				570		vw	$12_1^0 16_1^0$
670	663	670	679	664	677	m	$13_1^0 15_1^0$ / 14_2^0
		700	700	694	703	vw	$12_1^0 15_1^0$
824	824	833	832	826	843	m	$12_1^0 14_1^0$
910	908	911	904, 931	908	920	m	7_1^0
930	928	932	947	934	956	m	13_2^0
968	967	968	991	970	981	m	12_2^0 / $12_1^0 13_1^0$
1004	1005	1011	1009	1011	1017	m	$13_2^0 16_1^0$ [c, d] / 12_2^0 [e]
		1172		1165		m	$12_1^0 13_1^0 15_1^0$ / $12_1^0 14_2^0$
		1207		1210 [c]		m	$12_2^0 15_1^0$
1273	1275	1278	1274	1272	1287	m	6_1^0
1349	1349	1353		1352	1351	m	$11_1^0 14_1^0$ [f] / 14_4^0
		1405			1420	vw	13_3^0 / $7_1^0 12_1^0$
		1438			1469	m	12_3^0 / $12_1^0 13_2^0$ [e]
		1477				m	$6_1^0 15_1^0$ / $12_2^0 13_1^0$ [e]
	1513	1517	~1524	1518		m	$11_1^0 12_1^0$ [c] / 12_3^0 [e]
		1782				vw	$6_1^0 12_1^0$
2121	2123	2123	2105, 2124	2120	2127	m	4_1^0

2259	2260	2262	2259	2257	2261	vs	2_1^0
				2330	2311 [c]	vw	$2_1^0 16_1^0$
		2467		2460	2441	m	$2_1^0 15_1^0$
2538	2547	2569	2537, 2555	2557	2560	m/w	6_2^0
				2582		vw	$4_1^0 13_1^0$ / $2_1^0 14_1^0$
2640	2639			2653		vw	$2_1^0 15_2^0$
	2715	2727		2715 [d]		vw	$2_1^0 13_1^0$
2758	2753	2759		2750		w	$2_1^0 12_1^0$
2785	2783		2781	2791	2804	vw	$2_1^0 13_1^0 16_1^0$ / $2_1^0 14_1^0 15_1^0$
				2823		vw	$2_1^0 12_1^0 16_1^0$
				2910		vw	1_1^0 [c]
2932	2924	2933	2947	2926	~2926	w	$2_1^0 13_1^0 15_1^0$/ 1_1^0 / $2_1^0 14_2^0$
	2940			2952		vw	$2_1^0 12_1^0 15_1^0$
3071	3080		3084	3079	3084	w	$2_1^0 12_1^0 14_1^0$
3176	3173	3185		3167	3171	m	$2_1^0 7_1^0$
				3183		vw	$2_1^0 13_2^0$
3223	3222	3229		3217		vw	$2_1^0 12_2^0$ / $2_1^0 12_1^0 13_1^0$ [e]
3259	3258	3262	3254	3255		vw	$2_1^0 11_1^0$ / $2_1^0 12_2^0$ [e]
		3429				m	$2_1^0 12_1^0 13_1^0 15_1^0$ / $2_1^0 12_2^0 15_1^0$
		3462				vw	$2_1^0 11_1^0 15_1^0$ [b]
				3511		vw	$6_2^0 12_2^0$
3518	3527	3535	3511	3521	3521	m	$2_1^0 6_1^0$
	3616			3602		vw	$2_1^0 14_2^0$
		3671				vw	$2_1^0 13_3^0$ / $2_1^0 7_1^0 12_1^0$
		3696				m	$2_1^0 12_3^0$ / $2_1^0 12_1^0 13_2^0$ [e]
		3729				vw	$2_1^0 6_1^0 15_1^0$ / $2_1^0 12_2^0 13_1^0$ [e]
	3758	3769	3758	3750		m	$2_1^0 11_1^0 12_1^0$ / $2_1^0 12_3^0$ [e]
	4226	4245		4222			4_2^0
4364	4359	4373	4355	4356	4358	m	$2_1^0 4_1^0$
4504	4503	4514	4496	4496	4493	vs	2_2^0
4576				4567		vw	$2_2^0 16_1^0$
		4713		4694		m	$2_2^0 15_1^0$
4781, 4800 [c]	4789	4803	4785	4780	4790	m/w	$2_1^0 6_2^0$ / $2_2^0 14_1^0$
		4849		4811		vw	$2_1^0 4_1^0 13_1^0$
				4889		vw	$2_2^0 15_2^0$
	4965	4971				vw	$2_2^0 13_1^0$
4998	4994	4997		4979		vw	$2_2^0 12_1^0$
5030	5026	5040	5022	5021	5012	m	$2_2^0 13_1^0 16_1^0$ / $2_2^0 14_1^0 15_1^0$
				5052		vw	$2_2^0 12_1^0 16_1^0$
5176	5161	5174		5154		m	$2_2^0 13_1^0 15_1^0$ / $2_2^0 14_2^0$ and $2_1^0 1_1^0$
	5183	5200	5162	5180	5179	vw	$2_2^0 12_1^0 15_1^0$
	5314	5332				vw	$2_2^0 12_1^0 14_1^0$
5426	5413	5423		5399		m	$2_2^0 13_2^0$ and $2_2^0 7_1^0$
5476	5455	5464	5444	5445	5441	vw	$2_2^0 12_2^0$ / $2_2^0 12_1^0 13_1^0$ [e]
	5489	5499		5477		vw	$2_2^0 11_1^0$ / $2_2^0 12_2^0$ [e]
	5722			5724		vw	$2_1^0 6_2^0 12_2^0$
5745	5742	5771	5767	5749		w	$2_2^0 6_1^0$
	5847			5832		vw	$2_2^0 14_2^0$

				6444		w	$2_1^0 4_2^0$
	6597		6508	6572		m	$2_2^0 4_1^0$
6748	6740		6722	6713		s	2_3^0
	7005		6993	6993 [c]		vw	$2_2^0 6_2^0$ / $2_3^0 14_1^0$
				7017 [c]		w	$2_2^0 4_1^0 13_1^0$
				7100		vw	$2_3^0 15_2^0$
				7193		vw	$2_3^0 12_1^0$
7244			7227	7238 [c]		w	$2_3^0 13_1^0 16_1^0$ / $2_3^0 14_1^0 15_1^0$
				7363 [c]		vw	$2_3^0 13_1^0 15_1^0$ / $2_3^0 14_2^0$ and $2_2^0 1_1^0$
			7386	7389 [c]		w	$2_3^0 12_1^0 15_1^0$
				7617		vw	$2_3^0 13_2^0$ and $2_3^0 7_1^0$
			7650	7650		w	$2_3^0 12_2^0$ / $2_3^0 12_1^0 13_1^0$ [e]
				7932 [c]		vw	$2_2^0 6_2^0 12_2^0$
			7964	7964 [c]		w	$2_3^0 6_1^0$
			8782	8782		w	$2_3^0 4_1^0$
	8957		8927	8924		m	2_4^0

[a] This work, unpublished results.

[b] For Kr. Intensity may vary depending on the matrix. $2_n^0 12_1^0$ bands are stronger in Ar than in other hosts; see Figure 19. Abbreviations: s – strong, m – medium, w – weak, v – very.

[c] Tentative.

[d] Possible overlap with 11_1^0.

[e] New interpretation, coming from analogy with HC_5N spectroscopy and assumption of similar anharmonicity for analogous bending modes, *i.e.* ν_{12} for CH_3C_5N and ν_8 for HC_5N (observed in solid Kr at 506 cm^{-1}, while its overtone, $2\nu_8$, at 1011 cm^{-1} [91]).

[f] New interpretation, based on IR absorption measurements.

In principle, vibrational wavenumber values coming from electronic spectra are less precise than the ones reported in the previous ("Vibrational spectroscopy") section. However, they allowed derivation of a collection of anharmonicity constants [197] which match the theoretically predicted ones rather well, and therefore support the proposed assignments. The analysis of combination bands also permitted an indirect identification of ν_{16}, the lowest-wavenumber mode, which was unreachable using either IR or Raman instruments.

Splittings of the main vibronic bands, on the order of 70 – 80 cm^{-1}, most prominent for Ne, Kr and Xe hosts (see Figure 19), are probably due to aggregates (intermolecular complexes), as deduced from their excitation spectra (available only for the Ne matrix; the excitation patterns were different for the two components and mutually shifted). Additionally, side-bands separated from the main (*0-0*) feature by 22 and 44 cm^{-1} in Kr or 21, 28, and 56 cm^{-1} in Xe have a magnitude similar to phonons previously reported for these rare gas solids [205]. Alternatively, they may be due to matrix sites. Similar features have also been observed in IR absorption spectra (see section 3.2.1). Distinguishing between the various possibilities will require measurements of excitation spectra corresponding to individual components of the split bands.

Spectral features situated between the strongest phosphorescence bands are shown in Figure 20. Vibronic bands follow similar intensity patterns in all investigated matrices, except for Ar, where the dominance of $2_n^0 12_1^0$ over other $2_n^0 B_1^0$ instances (B being a bending mode) is

especially strong. This is similar to what was reported [91] for HC_5N, with the involvement of ν_8 bending (a zig-zag mode, closely related to the ν_{12} of CH_3C_5N).

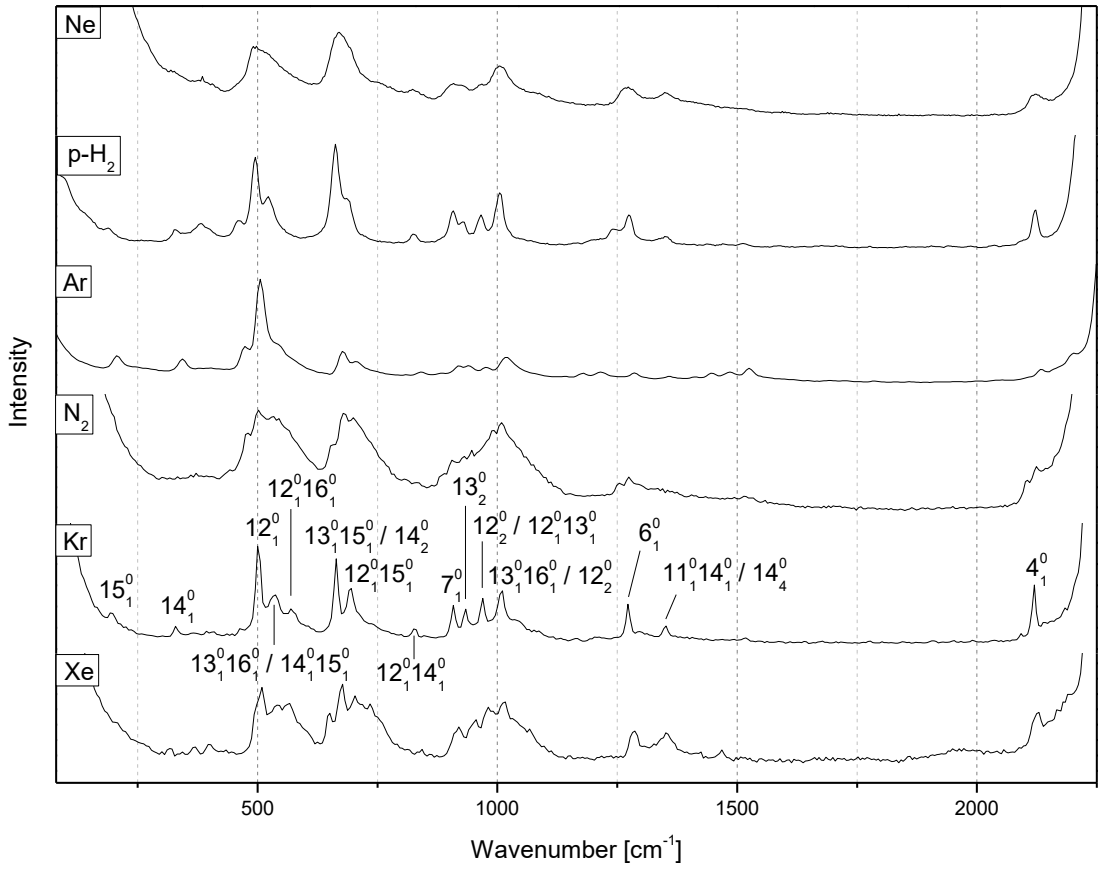

Figure 20. CH_3C_5N phosphorescence in various matrices. Spectra aligned with respect to the vibrationless $\tilde{a}$-$\tilde{X}$ origins, arbitrarily set to 0 cm^{-1}. Assignments refer to Kr matrix values.

Phosphorescence lifetimes of both molecules are compared in Table 15. The observed variation confirms the role of spin-orbit coupling that occurs due to the interaction with external atoms (stronger for the heavy ones), and may increase both the singlet-triplet intersystem crossing rate and the radiative relaxation of the triplet state. The increase of lifetime caused by the methyl group requires further studies.

Table 15. HC_5N and CH_3C_5N phosphorescence lifetime (τ [ms]) in cryogenic matrices.

Host gas	τ	
	HC_5N[a]	CH_3C_5N
Ne	n/a	~520
p-H_2	n/a	n/a
Ar	~200	~400
N_2	n/a	350
Kr	40	150
Xe	4	<1

[a] After Ref. [91].

3.2.2.3 Excited singlet electronic states

Figure 21 depicts the phosphorescence excitation spectra of matrix-isolated (Ne, *p*-H_2, Ar, N_2, Kr, Xe) CH_3C_5N and UV absorption of the gaseous compound. Clearly distinguished bands come mostly from $\tilde{B} - \tilde{X}$ transitions.

Spectral assignments were made with the aid of quantum chemical calculations, with analysis of hot bands in room-temperature UV absorption spectra of the gaseous compound (leading to the location of vibrationless system origins), as well as using analogies to well-characterized HC_5N spectroscopy, an analogy justified by the common C_5N motif (the chromophore).

No *0-0* transition was detected in the gas-phase $\tilde{B}\ ^1\mathrm{E} - \tilde{X}\ ^1\mathrm{A}_1$ spectrum of CH_3C_5N. Formally, this transition should be symmetry-allowed for the C_{3v} species CH_3C_5N, but not for the $\tilde{B}\ ^1\Delta - \tilde{X}\ ^1\Sigma^+$ transition of linear HC_5N. The lack of an observable *0-0* transition suggests that the molecular orbitals involved preserve $C_{\infty v}$ symmetry when passing from HC_5N to its methylated analogue. Nevertheless, $\tilde{B} - \tilde{X}$ transitions of CH_3C_5N may gain detectable intensity by coupling to an e-symmetry "bending" mode. Using this fact, the placement of the $\tilde{B} - \tilde{X}$ origin was deduced from measured hot vibronic bands originating in the ground-state ν_{15} and ν_{12} modes. While the ν_{15} transition did not show up in the preceding vibrational spectroscopy study, ν_{12} was easily detectable *via* IR absorption. The UV absorption spectrum of gaseous HC_5N exhibits an analogous hot band [91], which lends support of the present attribution. The *0-0* transition in cryogenic matrices was estimated for the $\tilde{B} - \tilde{X}$ system based on the *B*-state ν_{12} position of 467 cm^{-1} (found for the gas-phase spectrum, profiting from the knowledge of ν_{00}, using hot bands and IR spectroscopy data), and assuming a negligible gas-to-matrix spectral shift.

Noteworthy, solid Xe is the only matrix, in which ν_{11} was observed. It was not the only difference between Xe and other hosts. Another important difference concerned the relative intensity of $\tilde{A} - \tilde{X}$ and $\tilde{B} - \tilde{X}$ transitions. In particular, ν_9 of the $\tilde{A} - \tilde{X}$ system could be recognized in Xe matrix (this was also true for Kr). [197]

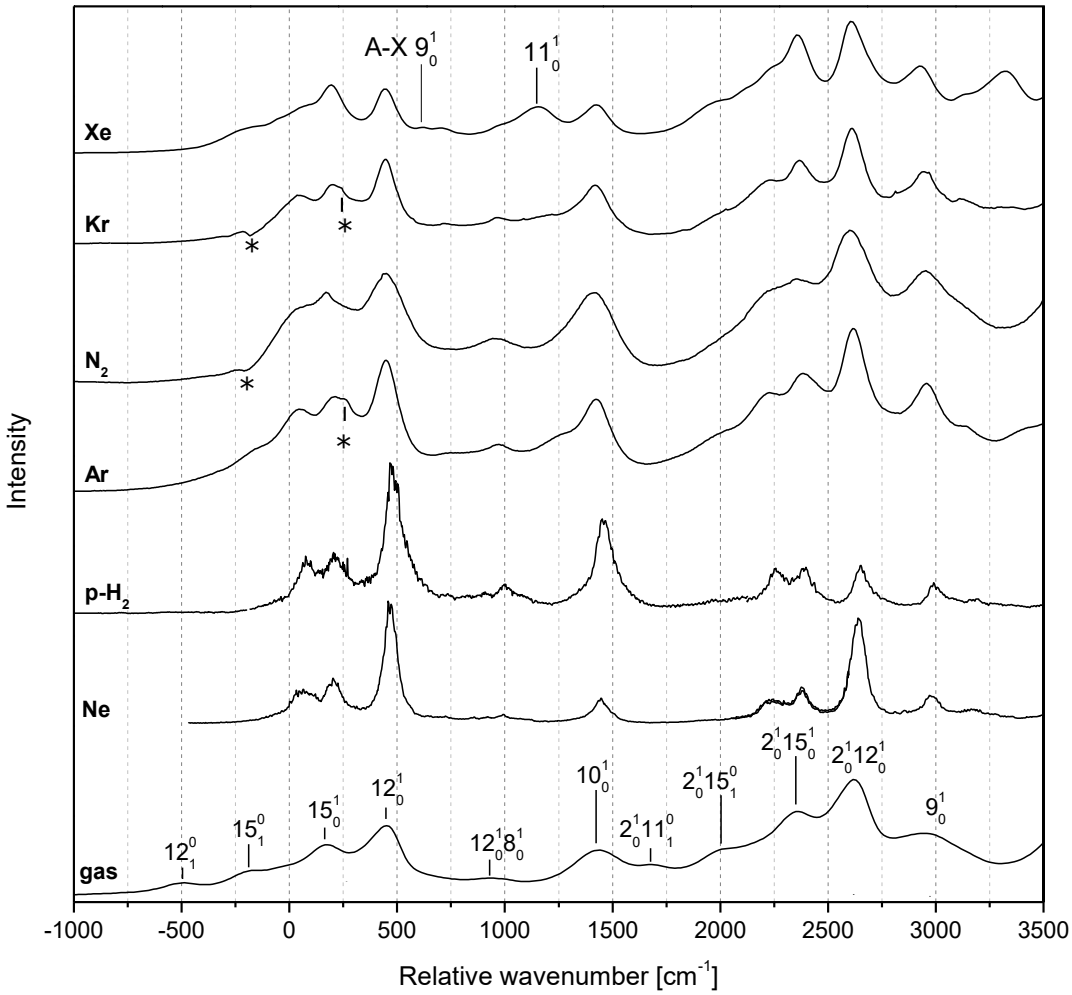

Figure 21. CH_3C_5N gas-phase UV-Vis absorption spectrum together with phosphorescence excitation spectra measured for the matrix-isolated compound. Spectra aligned with respect to the anticipated *0-0* positions, arbitrarily set to 0 cm^{-1}. Asterisks mark artifact bands.

Weak spectral features (most easily observed in solid N_2), at wavenumbers lower than those of $\tilde{B} - \tilde{X}$, are attributed to the $\tilde{A} - \tilde{X}$ system. $\tilde{A} - \tilde{X}$ and $\tilde{B} - \tilde{X}$ systems could be safely identified as originating in CH_3C_5N, since the excitation of their individual absorption features produced the same phosphorescence (Figure 22), with vibronic spacings corresponding to known vibrational frequencies of that molecule.

To deduce the origin of the $\tilde{A} - \tilde{X}$ system, a procedure similar to that applied for $\tilde{B} - \tilde{X}$ was employed, based on the $\tilde{A}$-state ν_{12} value (determined theoretically). This particular mode was chosen, since the molecular geometry in $\tilde{A}$ and $\tilde{B}$ states is very similar (see Figure 9), and the intensity pattern of the vibronic bands is expected to be (qualitatively) the same. Band 12_0^1, is the strongest of the $\tilde{B} - \tilde{X}$ system, and it was assumed to be also the most intense one of $\tilde{A} - \tilde{X}$.

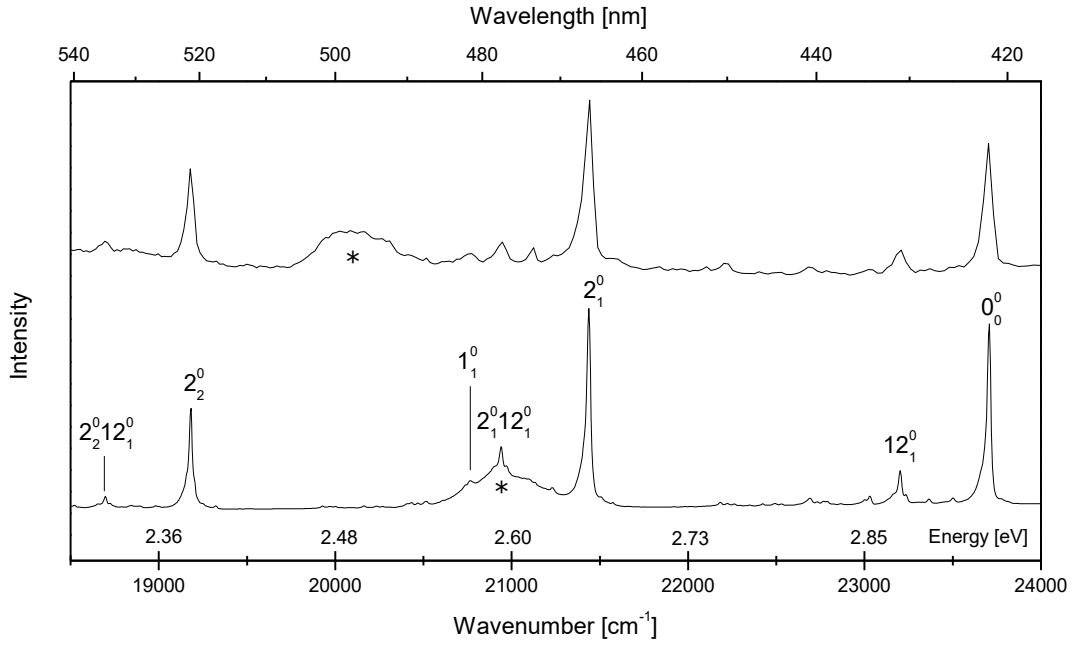

Figure 22. Phosphorescence of CH_3C_5N isolated in solid Ar. Excitation wavelengths coincide with the strongest (12_0^1) absorption bands of the $\tilde{A} - \tilde{X}$ (top) and $\tilde{B} - \tilde{X}$ (bottom) systems. Broad asterisked bands are the instrumental artifacts.

Wavenumbers of $\tilde{A} - \tilde{X}$ and $\tilde{B} - \tilde{X}$ bands, recognized in Ne and *p*-H_2 matrices, are listed in Table 16, together with (when available) respective Kr-matrix data. Spectra are dominated by the 2_0^n progression, promoted with the ν_{12} bending, very much like those reported for HC_5N [91]. Of note, vibronic progressions governed by triple-bond stretching modes (CC, CN, or largely delocalized) have also been observed in electronic absorption spectra of other acetylenic molecules: CH_3C_3N, CH_3C_4H, HC_3N, HC_4H, HC_6H, [206] or NC_4N, NC_6N [207,208].

Table 16 provides some updates of the analysis reported in Ref. [197]. The most important of these are:

- assignment of several previously unidentified bands (distinct progression) to 2_0^nx (see footnote *b* of Table 16);
- replacement of the $2_0^n 3_0^1$ attribution with $2_0^n 10_0^1 12_0^1$ (for symmetry reasons, coupling to e-symmetry vibrational modes is necessary);
- replacement of $\tilde{A}$-$\tilde{X}$ 11_0^1 with $\tilde{A}$-$\tilde{X}$ $12_0^1 14_0^2$.

Table 16. $\tilde{A} - \tilde{X}$ and $\tilde{B} - \tilde{X}$ vibronic wavenumber ($\bar{\nu}$ in cm^{-1}) values in phosphorescence excitation spectra of matrix-isolated CH_3C_5N. Assignments refer to $\tilde{B} - \tilde{X}$, unless otherwise stated.

Mode [a]	$\bar{\nu}$				
	in Ne		in *p*-H_2		in Kr
	absolute	relative to *0-0*	absolute	relative to *0-0*	relative to *0-0*
$\tilde{A}$-$\tilde{X}$ 14_0^1	~32530	-2186	~32300	-2131	
$\tilde{A}$-$\tilde{X}$ 12_0^1	32775	-1941	32495	-1936	
$\tilde{A}$-$\tilde{X}$ $12_0^1 14_0^2$	~33300	-1416	33025	-1406	-1374
phonon	~34785	69	34505	74	58
15_0^1	34921	205	34636	205	221
12_0^1	35183	467	34898	467	467
$12_0^1 15_0^1$ or $13_0^1 14_0^1$	35439	723			732, 750
$8_0^1 12_0^1$	35710	994	35428	997	982
10_0^1	36163	1447	35890	1459	1439
2_0^1x [b]	~36950	2234	~36690	2259	2229
$2_0^1 15_0^1$	37095	2379	~36815	2384	2387
$2_0^1 12_0^1$	37355	2639	37084	2653	2629
9_0^1	37697	2981	37422	2991	2959, 2970
$2_0^1 8_0^1 12_0^1$	~37883	3167	37623	3192	3150
$2_0^1 10_0^1$	38346	3630	38074	3643	3610
$2_0^1 10_0^1 12_0^1$	~38840	4124	~38590	4159	4107
2_0^2x [b]	~39140	4424	38849	4418	4395
$2_0^2 15_0^1$	39277	4561	38989	4558	4549
$2_0^2 12_0^1$	39526	4810	39239	4808	4786
$2_0^1 9_0^1$	39887	5171	39597	5166	5139
$2_0^2 8_0^1 12_0^1$	40062	5346	39781	5350	5317
$2_0^2 10_0^1$	40525	5809			5776
$2_0^2 10_0^1 12_0^1$	~41030	6314			6301
2_0^3x [b]	41305	6589			6543
$2_0^3 15_0^1$	41435	6719			6698
$2_0^3 12_0^1$	41679	6963			6933
$2_0^2 9_0^1$	42048	7332			7301
$2_0^3 10_0^1$	~42700				
$2_0^3 10_0^1 12_0^1$	43190	8474			8437
2_0^4x [b]	43475	8759			
$2_0^4 15_0^1$	43475	8759			8824
$2_0^4 12_0^1$	43614	8898			9067
$2_0^3 9_0^1$	44222	9506			9462
$2_0^4 10_0^1 12_0^1$	45340				
$2_0^4 10_0^1$	44823	10107			10074
$2_0^5 12_0^1$	45950	11234			
$2_0^4 9_0^1$	46350	11634			11618
$2_0^5 10_0^1$	46980				

[a] Based on Ref. [197].

[b] An unidentified ν_2-governed progression; "x" may stand for a phonon or for the ν_{16} mode.

Irrespective of the environment, the $\tilde{A} - \tilde{B}$ energetic separation remains practically the same: around 2320 cm^{-1} or 0.29 eV. The predicted value is 0.2 eV (Table 13) with other theoretical methods yielding 0.15 eV (CAM-B3LYP) or 0.21 eV (EOM-CCSD) [197]. Theory places the $\tilde{A} - \tilde{X}$ and $\tilde{B} - \tilde{X}$ transitions of CH_3C_5N at slightly lower energies than the corresponding transitions of HC_5N. Measurements confirm this with the difference being -460 cm^{-1} (estimated for $\tilde{A} - \tilde{X}$ transitions in Ar) and -475 cm^{-1} (for $\tilde{B} - \tilde{X}$).

Yet another interesting comparison between HC_5N and CH_3C_5N molecules concerns the gas-to-matrix shift. For the $\tilde{B} - \tilde{X}$ origin observed in Ar, it amounts to -846 cm^{-1} (CH_3C_5N) and -589 cm^{-1} (HC_5N). The effect can be roughly correlated with the polarizabilities of CH_3C_5N and HC_5N: 14.1 $Å^3$ and 11.2 $Å^3$ respectively (as calculated at the B3PW91/aug-cc-pVTZ level of theory [192]).

Figure 23 presents the relation between the wavenumber of the most intense band observed in *A*–*X* transition and the most intense band observed for the *B*–*X* transition (in both cases it is the 12_0^1 feature). One can see the proportional growth of both values. From the linear fit (intercept being negligible compared to relevant abscissa values and having no recognized physical meaning), one can see that $\tilde{A} - \tilde{X}$ excitation is systematically 9% lower in energy than $\tilde{B} - \tilde{X}$, irrespective of the environment.

Also the $\tilde{a} - \tilde{X}$ origin wavenumbers are linearly correlated to the $\tilde{B} - \tilde{X}$ origins, when the values found for different media are considered. The plot of Figure 23 offers a simple extrapolation method to estimate the magnitude of singlet-triplet separation for the gas-phase compound (24 100 cm^{-1}) and for the pure solid (23 100 cm^{-1}), where phosphorescence was not observed.

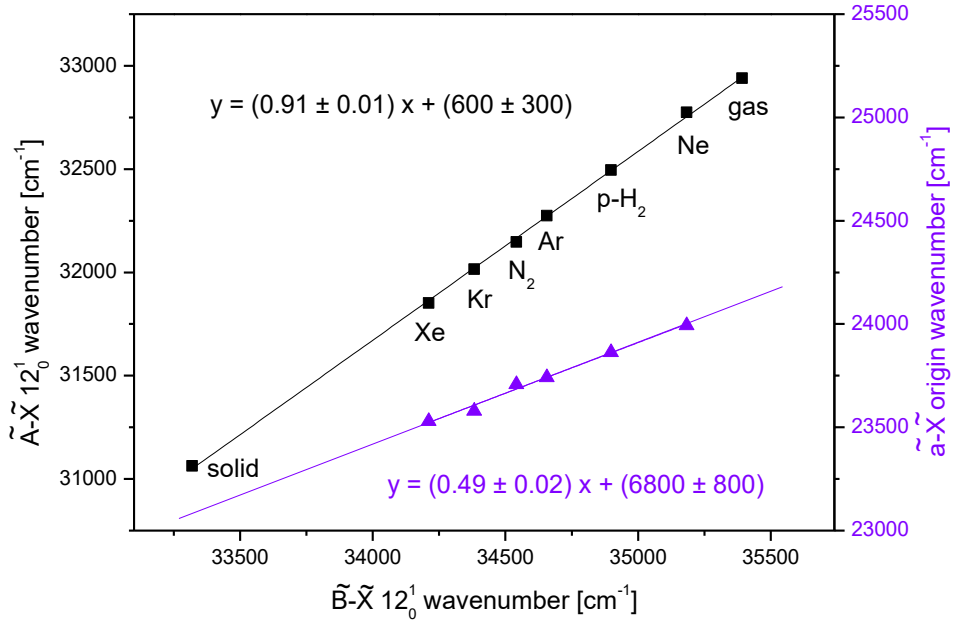

Figure 23. Dependence of the wavenumber of the most intense bands of $\tilde{A} - \tilde{X}$ (black squares) and $\tilde{a} - \tilde{X}$ (purple triangles) on the wavenumber of the most intense bands of $\tilde{B} - \tilde{X}$ electronic systems of CH_3C_5N, observed in various media. Gas- and solid-phase wavenumbers come from UV-Vis absorption, all other values are based on phosphorescence excitation spectra.

The last feature worth mentioning in this section is a strong, broad band appearing in CH_3C_5N phosphorescence excitation spectra, with a maximum clearly discernible for a Kr matrix at ~49 300 cm^{-1} (6.1 eV). Similarly, the absorption spectrum of pure solid CH_3C_5N shows a very intense band at 43 600 cm^{-1}. These transitions can be tentatively assigned to the $\tilde{D}\ ^1E - \tilde{X}\ ^1A_1$ system (calculated origin at 6.65 eV). [197]

4 PHOTOCHEMISTRY AND SPECTROSCOPY OF CYANOPOLYYNES – LONG CHAIN FORMATION

This part of the Thesis describes formation and spectroscopic characterization of long carbon-nitrogen chains: HC_7N, CH_3C_7N, HC_9N, and $C_{10}N_2$. Along with their formation, the appearance of C_5N^- was also observed.

Previous experimental and theoretical studies assisted in predicting some of the spectroscopic properties of these compounds formed in solid Kr or Ar matrices. The products could be detected due to their strong, long-lived (on the order of ms) electronic luminescence, and assignments were supported with quantum chemical calculations. This emission was interpreted as phosphorescence on the basis of its long lifetime and agreement between the experimental and predicted $\tilde{a} - \tilde{X}$ energy levels. No associated IR absorption bands were observed.

The first section of this chapter explains how the precursors were chosen. It is followed by a description of the results obtained for these molecules and a discussion of these results at the end of the chapter.

Over the course of these experiments, HC_5N was used as one of the precursors. The analysis of its phosphorescence spectrum was revisited and this new information appears in APPENDIX 1.

4.1 Starting point: the choice of precursors

Earlier studies [115,156,157] have shown that monocyanopolyynes and dicyanopolyynes can form in cryogenic UV-stimulated processes from shorter $HC_{2n+1}N$ species reacting with acetylenic-type molecules $C_{2m}H_2$. Photochemically-stimulated cryogenic synthesis has not as yet been reported for any methylated cyanopolyyne.

Chain elongation may happen in the rigid matrix environment when one of the precursors dissociates following the absorption of a photon and loses a hydrogen atom. The excess energy from this process must be dissipated and may soften the matrix locally. This may allow for the reactions between previously separated species. However, precursor molecules are larger than the interatomic separation between the neighbouring host atoms (~4 Å in solid Kr [209], a host mostly used here), and the bigger (longer) the precursors, the more difficult movement through these host atoms becomes. The experiments performed here involved mixing two specifically selected precursor substances with a rare gas and solidifying the mixture, followed by UV (ArF laser, 193 nm) irradiation for several hours.

HC_5N (the longest cyanopolyyne available through preparatory organic synthesis) and C_4H_2 were used as the precursors in formation of HC_9N so that the sum of carbon atoms in the precursors matches what is required to form the product. The dicyano species $C_{10}N_2$ was generated from HC_5N alone. HC_7N and C_5N^- were also observed over the course of photolysis in addition to the expected products.

To form CH_3C_7N, an appropriate methylated precursor was necessary. Since the goal was to form a polyynic molecule, the precursor had to possess –C≡C– unit(s) and a methyl group. An additional requirement was that the molecule be easy to photolyze which meant termination at one end with an easily detachable hydrogen atom. Propyne (CH_3C_2H) is the smallest molecule fulfilling these criteria (it is also an interstellar molecule). As the second precursor, a $HC_{2n+1}N$-type molecule, HC_5N, was chosen, providing a linear cyano-terminated carbon backbone. An experiment involving a CH_3C_2H + HC_3N mixture, expected to yield CH_3C_5N, was performed to verify the validity of this approach to chain elongation.

Conceivable $CH_3C_{2n+1}N$ formation mechanisms involve the loss of acetylenic hydrogens for both propyne and $HC_{2n+1}N$ precursors. Several photolysis studies of propyne have been performed previously (*e.g.* [210–216]). In particular, photolysis of propyne at 193 nm leads to formation of the following products: $CH_3CC^{\bullet}$, hydrogen (atomic and molecular), H_2CCCH, HCCH, and carbon clusters [214–216]. Given that the single C-C bond of propyne can break upon photolysis at these wavelengths, one would also expect to detect products of the reaction between $C_2H^{\bullet}$ and either HC_3N or HC_5N. These products should include HC_5N or HC_7N. In a UV-irradiated $Kr/CH_3C_2H/HC_3N$ matrix, HC_5N and CH_3C_5N were identified. Similarly, using the precursors CH_3C_2H + HC_5N, the product HC_7N was observed along with CH_3C_7N, providing the opportunity for an additional spectroscopic characterization of HC_7N. Test experiments were also performed involving the pairs CH_3C_5N + C_2H_2 and CH_3C_3N + C_2H_2. These tests produced no evidence for elongation of methylated cyanopolyynic chains.

Two different gas mixtures were used in order to differentiate between the produced CH_3C_7N and HC_7N molecules. Namely, cyanodiacetylene was deposited either in the same or twice smaller amount than that of propyne. Such a mixture should favour the formation of methylated species. Indeed, with propyne in excess ($Kr/CH_3C_2H/HC_5N$ ratio of 1000/2/1), CH_3C_7N seems to have formed more efficiently than for the matrix ratio of 1000/1/1.

4.2 HC_7N and CH_3C_7N

4.2.1 Theoretical predictions and previous works

Similarities in electronic emission spectra of HC_5N and CH_3C_5N were presented in Chapter 3.2.2. Similarities are also to be expected for the HC_7N/CH_3C_7N pair.

The results of quantum chemical calculations [192] for the lowest electronic energy levels of HC_7N and CH_3C_7N are presented in Table 17. Despite the obvious difference in molecular symmetry, general patterns of electronic state distribution are similar for both species, reflecting the similarity of chromophores. For states arising from HOMO-LUMO transitions, HC_7N states have higher energies compared to CH_3C_7N, a pattern also observed for HC_5N, and CH_3C_5N. The highest oscillator strength (*f*) is predicted for the *E–X* transition in both cases. The *a–X* transition energy of CH_3C_7N is practically identical to that of HC_7N, just as previously predicted and measured for the CH_3C_5N/HC_5N pair (Ref. [197] and Chapter 3.2). Vertical excitation energies are higher than the corresponding values for

0-0 transitions. Such differences (more pronounced for $\tilde{B}$ than for $\tilde{E}$ states) reflect dissimilarities in equilibrium geometry or in steepness of the potential energy surfaces of the ground and respective excited states. As might be guessed from missing entries in Table 17, *0-0* energy values were, in certain cases, impossible to derive due to numerical problems inherent to the applied method.

Table 17. Energy [eV], corresponding wavelength [nm], and oscillator strength for transitions involving the ground and excited electronic states of HC_7N and CH_3C_7N, as calculated at B3PW91/aug-cc-pVTZ level of theory [192]. Electronic configurations of the molecules are the following. HC_7N, $\tilde{X}\ ^1\Sigma^+$: [core] $(1\sigma)^2\ (2\sigma)^2\ (3\sigma)^2\ (4\sigma)^2\ (5\sigma)^2\ (6\sigma)^2\ (1\pi)^4\ (7\sigma)^2\ (2\pi)^4\ (8\sigma)^2\ (9\sigma)^2\ (3\pi)^4\ (4\pi)^4\ (1\pi^*)^0\ (2\pi^*)^0\ (1\sigma^*)^0$; CH_3C_7N, $\tilde{X}\ ^1A_1$: [core] $(1a_1)^2\ (2a_1)^2\ (3a_1)^2\ (4a_1)^2\ (5a_1)^2\ (6a_1)^2\ (7a_1)^2\ (1e)^4\ (2e)^4\ (8a_1)^2\ (3e)^4\ (4e)^4\ (5e)^4\ (1e^*)^0\ (1a_1{}^*)^0\ (2e^*)^0$.

HC_7N					CH_3C_7N				
State	Dominant orbital excitation	Vertical energy (λ)	f [a]	*0-0* transition energy (λ)	State	Dominant orbital excitation	Vertical energy (λ)	f [a]	*0-0* transition energy (λ)
$\tilde{A}\ ^1\Sigma^-$	4π→1π*	3.29 (377)	0	2.84 (437)	$\tilde{A}\ ^1A_2$	5e→1e*	3.23 (384)	0	2.75 (451)
$\tilde{B}\ ^1\Delta$	4π→1π*	3.40 (365)	0	2.96 (419)	$\tilde{B}\ ^1E$	5e→1e*	3.34 (371)	0	2.9 (428)
$\tilde{C}\ ^1\Sigma^-$	3π→1π*	5.10 (243)	0	4.79 (259)	$\tilde{C}\ ^1A_2$	4e→1e*	5.05 (246)	0	4.73 (262)
$\tilde{D}\ ^1\Delta$	3π→1π*	5.27 (235)	0	4.98 (249)	$\tilde{D}\ ^1E$	4e→1e*	5.22 (238)	0.0001	4.92 (252)
$\tilde{E}\ ^1\Sigma^+$	4π→1π*	5.84 (212)	2.9	5.63 (220)	$\tilde{E}\ ^1A_1$	5e→1e*	5.61 (221)	2.9	5.40 (230)
					$\tilde{F}\ ^1E$	5e→1a$_1$*	6.18 (201)	0	
					$\tilde{G}\ ^1A_2$	5e→2e*	6.2 (200)	0	
$\tilde{F}\ ^1\Sigma^+$	3π→1π*	6.23 (199)	0.78	5.86 (212)	$\tilde{H}\ ^1A_1$	4e→1e*	6.25 (198)	1.2	
					$\tilde{I}\ ^1E$	5e→2e*	6.25 (198)	0.0002	
$\tilde{a}\ ^3\Sigma^+$				2.25 (551)	$\tilde{a}\ ^3A'$ [b]				2.23 (556)

[a] Value of zero indicates a value of less than $5 \cdot 10^{-5}$.

[b] C_s geometry uncertain; C_{3v} also possible (less likely), leading to A_1 symmetry.

The nature of the $\tilde{E} - \tilde{X}$ transition in both molecules is similar to those of $\tilde{A} - \tilde{X}$ and $\tilde{B} - \tilde{X}$, as they all involve mainly HOMO and LUMO orbitals. Although both $\tilde{A} - \tilde{X}$ and $\tilde{B} - \tilde{X}$ are formally (as for HC_7N) or practically (as for $\tilde{B} - \tilde{X}$ CH_3C_7N; see page 61) forbidden, one may expect to see the $\tilde{B} - \tilde{X}$ absorption due to the coupling with one of the vibrational bending modes, a process already reported for HC_3N [72,128], HC_5N [91], CH_3C_3N [132], and CH_3C_5N [197]. $\tilde{A} - \tilde{X}$ transitions, requiring the violation of orbital symmetry selection rule (+/-), are expected to have very low intensity, and may not be detectable at all. In the case of CH_3C_5N [197], only traces of an $\tilde{A} - \tilde{X}$ transition were observed. Thus, both $\tilde{B}$ and $\tilde{E}$ states are of main interest for further discussion.

The molecular geometries of states $\tilde{X}$, $\tilde{B}$, $\tilde{E}$, and $\tilde{a}$ are depicted in Figure 24. Ground-state HC_7N and CH_3C_7N possess conjugated carbon-nitrogen backbones of similar geometry. The difference in bond lengths is not higher than 0.5 pm and both molecules seem identical at the CN ending of the chain. For both molecules, the geometry change accompanying the $\tilde{B} - \tilde{X}$ transition is almost identical to that of $\tilde{a} - \tilde{X}$. Consequently, one may expect the main vibronic progressions in $\tilde{B} - \tilde{X}$ absorption and in phosphorescence spectra to be shaped by vibrational modes of a similar nature, just as was observed for the HC_5N/CH_3C_5N pair [197]. In contrast, geometry changes occurring upon the transition from $\tilde{X}$ to $\tilde{E}$ are much different than those for $\tilde{a} - \tilde{X}$ or $\tilde{B} - \tilde{X}$, and because of this the $\tilde{E} - \tilde{X}$ bands of both chemicals are not expected to resemble their respective $\tilde{a} - \tilde{X}$ or $\tilde{B} - \tilde{X}$ bands. The $\tilde{E} - \tilde{X}$ geometry changes are also substantially different in comparing HC_5N to CH_3C_5N, and the respective $\tilde{E} - \tilde{X}$ bands are also expected to differ. The results of quantum chemical calculations predicting vibrational wavenumbers of HC_7N and CH_3C_7N in $\tilde{X}$, $\tilde{B}$ (for HC_7N) and $\tilde{E}$ states are presented in Table 18.

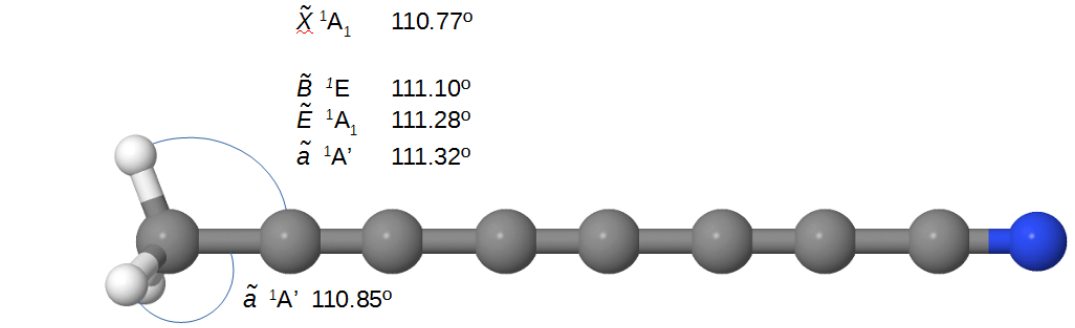

$\tilde{X}$ $^1A_1$	109.3	144.3	121.2	134.8	122.0	134.2	121.7	135.7	115.9
$\tilde{B}$ ^1E	+0.2	-0.8	+2.7	-4.3	+5.3	-5.5	+4.7	-3.2	+1.8
$\tilde{E}$ $^1A_1$	+0.6	-1.5	+2.3	+0.1	+1.5	+0.4	+2.2	-1.3	+2.0
$\tilde{a}$ $^1A'$	+0.2 +0.1	-0.5	+2.9	-4.7	+6.1	-6.4	+5.4	-3.4	+2.0

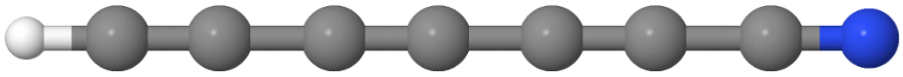

$\tilde{X}$ $^1\Sigma^+$	106.4	120.8	135.0	121.8	134.3	121.6	135.7	115.9
$\tilde{B}$ $^1\Delta$	0	+2.7	-4.3	+5.5	-5.7	+4.9	-3.2	+1.8
$\tilde{E}$ $^1\Sigma^+$	+0.3	+2.4	-0.6	+2.0	0	+2.4	-1.3	+2.0
$\tilde{a}$ $^3\Sigma^+$	0	+3.0	-4.8	+6.3	-6.5	+5.4	-3.3	+1.8

Figure 24. CH_3C_7N and HC_7N geometry as derived with B3PW91/aug-cc-pVTZ [192]. Distances in pm. Distances in excited state relative to the ground state.

Table 18. Harmonic wavenumbers of vibrational modes ([cm^{-1}]; scaling factor 0.96) for the ground and selected excited electronic states of HC_7N and CH_3C_7N, as derived at the B3PW91/aug-cc-pVTZ level of theory [192]. Vibrational modes of similar nature are horizontally aligned (occasionally resulting in a reversal in the order of wavenumbers). See the "APPENDIX 2" (p. 125 and p. 127) for visualization of modes. Mode symmetry descriptions refer strictly to the ground electronic states.

HC_7N				CH_3C_7N		
Mode	$\tilde{X}$	$\tilde{B}$	$\tilde{E}$	Mode	$\tilde{X}$	$\tilde{E}$
σ symmetry				a_1 symmetry		
ν_1	3324	3316	3290			
				ν_1	2910	2841
ν_2	2253	2033	2172	ν_2	2260	2180
				ν_3 [a]	2208	2132
ν_3	2197	2117	2073	ν_4	2187	1969
ν_4 [a]	2154	1907	1949			
ν_5	2049	1819	1855	ν_5	2093	1917
ν_6	1295	1393	1252	ν_6	1364	1323
				ν_7	1333	1295
				ν_8	1066	1061
ν_7	902	926	884	ν_9	758	745
ν_8	464	477	456	ν_{10}	402	395
π symmetry				e symmetry		
				ν_{11}	2976	2894
				ν_{12}	1398	1352
				ν_{13}	991	953
ν_9	643	522	541			
ν_{10}	602	553	517	ν_{14}	574	490
ν_{11}	523	483	434	ν_{15}	518	437
ν_{12}	461	434	412	ν_{16}	463	417
ν_{13}	287	290	211	ν_{17}	340	193
				ν_{18}	226	212
ν_{14}	162	153	71	ν_{19}	124	57
ν_{15}	61	60	41	ν_{20}	47	39

[a] ν_4 of HC_7N is characterized by similar movement of backbone atoms as ν_3 of CH_3C_7N.

The most relevant previously published report on HC_7N includes a variety of spectroscopic studies. Its electronic luminescence in solid Ar and Kr has been reported [157,217]. Part of the HC_7N phosphorescence excitation spectrum, although without any associated interpretation, is available [116], as well. The IR absorption spectroscopy of solid Ar-isolated HC_7N revealed traces of two bands: ν_3 at 2202.0 cm^{-1} and ν_1 at 3323.1 cm^{-1} [157]. This compound has also been studied in liquid solutions, where its UV-Vis absorption was measured [98,103,105,218].

The only IR absorption spectrum of CH_3C_7N published so far is the one measured for a CCl_4 solution [147] although no table of absorption wavenumbers was provided. Following digitization of the spectrum, absorption wavenumbers were determined to be 2190, 2212, 2243, and 2287 cm^{-1} with a precision of ±1 cm^{-1}. Theoretical results available for CH_3C_7N (Table 18) predict two very intense IR transitions, ν_3 and ν_4, matching the reported ones [147]. Other bands should be at least an order of magnitude weaker. The 2243 and 2287 cm^{-1} bands observed in CCl_4 could correspond to the ν_2 band, possibly split by an anharmonic interaction (such interactions in that region were reported for CH_3C_5N, see Ref.

[196] or Chapter 3.2.1). The same study also reports UV-Vis absorption of the compound in an ether solution where an intense band at 223.5 nm and a series of much weaker ones at 280, 298.5, 319.5 and 343.5 nm were detected.

4.2.2 Phosphorescence

Luminescence from photoproduct(s) generated in a $Kr/CH_3C_2H/HC_5N$ matrix was detected in spectral windows around 19 700 cm^{-1} (2.44 eV) and 17 500 cm^{-1} (2.17 eV). The luminescence featured a vibronic progression resembling those observed for other cyanopolyynes. Two intense bands appeared close to one another in both regions and were separated from one another by ~60 cm^{-1} (Figure 25). The one of lower wavenumber is coincident with an already known [157,217] HC_7N emission band (2.44 eV, compared to the predicted value of 2.25 eV, Table 17). It was better distinguished upon the excitation at 46 380 cm^{-1} (5.75 eV), in agreement with what has been previously observed for HC_7N. The other band, with a dissimilar excitation spectrum (see Figure 26) having a maximum absorption at 43 180 cm^{-1} (5.35 eV), was very likely CH_3C_7N. The theory predicted (Table 17) HC_7N transition of slightly higher energy than that of methylated analogue, nevertheless, this difference is negligible at the level of theory applied.

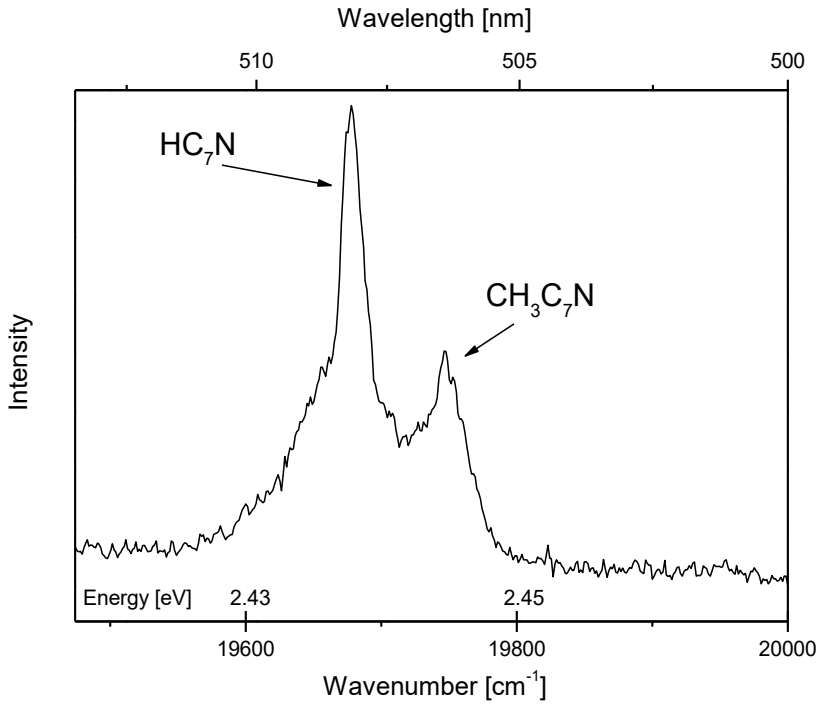

Figure 25. CH_3C_7N and HC_7N luminescence from a previously photolysed (193 nm) $Kr/CH_3C_2H/HC_5N$ (1000/1/1) matrix, excited at 46 840 cm^{-1} (5.81 eV, 213.5 nm).

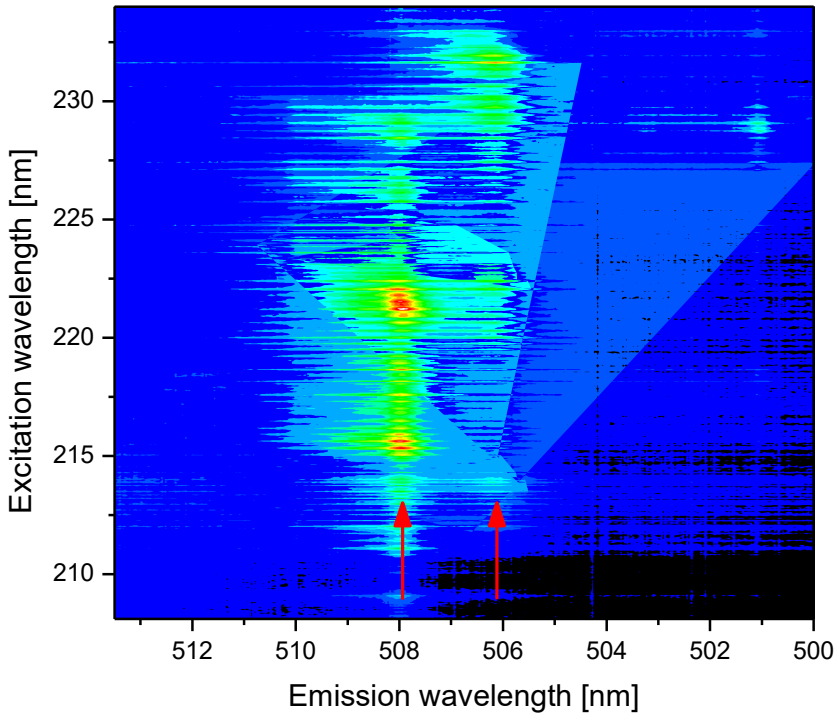

Figure 26. The excitation-emission map[1] of a previously photolysed (193 nm) Kr/CH_3C_2H/HC_5N (1000/1/1) matrix showing spectral features (red arrows) coming from two different species: HC_7N and CH_3C_7N (see Figure 25). Colours correspond to the observed intensity with red being the highest and blue/black being the lowest.

Table 19 presents the observed vibronic bands of the HC_7N phosphorescence (Figure 27) excited at the maximum of UV absorption (interpreted later as $\tilde{E} - \tilde{X}$ absorption) in a previously photolysed Kr/CH_3C_2H/HC_5N matrix. HC_7N wavenumbers measured in Ar/HC_5N/C_2H_2 [157] and Kr/HC_5N/C_2H_2 [217] experiments are given for comparison. A very weak broad feature was found here approximately 2200 cm^{-1} lower than the expected lowest energy band of HC_7N. No excitation spectra exist to confirm its common origin with known HC_7N bands. However, at other excitation wavelengths, where the HC_7N bands were significantly weaker or not present at all, this band also did not appear. The spacing of ~2200 cm^{-1} matches well the already reported ν_3 progression and it can therefore be identified as 3_3^0.

Table 19. Phosphorescence bands of HC_7N in solid krypton. Wavenumber ($\bar{\nu}$) values in cm^{-1}. Relative wavenumbers ($\Delta\bar{\nu}$) calculated with respect to the preceding element of the vibronic progression.

Ar [157]		Kr [217]		Kr (this work)		
$\bar{\nu}$	$\Delta\bar{\nu}$	$\bar{\nu}$	$\Delta\bar{\nu}$	$\bar{\nu}$	$\Delta\bar{\nu}$	Assignment
19764	-	19700	-	19690	-	0_0^0
17565	2199	17500	2200	17490	2200	3_1^0
15378	2187	15310	2190	15310	2180	3_2^0
				13140 [a]	2170	3_3^0

[a] Higher uncertainty, due to a large band breadth (±20 cm^{-1}).

[1] For technical details, see Chapter 2.8.3.

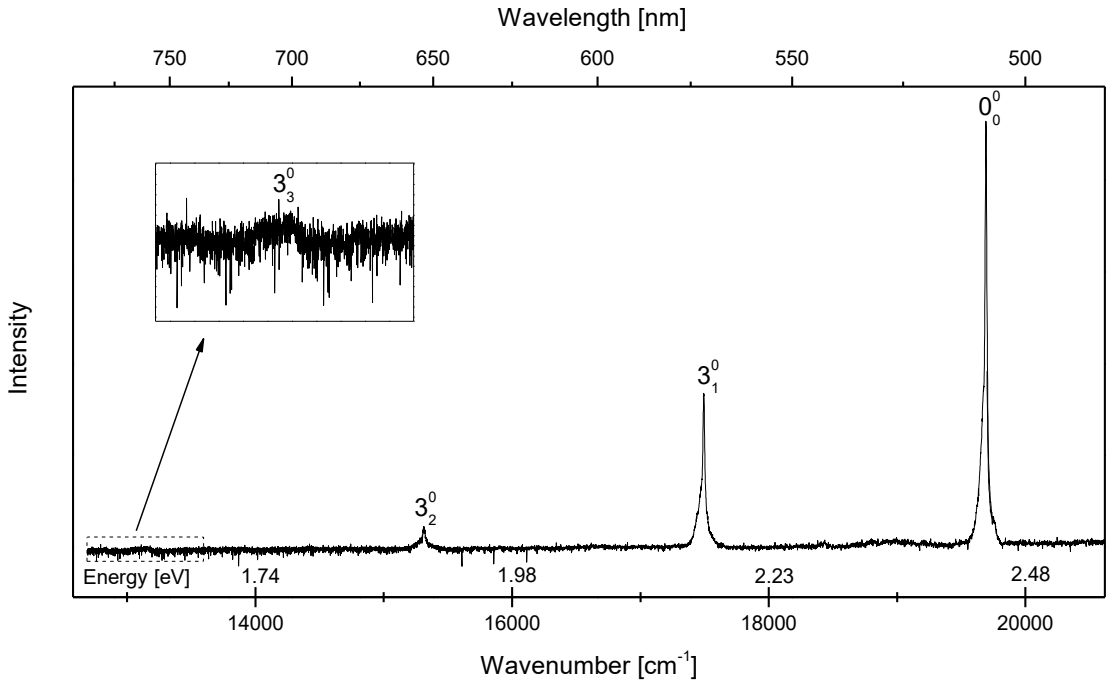

Figure 27. HC_7N phosphorescence spectrum coming from a previously photolysed (193 nm) $Kr/CH_3C_2H/HC_5N$ (1000/2/1) matrix, excited at 46 380 cm^{-1} (5.75 eV, 215.6 nm).

As mentioned, excitation at 43 180 cm^{-1} (5.35 eV) led preferably to the phosphorescence of CH_3C_7N. Figure 28 depicts the corresponding spectrum. The energy of the emission of the most intense band at 2.45 eV matches reasonably well with what is expected for vibrationless origin of the singlet-triplet transition, 2.23 eV (Table 17). The observed spacing between bands is 2200 cm^{-1}, in good agreement with calculations for either ν_4 (2187 cm^{-1}) or ν_3 (2208 cm^{-1}) in the ground electronic state (see Table 18). Using the case of HC_7N as a guide, preference should be given to the pseudosymmetric mode ν_4. Similar reasoning was used in the analysis of the spectrum of CH_3C_5N based on its similarity to HC_5N, see Chapter 3.2 or Ref. [196]. However, alike HC_7N/CH_3C_7N "splitting" observed in the consecutive elements of the vibronic progression (see p. 72), indicates that a vibrational quantum governing the progression of CH_3C_7N should be very close to 2200 cm^{-1}, the value found for analogous progression of HC_7N. This points to the mode ν_3 rather than ν_4. Interestingly, neither of the two is directly related to the change of molecular geometry accompanying the considered electronic transition. The broadness of observed vibronic band around 17 550 cm^{-1} may suggest some overlapping of the modes ν_3 and ν_4. In another experiment, the less intense feature showed two distinct maxima: at 17 530 cm^{-1} and at 17 550 cm^{-1}. An additional argument comes from the fact, that both ν_3 and ν_4 are predicted to have comparably high Raman activities [192]. Such modes have already been shown to shape the main vibronic progressions of similar cyanopolyynic molecules [92,115,217].

Both emission bands (detected at 19 750 cm^{-1} and 17 550 cm^{-1}) were confirmed, by measuring the corresponding excitation spectra, to come from the same species.

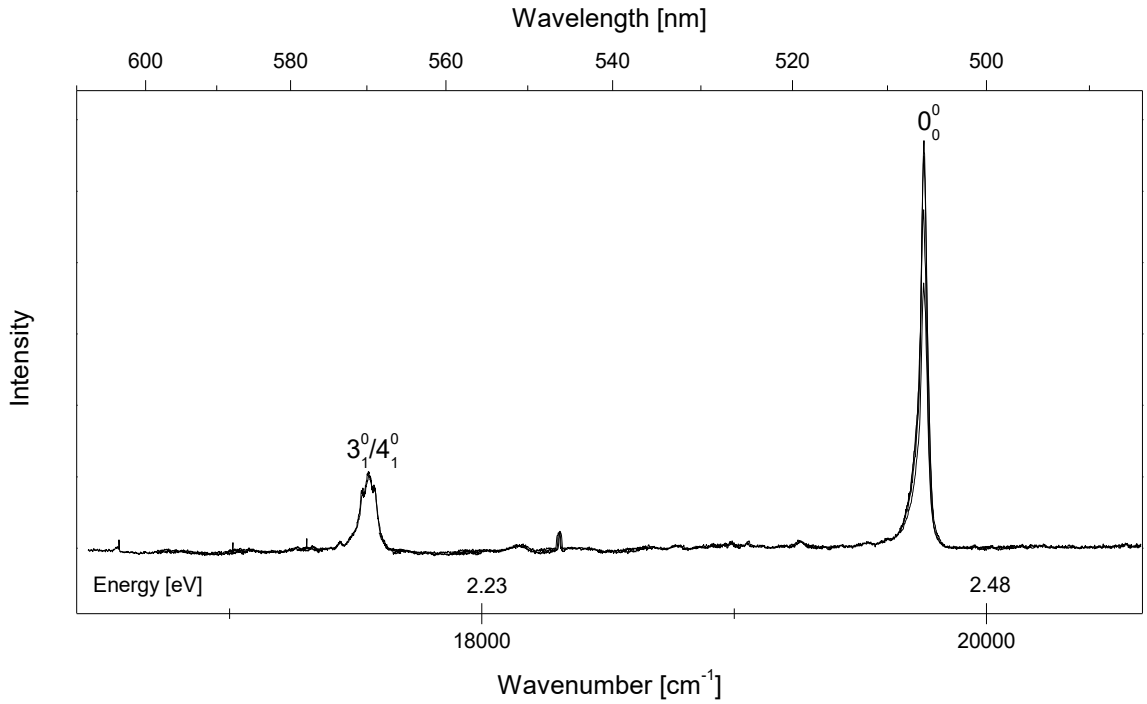

Figure 28. CH_3C_7N phosphorescence from a previously photolysed (193 nm) Kr/CH_3C_2H/HC_5N (1000/2/1) matrix, excited at 43 180 cm^{-1} (5.35 eV, 231.6 nm).

Phosphorescence lifetimes of HC_7N and CH_3C_7N were measured, yielding the decays depicted in Figure 29. Upon excitation at 46 380 cm^{-1} (5.75 eV), the band assigned to the origin of the $\tilde{a}\ ^3\Sigma^+ \rightarrow \tilde{X}\ ^1\Sigma^+$ system of HC_7N showed mono-exponential decay with $\tau = (8.2 \pm 0.1)$ ms. The decay in a Kr matrix is faster than what was reported for solid Ar which also exhibited a mono-exponential curve with $\tau = (34 \pm 1.5)$ ms [157]. The second band, assigned to CH_3C_7N, showed a double-exponential decay when excited at 43 180 cm^{-1} (5.35 eV). Given that the CH_3C_7N band is contaminated at 43 180 cm^{-1}, with a contribution from HC_7N (see Figure 26), it was reasonable to fix one of the decay time components at 8.2 ms. The least-squares fitting then gave $\tau = (22.8 \pm 0.3)$ ms as the second component, attributable to CH_3C_7N.

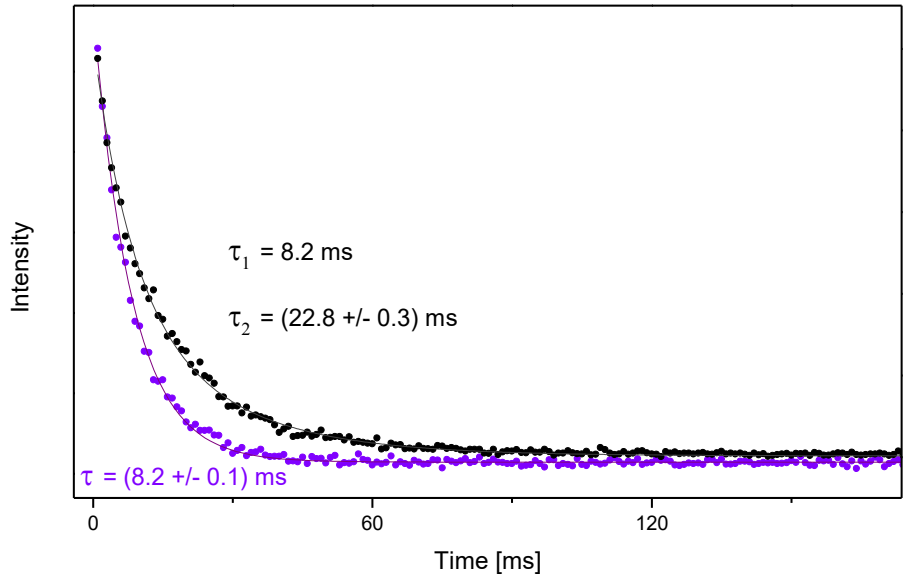

Figure 29. Phosphorescence lifetime decay: mono-exponential due to HC_7N (purple), resulting from laser excitation at 46 380 cm^{-1} (5.75 eV, 215.6 nm) and double-exponential due to overlapping emission from two compounds: HC_7N and CH_3C_7N (black), resulting from laser excitation at 43 180 cm^{-1} (5.35 eV, 231.6 nm).

4.2.3 Singlet excited electronic states

The excitation spectrum of HC_7N phosphorescence was measured here from 25 000 cm^{-1} to 52 080 cm^{-1}. A part of the spectrum is presented in Figure 30. Spectral features observed in the 27 000 cm^{-1} – 34 000 cm^{-1} region are interpreted as $\tilde{B}\ ^1\Delta - \tilde{X}\ ^1\Sigma^+$. Since $\Delta - \Sigma$ transitions are symmetry-forbidden, the *0-0* feature cannot be present in luminescence excitation or UV absorption spectra. The same was true for analogous electronic systems of HC_3N [72] and HC_5N [91]. The $\tilde{B}\ ^1\Delta - \tilde{X}\ ^1\Sigma^+$ transitions may occur when coupled to π-symmetry vibrations (Herzberg-Teller effect, see *e.g.* [219,220] and references therein). For HC_3N and HC_5N, such promoting bending modes were found to be of a 'zig-zag' type. This would suggest the same role for the ν_{10} mode of HC_7N whose predicted *B*-state wavenumber is 553 cm^{-1} (see "APPENDIX 2" for visualization). However, the main bands of the most prominent vibronic progression, spaced by ~2100 cm^{-1}, are clearly doubled, suggesting the involvement of yet another promoting π-symmetry vibration. This promotor might be ν_{12} (*B*-state wavenumber prediction: 434 cm^{-1}), a bending where the terminal HCC and CN undergo motions analogous to that of the 'zig-zag' mode ν_{10}. Given that the lowest-wavenumber doublet was detected at 27 620/27 640 cm^{-1}, the $\tilde{B} - \tilde{X}$ origin is expected at 3.36 or 3.37 eV (27 090 or 27 190 cm^{-1}). The inequality of the last two values reflects problems with assessing the true wavenumbers and/or identities of the considered π-symmetry vibrations. Further profiting from analogies with shorter $HC_{2n+1}N$ species which feature similar molecular distortions upon $\tilde{B} - \tilde{X}$ excitation, from a similar pattern of the excited electronic state distribution, and from similarities in observed phosphorescence spectra, the spacing of the main vibronic progression can be attributed to the ν_3 pseudosymmetric stretch. Wavenumbers of the bands assigned in Figure 30 (observed for the $Kr/C_4H_2/HC_5N$ sample) are listed in Table 20.

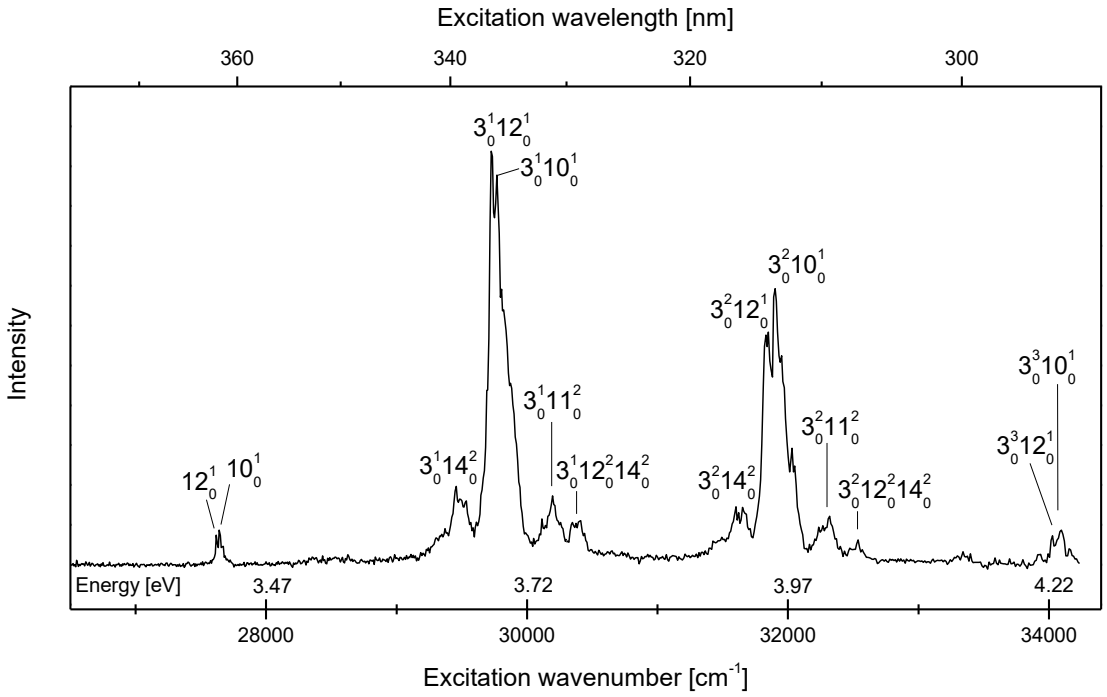

Figure 30. Excitation spectrum of HC_7N phosphorescence (detected at 17 500 cm^{-1}, 2.17 eV, *i.e.* for the second intense phosphorescence band), coming from a previously photolysed (193 nm) $Kr/C_4H_2/HC_5N$ (1000/1/1) matrix. Spectrum reflects the $\tilde{B} - \tilde{X}$ absorption. The applied laser intensity correction may distort the phosphorescence intensity pattern.

Table 20. List of the most intense bands in HC_7N $\tilde{B} - \tilde{X}$ excitation spectrum. Wavenumber ($\bar{\nu}$) values in cm^{-1}.

$\bar{\nu}$	Assignment
27620	12_0^1
27640	10_0^1
29460	$3_0^1 14_0^2$
29730	$3_0^1 12_0^1$
29770	$3_0^1 10_0^1$
30190	$3_0^1 11_0^2$
30390	$3_0^1 12_0^2 14_0^2$
31600	$3_0^2 14_0^2$
31840	$3_0^2 12_0^1$
31900	$3_0^2 10_0^1$
32320	$3_0^2 11_0^2$
32540	$3_0^2 12_0^2 14_0^2$
34030	$3_0^3 12_0^1$
34090	$3_0^3 10_0^1$

No strong spectral features were observed at energies higher than those of the $\tilde{B} - \tilde{X}$ system, up to $\tilde{E} - \tilde{X}$ transitions. A weak structure appeared around 35 360 cm^{-1} (4.38 eV). It remains unassigned.

Figure 31 presents another fragment of the HC_7N excitation spectrum, allowing comparison with the UV absorption of HC_7N in acetonitrile, as reported in Wakabayashi *et al.* [98]. The breadths of observed bands are larger for the liquid solution than for a solid Kr matrix, but

the gas-to-acetonitrile and gas-to-matrix wavenumber shifts seem similar. This spectrum of HC_7N observed for $Kr/C_4H_2/HC_5N$ does not qualitatively differ from the one produced in the $Kr/CH_3C_2H/HC_5N$ experiment (*cf.* Figure 31 and Figure 32). The observed vibronic bands are assigned to the fully allowed $\tilde{E} - \tilde{X}$ system which has a theoretically predicted vertical transition energy of 5.84 eV (see Table 17). The strongest emission was observed for excitation around 5.77 eV (215 nm) and 5.61 eV.[1] The same values were reported in Ref. [217]. The ensuing vibronic spacing of approximately 1300-1400 cm^{-1} may originate in the ν_6 vibrational mode, although the collected data did not permit for the detailed interpretation of this excitation spectrum, nor for finding the vibrationless origin. The most intense bands are listed in Table 21.

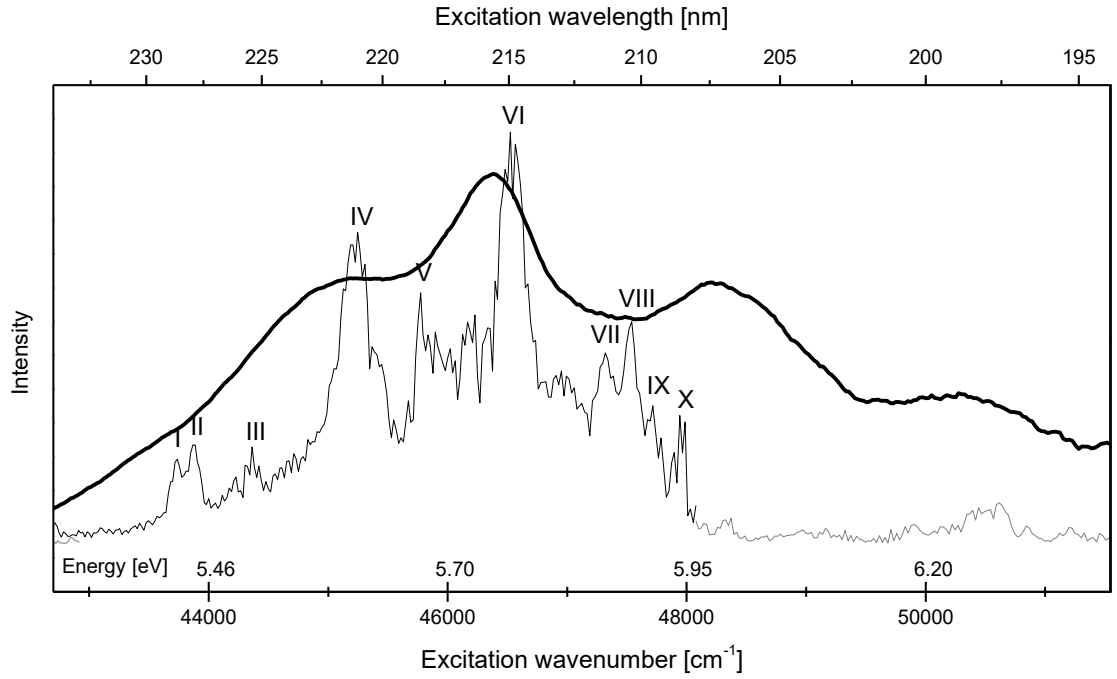

Figure 31. $\tilde{E} - \tilde{X}$ transition in the excitation spectrum of HC_7N phosphorescence (detected at 17 500 cm^{-1}, 2.17 eV), observed for a previously photolysed (193 nm) $Kr/C_4H_2/HC_5N$ (1000/1/1) matrix. Bold trace (reproduced from Ref. [98]) corresponds to the absorption spectrum of HC_7N in acetonitrile. The applied laser intensity correction may distort the phosphorescence intensity pattern.

[1] The excitation wavelength producing the maximal emission ranged from 215.6 nm (matrix with propyne excess) to 215.1 nm (without propyne excess) to 214.9 nm ($Kr/C_4H_2/HC_5N$ matrix). No systematic study of this variability was performed.

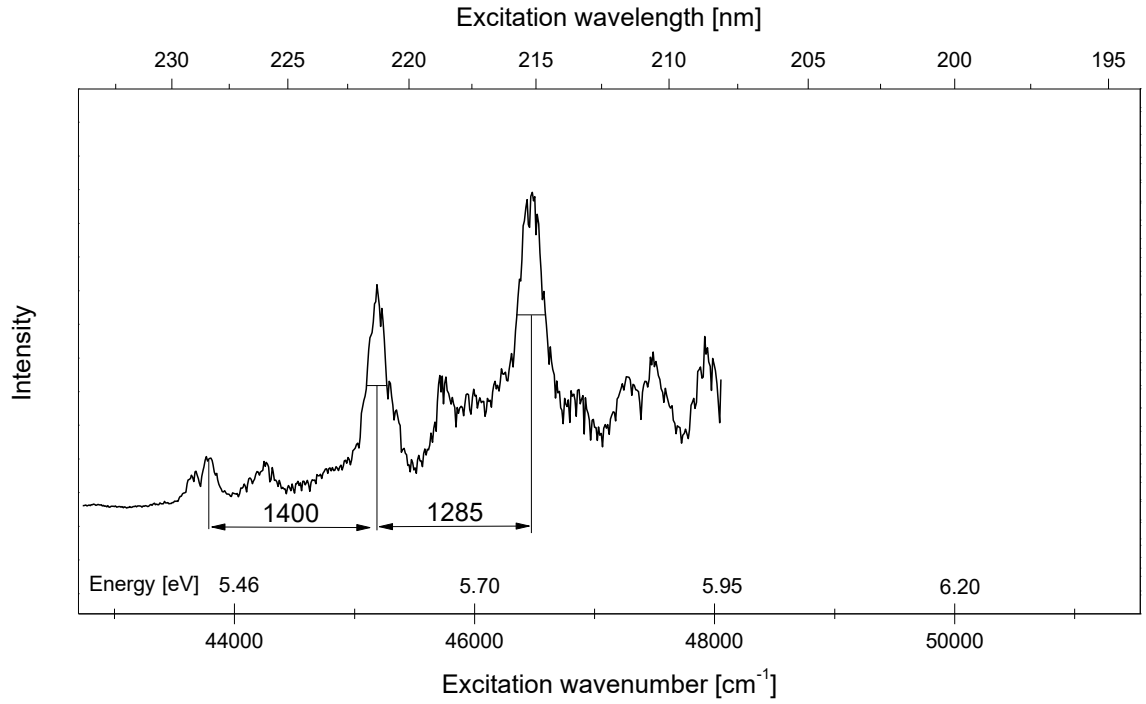

Figure 32. $\tilde{E} - \tilde{X}$ transition in the excitation spectrum of HC_7N phosphorescence (detected at 19 700 cm^{-1}, 2.44 eV), observed for a previously photolysed (193 nm) $Kr/CH_3C_2H/HC_5N$ (1000/1/1) matrix. The applied laser intensity correction may distort the phosphorescence intensity pattern.

Table 21. List of the most intense bands in HC_7N $\tilde{E} - \tilde{X}$ excitation spectrum (marked in Figure 31). Wavenumber ($\bar{\nu}$) values in cm^{-1}.

Band	$\bar{\nu}$
I	43710
II	43840
III	44310
IV	45220
V	45760
VI	46510
VII	47300
VIII	47510
IX	47720
X	47940

Bands of the CH_3C_7N excitation spectrum (phosphorescence detected at 19 750 cm^{-1}) were searched for in the 26 320 – 52 080 cm^{-1} range. Those uncovered within the 42 740 – 48 080 cm^{-1} region are shown in Figure 33 and listed in Table 22. They may reflect the previously reported [147] broad absorption feature at 44 740 cm^{-1} reported for CH_3C_7N in an ether solution. The first band of the excitation spectrum is located at 5.35 eV, very close to the predicted origin of the fully allowed $\tilde{E} - \tilde{X}$ system (5.40 eV, see Table 17). Several other bands of this system have also been detected. The main vibronic spacing of ~1800 cm^{-1} is significantly smaller than the closest theoretical prediction for $\tilde{E}$ state vibrational modes (ν_5 with a value of 1917 cm^{-1} or ν_4 with a value of 1969 cm^{-1}; see Table

18). This discrepancy may come from broad spectral features, low S/N, possible anharmonic interactions, or other not recognized phenomena.

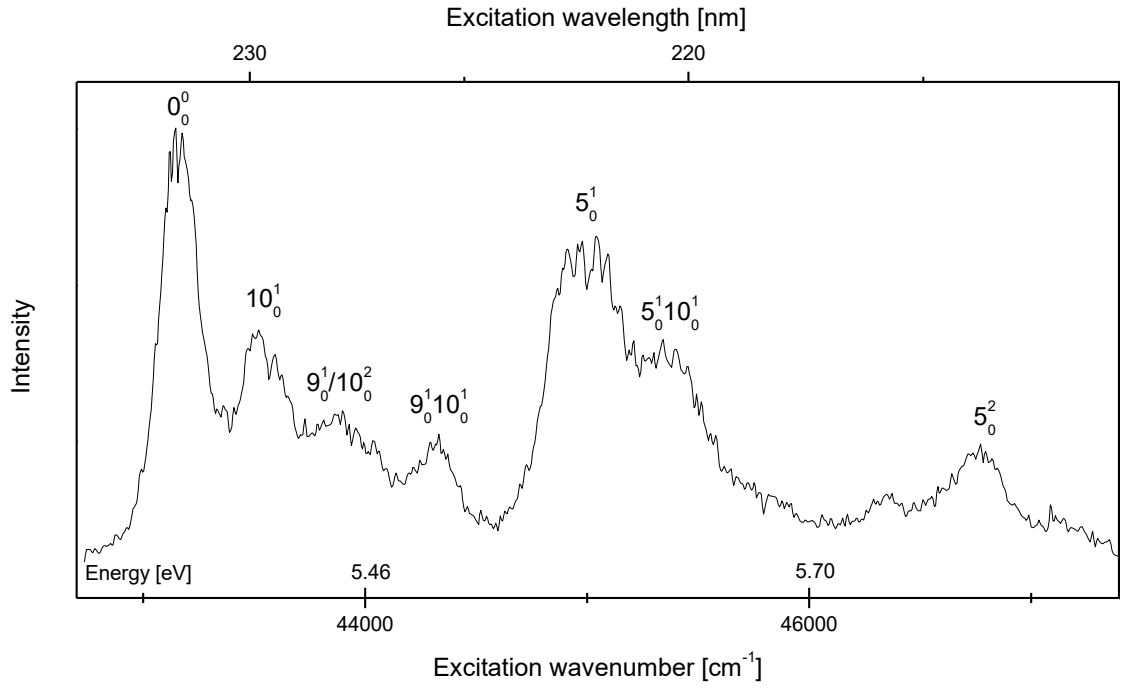

Figure 33. Phosphorescence excitation spectrum (observed at 19 750 cm^{-1}, 2.45 eV) assigned to the $\tilde{E} - \tilde{X}$ electronic system of CH_3C_7N. Kr/CH_3C_2H/HC_5N (1000/2/1) matrix irradiated at 193 nm. The applied laser intensity correction may distort the phosphorescence intensity pattern.

Table 22. Vibronic bands attributed to the $\tilde{E} - \tilde{X}$ electronic system of CH_3C_7N. Wavenumber ($\bar{\nu}$ [cm^{-1}]) values rounded to the nearest 10. Relative wavenumber ($\Delta\bar{\nu}$) values give the distance from the preceding bands of the main (5_0^n) vibronic progression.

$\bar{\nu}$	$\Delta\bar{\nu}$	Tentative assignment
43160	0	0_0^0
43550	390	10_0^1
43900	740	9_0^1 / 10_0^2
44330	1170	$9_0^1 10_0^1$
45000	1840	5_0^1
45400	400	$5_0^1 10_0^1$
46350	1350	x [a]
46770	1770	5_0^2

[a] Unassigned.

The other region of the CH_3C_7N phosphorescence excitation spectrum with detectable (albeit weak) spectral features was probed around 3.3-3.9 eV. This revealed a band around 3.64 eV, attributed to the $\tilde{B} - \tilde{X}$ system of CH_3C_7N. This assignment is based on two factors: the good match with theoretical predictions (Table 17) and transition energies similar to those observed for HC_7N. The similarity of the HC_7N and CH_3C_7N chromophores (illustrated by the energies corresponding to their $\tilde{E} - \tilde{X}$ transitions), and the similarity of $\tilde{B} - \tilde{X}$ systems in methyl- and hydrogen-capped cyanopolyynes (exemplified by the pairs HC_3N/CH_3C_3N [72,128,132] and HC_5N/CH_3C_5N [197] or Chapter 3.2) suggested that the

$\tilde{B} - \tilde{X}$ transition of CH_3C_7N should be detected in the same spectral range as that of HC_7N. The known spectra of the previously mentioned pairs of compounds indicate that the forbiddance of $\tilde{B} - \tilde{X}$ transitions (and hence the lack of vibrationless origin bands), formally effective only for $HC_{2n+1}N$ species, in practice extends also to $CH_3C_{2n+1}N$ derivatives. Therefore, the first (lowest-energy) $\tilde{B} - \tilde{X}$ band of CH_3C_7N, barely discernible at 29 330 cm^{-1} (3.64 eV), is not expected to mark the position of the *0-0* transition. This feature is more likely due to the coupling of $\tilde{B} - \tilde{X}$ with an appropriate vibration such as a 'zig-zag' distortion of the carbon-nitrogen chain (see the discussion regarding HC_7N), probably combined with a stretching mode. This last conjecture is suggested by the energy of the 29 330 cm^{-1} transition which is much higher than predicted for the $\tilde{B} - \tilde{X}$ origin. It is also supported by analogy to HC_7N, where 29 730/29 770 cm^{-1} bands were interpreted as due to bending modes coupled with a stretching. Another very weak feature that might be attributed to the $\tilde{B} - \tilde{X}$ system was observed around 31 400 cm^{-1}, apparently keeping the characteristic spacing of the main progression (2070 cm^{-1}). The analysis of respective vibrational modes suggests ν_{14} as the one promoting the $\tilde{B} - \tilde{X}$ transitions. This locates the system origin at 3.31 eV (the excited-state ν_{14} value was approximated based on the values in $\tilde{X}$ and $\tilde{E}$ states, as no predictions concerning the *B*-state vibrational levels are currently available), which can be compared to 2.9 eV, calculated for the *0-0* transition (see Table 17). Nevertheless, comparison with HC_7N case permits such attribution.

Similar to HC_7N, no $\tilde{C} - \tilde{X}$ nor $\tilde{D} - \tilde{X}$ transitions were observed. However, a weak feature has been detected (as a broad shoulder band overlapping the HC_7N emission) at 49 950 – 50 100 cm^{-1} (6.19 – 6.21 eV). It may correspond to the $\tilde{H}$ state with a predicted energy of 6.25 eV.

As presented in Figure 33, the strongest CH_3C_7N phosphorescence is produced using excitation at 43 160 cm^{-1}. However, quanta of that energy destroy the molecule over time. Even with an unfocused excitation laser beam, spectra collected in consecutive time intervals of 20 min showed product loss. Future experiments should be performed with lower excitation laser power (or another excitation energy) to prevent destruction, especially critical for the detection of weak CH_3C_7N phosphorescence bands. Such destruction may partly explain the relative ease of HC_7N detection compared to CH_3C_7N although it may also be more difficult to assemble CH_3C_7N than HC_7N (out of propyne and dicyanoacetylene). Formation of CH_3C_7N probably involves the movement of a bigger fragment ($CH_3C_2^{\bullet}$) than needed for the HC_7N ($HC_2^{\bullet}$).

4.3 HC_9N

4.3.1 Theoretical predictions and previous works

Theoretical predictions for the excited electronic states of HC_9N are listed in Table 23. Of particular importance are the states $\tilde{B}$ and $\tilde{E}$, as their electronic structures stem mainly from HOMO-LUMO excitation. Molecular geometries in these singlet states, as well as in the ground and lowest triplet state *a*, are shown in Figure 34. Vibrational mode wavenumbers of the ground and of two excited electronic states are listed in Table 24. For the visualization of vibrational modes, see Table 38 in "APPENDIX 2" (p. 131).

Table 23. Energy [eV], respective wavelength [nm], and oscillator strength for transitions involving the ground ($X\ ^1\Sigma^+$) and excited electronic states of HC_9N, as derived with B3PW91/aug-cc-pVTZ [192]. Ground state electronic configuration: [core] $(1\sigma)^2\ (2\sigma)^2\ (3\sigma)^2\ (4\sigma)^2\ (5\sigma)^2\ (6\sigma)^2\ (7\sigma)^2\ (8\sigma)^2\ (9\sigma)^2\ (10\sigma)^2\ (1\pi)^4\ (2\pi)^4\ (11\sigma)^2\ (3\pi)^4\ (4\pi)^4\ (5\pi)^4\ (1\pi^*)^0\ (2\pi^*)^0\ (1\sigma^*)^0$.

State	Dominant orbital excitation	Vertical energy (λ)	f [a]	*0-0* transition energy (λ)
$\tilde{A}\ ^1\Sigma^-$	$5\pi\rightarrow1\pi^*$	2.84 (437)	0	2.39 (519)
$\tilde{B}\ ^1\Delta$	$5\pi\rightarrow1\pi^*$	2.93 (423)	0	2.52 (492)
$\tilde{C}\ ^1\Sigma^-$	$4\pi\rightarrow1\pi^*$	4.38 (283)	0	4.10 (302)
$\tilde{D}\ ^1\Delta$	$4\pi\rightarrow1\pi^*$	4.53 (274)	0	4.27 (290)
$\tilde{E}\ ^1\Sigma^+$	$5\pi\rightarrow1\pi^*$	5.06 (245)	2.8	4.88 (254)
$\tilde{F}\ ^1\Sigma^-$	$5\pi\rightarrow2\pi^*$	5.30 (234)	0	4.98 (249)
$\tilde{G}\ ^1\Delta$	$5\pi\rightarrow2\pi^*$	5.32 (233)	0	5.00 (248)
$\tilde{H}\ ^1\Sigma^+$	$4\pi\rightarrow1\pi^*$ $5\pi\rightarrow2\pi^*$	5.40 (230)	1.7	5.11 (243)
$\tilde{a}\ ^3\Sigma^{+b}$				2.16 (574)

[a] Value of zero indicates a value of less than $5 \cdot 10^{-5}$.

[b] Orbital symmetry (+/-) less certain.

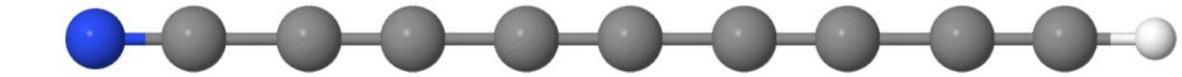

$\tilde{X}\ ^1\Sigma$	115.9	135.6	121.7	134.0	122.2	133.8	122.0	134.9	120.8	106.4
$\tilde{B}\ ^1\Delta$	+1.2	-2.3	+3.6	-4.8	+5.1	-5.1	+4.2	-3.3	+1.9	0
$\tilde{E}\ ^1\Sigma$	+1.8	-1.6	+2.5	-0.7	+1.5	+0.2	+1.8	-1.4	+2.1	+0.2
$\tilde{a}\ ^3\Sigma$	+1.3	-2.4	+4.0	-5.4	+5.7	-5.8	+4.7	-3.6	+2.1	0

Figure 34. HC_9N geometry in its ground and selected excited electronic states as derived at the B3PW91/aug-cc-pVTZ level of theory [192]. Distances in pm. Relative interatomic distances are given for the excited electronic states, calculated with respect to the ground state.

Table 24. Harmonic wavenumbers of vibrational modes ($\bar{\nu}$ [cm^{-1}]; scaling factor 0.96) for the ground and two excited electronic states of HC_9N, as derived at the B3PW91/aug-cc-pVTZ level of theory [192].

Mode		$\tilde{\nu}$		
		$\tilde{X}$	$\tilde{B}$	$\tilde{E}$
σ symmetry				
ν_1	σ	3324	3318	3298
ν_2	σ	2250	2098	2150 [a]
ν_3	σ	2201	2059	2059 [a]
ν_4	σ	2146	2000	2033
ν_5	σ	2122	1900	1956
ν_6	σ	2037	1848	1893
ν_7	σ	1369	1479	1346
ν_8	σ	1074	1106	1071
ν_9	σ	736	741	730
ν_{10}	σ	376	386	374
π symmetry				
ν_{11}	π	764	754	712
ν_{12}	π	640	559	562
ν_{13}	π	578	547	519
ν_{14}	π	511	486	458
ν_{15}	π	451	432	419
ν_{16}	π	301	309	253
ν_{17}	π	198	191	147
ν_{18}	π	107	105	88
ν_{19}	π	40	39	35

[a] Problematic to assess the corresponding ground state vibrations.

Previous experiments and theoretical investigations carried out for the cyanopolyyne series demonstrated an approximately linear dependence of the vibrationless (*0-0*) $\tilde{a} - \tilde{X}$ transition wavelength on the chain length [115,116] (Figure 35). The linear dependence can be rationalized in terms of the classical particle-in-a-box model [221] and extrapolation of the trend provides a reasonable estimate of HC_9N phosphorescence wavelength. A qualitatively similar prediction has been obtained with quantum chemical calculations: 2.16 eV (B3PW91, Table 23) or 2.18 eV (CAM-B3LYP, Figure 35).

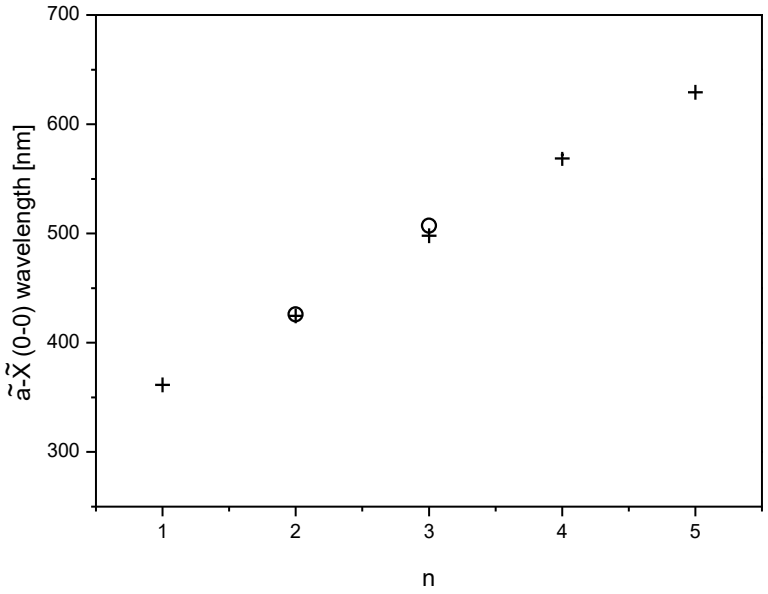

Figure 35. $\tilde{a} - \tilde{X}$ origin wavelength as a function of carbon chain length for $HC_{2n+1}CN$ molecules. Circles mark the experimental values (note the lack of phosphorescence for HC_3N). Crosses correspond to CAM-B3LYP/aug-cc-pVTZ predictions [192]. Experimental value for HC_5N after Ref. [91].

No HC_9N luminescence has been reported previously although its electronic absorption in solutions has been described [98,103,105,218] (see Chapter 1.2).

4.3.2 Phosphorescence

Figure 36 presents the electronic emission spectrum of ArF laser-photolysed $Kr/C_4H_2/HC_5N$ (1000/1/1) matrix. Three main groups of bands were observed in Kr matrices (only two in solid Ar), with an easily recognized vibronic spacing, characteristic of a triple bond stretching excitation. These dominant bands were attributed to the phosphorescence of HC_9N based on the measured *0-0* transition energy of 2.14 eV (17 300 cm^{-1}) which is almost coincident with the B3PW91-derived (Table 23) value of 2.16 eV.

The observed splitting of the main phosphorescence band comes from the presence of two matrix sites, as deduced from the corresponding excitation spectra which showed that the bands share a common chemical origin.

Two separate vibronic progressions are observed in the phosphorescence, with spacings of 2143 cm^{-1} and 2170 cm^{-1}. The former can be assigned to the vibrational mode ν_4 of HC_9N, the one responsible for a triple bond stretching (theoretically predicted at 2146 cm^{-1}, see Table 24). The predicted wavenumber of the other stretching mode in this region, ν_3, is much higher (2201 cm^{-1}, see Table 24) and was excluded for this reason. Previous reports on low-temperature phosphorescence of $HC_{2n+1}N$ molecules [91,115,116,157] have shown prominent vibronic patterns shaped by modes of the same nature. The mode ν_4 features the highest Raman activity [222], just as was observed for the stretches which govern the main vibronic progressions in phosphorescence of other cyanopolyynes [92,115,217]. The spacing of 2170 cm^{-1}, found in the second progression, can be associated with $2\nu_8$ (harmonic prediction: $2 \cdot 1074$ cm^{-1}). A similar vibronic spacing, also due to a C-C stretching overtone, was observed in the case of HC_5N ($2\nu_5$) [91].

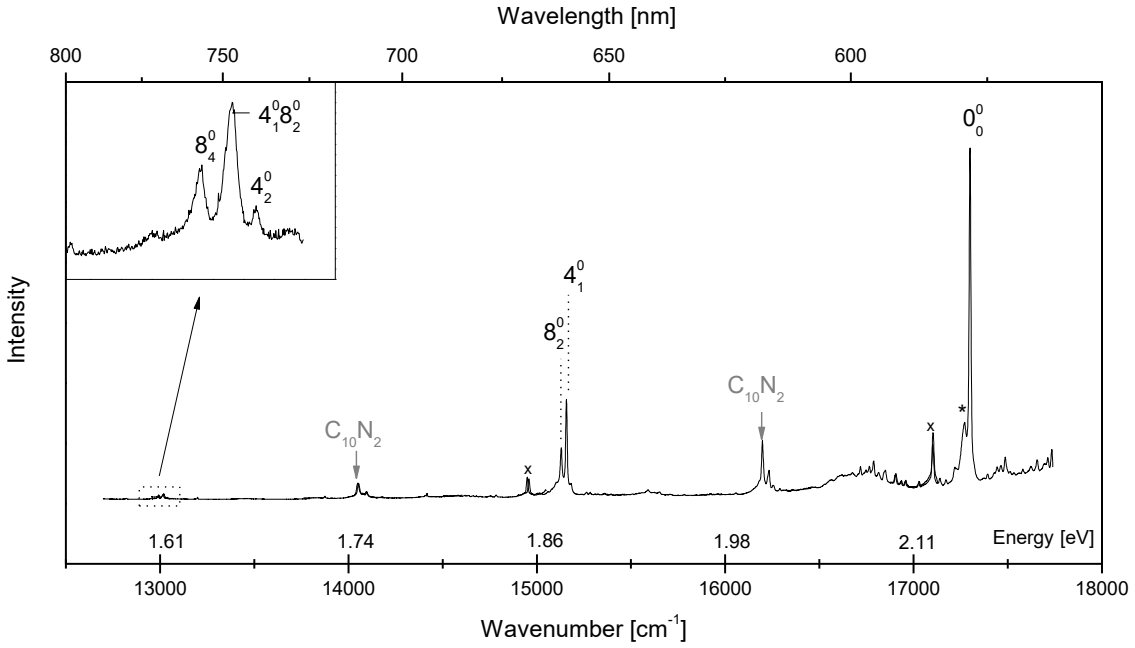

Figure 36. HC_9N-dominated phosphorescence of a photolysed (193 nm) $Kr/C_4H_2/HC_5N$ (1000/1/1) matrix, excited at 36 540 cm^{-1} (4.53 eV, 273.7 nm). Asterisked band is assigned to a secondary matrix site. Bands marked with crosses belong neither to HC_9N nor to $C_{10}N_2$, as evidenced by respective phosphorescence excitation spectra.

Table 25. Electronic emission bands interpreted as HC_9N phosphorescence in solid Ar and Kr. Wavenumbers ($\tilde{\nu}$) in cm^{-1}. Relative values give distances from the vibrationless origin.

$\tilde{\nu}$				Assignment
Ar		Kr		
Absolute	Relative	Absolute	Relative	
17379	0	17300	0	0_0^0
15231	2148	15157	2143	4_1^0
15205	2174	15130	2170	8_2^0
		13038	4262	4_2^0
		13018	4282	$4_1^0 8_2^0$
		12992	4308	8_4^0

The phosphorescence decay time of (3.9 ± 0.1) ms (*0-0* band) was markedly smaller than for other members of the homologous series (see the discussion in section 4.6).

4.3.3 Singlet excited electronic states

The phosphorescence excitation spectrum showed two distinct systems. First, a series of bands was detected in the 26 000 – 34 000 cm^{-1} region (Figure 37). These were assigned to the $\tilde{B}\ ^1\Delta - \tilde{X}\ ^1\Sigma^+$ symmetry-forbidden system of HC_9N, based on very similar spectral patterns observed for the shorter $HC_{2n+1}N$ molecules HC_3N [72], HC_5N [91] and HC_7N (see Chapter 4.2). The vibronic progression characterized by a spacing of ~2100 cm^{-1} can be assigned to the ν_2 mode. This mode distorts the molecule in a manner reminiscent of the geometry change accompanied by transition between the $\tilde{X}$ and $\tilde{B}$ states. DFT predicts a vibrationless origin of $\tilde{B} - \tilde{X}$ at 2.52 eV (Table 23) although no band is expected to show up in the spectrum, as the transitions are possible only *via* coupling to π-symmetry (bending)

vibrational modes. Such promoting modes, already identified as ν_5 for HC_3N, ν_8 for HC_5N, and ν_{10} (and/or ν_{12}) for HC_7N, share similar molecular distortion patterns ('zig-zag'), easily recognized in the ν_{11} bending of HC_9N (predicted $\tilde{B}$-state wavenumber: 754 cm^{-1}). The location of $\tilde{B} - \tilde{X}$ system origin, approximately 750 cm^{-1} lower than 26 530 cm^{-1} (the position of the first detected element of the vibronic progression governed by ν_2 stretching, marked in Figure 37), *i.e.* at approximately 25 780 cm^{-1} (3.20 eV), is very close to the analogous $\tilde{B} - \tilde{X}$ origin deduced for HC_7N (Chapter 4.2.3). Theory predicts a more substantial bathochromic shift accompanying such a chain elongation and suggests that there should be yet another element of the ν_2 progression at around 3.03 eV (out of the detection range). If this is so, the $\tilde{B} - \tilde{X}$ origin should fall at around 23 700 cm^{-1} (2.94 eV), much closer to the DFT-predicted value (2.52 eV; see Table 23). For the assignment of detected bands, see Table 26.

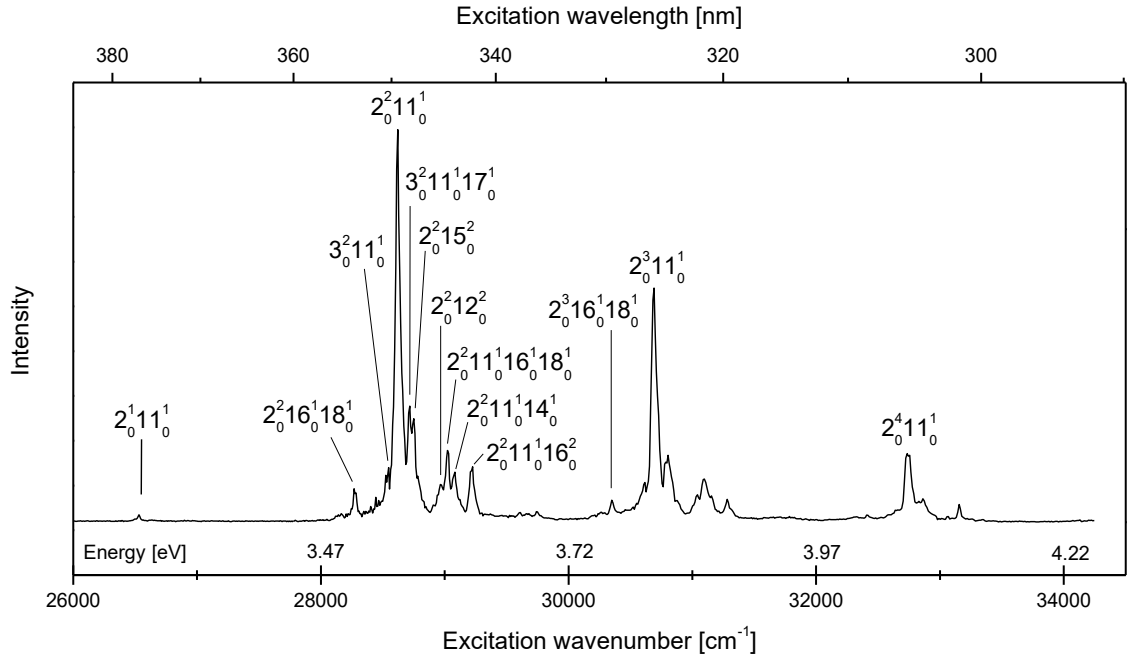

Figure 37. $\tilde{B}\ ^1\Delta - \tilde{X}\ ^1\Sigma^+$ system detected in the phosphorescence excitation spectrum of HC_9N, coming from a previously photolysed (193 nm) $Kr/C_4H_2/HC_5N$ (1000/1/1) matrix. Detection centred at the most intense phosphorescence band (17 300 cm^{-1}, 2.14 eV). The applied laser intensity correction may distort the phosphorescence intensity pattern.

Table 26. Vibronic bands of the $\tilde{B}\ ^1\Delta - \tilde{X}\ ^1\Sigma^+$ system, as assigned in the phosphorescence excitation spectrum of HC_9N in solid Kr. Wavenumbers ($\tilde{\nu}$) in cm^{-1}. Relative values give distances from the band recognized as $2_0^1 11_0^1$.

$\tilde{\nu}$		Assignment
Absolute	Relative	
26533	0	$2_0^1 11_0^1$
26925	392	$2_0^1 11_0^1 16_0^1 18_0^1$
27150	617	$2_0^1 11_0^1 16_0^2$
28165	1632	$2_0^2 17_0^1 18_0^1$
28274	1741	$2_0^2 16_0^1 18_0^1$
28546	2013	$3_0^2 11_0^1$
28623	2090	$2_0^2 11_0^1$
28719	2186	$3_0^2 11_0^1 17_0^1$
28753	2220	$2_0^2 15_0^2$
28970	2437	$2_0^2 12_0^2$
29027	2494	$2_0^2 11_0^1 16_0^1 18_0^1$
29083	2550	$2_0^2 11_0^1 14_0^1$
29225	2692	$2_0^2 11_0^1 16_0^2$
29606	3073	$2_0^2 11_0^1 12_0^1 15_0^1$
29743	3210	$2_0^2 11_0^1 12_0^2$
30267	3734	$2_0^3 17_0^1 18_0^1$
30349	3816	$2_0^3 16_0^1 18_0^1$
30613	4080	$3_0^3 11_0^1$
30691	4158	$2_0^3 11_0^1$
30780	4247	$3_0^3 11_0^1 17_0^1$
30807	4274	$2_0^3 15_0^2$
31040	4507	$2_0^3 12_0^2$
31098	4565	$2_0^3 11_0^1 16_0^1 18_0^1$
31155	4622	$2_0^3 11_0^1 14_0^1$
31281	4748	$2_0^3 11_0^1 16_0^2$
32324	5791	$2_0^4 17_0^1 18_0^1$
32408	5875	$2_0^4 16_0^1 18_0^1$
32639	6106	$3_0^4 11_0^1$
32734	6201	$2_0^4 11_0^1$
32828	6295	$3_0^4 11_0^1 17_0^1$
32862	6329	$2_0^4 15_0^2$
33152	6619	$2_0^4 11_0^1 16_0^1 18_0^1$

The other system observed in the 35 000 – 50 000 cm^{-1} region, recognized as fully allowed $\tilde{E}\ ^1\Sigma^+ - \tilde{X}\ ^1\Sigma^+$ transition, is more complicated, much like for HC_7N. The phosphorescence excitation spectrum of HC_9N can be compared to UV absorption measurements obtained by laser ablation of graphite in acetonitrile [98] (see Figure 38). A similar, though less detailed spectrum (not reproduced here), has also been obtained with a carbon arc immersed in liquid ammonia [218].

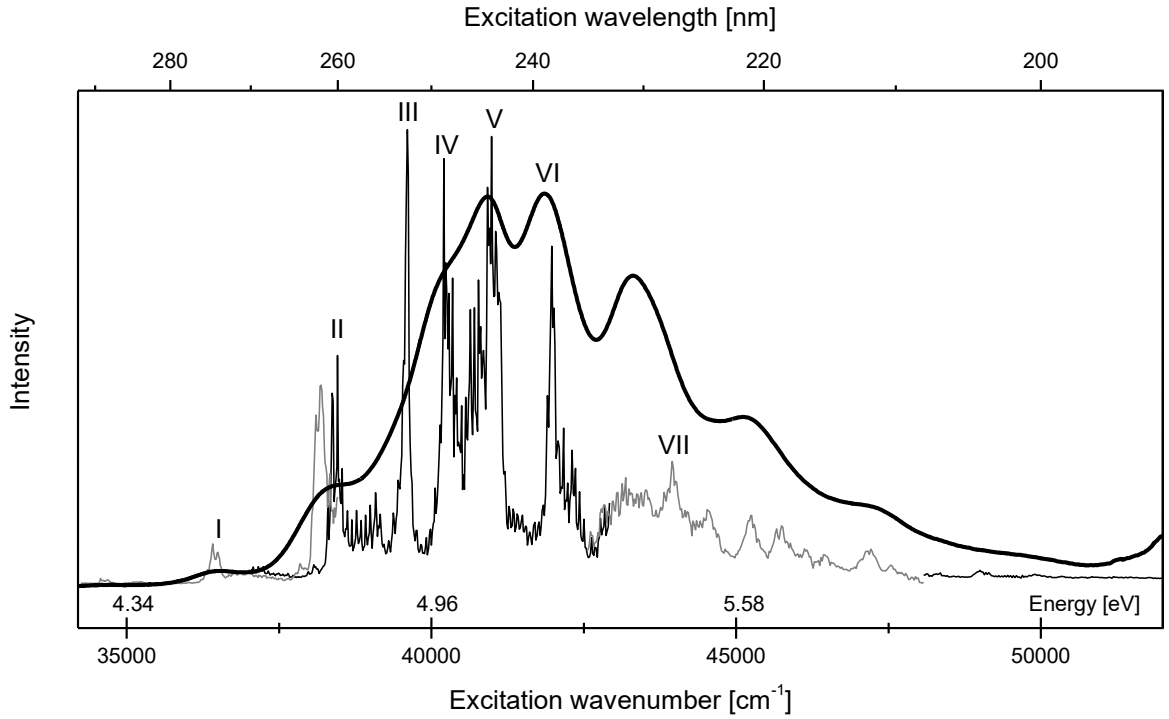

Figure 38. Part of the HC_9N phosphorescence excitation spectrum (detection centred around 17 300 cm^{-1}, 2.14 eV) from a previously photolysed (193 nm) Kr/C_4H_2/HC_5N (1000/1/1) sample, compared to the absorption spectrum of HC_9N in acetonitrile (bold; Wakabayashi *et al.* [98]). Both approaches show the fully allowed $\tilde{E}\ ^1\Sigma^+ - \tilde{X}\ ^1\Sigma^+$ system. Roman numerals refer to the entries in Table 27. (Black and grey colour denote adjacent ranges of laser scanning; lack of overlap around 38 000 cm^{-1} stems from wavelength calibration problems inherent to the experimental set-up.) The applied laser intensity correction may distort the phosphorescence intensity pattern.

The complicated structure of this electronic system has so far prevented reliable spectral assignments. A preliminary interpretation of main features is presented in Table 27. The $\tilde{E} - \tilde{X}$ vertical excitation energy is computed as 5.06 eV using DFT (Table 23) and agrees with the transition energy corresponding to the signal maximum seen in Figure 38. On the other hand, the tentatively recognized system origin (around 36 750 cm^{-1} or 4.56 eV), is noticeably lower than what has been theoretically predicted (4.88 eV, Table 23).

Table 27. Vibronic bands of the HC_9N $\tilde{E}\ ^1\Sigma^+ - \tilde{X}\ ^1\Sigma^+$ system, as assigned in the phosphorescence excitation spectrum of HC_9N in solid Kr. Wavenumbers in cm^{-1}. Band numbers refer to Figure 38.

Band	$\tilde{\nu}$	Tentative assignment
I	36750 [a]	0_0^0
II	38450	6_0^1
III	39610	x [b]
IV	40210	6_0^2
V	40990	$x + 11_0^2$
VI	41980	6_0^3
VII	43920	y [b]

[a] Less certain, estimated position.

[b] Unassigned; *x* and *y* denote as yet unidentified vibrational modes.

4.4 $C_{10}N_2$

4.4.1 Theoretical predictions and previous works

Theoretical results concerning the electronic spectroscopy of $C_{10}N_2$ are listed in Table 28. Transitions to states $\tilde{B}$, $\tilde{H}$ and $\tilde{a}$ correspond mostly to HOMO-LUMO excitations and are expected to be important in measured spectra. Interatomic distances in $\tilde{X}$, $\tilde{H}$, and $\tilde{a}$ states are shown in Figure 39 (state $\tilde{B}$ was excluded from that analysis, as the $\tilde{B} - \tilde{X}$ transitions were expected to fall out of the range accessible for these experiments, limited to λ<400 nm). DFT-derived vibrational wavenumber values [192] for the ground and for the fully permitted excited electronic states are listed in Table 29.

Table 28. Energy [eV], corresponding wavelength [nm], and oscillator strength for transitions involving the ground ($X\ ^1\Sigma_g^+$) and excited electronic states of $C_{10}N_2$, as derived with B3PW91/aug-cc-pVTZ [192]. Electronic configuration of the ground state is: [core] $(1\sigma_u)^2\ (1\sigma_g)^2\ (2\sigma_g)^2\ (2\sigma_u)^2\ (3\sigma_g)^2\ (3\sigma_u)^2\ (4\sigma_g)^2\ (4\sigma_u)^2\ (5\sigma_g)^2\ (5\sigma_u)^2\ (6\sigma_g)^2\ (1\pi_u)^4\ (1\pi_g)^4\ (2\pi_u)^4\ (6\sigma_u)^2\ (7\sigma_g)^2\ (2\pi_g)^4\ (3\pi_u)^4\ (3\pi_g)^4\ (1\pi_u^*)^0\ (1\pi_g^*)^0\ (1\sigma_g^*)^0$.

State	Dominant orbital excitation	Vertical energy (λ)	f [a]	*0-0* transition energy (λ)
$\tilde{A}\ ^1\Sigma_u^-$	$3\pi_g \rightarrow 1\pi_u^*$	2.62 (473)	0	2.18 (569)
$\tilde{B}\ ^1\Delta_u$	$3\pi_g \rightarrow 1\pi_u^*$	2.71 (458)	0	2.30 (539)
$\tilde{C}\ ^1\Sigma_g^-$	$3\pi_u \rightarrow 1\pi_u^*$	4.01 (309)	0	3.74 (332)
$\tilde{D}\ ^1\Delta_g$	$3\pi_u \rightarrow 1\pi_u^*$	4.16 (298)	0	3.90 (318)
$\tilde{E}\ ^1\Sigma_g^-$	$3\pi_g \rightarrow 1\pi_g^*$	4.81 (258)	0	4.53 (274)
$\tilde{F}\ ^1\Delta_g$	$3\pi_g \rightarrow 1\pi_g^*$	4.82 (257)	0	4.54 (273)
$\tilde{G}\ ^1\Sigma_g^{+\,b}$	$3\pi_u \rightarrow 1\pi_u^*$ $3\pi_g \rightarrow 1\pi_g^*$	4.84 (256)	0	4.56 (272)
$\tilde{H}\ ^1\Sigma_u^+$	$3\pi_g \rightarrow 1\pi_u^*$	4.80 (258)	5.2	4.65 (267)
$\tilde{a}\ ^3\Sigma_u^+$	$3\pi_g \rightarrow 1\pi_u^*$			1.75 (708)

[a] A value of zero indicates a result of less than $5 \cdot 10^{-5}$.

[b] Orbital symmetry (+/-) less certain.

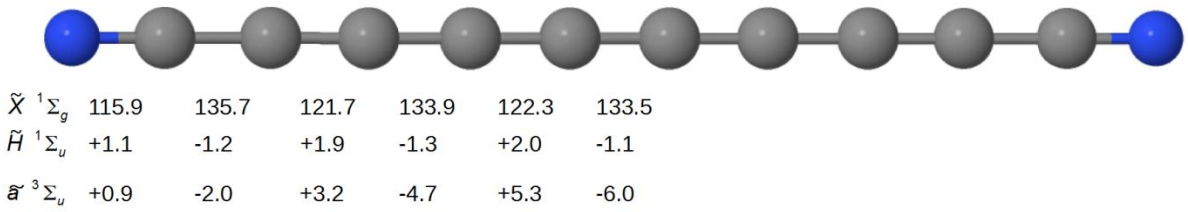

Figure 39. $C_{10}N_2$ geometry in the ground and selected excited states, as derived at the B3PW91/aug-cc-pVTZ level of theory [192]. Distances in pm. Excited electronic state entries listed as relative to those of the ground state. $D_{\infty h}$ symmetry was assumed.

Table 29. Harmonic wavenumbers of vibrational modes ($\tilde{\nu}$, in cm^{-1}); scaled by 0.96) for the $\tilde{X}\ ^1\Sigma_g^+$ and $\tilde{H}\ ^1\Sigma_u^+$ excited electronic states of $C_{10}N_2$, as derived at the B3PW91/aug-cc-pVTZ level of theory [192].

Mode	Symmetry	$\tilde{\nu}$	
		$\tilde{X}$	$\tilde{H}$
σ symmetry			
ν_1	σ_g	2254	2194
ν_2	σ_g	2140	2067
ν_3	σ_g	2115	2017
ν_4	σ_g	1414	1431
ν_5	σ_g	908	911
ν_6	σ_g	314	315
ν_7	σ_u	2241	2174
ν_8	σ_u	2199	2096
ν_9	σ_u	2061	1941
ν_{10}	σ_u	1180	1190
ν_{11}	σ_u	617	621
π symmetry			
ν_{12}	π_g	554	509
ν_{13}	π_g	512	462
ν_{14}	π_g	437	392
ν_{15}	π_g	222	210
ν_{16}	π_g	75	75
ν_{17}	π_u	561	515
ν_{18}	π_u	492	455
ν_{19}	π_u	308	288
ν_{20}	π_u	142	139
ν_{21}	π_u	28	30

Measurements of IR absorption of solid films of $C_{2n}N_2$ (n = 4-9) compounds have been reported [104], where the strongest $C_{10}N_2$ band (assigned to CN stretching) appeared at 2237 cm^{-1}. Other triple bond stretchings were found at 2186 and 2120 cm^{-1}, and had much lower intensity. These values agree with the current predictions for $C_{10}N_2$ (Table 29). The same study also provides a UV-Vis absorption spectrum of the compound in acetonitrile, with maxima at 259, 246, 235 and 223 nm. Other reports on $C_{10}N_2$ spectroscopy include a UV-Vis absorption spectrum for an *n*-octane solution [223] with emissions at 303, 283, 268, 253, 243, and 232 nm.

Just as in the case of monocyanopolyynes (see p. 84), a plot of the $\tilde{a} - \tilde{X}$ origin wavelength *vs.* dicyanopolyyne chain length (Figure 40) can be extrapolated to estimate the spectral region in which $C_{10}N_2$ phosphorescence should be found. CAM-B3LYP results follow the linear trend, predicting a value of 2.04 eV for $C_{10}N_2$ while the B3PW91 prediction (1.75 eV, Table 28) was markedly lower.

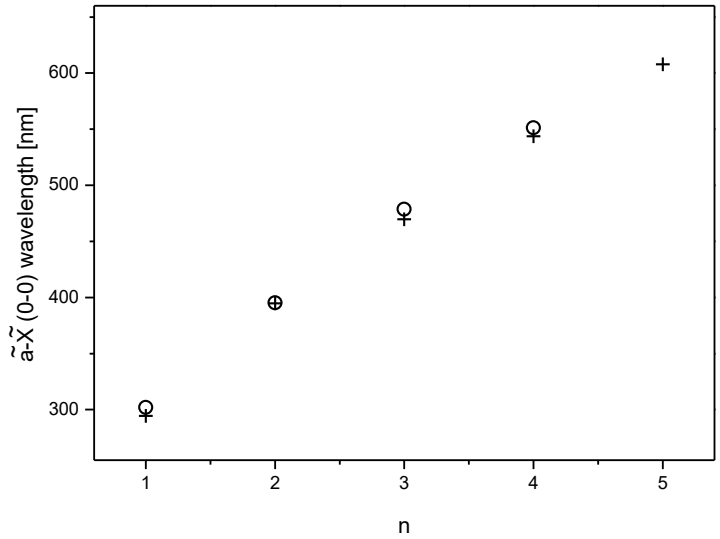

Figure 40. $\tilde{a} - \tilde{X}$ origin wavelength as a function of carbon chain length for $C_{2n}N_2$ molecules. Crosses correspond to theoretical predictions (CAM-B3LYP/aug-cc-pVTZ) [192]. Plot analogous to that of Figure 35. Experimental values after Ref. [116].

4.4.2 Phosphorescence

ArF laser-irradiated matrices containing HC_5N, excited at 38 390 cm^{-1} (4.76 eV), emitted a long-lived luminescence, identified as the phosphorescence of $C_{10}N_2$ (Figure 41). The band at 16 180 cm^{-1} (2.01 eV) was assigned to the origin of the $\tilde{a}\ ^3\Sigma_u^+ - \tilde{X}\ ^1\Sigma_g^+$ system.

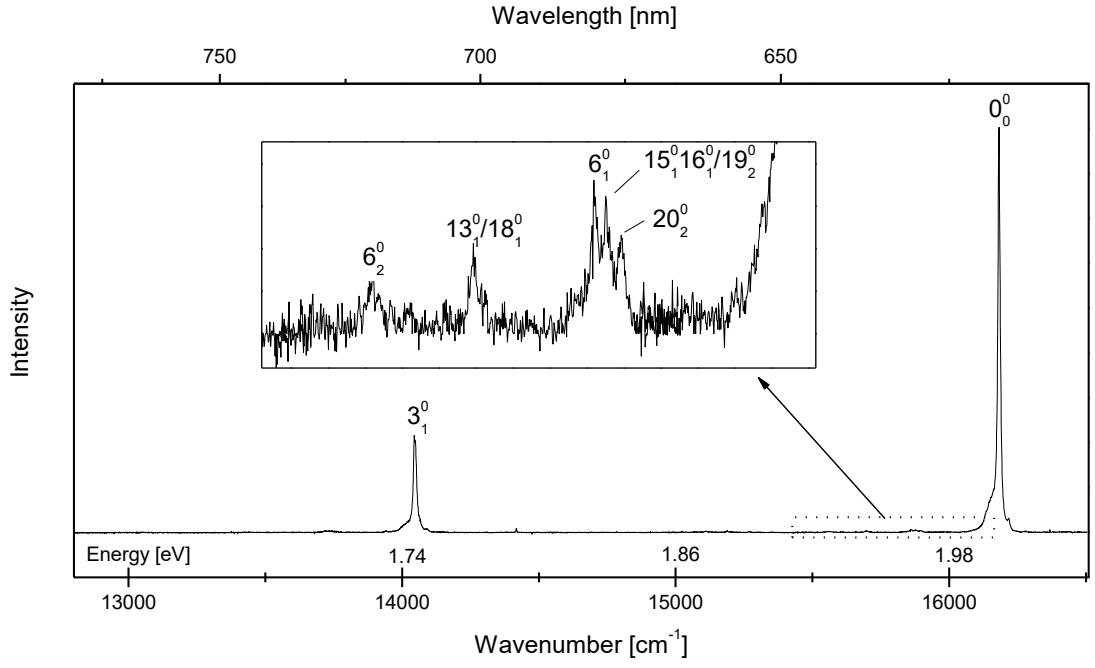

Figure 41. $C_{10}N_2$ phosphorescence from a previously photolysed (193 nm) Kr/HC_5N (1000/1) matrix, excited at 38 390 cm^{-1} (4.76 eV, 260.5 nm).

Observed bands, together with their proposed assignments, are listed in Table 30. The main progression shows a vibronic spacing of ~2140 cm^{-1}. This may be due to one of the two DFT-predicted stretching modes (Table 29), namely ν_3 (2115 cm^{-1}) or ν_2 (2140 cm^{-1}), both

of which have the required σ_g-symmetry[1]. In this case, ν_3 is preferred as it exhibits a pattern of vibrational distortion (alternate shrinking-expansion of consecutive interatomic distances along the chain) qualitatively similar to the geometry change experienced by the molecule upon its $\tilde{a} - \tilde{X}$ transition (Figure 39). One additional argument in favour of ν_3 comes from the fact that this mode has the highest Raman scattering activity [222], just as has been observed for shorter $C_{2n}N_2$ molecules [89,115,116,217,224].

Table 30. Vibronic bands in $C_{10}N_2$ phosphorescence. Wavenumbers ($\tilde{\nu}$) in cm^{-1}. Relative values give distances from the vibrationless origin.

$\tilde{\nu}$		Assignment
Absolute	Relative	
16218	-36	Site [a]
16182	0	0_0^0
15897	285	20_2^0
15876	306	$15_1^0 16_1^0$
15860	322	6_1^0
15696	486	13_1^0 / 18_1^0
15561	621	6_2^0
14046	2136 [b]	3_1^0
13940	2242	1_1^0
~13760 [c]	2424	$3_1^0 20_2^0$
~13740 [c]	2442	$3_1^0 15_1^0 16_1^0$
13718	2464	$3_1^0 6_1^0$

[a] Tentative.

[b] Two sites separated by 4 cm^{-1}; mean value is given.

[c] Broad, mutually overlapping. Tentative assignment.

The phosphorescence lifetime measured for the *0-0* band is (4.4 ± 0.1) ms, *i.e.* longer than that of HC_9N. The differences in lifetimes of observed molecules are discussed in section 4.6.

4.4.3 Singlet excited electronic states

The measured phosphorescence excitation spectrum was compared with the UV absorption of $C_{10}N_2$ in acetonitrile solution reported in Schermann *et al.* [104] (see Figure 42). Just as in the matrix spectrum, the vibronic spacings observed by Schermann *et al.* were not regular. Neglecting the breadth of features observed in spectrum of a liquid solution, the

[1] Taking into account the u symmetry of the electric dipole moment operator, the transition can only occur between the g- and u-symmetry states, so that the product of these three (g × u × u) is of the g symmetry, and, consequently, the transition moment integral does not vanish. For the orbitally allowed $\tilde{a}\ ^3\Sigma_u^+$- $\tilde{X}\ ^1\Sigma_g^+$ system of $C_{10}N_2$, in order to preserve the original (vibrationless) *gerade-ungerade* parities, the vibronic transitions may only involve the vibrational modes (fundamental, overtone or combination) of the overall g-symmetry.

general appearance resembles what was measured here, as does the observed progression. A similar absorption pattern was also reported for an *n*-octane solution [223].

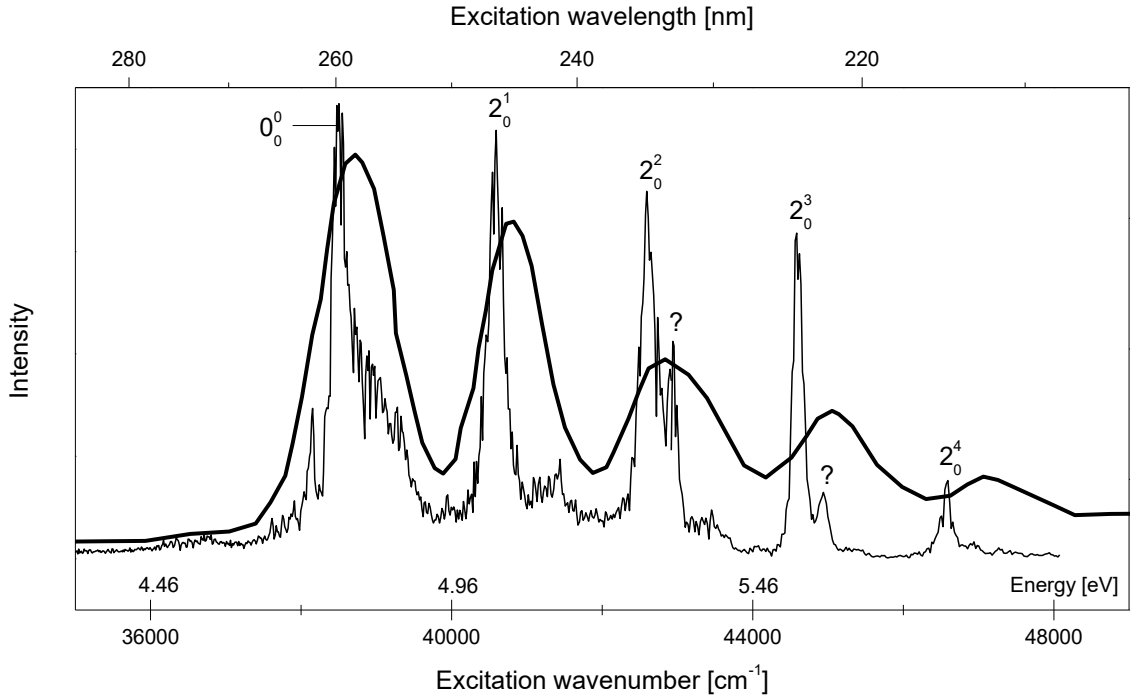

Figure 42. Excitation spectrum of $C_{10}N_2$ phosphorescence, detected at 16 200 cm^{-1} (2.01 eV) coming from a previously photolysed (193 nm) Kr/C_4H_2/HC_5N (1000/1/1) matrix. UV absorption spectrum of $C_{10}N_2$ in liquid acetonitrile (bold trace; digitized data from Ref. [104]) is given for comparison. The applied laser intensity correction may distort the phosphorescence intensity pattern.

The first intense band falls at 38 510 cm^{-1} (4.77 eV), in good agreement with the predicted origin of the fully allowed $\tilde{H}\ ^1\Sigma_u^+ - \tilde{X}\ ^1\Sigma_g^+$ system (4.65 eV). The main bands observed in the phosphorescence excitation spectrum are presented in Table 31, together with their proposed assignments. Spacings of the prominent vibronic progression reflect the activation of a triple-bond symmetric stretch. Theoretical predictions of *H*-state vibrational movements and wavenumbers indicate the probable involvement of mode ν_2.

Table 31. Vibronic bands in $C_{10}N_2$ phosphorescence excitation spectrum, reflecting the $\tilde{H}\ ^1\Sigma_u^+ - \tilde{X}\ ^1\Sigma_g^+$ transitions. Wavenumbers ($\tilde{\nu}$) in cm^{-1}. Relative values give distances from the preceding progression elements.

$\tilde{\nu}$				Assignment
Acetonitrile solution [a]		Kr matrix		
Absolute	Relative	Absolute	Relative	
38 720	0	38 500	0	0_0^0
40 780	2060	40 590	2090	2_0^1
42 840	2060	42 590	2000	2_0^2
		42 940	350	?
45 070	2230	44 580	1990	2_0^3
		44 940	360	?
47 150	2080	46 590	2010	2_0^4

[a] Based on a digitized spectrum from Ref. [104]; estimated digitization error ± 30 cm^{-1}.

4.5 C_5N^-

4.5.1 Theoretical predictions and previous works

Theoretical predictions concerning the excited electronic levels of C_5N^- anion are presented in Table 32. The electron detachment energy, 4.45 eV [153] (4.6 eV predicted with RCCSD(T) [225]), falls between the states $\tilde{B}$ and $\tilde{C}$. Excitation to $\tilde{C}$ and to higher states should therefore end up undergoing 'autoionization'[1]. A high density of electronic states in the 5-6 eV region (also containing high-*f* transitions) is also evident. The electronic states of particular interest here, apart from the ground state, are $\tilde{B}\ ^1\Delta$ and $\tilde{a}\ ^3\Sigma^+$. The molecular geometry in these states is presented in Figure 43.

Table 32. Energy [eV], corresponding wavelength [nm], and oscillator strength (*f*) for vertical transitions involving the ground $\tilde{X}\ ^1\Sigma^+$) and excited electronic states of C_5N^-, as derived with CAM-B3LYP/aug-cc-pVQZ [192]. Electronic configuration of the ground state: [core] $(1\sigma)^2\ (2\sigma)^2\ (3\sigma)^2\ (4\sigma)^2\ (5\sigma)^2\ (1\pi)^4\ (6\sigma)^2\ (2\pi)^4\ (7\sigma)^2\ (3\pi)^4\ (3s(N))^0\ (1\pi^*)^0\ (3s(C))^0\ (\pi_{Ryd}^*)^0\ (\sigma_{Ryd}^*)^0\ (2\pi^*)^0$, where $(7\sigma)^2$ denotes a lone electron pair on carbon.

State	Dominant orbital excitation	Vertical transition energy (λ)	f [a]
$\tilde{A}\ ^1\Sigma^-$	$3\pi\rightarrow1\pi^*$	3.50 (354)	0
$\tilde{B}\ ^1\Delta$	$3\pi\rightarrow1\pi^*$	3.65 (340)	0
$\tilde{C}\ ^1\Pi$	$3\pi\rightarrow3s(N)$ $3\pi\rightarrow3s(C)$ $3\pi\rightarrow\sigma_{Ryd}$	5.07 (245)	0.013
$\tilde{D}\ ^1\Pi$	$7\sigma\rightarrow1\pi^*$	5.13 (242)	0.045
$\tilde{E}\ ^1\Pi$	$3\pi\rightarrow3s(N)$ $3\pi\rightarrow3s(C)$	5.49 (226)	0.013
$\tilde{F}\ ^1\Sigma^+$	$7\sigma\rightarrow3s(C)$ $3\pi\rightarrow\pi_{Ryd}^*$ $3\pi\rightarrow1\pi^*$	5.61 (221)	0.74
$\tilde{G}\ ^1\Delta$		5.70 (218)	0
$\tilde{H}\ ^1\Sigma^-$		5.73 (216)	0
$\tilde{I}\ ^1\Sigma^+$		5.75 (216)	0.24
$\tilde{J}\ ^1\Pi$		5.89 (210)	0.011
$\tilde{K}\ ^1\Sigma^+$		6.08 (204)	0.32
$\tilde{L}\ ^1\Sigma^-$		6.15 (202)	0
$\tilde{M}\ ^1\Delta$		6.22 (199)	0
$\tilde{N}\ ^1\Sigma^-$		6.33 (196)	0
$\tilde{O}\ ^1\Sigma^+$		6.34 (196)	0.055
$\tilde{a}\ ^3\Sigma^+$		2.63 (471)	

[a] A value of zero indicates a result of less than $5 \cdot 10^{-5}$.

[1] Understood, as going from a Z-charged state to a (Z + 1)-charged state. In the case of an anion, it leads to the neutralization of the molecule.

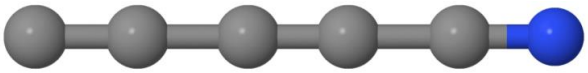

$\tilde{X}\ ^1\Sigma^+$	124.2	134.4	121.9	135.6	115.7
$\tilde{B}\ ^1\Delta$	+5.1	-4.5	+5.8	-3.6	+2.7
$\tilde{a}\ ^3\Sigma^+$	+5.8	-5.7	+6.7	-4.1	+2.8

Figure 43. Geometry of C_5N^- in selected electronic states, as predicted at the CAM-B3LYP/aug-cc-pVTZ level of theory [192]. Distances for the ground state in pm. Excited electronic state entries listed as relative to those of the ground state.

Literature reports on C_5N^- spectroscopy, of particular interest to this work, include the identification of this anion in UV-irradiated HC_5N-doped argon matrices [94]. This was based on the detection of three relevant, theoretically predicted, IR absorption bands. No C_5N^- phosphorescence has been reported in the literature so far.

4.5.2 Phosphorescence

C_5N^- was detected in photolysed HC_5N-containing[1] matrices. Bands appearing as a doublet were observed in the luminescence spectrum around 21 700 cm^{-1} (2.69 eV), close to the value of 21 200 cm^{-1} (2.63 eV) which was predicted for the $\tilde{a} - \tilde{X}$ origin of C_5N^- (Table 32). The doublet was the strongest when excitation at 28 810 cm^{-1} (3.57 eV) was used. This doublet was separated from three other, similar features appearing at lower energies (see Figure 44), by values corresponding to the vibrational wavenumbers ν_1, ν_2, and ν_3 of C_5N^- (Table 33) which were previously determined from IR absorption spectra [94]. These complicated, lower energy spectral features resemble multiplets more than doublets, the two dominant components can nevertheless be discerned. Such structures may have their origin in distinct matrix sites or, if the matrix-isolated molecule is not linear, in different conformations (*cis*/*trans*) whose transition energies are slightly different. Another possibility is that lattice phonons couple to the electronic transition. However, this last explanation is less probable given the sharpness of the observed spectral profiles. Phonons should produce a broad feature accompanied by a sharp component at a slightly higher wavenumber.

Table 33. Vibronic bands in C_5N^- phosphorescence observed in solid Kr and Ar. All wavenumber ($\tilde{\nu}$) values in cm^{-1}. Relative values give distances from the vibrationless origin.

$\tilde{\nu}$							Assignment
Kr				Ar			
Absolute [a]		Doublet separation	Relative [b]	Absolute	Relative [b]	$\tilde{\nu}_{IR}$ [c]	
21726	21696	30		21719			0_0^0
19793	19761	32	1933	~19800	~1919 [d]	1923.2	3_1^0
19603	19568	35	2123	19610	2109	2111.3	2_1^0
19527	19496	31	2199	19538	2181	2183.8	1_1^0

[a] Two columns correspond to doublet components separated by a distance given in the following column.

[b] Measured for high wavenumber doublet components or for the band maxima, in case of Kr and Ar matrices, respectively.

[c] IR absorption data after Ref. [94].

[d] Broad, weak band.

[1] The investigated samples included Kr/HC_5N, $Kr/C_4H_2/HC_5N$, $Ar/C_4H_2/HC_5N$, and $Kr/CH_3C_2H/HC_5N$.

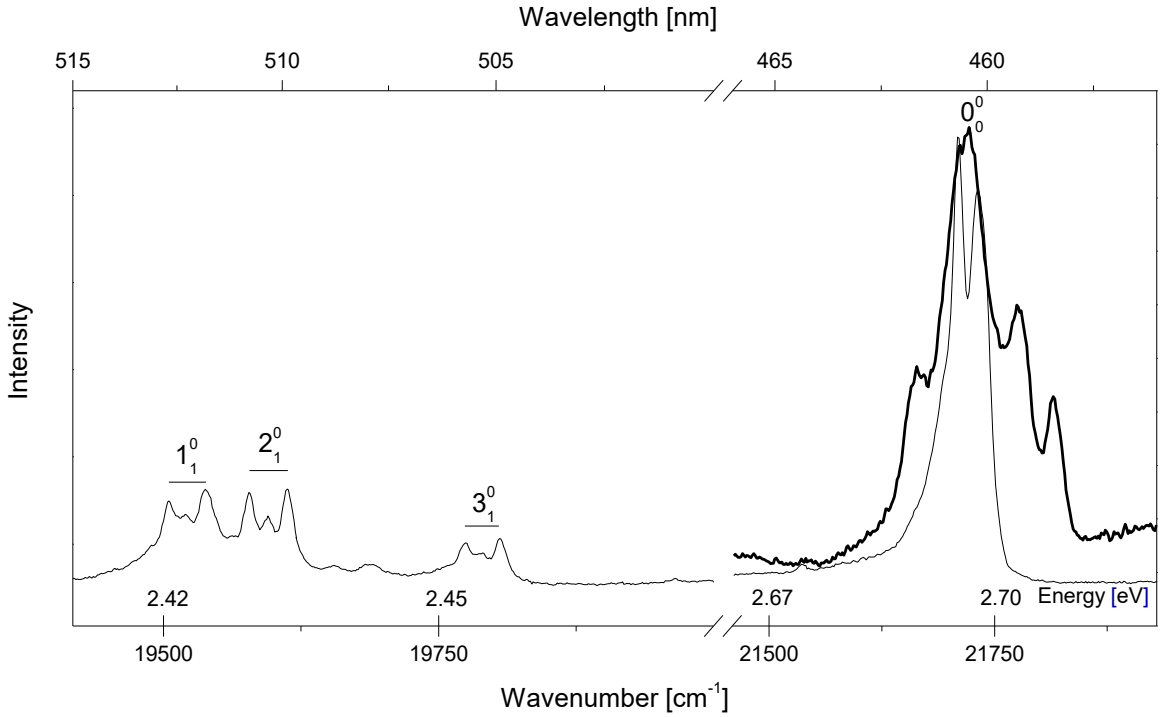

Figure 44. Phosphorescence from a previously photolysed (193 nm) Kr/C_4H_2/HC_5N (1000/1/1) matrix excited with 28 810 cm^{-1} (3.57 eV, 347.1 nm) laser radiation. Bold trace shows the most intense C_5N^- feature detected in the analogous Ar/C_4H_2/HC_5N experiment (excitation at 34 840 cm^{-1}, 4.32 eV, 287 nm).

The emission described here is very long-lived, its decay even being observable by eye. Lifetime measurement in a Kr matrix yielded a double-exponential decay (see Figure 45) with a longer component of (242 ± 1) ms. Differences in the luminescence decay observed between the doublet components suggest the involvement of dissimilar matrix sites or molecular conformations. The phosphorescence lifetime reported for the smaller analogue, C_3N^-, was twice as long (~0.5 s [86]). A larger number of internal degrees of freedom in the case of C_5N^- may lead to more efficient non-radiative relaxation and end up decreasing the phosphorescence lifetime.

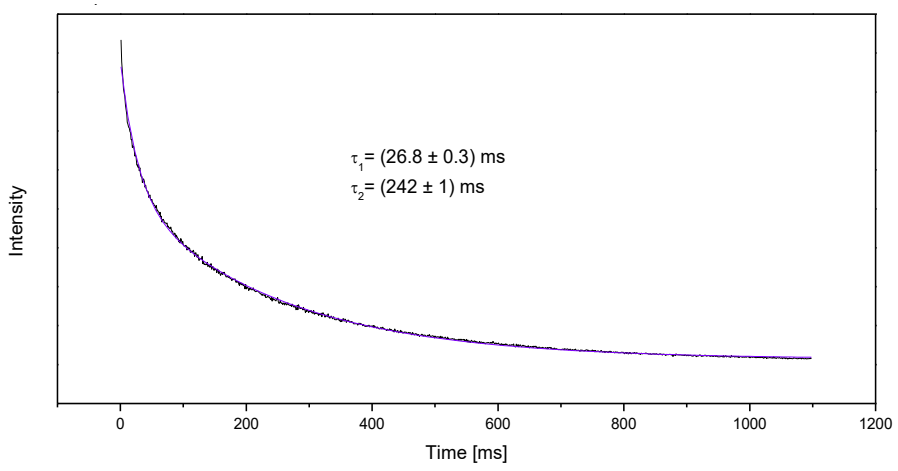

Figure 45. C_5N^- phosphorescence decay (in solid krypton). Emission detected at 21 730 cm^{-1} (2.69 eV, 460.1 nm), excited at 26 470 cm^{-1} (4.52 eV, 274.2 nm). Purple trace shows the double-exponential fitting curve.

4.5.3 Singlet excited electronic states

The C_5N^- phosphorescence excitation spectrum (observed at the origin of $\tilde{a} - \tilde{X}$) is presented in Figure 46. Apart from more energetic features, the detected vibronic bands most likely belong to the $\tilde{B} - \tilde{X}$ system based on the analogous isoelectronic HC_5N molecule, although the possible presence of $\tilde{A} - \tilde{X}$ transitions cannot be excluded. The anion emission starts to appear with excitation around 26 800 cm^{-1} (3.33 eV). Maximal signal from the $\tilde{B} - \tilde{X}$ transition was found for the excitation wavenumber of 34 630 cm^{-1} (4.29 eV). The most intense bands are separated by approximately 1900 cm^{-1}. Theoretical predictions suggest 1862 and 1990 cm^{-1} (B3PW91/aug-cc-pVTZ [192]) or 1912 and 2033 cm^{-1} (CAM-B3LYP/aug-cc-pVTZ [192]) for the highest *B*-state vibrational wavenumbers. Neither of the two vibrations distorts the molecule in a way similar to what is observed when it undergoes a $\tilde{B} - \tilde{X}$ transition. Calculations indicate that the vertical $\tilde{B} - \tilde{X}$excitation energy should be 3.65 eV (see Table 32) which is in qualitative agreement with the lower-energy bands of Figure 46. It is, however, difficult to differentiate between the spectral features of $\tilde{B} - \tilde{X}$ and those stemming from higher energy transitions. A threshold for electron detachment of 4.45 eV has been meaured using photoelectron spectroscopy [153]. Absorption leading to electron detachment may be stronger (and broader) than less energetic processes. Several factors may contribute to the distortion of the presented phosphorescence excitation spectrum, in particular:

- C_5N^- tends to be destroyed during the photolysis (although this process has not yet been quantified);
- calibration problems inherent to the OPO operation, affecting the merging of adjacent excitation wavelength ranges (as discussed in Chapter 2.2.2).

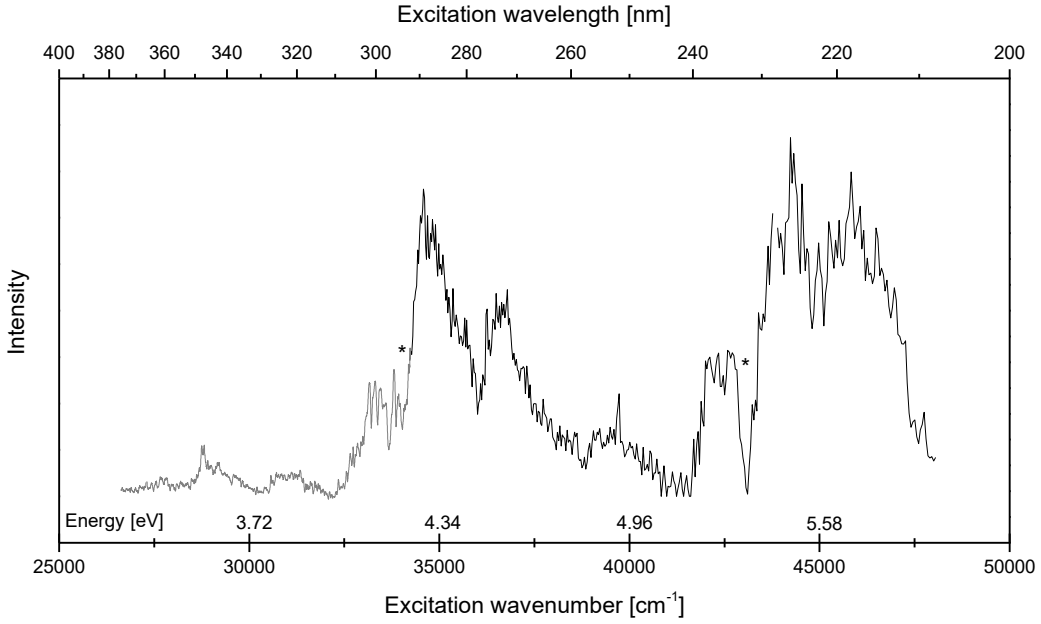

Figure 46. C_5N^- phosphorescence excitation spectrum, as detected at the origin of $\tilde{a} - \tilde{X}$ (21 700 cm^{-1}, 2.69 eV) coming from a previously photolysed (193 nm) Kr/HC_5N (1000/1) matrix. Asterisks mark the junction of adjacent excitation wavelength ranges. The applied laser intensity correction may distort the phosphorescence intensity pattern.

The possibility that the data of Figure 46 partly reflect an action spectrum for the $HC_5N \rightarrow C_5N^- + H^+$ process has been rejected as no match with HC_5N absorption could be found.

4.6 Discussion

A. Detection method

The phosphorescence of several cyanopolyynic compounds, namely CH_3C_5N, CH_3C_7N, HC_9N, $C_{10}N_2$, and C_5N^-, was observed here for the first time. This phosphorescence proved to be strong enough to detect even minute traces of these species, although no IR absorption could be measured. This comes as no surprise, since earlier experiments designed to produce longer chains from $HC_3N + C_2H_2$ or $HC_5N + C_2H_2$ as precursors *in situ* produced only very weak IR bands of HC_5N or HC_7N that were at the limit of detection for the measurements.

Thanks to the use of tuneable excitation sources, signals from different photoproducts could be separated. This was particularly important in experiments involving phosphorescing precursors and/or production of multiple products whose phosphorescence signals overlapped.

In general, krypton matrices were preferred over argon. Measurements in Ar matrices usually led to complicated band splittings and broader structures which were difficult to interpret, a situation well illustrated by CH_3C_5N and C_5N^-. Although not quantified, phosphorescence measured in Kr seemed stronger than in Ar, likely due to the external heavy atom effect.

There are evident differences in phosphorescence lifetimes of species belonging to the four homologous series of interest. Table 34 shows the values measured for compounds in Kr matrices. Literature data come from differently prepared samples including pure substances isolated in solid Kr (C_4N_2, HC_5N), ArF photolysis of HC_3N-doped solid Kr (C_6N_2), or cold-window-radial-discharge of a Kr/HC_3N mixture before its solidification (C_8N_2). There is a pronounced decrease of lifetime as the length of polyynic chains increases. This suggests that more internal degrees of freedom in the longer chains allow an increase in the significance of non-radiative relaxation which then decreases the lifetime of phosphorescence. Lower transition energies with shorter lifetimes may make observation of phosphorescence of even longer chains difficult with the experimental set-up used for this work. Monocyanopolyynes are characterized by shorter phosphorescence lifetimes than respective (*i.e.* isoelectronic) dicyanopolyynes. This suggests that non-radiative $S_0 \leftarrow T_1$ relaxation is easier for monocyanopolyynes. This may be due to the special role of large CH stretching quanta in coupling T_1 with excited vibrational levels of the ground state. Also, the number of vibrational modes, and hence the density of vibrational states where S_0 and T_1 intersect, is bigger for monocyanopolyynes than for the isoelectronic dicyanopolyynes. These arguments fail when it comes to explaining the long decay times observed for the methylated derivatives. Termination with CH seems to better contribute to the depopulation of the triplet state than does termination with CH_3.

Very long phosphorescence lifetimes, indicating much lower $S_0 \leftarrow T_1$ non-radiative conversion efficiency, are observed for the anions. The associated non-radiative and radiative $S_0 \leftarrow T_1$ relaxation processes deserve further studies.

Table 34. Phosphorescence lifetime (τ [ms]) for cyanopolyynes in solid Kr.

HC_nN	τ	C_nN_2	τ	CH_3C_nN	τ	C_nN^-	τ
-	-	C_2N_2	n/a	-	-	C_3N^-	~500 [a]
HC_5N [b]	40	C_4N_2 [c]	52	CH_3C_5N	150	C_5N^-	242
HC_7N	8.2	C_6N_2 [b]	35	CH_3C_7N	23		
HC_9N	3.7	C_8N_2 [b]	13				
		$C_{10}N_2$	4.4				

[a] After Ref. [86].
[b] After Ref. [217].
[c] After Ref. [224].

B. Regularities in homologous series

In a series of polyynes, UV absorption wavelengths change linearly with molecule length [221,226]. This can be explained by applying a simple particle-in-a-box model, where an electron (a 'particle') is delocalized in a system of conjugated bonds (a 'box'). An analogous relation, $\lambda_{00}(n)$, where n is the number of CC units in the chain, has also been reported for cyanopolyyne phosphorescence (*e.g.* [115,116]). All compounds for which phosphorescent properties were discovered here, including methylated cyanopolyynes, follow the same tendency (see Figure 47, left).

A similar relation, involving the squared UV-Vis absorption wavelength (a so-called Lewis-Calvin plot [227]), was reported for a series of dicyanopolyynes ranging from C_8N_2 to $C_{18}N_2$ [104]. This relation can be rationalized in terms of a simple harmonic oscillator model with a delocalized electron oscillating along the chain. The squared wavelength of cyanopolyyne *0-0* phosphorescence bands, plotted against the chain length, $\lambda_{00}^2(n)$, is shown in the right panel of Figure 47.

Comparing these two models for $HC_{2n+1}N$, $NC_{2n}N$ and $CH_3C_{2n+1}N$ series, Lewis-Calvin plots produce marginally better linearity. However, both methods are useful for estimating the $\tilde{a} - \tilde{X}$ vibrationless origin wavelengths, within the studied range of chain sizes. The results of DFT predictions have been added to the plots drawn for the $C_{2n+1}N^-$ series, where only two points (C_3N^-, C_5N^-) are experimentally reachable (no C_7N^- phosphorescence has thus far been observed). Taking these computational results into account, the linearity seems to be better for $\lambda_{00}(n)$ than for $\lambda_{00}^2(n)$.

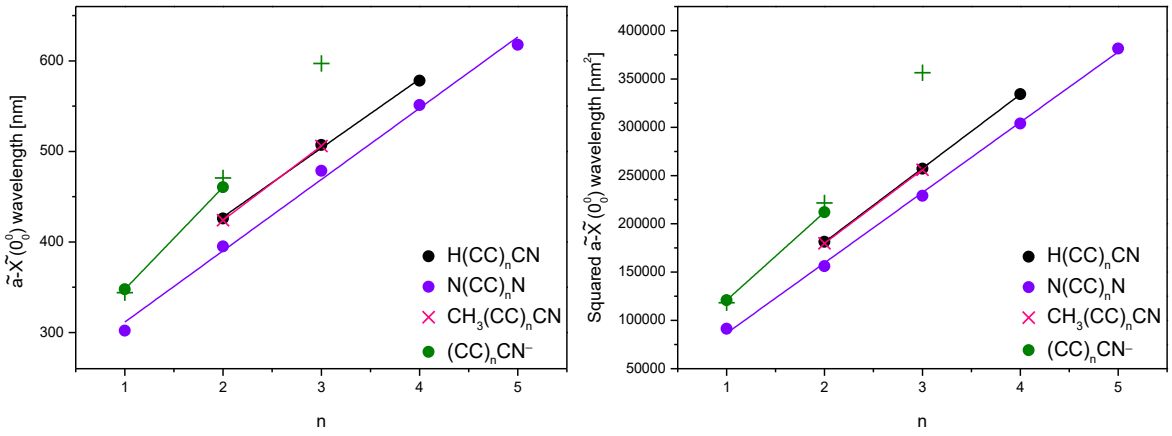

Figure 47. The dependence of phosphorescence wavelength λ_{00} (left panel) and λ_{00}^2 (right panel) on the length of molecular backbone, for the series of cyanopolyynic molecules photochemically formed in solid Kr. Green plus signs refer to the wavelengths predicted at CAM-B3LYP/aug-cc-pVTZ level of theory (this work and [192]). Experimental values for C_3N^-, HC_5N, C_2N_2, C_4N_2, C_6N_2, and C_8N_2 come from Refs. [86,91,116].

As anticipated based on what is known for HC_5N and CH_3C_5N phosphorescence, HC_7N and CH_3C_7N turned out to have almost coincident $\tilde{a} - \tilde{X}$ origin wavelengths. The difference between HC_7N and CH_3C_7N was smaller than for their shorter analogues, as expected for a larger carbon-nitrogen chain chromophore where the terminating group will have less influence. This pattern suggests that even more similarity should be observed between HC_9N and CH_3C_9N $\tilde{a} - \tilde{X}$ emission wavelengths.

Results of CAM-B3LYP and B3PW91 calculations showed significant differences between these methods in predicting the vibrationless $\tilde{a} - \tilde{X}$ origins for the longest investigated dicyanopolynic molecule $C_{10}N_2$. However, extrapolation of relevant experimental data (Figure 35 and Figure 40) gave reasonable estimates for these values (Figure 47). This contrast reflects the fact that the accuracy of quantum chemical calculations decreases with increasing size of electronic systems, unlike the reliability of extrapolation from experimental values.

Other observed transitions were singlet-singlet transitions. All of them shared similar character, involving HOMO-LUMO excitations of either $\pi - \pi^*$ or, for the C_{3v} molecules, $e - e^*$. The HOMO-LUMO energy gap decreases with the chain length, the same trend was previously reported for a group of related molecules [113] . Two main systems of transitions could be distinguished: a fully allowed one and a formally (or practically) forbidden one. The forbidden $\tilde{B} - \tilde{X}$ system[1] was generally rendered detectable through coupling with a bending vibration of the $C_{2n+1}N$ chromophore. This bending, further coupled to a triple-bond stretching mode, promoted the main vibronic progressions, easily recognized in phosphorescence excitation spectra.

[1] These were observed for all investigated long chains with the exception of $C_{10}N_2$, where $\tilde{B}$-$\tilde{X}$ falls out of the accessible range.

The wavelength of the vibrationless $\tilde{B} - \tilde{X}$ transition can also be plotted against the monocyanopolyyne chain length (Figure 48). Linearity is not much worse than for the $\tilde{a} - \tilde{X}$ transitions, even though the assignment of the $\tilde{B} - \tilde{X}$ band systems (and hence the placement of system origins) was less evident. Lack of sufficient experimental data did not permit similar analyses for the compounds of other homologous series.

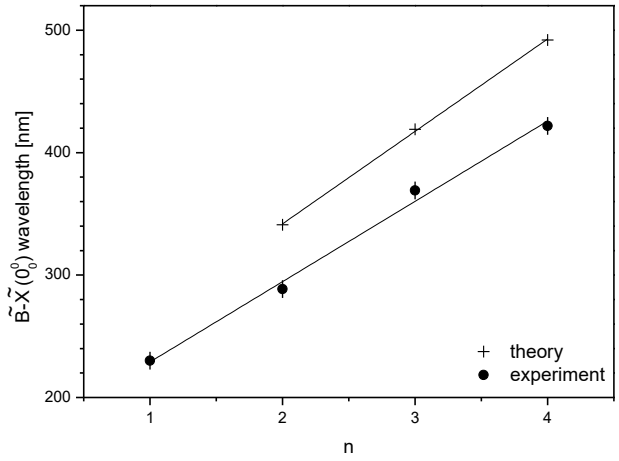

Figure 48. Dependence of the $\tilde{B}$-$\tilde{X}$ system origin on the carbon chain length (*n*), for $HC_{2n+1}N$ molecules. Based on the present Kr-matrix measurements, with the exception of *n* = 1 entry (solid Ar [228]). Theoretical predictions acquired at a common level of theory (B3PW91/aug-cc-pVTZ) were available [192] only for *n* = 2, 3, and 4 species.

C. Vibrational progressions in electronic spectra

Distinct band progressions with vibronic spacings of approximately 2000-2200 cm^{-1} were easily discerned in all phosphorescence spectra registered here. This energy range corresponds to the excitation of a triple bond stretching mode. The actual molecular distortion pattern of the vibration shaping the progression was related to the geometry change (shrinking-elongation of interatomic distances) accompanying the transition between $\tilde{X}$ and $\tilde{a}$ states.

Similar vibrational modes were also found to govern the main vibronic progressions of $\tilde{B}$-$\tilde{X}$ absorption spectra (observed either directly or *via* phosphorescence excitation). Just as in the case of $\tilde{a}$-$\tilde{X}$ systems, this observation should be linked with the predicted geometry changes induced by the transitions, which were qualitatively similar in all investigated compounds. When it comes to higher energy transitions, molecules are expected to exhibit more diversity in their geometric rearrangement patterns. However, the fully allowed $\tilde{E} - \tilde{X}$ or $\tilde{H} - \tilde{X}$ systems could not be thoroughly interpreted in the framework of this work.

Previous investigations of similar compounds [89,115,116,157,217,224] showed that the mode responsible for the leading vibronic progression is the one having the highest Raman activity. This trend seems to be also preserved here. The shortcomings of theoretical results in predicting anharmonic interactions for larger molecules and the scarcity/absence of vibrational spectroscopy data with which to compare impedes a more detailed analysis.

D. Intermolecular complexes as starting points for photochemical reactions

For a bimolecular photochemical reaction to occur in a cryogenic matrix, at least one of the molecules involved should first be electronically excited or dissociated. Subsequently, the excited precursor or a primary photolysis product may react with another precursor molecule. Considering the linear geometries of the reagents and expected products, the excited species or primary photolysis product may need to reorient within their respective rare gas cages in the course of the reaction. In a rigid environment, this requires substantial energy to be delivered. It might also be that reactions occur within already existing intermolecular complexes. The following mechanism has been proposed previously [115] for the formation of long monocyanopolyynes in cryogenic matrices, following observation of HC_5N production:

$$HC_3N\cdots HC_3N + h\nu \rightarrow HC_5N + CN^{\bullet} + H^{\bullet}. \qquad \text{(R4)}$$

A similar scheme, involving an intermolecular complex with acetylene ($HC_3N\cdots HC_2H$), has also been proposed for the same molecule (HC_5N) [156].

The linear bimolecular complexes $HC_3N\cdots C_4H_2$ and $HC_5N\cdots C_2H_2$ have been studied theoretically (B3LYP/6-31G**) as precursors in UV-assisted synthesis of HC_7N in cryogenic matrices. [229] [230]

The $HC_5N\cdots C_4H_2$ complex[1] was considered here as a precursor that might lead to the formation of HC_9N. Two structures were obtained [192] at the CAM-B3LYP/aug-cc-pVTZ level of theory: I-shaped (Figure 49) and T-shaped (Figure 50). The first of these is the arrangement one might expect, considering the tendency of the smaller HC_3N molecule to arrange into H-bonded structures.

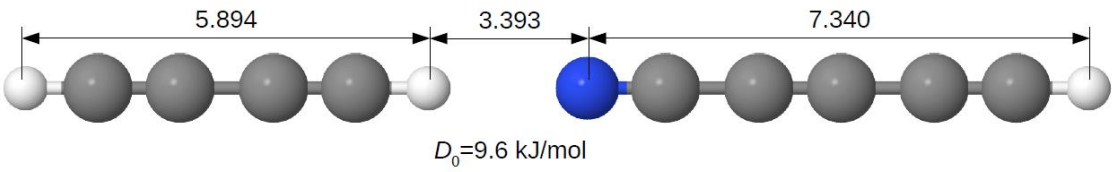

Figure 49. I-shaped structure of the $HC_5N\cdots C_4H_2$ complex, as derived with CAM-B3LYP/aug-cc-pVTZ [192]. Distances in Å.

[1] Pure HC_7N is not available, hence no experimental study on $C_2H_2\cdots HC_7N$ complexes could be performed. Consequently, no theoretical study was undertaken.

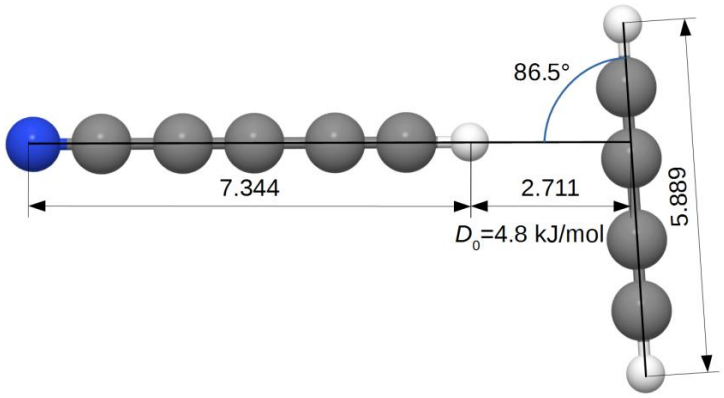

Figure 50. T-shaped structure of the $HC_5N\cdots C_4H_2$ complex, as derived with CAM-B3LYP/aug-cc-pVTZ [192]. Distances in Å.

A theoretical search for other bimolecular complexes did not yield any converging structures. A comparison of dissociation energy values (D_0) for these two complexes indicates that the I-complex is more tightly bound by 4.8 kJ/mol than the T-shaped one. This reflects the strengths of respective hydrogen bonds. The difference in zero-point electronic energies is 4.6 kJ/mol, as derived at CAM-B3LYP/aug-cc-pVTZ level of theory [192].

The vibrational energy levels were calculated (CAM-B3LYP/aug-cc-pVTZ, [192]) for both geometries of $HC_5N\cdots C_4H_2$ complexes and for the separated monomers. According to these predictions, a series of 3 bands should be seen in the CH stretching region for the I-shaped complex. They should be shifted by -62, -8, +2 cm^{-1} and -55, -1, +9 cm^{-1} from the closest strong C_4H_2 and HC_5N bands, respectively. Analogous values expected for the T-shaped complex are: -41, -6, -3 cm^{-1} and -34, +1, +4 cm^{-1}. Another intense spectral feature, the CN stretching band of the HC_5N monomer, should be shifted by +2 cm^{-1} and -4 cm^{-1}, for I-shaped and T-shaped complexes, respectively. No bands that could correspond to these structures were observed in the IR absorption spectra of the samples studied here. Either the respective bands, whose predicted intensity values are twice those of monomers, were too weak (*i.e.* not enough complexes were formed to be detectable), or there were overlaps with the bands of monomeric HC_5N and C_4H_2 molecules.

As already presented, long cyanopolyynic molecules did form in a UV-irradiated cryogenic $Kr/C_4H_2/HC_5N$ mixture. The lack of any detectable bimolecular complexes may suggest that their presence is not crucial for the observed chain elongation processes, contrary to what was previously postulated for formation of HC_5N (*via* $HC_3N + C_2H_2$ coupling) [156]. The intermolecular complexes predicted by theory do not have a proper geometry for straightforward synthesis of longer chains in a rigid environment. Even if complexes existed, many host atoms would have to rearrange together with precursors, in order to undergo reaction. This is especially true of the linear structure. The T-shaped complex is more likely to serve as a precursor for long chain formation and it would not be surprising if at least part of HC_9N was generated *via* that route. On the other hand, had the intermolecular complex formation been crucial for the synthesis of a longer chain, the lack of detectable IR bands for the complex may help explain the fact that no IR absorption bands were detected for the HC_9N products either. Both may have been below the detection limit using IR absorption.

E. Cyanopolyyne formation in cryogenic matrices

While reaction R4 could explain the presence of HC_5N in a UV-irradiated HC_3N-doped cryogenic matrix, a mechanism explaining the appearance of C_6N_2 did not need to invoke any previous formation of intermolecular complexes [115] :

$$HC_3N + h\nu \rightarrow H^{\bullet} + C_3N^{\bullet}, \quad \text{(R5)}$$

$$C_3N^{\bullet} + HC_3N + h\nu \rightarrow C_3N^{\bullet} + H^{\bullet} + C_3N^{\bullet} \rightarrow C_6N_2 + H^{\bullet}. \quad \text{(R6)}$$

The question remains as to whether syntheses of HC_9N and $C_{10}N_2$ can be explained in a similar way, either using well-defined complexes or radical-radical reactions. On the other hand, the reactions of radicals with closed-shell molecules were previously proposed for the formation of HC_7N from either $HC_3N + C_4H_2$ (R7-R8) or $HC_5N + C_2H_2$ (R7, R9) [157]:

$$HC_{2n+1}N + h\nu \rightarrow H^{\bullet} + C_{2n+1}N^{\bullet}, \quad \text{(R7)}$$

$$C_3N^{\bullet} + HC_4H \rightarrow HC_7N + H^{\bullet}, \quad \text{(R8)}$$

$$C_5N^{\bullet} + HC_2H \rightarrow HC_7N + H^{\bullet}. \quad \text{(R9)}$$

Acetylenic radicals $C_2H^{\bullet}$ or $C_4H^{\bullet}$ might also be created in pathways analogous to (R7) and subsequently react with respective neutral cyanopolyynes to give the same final products (HC_7N and $H^{\bullet}$). However, it was shown in [157] that product formation should be dominated by the (R7-R8) or (R7, R9) paths.

If HC_9N and $C_{10}N_2$ form *via* different mechanisms, then they may also show two qualitatively different growth curves. Formation of HC_9N from the nearest neighbours (in a well defined complex or not), with one of the partners being stripped of its hydrogen would necessitate absorbing a single photon. In the case of $C_{10}N_2$, two photons would be required for the creation of two, not necessarily neighbouring, radicals. To test this, two samples were prepared under conditions as similar as possible, such that their initial composition, verified by IR spectroscopy, did not show any obvious differences. Two separate samples were needed, for HC_9N and for $C_{10}N_2$, as it was not possible to observe the formation of both molecules at the same time, given a limited spectral range simultaneously covered by the spectrograph/camera set-up (see Chapter 2.2.2). The time evolution of phosphorescence intensity (proportional to product concentration) was monitored during the 193 nm (ArF laser) photolysis by applying OPO pulses that selectively excited either the $\tilde{E}$ state of HC_9N or $\tilde{H}$ state of $C_{10}N_2$, and by measuring the $\tilde{a} - \tilde{X}$ emission intensity (at 17 300 cm^{-1} or 16 200 cm^{-1}, respectively).

The time evolution curves obtained for $C_{10}N_2$ and HC_9N products are shown in Figure 51. The phosphorescence signal increased with increasing photolysis time producing the curve of a character similar to logarithmic growth (the rate of production was therefore slowing down) in both cases. This is different than the evolution of species obtained from HC_3N, where the production rates were either growing (C_6N_2) or decreasing (HC_5N) with the time of irradiation [115], during the initial stages of the photolysis. Crépin *et al.* [115] rationalizes the growth rate by pointing to the initial increase of $C_3N^{\bullet}$ concentration with

time, which made the recombination of these radicals (into C_6N_2) more and more probable. Eventually, a shortage of precursors prevailed, leading to saturation. Here, growth curves of both targeted molecules (HC_9N, $C_{10}N_2$) resemble that of HC_5N and there was no evidence of any need to accumulate radicals. The only conclusion that can currently be drawn from the time evolution data is that the observed UV-driven creation of a large mononitrile or dinitrile in matrices, in a bimolecular process, requires the interaction of a photolyzing photon with only one of the reacting precursor species, either *via* (R7) or

$$HC_4H + h\nu \rightarrow H^{\bullet} + C_4H^{\bullet}. \qquad \text{(R10)}$$

Subsequently, any of the following reactions, in line with the schemes proposed in Ref. [157], seems *a priori* possible, provided that the initial arrangement of reagents is favourable and that the environment accommodates large deformations of the original matrix cages:

$$C_5N^{\bullet} + HC_4H \rightarrow \mathbf{HC_9N} + H^{\bullet}, \qquad \text{(R11)}$$

$$HC_5N + {}^{\bullet}C_4H \rightarrow \mathbf{HC_9N} + H^{\bullet}. \qquad \text{(R12)}$$

In addition to these reactions, one may expect:

$$C_5N^{\bullet} + HC_5N \rightarrow \mathbf{NC_{10}N} + H^{\bullet} \qquad \text{(R13)}$$

or

$$HC_4H + {}^{\bullet}C_4H \rightarrow HC_8H + H^{\bullet}. \qquad \text{(R14)}$$

No conclusive identification of tetraacetylene has thus far been possible in experiments with UV-irradiated $HC_5N + C_4H_2$ mixtures isolated in rare gas solids.

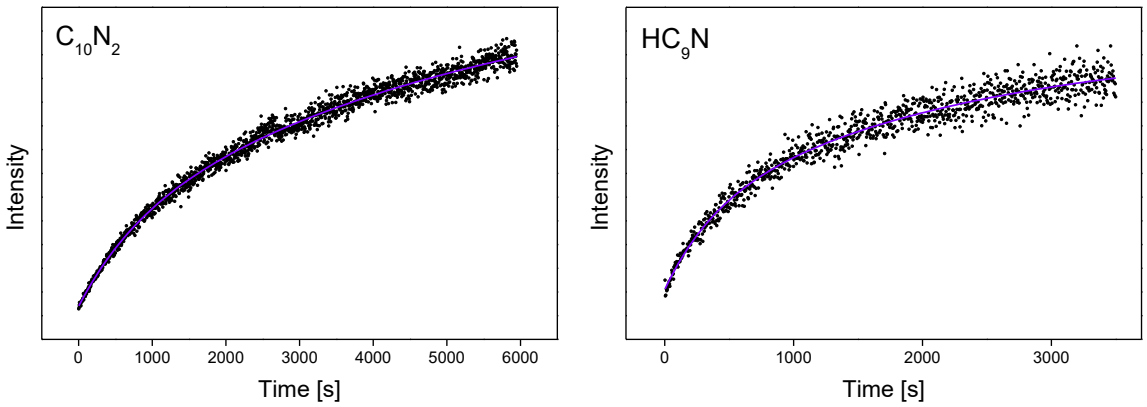

Figure 51. Time evolution of $C_{10}N_2$ (left) and HC_9N (right) formation, as monitored by phosphorescence intensity in irradiated (193 nm) Kr/C_4H_2/HC_5N (1000/1/1) matrices.

Formation of long chains from two radicals is excluded as the main path, as it would take much more time at the beginning of the process and would accelerate as more radicals are produced. This is not what is observed (see Figure 51). The importance of secondary photolysis products in the first stages of the photolysis can also be neglected.

In HC_5N + CH_3C_2H experiments, very strong phosphorescence from one of the precursors (HC_5N) overlaps that of the cyanotriyynic products HC_7N and CH_3C_7N. No studies of growth as a function of time could be accomplished for these two. However, in analogy to the mechanisms discussed above, the following scheme may be at work once $C_5N^{\bullet}$ (produced *via* R7) becomes available:

$C_5N^{\bullet} + CH_3C_2H \rightarrow \mathbf{HC_7N} + CH_3^{\bullet}$, (R15a)

$C_5N^{\bullet} + CH_3C_2H \rightarrow \mathbf{CH_3C_7N} + H^{\bullet}$. (R15b)

Then, in more general terms (R denoting H, CN or CH_3), one obtains:

$HC_{2n+1}N + h\nu \rightarrow H^{\bullet} + C_{2n+1}N^{\bullet}$, (R16)

$C_{2n+1}N^{\bullet} + HC_{2m}R \rightarrow RC_{2n+2m+1}N + H^{\bullet}$, (R17a)

$C_{2n+1}N^{\bullet} + HC_{2m}R \rightarrow HC_{2n+2m+1}N + R^{\bullet}$. (R17b)

Although the above scheme is aimed at explaining the reactions occurring in cryogenic matrices, not in the interstellar medium, it is nevertheless in accordance with what Cherchneff *et al.* proposed for monocyanopolyyne formation in the circumstellar shell IRC + 10216 [36,37].

The (R16-R17) scheme may yield all the observed monocyanopolyynes and dicyanopolyynes. A number of alternative paths may also play role here. The propyne photolysis may also take place:

$CH_3C_2H + h\nu \rightarrow CH_3C_2^{\bullet} + H^{\bullet}$, (R18a)

$CH_3C_2H + h\nu \rightarrow CH_3^{\bullet} + C_2H^{\bullet}$, (R18b)

which can be followed *e.g.* by:

$CH_3C_2^{\bullet} + HC_5N \rightarrow \mathbf{HC_7N} + CH_3^{\bullet}$ (R19a)

$CH_3C_2^{\bullet} + HC_5N \rightarrow \mathbf{CH_3C_7N} + H^{\bullet}$. (R19b)

or by the reactions involving the products of (R18b) attacking HC_5N.

It should however be mentioned that the reaction CH_3C_5N + C_2H_2, as well as CH_3C_3N + C_2H_2, were attempted and did not yield detectable $HC_{2n+1}N$ molecules (neither did they produce any $CH_3C_{2n+1}N$ species). This suggest that it is easier to detach the methyl group from propyne (R15a, R19a) than from a methylcyano(poly)yne molecule.

Finally, one can remark that the discussed processes could possibly occur involving a precursor molecule excited to a high electronic level rather than converted into a free radical (*i.e.* the separate dissociation step might not be distinguishable).

5 SUMMARY AND FUTURE STUDIES

5.1 Summary

This dissertation describes the experimental results obtained for a group of astrochemically-relevant molecules from the cyanoacetylene family. The use of the cryogenic matrix isolation technique and spectroscopic methods (in particular: laser-induced luminescence measurements) proved to be appropriate for answering the questions stated at the beginning of this work. The following list sums up the most important results.

1. Spectroscopic characterization of the molecules of interest.
    a. IR absorption measurements were performed for several methylcyanoacetylene (CH_3C_3N) isomers available as pure substances, namely allenyl cyanide, allenyl isocyanide, propargyl cyanide, and propargyl isocyanide. This was an indispensable preliminary step before studying the photochemistry of CH_3C_3N.
    b. Combined IR absorption, Raman scattering, and electronic luminescence spectroscopy analyses allowed for the most complete, up to date, characterization of the vibrational modes of gaseous and cryogenic matrix-isolated methylcyanodiacetylene, CH_3C_5N. The results have been partly published [196].
    c. Strong phosphorescence of CH_3C_5N, CH_3C_7N, HC_9N, $C_{10}N_2$, and C_5N^-, observed here for the first time, was shown to permit for the sensitive detection of these molecules. Phosphorescence excitation spectra (measured mainly with the use of tunable lasers), gave insight to excited singlet electronic states, much more efficiently than any standard spectrophotometric approach. Corresponding vibronic bands have been analysed.
    d. Spectroscopic measurements of CH_3C_5N, HC_7N, CH_3C_7N, HC_9N, and $C_{10}N_2$ yielded the energies of certain excited electronic states, in particular the second excited singlet and the lowest triplet states. Environment effects were studied for CH_3C_5N in several cryogenic matrices, as well as in the gas and solid phase. Results concerning the electronic spectroscopy of CH_3C_5N are partly published [197].
    e. Phosphorescence spectroscopy of HC_5N was revisited; new vibronic bands have been identified.
2. Photochemical studies.
    a. Isomerization of CH_3C_3N. A mechanism leading to the two unambiguously identified products, allenyl cyanide and propargyl cyanide, has been proposed. Other C_4H_3N isomers were searched for on the basis of theoretical predictions (Custer *et al*. [193]), without positive identifications. Several photolysis products remain unidentified.
    b. Mono- and dicyanotetraacetylene molecules (HC_9N, $C_{10}N_2$) were successfully formed from smaller (cyano)acetylenic precursors in UV-

stimulated cryogenic processes. The method has also proved effective for the creation of the methylated cyanopolyynes CH_3C_5N and CH_3C_7N. Mechanisms previously proposed for the similar cryogenic assembling of HC_5N, C_4N_2, C_6N_2 (from HC_3N [115]), and HC_7N (from a $HC_5N + C_2H_2$ mixture [157]) were revisited in the context of longer or CH_3-containing chains. Present results suggest the validity of the adopted approach for the syntheses and spectral studies of even longer unsaturated carbon-nitrogen chains.

3. The influence of the methyl group on the spectroscopy of cyanopolyynes was investigated based on HC_5N/CH_3C_5N and HC_7N/CH_3C_7N pairs. With each pair, the chromophore remains the same ($C_{2n+1}N$). This is reflected in the similarity of their electronic spectra. However, noticeably longer phosphorescence lifetimes have been measured for the methylated compounds. Peculiarities stemming from the C_{3v} symmetry (as compared to $C_{\infty v}$) were most clearly manifested in IR spectra of CH_3C_5N, taking the form of rovibrational features (*Q* bands) of certain perpendicular bands.
4. The influence of chain length was thoroughly analysed for the electronic spectroscopy of $HC_{2n+1}N$, $NC_{2n}N$, and $CH_3C_{2n+1}N$ molecules. Within each of these families, the $\tilde{a} - \tilde{X}$ origin wavelength was found to change linearly with the length of the conjugated backbone (the chromophore). Independently of the chain length, the main vibronic progressions discerned in phosphorescence and in singlet-singlet absorption spectra were shaped mostly by a centrosymmetric (for $D_{\infty h}$ species) or pseudo-centrosymmetric (for $C_{\infty v}$ species) vibration modes (~2200 cm^{-1}), characteristic of triple bonds stretchings. Another similarity is that all $\tilde{B} - \tilde{X}$ transitions studied gained intensity *via* coupling to similar vibrations, namely those generating 'zig-zag' distortions of the conjugated carbon-nitrogen backbone.

5.2 Further studies

1. Follow-up experiments.

In many instances, the analyses of the spectra could not be completed using available resources. This applies to CH_3C_5N, where additional experiments involving isotopically substituted compounds should help in providing the missing spectral assignments or verifying those in doubt. Even more importantly, cryogenic matrix-related effects accompanying the perpendicular bands of C_{3v}-symmetry species (exemplified with the IR spectrum of CH_3C_5N in solid *p*-H_2), are worth further studies, possibly starting with propyne as a simple model compound.

The $\tilde{B} - \tilde{X}$ and $\tilde{E} - \tilde{X}$ transitions of CH_3C_7N also could not be fully interpreted using data from phosphorescence excitation spectroscopy. More measurements are needed using a tuneable laser source, with mild (less destructive) excitation conditions. Furthermore, performing the photolysis of HC_5N isolated in various cryogenic hosts (other than those already tested: Ar and Kr) should help in the assignment of characteristic doublets appearing in C_5N^- emission spectra and also in understanding the origin of some features appearing in phosphorescence excitation spectra of that anion, coming probably from an electron

photodetachment process. The use of various hosts may also help in studying the $\tilde{E} - \tilde{X}$ systems of HC_7N and HC_9N.

An obvious line of future research is the quest for phosphorescence spectra of mono- or dicyanopentayne ($HC_{11}N$, $NC_{12}N$) or of previously unreported methylated cyanopolyynes. Transition wavelengths could be estimated by extrapolating available data for $HC_{2n+1}N$ (n = 2, 3, 4), $NC_{2n}N$ (n = 1, 2, 3, 4, 5), and $CH_3C_{2n+1}N$ (n = 2, 3) molecules. To produce $HC_{11}N$, the precursors triacetylene (C_6H_2) and HC_5N are already available *via* preparatory organic chemical synthesis although production and handling of C_6H_2 is quite demanding. The chemistry of cyanopolyynes may also be of use for astrophysics, considering that these molecules were proposed as astrochemical clocks [231]. Inert gas cryogenic matrix experiments may only distantly mimic processes occurring in the interstellar environment, but they do serve as a starting point for further developments.

Thermoluminescence accompanying matrix warm-up should be rigorously investigated in future experiments, as it may aid in identification of recombining species (the presence of CN radicals, for instance, can be deduced from the observed thermophosphorescence of C_2N_2).

2. New experiments involving other techniques.

Weak bands (*e.g.* the $\tilde{A} - \tilde{X}$ features of CH_3C_5N) or even strongly forbidden ones (like the singlet-triplet transitions of cyanopolyynes) can be investigated in the gas phase with cavity ring-down spectroscopy. Such studies may be of value for planetology (atmospheres of certain Solar System bodies, Titan in particular).

Mass-spectrometric analysis of photoproducts generated in matrices (carried out during the evaporation of a matrix) may help in the identification of relatively stable, closed-shell molecules. However, such measurements would not be sensitive to isomeric differences and would likely be blind to radicals and ions formed in a matrix as they would recombine prior to detection.

Measurement of phosphorescence quantum yields would be useful in quantifying reaction products, potentially lending insight into reaction mechanisms. A method similar to the one reported in Penzkofer [232] could possibly be used to measure phosphorescence quantum yields, with an appropriately chosen reference compound.

Another interesting avenue of research involves using non-inert cryogenic solids of astrophysical significance for isomerization or chain-growth processes. Performing these reactions in solids made up of water, carbon monoxide, hydrogen, methane, or a mixture thereof are needed to provide insight into how these hosts modify chemical evolution. Preliminary experiments reported here using parahydrogen are already one step in this direction.

3. Additional theoretical studies.

Several products formed in the photolysis experiments remain unidentified, some of which are luminescent. Future spectral assignments will necessitate reliable theoretical predictions of related radicals, ions and isomers of species already identified.

In order to get a more complete view of the chain-coupling or isomerization processes taking place, a detailed theoretical study of the energetics, including the heats of formation for all reagents and products, would be needed. Molecular dynamics simulations of matrix growth processes would also contribute to the description of these phenomena by rationalizing the differences in spectra observed for various host materials.

Science never solves a problem without creating ten more.

G. B. Shaw

REFERENCES

[1] L.J. Allamandola, Interstellar problems and matrix solutions, J. Mol. Struct. 157 (1987) 255–273.

[2] S. Arrhenius, Worlds in the Making: The Evolution of the Universe, Harper & Brothers, 1908.

[3] Droga związków chemicznych od przestrzeni kosmicznej do powierzchni planety. (http://astrochem.freehost.pl/astrochemia/grafika/rys10.png; accessed January 8, 2017).

[4] I.R. Sims, Low-temperature reactions: Tunnelling in space, Nat. Chem. 5 (2013) 734–736. doi:10.1038/nchem.1736.

[5] M.B. Bell, P.A. Feldman, S. Kwok, H.E. Matthews, Detection of $HC_{11}N$ in IRC + 10°216, Nature. 295 (1982) 389–391. doi:10.1038/295389a0.

[6] M.B. Bell, P.A. Feldman, M.J. Travers, M.C. McCarthy, C.A. Gottlieb, P. Thaddeus, Detection of $HC_{11}N$ in the Cold Dust Cloud TMC-1, Astrophys. J. Lett. 483 (1997) L61. doi:10.1086/310732.

[7] P. Thaddeus, M.C. McCarthy, M.J. Travers, C.A. Gottlieb, W. Chen, New carbon chains in the laboratory and in interstellar space, Faraday Discuss. 109 (1998) 121–135. doi:10.1039/a800286j.

[8] B.E. Turner, Detection of Interstellar Cyanoacetylene, Astrophys. J. Lett. 163 (1971) L35. doi:10.1086/180662.

[9] D.F. Dickinson, Detection of cyanoacetylene at 18 GHz, Astrophys. Lett. 12 (1972) 235–6.

[10] R.X. McGee, M. Balister, L.M. Newton, Interstellar cyanoacetylene $J = 2 \rightarrow 1$, $J = 4 \rightarrow 3$ transitions, Mon. Not. R. Astron. Soc. 180 (1977) 585–592. doi:10.1093/mnras/180.4.585.

[11] F.F. Gardner, G. Winnewisser, Observations of the $J = 1 \rightarrow 0$ Transitions of the (13) C Isotopic Species of Cyanoacetylene (hcccn) in the Direction of Sagittarius B2, Astrophys. J. 197 (1975) L73. doi:10.1086/181781.

[12] R. Mauersberger, C. Henkel, L.J. Sage, Dense gas in nearby galaxies. III - HC_3N as an extragalactic density probe, Astron. Astrophys. 236 (1990) 63–68.

[13] K. Taniguchi, M. Saito, H. Ozeki, ^{13}C Isotopic Fractionation of HC_3N in Star-forming Regions: Low-mass Star-forming Region L1527 and High-mass Star-forming Region G28.28-0.36, Astrophys. J. 830 (2016) 106. doi:10.3847/0004-637X/830/2/106.

[14] V.G. Kunde, A.C. Aikin, R.A. Hanel, D.E. Jennings, W.C. Maguire, R.E. Samuelson, C_4H_2, HC_3N and C_2N_2 in Titan's atmosphere, Nature. 292 (1981) 686–688. doi:10.1038/292686a0.

[15] A. Coustenis, The atmospheric structure of Titan from Voyager to Cassini, AGU Spring Meet. Abstr. 44 (2007). http://adsabs.harvard.edu/abs/2007AGUSM.P44A..03C (accessed December 5, 2016).

[16] D. Bockelée-Morvan, D.C. Lis, J.E. Wink, D. Despois, J. Crovisier, R. Bachiller, D.J. Benford, N. Biver, P. Colom, J.K. Davies, E. Gérard, B. Germain, M. Houde, D. Mehringer, R. Moreno, G. Paubert, T.G. Phillips, H. Rauer, New molecules found in comet C/1995 O1 (Hale-Bopp). Investigating the link between cometary and interstellar material, Astron. Astrophys. 353 (2000) 1101–1114.

[17] K. Kawaguchi, M. Ohishi, S.-I. Ishikawa, N. Kaifu, Detection of isocyanoacetylene HCCNC in TMC-1, Astrophys. J. 386 (1992) L51–L53.

[18] K. Kawaguchi, S. Takano, M. Ohishi, S.-I. Ishikawa, K. Miyazawa, N. Kaifu, K. Yamashita, S. Yamamoto, S. Saito, Y. Ohshima, Y. Endo, Detection of HNCCC in TMC-1, Astrophys. J. 396 (1992) L49–L51.

[19] C.H. Hu, H.F. Schaefer, Cyanovinylidene: an observable unsaturated carbene and a possible interstellar molecule, J. Phys. Chem. 97 (1993) 10681–10686. doi:10.1021/j100143a026.

[20] R. Kołos, M. Gronowski, J.C. Dobrowolski, Prospects for the Detection of Interstellar Cyanovinylidene, Astrophys. J. 701 (2009) 488. doi:10.1088/0004-637X/701/1/488.

[21] Y. Osamura, K. Fukuzawa, R. Terzieva, E. Herbst, A Molecular Orbital Study of the HC_3NH^{++} e^- Dissociative Recombination and Its Role in the Production of Cyanoacetylene Isomers in Interstellar Clouds, Astrophys. J. 519 (1999) 697. doi:10.1086/307406.

[22] R.A. Sanchez, J.P. Ferris, L.E. Orgel, Cyanoacetylene in prebiotic synthesis, Science. 154 (1966) 784–785.

[23] J.P. Ferris, R.A. Sanchez, L.E. Orgel, Studies in prebiotic synthesis. 3. Synthesis of pyrimidines from cyanoacetylene and cyanate, J. Mol. Biol. 33 (1968) 693–704.

[24] R.A. Sanchez, L.E. Orgel, Studies in prebiotic synthesis, J. Mol. Biol. 47 (1970) 531–543. doi:10.1016/0022-2836(70)90320-7.

[25] J.P. Ferris, O.S. Zamek, A.M. Altbuch, H. Freiman, Chemical evolution, J. Mol. Evol. 3 (1974) 301–309. doi:10.1007/BF01796045.

[26] M.P. Robertson, S.L. Miller, An efficient prebiotic synthesis of cytosine and uracil, Nature. 375 (1995) 772–774. doi:10.1038/375772a0.

[27] M.P. Robertson, S.L. Miller, An efficient prebiotic synthesis of cytosine and uracil, Nature. 377 (1995) 257–257. doi:10.1038/377257a0.
[28] S.L. Miller, Current status of the prebiotic synthesis of small molecules, Chem. Scr. 26B (1986) 5–11.
[29] L.E. Orgel, Is Cyanoacetylene Prebiotic?, Orig. Life Evol. Biosph. 32 (2002) 279–281. doi:10.1023/A:1016509009433.
[30] R.L. Snell, F.P. Schloerb, J.S. Young, A. Hjalmarson, P. Friberg, Observations of HC_3N, HC_5N, and HC_7N in molecular clouds, Astrophys. J. 244 (1981) 45–53. doi:10.1086/158683.
[31] N.W. Broten, T. Oka, L.W. Avery, J.M. MacLeod, H.W. Kroto, The detection of HC_9N in interstellar space, Astrophys. J. 223 (1978) L105. doi:10.1086/182739.
[32] M.B. Bell, L.W. Avery, J.M. MacLeod, H.E. Matthews, The excitation temperature of HC_9N in the circumstellar envelope of IRC + 10216, Astrophys. J. 400 (1992) 551–555. doi:10.1086/172017.
[33] Truong-Bach, D. Graham, Nguyen-Q-Rieu, HC_9N from the Envelopes of IRC+10216 and CRL:2688, Astron. Astrophys. 277 (1993) 133.
[34] R.A. Loomis, C.N. Shingledecker, G. Langston, B.A. McGuire, N.M. Dollhopf, A.M. Burkhardt, J. Corby, S.T. Booth, P.B. Carroll, B. Turner, A.J. Remijan, Non-detection of HC11N towards TMC-1: constraining the chemistry of large carbon-chain molecules, Mon. Not. R. Astron. Soc. 463 (2016) 4175–4183. doi:10.1093/mnras/stw2302.
[35] J.R. Pardo, J. Cernicharo, J.R. Goicoechea, T.G. Phillips, The Slowly Expanding Envelope of CRL 618 Probed with HC3N Rotational Ladders, Astrophys. J. 615 (2004) 495. doi:10.1086/424379.
[36] I. Cherchneff, A.E. Glassgold, The Formation of Carbon Chain Molecules in IRC +10216, Astrophys. J. Lett. 419 (1993) L41. doi:10.1086/187132.
[37] I. Cherchneff, A.E. Glassgold, G.A. Mamon, The formation of cyanopolyyne molecules in IRC + 10216, Astrophys. J. 410 (1993) 188–201. doi:10.1086/172737.
[38] P.M. Solomon, K.B. Jefferts, A.A. Penzias, R.W. Wilson, Detection of Millimeter Emission Lines from Interstellar Methyl Cyanide, Astrophys. J. Lett. 168 (1971) L107. doi:10.1086/180794.
[39] H.E. Matthews, T.J. Sears, Detection of the J = 1 - 0 transition of CH_3CN, Astrophys. J. Lett. 267 (1983) L53–L57. doi:10.1086/184001.
[40] P.F. Goldsmith, R. Krotkov, R.L. Snell, R.D. Brown, P. Godfrey, Vibrationally excited CH_3CN and HC_3N in Orion, Astrophys. J. 274 (1983) 184–194. doi:10.1086/161436.
[41] S. Cazaux, A.G.G.M. Tielens, C. Ceccarelli, A. Castets, V. Wakelam, E. Caux, B. Parise, D. Teyssier, The Hot Core around the Low-Mass Protostar IRAS 16293–2422: Scoundrels Rule!, Astrophys. J. Lett. 593 (2003) L51. doi:10.1086/378038.
[42] N.W. Broten, J.M. MacLeod, L.W. Avery, P. Friberg, A. Hjalmarson, B. Hoglund, W.M. Irvine, The detection of interstellar methylcyanoacetylene, Astrophys. J. 276 (1984) L25. doi:10.1086/184181.
[43] L.E. Snyder, T.L. Wilson, C. Henkel, P.R. Jewell, C.M. Walmsley, Detection of Interstellar Methylcyanodiacetylene in the Dark Dust Cloud TMC 1, in: 1984: p. 959. http://cdsads.u-strasbg.fr/abs/1984BAAS...16Q.959S (accessed October 23, 2015).
[44] L.E. Snyder, J.M. Hollis, P.R. Jewell, F.J. Lovas, A. Remijan, Confirmation of Interstellar Methylcyanodiacetylene (CH_3C_5N), Astrophys. J. 647 (2006) 412. doi:10.1086/505323.
[45] E. Herbst, C.M. Leung, Gas-phase production of complex hydrocarbons, cyanopolyynes, and related compounds in dense interstellar clouds, Astrophys. J. Suppl. Ser. 69 (1989) 271. doi:10.1086/191314.
[46] T.I. Hasegawa, E. Herbst, Three-phase chemical models of dense interstellar clouds: gas, dust particle mantles and dust particle surfaces, Mon. Not. R. Astron. Soc. 263 (1993) 589–606. doi:10.1093/mnras/263.3.589.
[47] G.E. Hassel, E. Herbst, R.T. Garrod, Modeling the Lukewarm Corino Phase: Is L1527 Unique?, Astrophys. J. 681 (2008) 1385. doi:10.1086/588185.
[48] J. Kalvāns, I. Shmeld, Subsurface chemistry of mantles of interstellar dust grains in dark molecular cores, Astron. Astrophys. 521 (2010) A37. doi:10.1051/0004-6361/201014190.
[49] A. Belloche, H.S.P. Müller, K.M. Menten, P. Schilke, C. Comito, Complex organic molecules in the interstellar medium: IRAM 30 m line survey of Sagittarius B2(N) and (M), Astron. Astrophys. 559 (2013) A47. doi:10.1051/0004-6361/201321096.
[50] A.J. Remijan, F. Wyrowski, D.N. Friedel, D.S. Meier, L.E. Snyder, A Survey of Large Molecules toward the Proto-Planetary Nebula CRL 618, Astrophys. J. 626 (2005) 233–244. doi:10.1086/429750.
[51] N. Balucani, O. Asvany, Y. Osamura, L.C.L. Huang, Y.T. Lee, R.I. Kaiser, Laboratory investigation on the formation of unsaturated nitriles in Titan's atmosphere, Planet. Space Sci. 48 (2000) 447–462. doi:10.1016/S0032-0633(00)00018-0.
[52] H.B. Niemann, S.K. Atreya, S.J. Bauer, G.R. Carignan, J.E. Demick, R.L. Frost, D. Gautier, J.A. Haberman, D.N. Harpold, D.M. Hunten, G. Israel, J.I. Lunine, W.T. Kasprzak, T.C. Owen, M. Paulkovich, F. Raulin, E. Raaen, S.H. Way, The abundances of constituents of Titan's atmosphere from the GCMS instrument on the Huygens probe, Nature. 438 (2005) 779–784. doi:10.1038/nature04122.

[53] V. Vuitton, R.V. Yelle, M.J. McEwan, Ion chemistry and N-containing molecules in Titan's upper atmosphere, Icarus. 191 (2007) 722–742. doi:10.1016/j.icarus.2007.06.023.
[54] J.C. Loison, E. Hébrard, M. Dobrijevic, K.M. Hickson, F. Caralp, V. Hue, G. Gronoff, O. Venot, Y. Bénilan, The neutral photochemistry of nitriles, amines and imines in the atmosphere of Titan, Icarus. 247 (2015) 218–247. doi:10.1016/j.icarus.2014.09.039.
[55] F.J. Lovas, A.J. Remijan, J.M. Hollis, P.R. Jewell, L.E. Snyder, Hyperfine Structure Identification of Interstellar Cyanoallene toward TMC-1, Astrophys. J. Lett. 637 (2006) L37. doi:10.1086/500431.
[56] A. Singh, Shivani, A. Misra, P. Tandon, Formation of cyanoallene (buta-2, 3-dienenitrile) in the interstellar medium: a quantum chemical and spectroscopic study, Res. Astron. Astrophys. 14 (2014) 275. doi:10.1088/1674-4527/14/3/002.
[57] H. Jones, J. Sheridan, The microwave spectrum of 3-butynenitrile, J. Mol. Struct. 78 (1982) 303–305. doi:10.1016/0022-2860(82)80017-3.
[58] J. Demaison, I. Pohl, H.D. Rudolph, Millimeter-wave spectrum of 3-butynenitrile: Dipole moment and centrifugal distortion constants, J. Mol. Spectrosc. 114 (1985) 210–218. doi:10.1016/0022-2852(85)90349-2.
[59] D. McNaughton, N.G. Romeril, M.F. Lappert, H.W. Kroto, The microwave spectra of 1-cyanoprop-2-yne HC=CCH$_2$CN) and 1-isocyanoprop-2-yne HC=CCH$_2$NC, J. Mol. Spectrosc. 132 (1988) 407–412. doi:10.1016/0022-2852(88)90335-9.
[60] W. Jäger, H. Krause, H. Mäder, M.C.L. Gerry, Rotational spectrum of 3-butynenitrile in the microwave and radiofrequency range using one- and two-dimensional Fourier transform techniques, J. Mol. Spectrosc. 143 (1990) 50–60. doi:10.1016/0022-2852(90)90260-W.
[61] Molecules in Space | I. Physikalisches Institut. https://www.astro.uni-koeln.de/cdms/molecules (accessed December 5, 2016).
[62] A.J. Markwick, T.J. Millar, S.B. Charnley, On the Abundance Gradients of Organic Molecules along the TMC-1 Ridge, Astrophys. J. 535 (2000) 256. doi:10.1086/308814.
[63] D. Quan, E. Herbst, Possible gas-phase syntheses for seven neutral molecules studied recently with the Green Bank Telescope, Astron. Astrophys. 474 (2007) 10. doi:10.1051/0004-6361:20078246.
[64] N. Kerisit, C. Rouxel, S. Colombel-Rouen, L. Toupet, J.-C. Guillemin, Y. Trolez, Synthesis, Chemistry, and Photochemistry of Methylcyanobutadiyne in the Context of Space Science, J. Org. Chem. (2016). doi:10.1021/acs.joc.6b00205.
[65] R.K. Khanna, M.A. Perera-Jarmer, M.J. Ospina, Vibrational infrared and raman spectra of dicyanoacetylene, Spectrochim. Acta Part Mol. Spectrosc. 43 (1987) 421–425. doi:10.1016/0584-8539(87)80128-9.
[66] P. Thaddeus, C.A. Gottlieb, H. Gupta, S. Brünken, M.C. McCarthy, M. Agúndez, M. Guélin, J. Cernicharo, Laboratory and Astronomical Detection of the Negative Molecular Ion C_3N^-, Astrophys. J. 677 (2008) 1132. doi:10.1086/528947.
[67] J. Cernicharo, M. Guélin, M. Agúndez, M.C. McCarthy, P. Thaddeus, Detection of C_5N^- and Vibrationally Excited C_6H in IRC +10216, Astrophys. J. Lett. 688 (2008) L83. doi:10.1086/595583.
[68] R.C. Fortenberry, Interstellar Anions: The Role of Quantum Chemistry, J. Phys. Chem. A. 119 (2015) 9941–9953. doi:10.1021/acs.jpca.5b05056.
[69] H. Ding, A.E. Boguslavskiy, T.W. Schmidt, J.P. Maier, Gas phase electronic spectrum of the nitrogen terminated nanowire $NC_{16}N$, Chem. Phys. Lett. 392 (2004) 225–228. doi:10.1016/j.cplett.2004.05.061.
[70] A. Bilić, J.R. Reimers, N.S. Hush, Adsorption of Pyridine on the Gold(111) Surface: Implications for "Alligator Clips" for Molecular Wires, J. Phys. Chem. B. 106 (2002) 6740–6747. doi:10.1021/jp020590i.
[71] V.A. Job, G.W. King, The electronic spectrum of cyanoacetylene: Part I. Analysis of the 2600-Å system, J. Mol. Spectrosc. 19 (1966) 155–177. doi:10.1016/0022-2852(66)90238-4.
[72] V.A. Job, G.W. King, The electronic spectrum of cyanoacetylene: Part II. Analysis of the 2300-Å system, J. Mol. Spectrosc. 19 (1966) 178–184. doi:10.1016/0022-2852(66)90239-6.
[73] T. Titarchuk, J.B. Halpern, The excitation spectrum of cyanoacetylene (HC_3N) and emission from C3N fragments, Chem. Phys. Lett. 323 (2000) 305–311. doi:10.1016/S0009-2614(00)00517-0.
[74] H. Okabe, V.H. Dibeler, Photon impact studies of C_2HCN and CH_3CN in the vacuum ultraviolet; heats of formation of C_2H and CH_3CN, J. Chem. Phys. 59 (1973) 2430–2435. doi:10.1063/1.1680354.
[75] J.A. Halpern, G.E. Miller, H. Okabe, W. Nottingham, The UV photochemistry of cyanoacetylene, J. Photochem. Photobiol. Chem. 42 (1988) 63–72. doi:10.1016/1010-6030(88)80049-2.
[76] K. Seki, M. He, R. Liu, H. Okabe, Photochemistry of Cyanoacetylene at 193.3 nm, J. Phys. Chem. 100 (1996) 5349–5353. doi:10.1021/jp952787z.
[77] R. Silva, W.K. Gichuhi, V.V. Kislov, A. Landera, A.M. Mebel, A.G. Suits, UV Photodissociation of Cyanoacetylene: A Combined Ion Imaging and Theoretical Investigation, J. Phys. Chem. A. 113 (2009) 11182–11186. doi:10.1021/jp904183a.

[78] D.W. Clarke, J.P. Ferris, Photodissociation of cyanoacetylene: application to the atmospheric chemistry of Titan, Icarus. 115 (1995) 119–125.
[79] R. Kołos, A.L. Sobolewski, The infrared spectroscopy of HNCCC: matrix isolation and density functional theory study, Chem. Phys. Lett. 344 (2001) 625–630. doi:10.1016/S0009-2614(01)00793-X.
[80] R. Kołos, J. Waluk, Matrix-isolated products of cyanoacetylene dissociation, J. Mol. Struct. 408–409 (1997) 473–476. doi:10.1016/S0022-2860(96)09573-7.
[81] L. Khriachtchev, A. Lignell, H. Tanskanen, J. Lundell, H. Kiljunen, M. Räsänen, Insertion of Noble Gas Atoms into Cyanoacetylene: An ab Initio and Matrix Isolation Study, J. Phys. Chem. A. 110 (2006) 11876–11885. doi:10.1021/jp063731f.
[82] R. Kołos, A.L. Sobolewski, The infrared spectroscopy of HNCCC: matrix isolation and density functional theory study, Chem. Phys. Lett. 344 (2001) 625–630. doi:10.1016/S0009-2614(01)00793-X.
[83] Z. Guennoun, I. Couturier-Tamburelli, N. Piétri, J.P. Aycard, UV photoisomerisation of cyano and dicyanoacetylene: the first identification of CCNCH and CCCNCN isomers – matrix isolation, infrared and ab initio study, Chem. Phys. Lett. 368 (2003) 574–583. doi:10.1016/S0009-2614(02)01898-5.
[84] R. Kołos, A novel source of transient species for matrix isolation studies, Chem. Phys. Lett. 247 (1995) 289–292. doi:10.1016/0009-2614(95)01213-9.
[85] R. Kołos, M. Gronowski, P. Botschwina, Matrix isolation IR spectroscopic and ab initio studies of C_3N^- and related species, J. Chem. Phys. 128 (2008) 154305. doi:10.1063/1.2902289.
[86] M. Turowski, M. Gronowski, S. Boyé-Péronne, S. Douin, L. Monéron, C. Crépin, R. Kołos, The C3N− anion: First detection of its electronic luminescence in rare gas solids, J. Chem. Phys. 128 (2008) 164304. doi:10.1063/1.2904876.
[87] A.M. Smith-Gicklhorn, M. Lorenz, R. Kołos, V.E. Bondybey, Vibrational spectroscopy of matrix-isolated, mass-selected cyanoacetylene cations, J. Chem. Phys. 115 (2001) 7534–7542. doi:10.1063/1.1405019.
[88] S.A. Barts, J.B. Halpern, The emission spectrum of C_2N_2, Chem. Phys. Lett. 161 (1989) 207–211. doi:10.1016/S0009-2614(89)87061-7.
[89] J.-W. Chang, Y.-P. Lee, The C_2N_2 $a\ ^3\Sigma^+_u \rightarrow X\ ^1\Sigma^+_g$ chemiluminescence in matrices, J. Mol. Struct. 157 (1987) 155–165. doi:10.1016/0022-2860(87)87090-4.
[90] P. Botschwina, Ä. Heyl, M. Oswald, T. Hirano, Ab initio anharmonic force fields and spectroscopic properties for HC_5N and HC_5NH^+, molecules of interest to astrochemistry, Spectrochim. Acta. A. Mol. Biomol. Spectrosc. 53 (1997) 1079–1090. doi:10.1016/S1386-1425(97)00018-8.
[91] M. Turowski, C. Crépin, M. Gronowski, J.-C. Guillemin, A. Coupeaud, I. Couturier-Tamburelli, N. Piétri, R. Kołos, Electronic absorption and phosphorescence of cyanodiacetylene, J. Chem. Phys. 133 (2010) 074310. doi:10.1063/1.3472978.
[92] M. Turowski, C. Crépin, S. Douin, M. Gronowski, I. Couturier-Tamburelli, N. Piétri, A. Wasiak, R. Kołos, Low temperature Raman spectra of cyanobutadiyne (HC_5N), Vib. Spectrosc. 62 (2012) 268–272. doi:10.1016/j.vibspec.2012.05.005.
[93] J.-C. Guillemin, Y. Trolez, A. Moncomble, Synthesis, chemistry and photochemistry of cyanobutadiyne (HCCCCCN), Adv. Space Res. 42 (2008) 2002–2007. doi:10.1016/j.asr.2007.08.013.
[94] A. Coupeaud, M. Turowski, M. Gronowski, N. Piétri, I. Couturier-Tamburelli, R. Kołos, J.-P. Aycard, C5N− anion and new carbenic isomers of cyanodiacetylene: A matrix isolation IR study, J. Chem. Phys. 128 (2008) 154303. doi:10.1063/1.2894875.
[95] M. Turowski, M. Gronowski, J.-C. Guillemin, R. Kołos, Generation of H–Kr–C_5N and H–Xe–C_5N molecules, J. Mol. Struct. 1025 (2012) 140–146. doi:10.1016/j.molstruc.2012.04.088.
[96] M. Gronowski, R. Kołos, Isomers of cyanodiacetylene: Theoretical structures and IR spectra, Chem. Phys. Lett. 428 (2006) 245–248. doi:10.1016/j.cplett.2006.07.041.
[97] A. Coupeaud, M. Turowski, M. Gronowski, N. Piétri, I. Couturier-Tamburelli, R. Kołos, J.-P. Aycard, Spectroscopy of cyanodiacetylene in solid argon and the photochemical generation of isocyanodiacetylene, J. Chem. Phys. 126 (2007) 164301. doi:10.1063/1.2720842.
[98] T. Wakabayashi, M. Saikawa, Y. Wada, T. Minematsu, Isotope scrambling in the formation of cyanopolyynes by laser ablation of carbon particles in liquid acetonitrile, Carbon. 50 (2012) 47–56. doi:10.1016/j.carbon.2011.07.053.
[99] F.M. Devienne, C. Barnabé, G. Ourisson, Synthesis of further biological compounds in interstellar-like conditions, Comptes Rendus Chim. 5 (2002) 651–653. doi:10.1016/S1631-0748(02)01420-0.
[100] M. Iida, Y. Ohshima, Y. Endo, Laboratory detection of HC_9N using a Fourier transform microwave spectrometer, Astrophys. J. 371 (1991) L45. doi:10.1086/185998.
[101] M.C. McCarthy, E.S. Levine, A.J. Apponi, P. Thaddeus, Experimental Structures of the Carbon Chains HC_7N, HC_9N, and $HC_{11}N$ by Isotopic Substitution, J. Mol. Spectrosc. 203 (2000) 75–81. doi:10.1006/jmsp.2000.8149.
[102] H.W. Kroto, J.R. Heath, S.C. Obrien, R.F. Curl, R.E. Smalley, Long carbon chain molecules in circumstellar shells, Astrophys. J. 314 (1987) 352–355. doi:10.1086/165065.

[103] F. Cataldo, Polyynes and Cyanopolyynes: Their Synthesis with the Carbon Arc Gives the Same Abundances Occurring in Carbon-Rich Stars, Orig. Life Evol. Biospheres. 36 (2006) 467–475. doi:10.1007/s11084-006-9051-4.

[104] G. Schermann, T. Grösser, F. Hampel, A. Hirsch, Dicyanopolyynes: A Homologuous Series of End-Capped Linear sp Carbon, Chem. – Eur. J. 3 (1997) 1105–1112. doi:10.1002/chem.19970030718.

[105] G. Forte, L. D'Urso, E. Fazio, S. Patanè, F. Neri, O. Puglisi, G. Compagnini, The effects of liquid environments on the optical properties of linear carbon chains prepared by laser ablation generated plasmas, Appl. Surf. Sci. 272 (2013) 76–81. doi:10.1016/j.apsusc.2012.03.156.

[106] D.E. Woon, E. Herbst, Quantum Chemical Predictions of the Properties of Known and Postulated Neutral Interstellar Molecules, Astrophys. J. Suppl. Ser. 185 (2009) 273. doi:10.1088/0067-0049/185/2/273.

[107] P. Botschwina, M. Horn, Accurate Equilibrium Structure and Electric Dipole Moment of HC_9N: Predictions on the Basis of Large-Scale Coupled Cluster Calculations, J. Mol. Spectrosc. 185 (1997) 191–193. doi:10.1006/jmsp.1997.7399.

[108] P. Thaddeus, M.C. McCarthy, Carbon chains and rings in the laboratory and in space, Spectrochim. Acta. A. Mol. Biomol. Spectrosc. 57 (2001) 757–774. doi:10.1016/S1386-1425(00)00442-X.

[109] R.J. Boyd, W.E. Jones, K.W. Ling, Geometries, energies and polarities of cyanopolyynes, Chem. Phys. 58 (1981) 203–210. doi:10.1016/0301-0104(81)80057-2.

[110] J.Y. Qi, M.D. Chen, W. Wu, Q.E. Zhang, C.T. Au, Parity alternation of interstellar molecules cyanopolyynes HC_nN (n = 1–17), Chem. Phys. 364 (2009) 31–38. doi:10.1016/j.chemphys.2009.08.008.

[111] R.M. Vichietti, R.L.A. Haiduke, The infrared fundamental intensities of some cyanopolyynes, Spectrochim. Acta. A. Mol. Biomol. Spectrosc. 90 (2012) 1–11. doi:10.1016/j.saa.2012.01.005.

[112] R.M. Vichietti, R.L. Haiduke, A theoretical systematic study of a series of isocyanopolyynes., Spectrochim. Acta. A. Mol. Biomol. Spectrosc. 114 (2013) 197–204. doi:10.1016/j.saa.2013.05.066.

[113] R.E. Connors, J.L. Roebber, K. Weiss, Vacuum ultraviolet spectroscopy of cyanogen and cyanoacetylenes, J. Chem. Phys. 60 (1974) 5011–5024. doi:10.1063/1.1681016.

[114] A.M. Smith, G. Schallmoser, A. Thoma, V.E. Bondybey, Infrared spectral evidence of N≡C–C≡C–N≡C: Photoisomerization of N≡C–C≡C–C≡N in an argon matrix, J. Chem. Phys. 98 (1993) 1776–1785. doi:10.1063/1.464266.

[115] C. Crépin, M. Turowski, J. Ceponkus, S. Douin, S. Boyé-Péronne, M. Gronowski, R. Kołos, UV-induced growth of cyanopolyyne chains in cryogenic solids, Phys. Chem. Chem. Phys. PCCP. 13 (2011) 16780–16785. doi:10.1039/c1cp21326a.

[116] M. Turowski, C. Crépin, S. Douin, R. Kołos, Formation and Spectroscopy of Dicyanotriacetylene (NC_8N) in Solid Kr, J. Phys. Chem. A. (2014). doi:10.1021/jp509908z.

[117] J. Agreiter, A.M. Smith, M. Härtle, V.E. Bondybey, Laser-induced fluorescence of matrix-isolated $C_4N_2^+$, Chem. Phys. Lett. 225 (1994) 87–96. doi:10.1016/0009-2614(94)00597-4.

[118] J. Agreiter, A.M. Smith, V.E. Bondybey, Laser-induced fluorescence of matrix-isolated $C_6N_2^+$ and of C8N2+, Chem. Phys. Lett. 241 (1995) 317–327. doi:10.1016/0009-2614(95)00642-H.

[119] J. Sheridan, L.F. Thomas, Microwave Spectrum of Methyl-Cyanoacetylene, Nature. 174 (1954) 798–798. doi:10.1038/174798a0.

[120] A. Moïses, D. Boucher, J. Burie, J. Demaison, A. Dubrulle, Millimeter-wave spectrum of methylcyanoacetylene, J. Mol. Spectrosc. 92 (1982) 497–498. doi:10.1016/0022-2852(82)90118-7.

[121] K.M.T. Yamada, M. Bester, M. Tanimoto, G. Winnewisser, Pure rotational spectrum of cyanopropyne in the v12 = 1 vibrational state, J. Mol. Spectrosc. 126 (1987) 118–128. doi:10.1016/0022-2852(87)90082-8.

[122] M. Bester, M. Tanimoto, B. Vowinkel, G. Winnewisser, K. Yamada, Rotational Spectrum of Methylcyanoacetylene. A New Millimeter Wave Spectrometer, Z. Naturforschung Teil A. 38 (1983) 64.

[123] R. Tubino, G. Dellepiane, G. Zerbi, Vibrational Spectrum and Vibro-Rotational Analysis of Cyanopropyne, J. Chem. Phys. 50 (1969) 621–627. doi:10.1063/1.1671109.

[124] G. Bossis, Le moment dipolaire et l'absorption en infrarouge lointain du cyanopropyne, existence d'une tres forte contribution des dipoles temporaires induits, Mol. Phys. 31 (1976) 1897–1908. doi:10.1080/00268977600101491.

[125] N. Dello Russo, R.K. Khanna, Laboratory Infrared Spectroscopic Studies of Crystalline Nitriles with Relevance to Outer Planetary Systems, Icarus. 123 (1996) 366–395. doi:10.1006/icar.1996.0165.

[126] M. Khlifi, F. Raulin, Infrared intensifies and frequencies of 2-butynenitrfie: Application to the atmosphere of Titan, Spectrochim. Acta Part Mol. Spectrosc. 47 (1991) 171–176. doi:10.1016/0584-8539(91)80088-Z.

[127] F. Cerceau, F. Raulin, R. Courtin, D. Gautier, Infrared spectra of gaseous mononitriles: Application to the atmosphere of Titan, Icarus. 62 (1985) 207–220. doi:10.1016/0019-1035(85)90118-6.

[128] P. Bruston, H. Poncet, F. Raulin, C. Cossart-Magos, R. Courtin, UV spectroscopy of Titan's atmosphere, planetary organic chemistry, and prebiological synthesis: I. Absorption spectra of gaseous propynenitrile and 2-butynenitrile in the 185- to 250-nm region, Icarus. 78 (1989) 38–53. doi:10.1016/0019-1035(89)90068-7.

[129] A. Arnau, I. Tuñón, J. Andrés, E. Silla, Theoretical rotational constants of MeCnN species, Chem. Phys. Lett. 166 (1990) 54–56. doi:10.1016/0009-2614(90)87049-W.

[130] V.A. Basiuk, R. Navarro-González, Y. Benilan, F. Raulin, PM3, AM1, MINDO3 semi-empirical IR spectra simulations for some nitriles of interest for Titan's chemistry, Spectrochim. Acta. A. Mol. Biomol. Spectrosc. 56 (2000) 1157–1165. doi:10.1016/S1386-1425(99)00214-0.

[131] G. Bieri, E. Heilbronner, V. Hornung, E. Kloster-Jensen, J.P. Maier, F. Thommen, W. von Niessen, Electronic states of substituted haloacetylene and cyanoacetylene radical cations, Chem. Phys. 36 (1979) 1–14. doi:10.1016/0301-0104(79)85099-5.

[132] N. Lamarre, B. Gans, L.A. Vieira Mendes, M. Gronowski, J.-C. Guillemin, N. De Oliveira, S. Douin, M. Chevalier, C. Crépin, R. Kołos, S. Boyé-Péronne, Excited electronic structure of methylcyanoacetylene probed by VUV Fourier-transform absorption spectroscopy, J. Quant. Spectrosc. Radiat. Transf. 182 (2016) 286–295. doi:10.1016/j.jqsrt.2016.06.020.

[133] H.-G. Cho, L. Andrews, Matrix infrared spectra and density functional calculations of the H_2CCN and H_2CNC radicals produced from CH_3CN, J. Phys. Chem. A. 115 (2011) 8638–8642. doi:10.1021/jp204887y.

[134] H.-G. Cho, Matrix Infrared Spectra and DFT Computations of CH_2CNH and CH_2NCH Produced from CH_3CN by Laser-Ablation Plume Radiation, Bull. Korean Chem. Soc. 34 (2013) 1361–1365. doi:10.5012/bkcs.2013.34.5.1361.

[135] H. Bürger, D. Lentz, B. Meisner, N. Nickelt, D. Preugschat, M. Senzlober, Syntheses and 1H-, 13C- and ^{15}N-NMR Spectra of Ethynyl Isocyanide, H−C≡C−N≡C, D−C≡C−N≡C and Prop-1-ynyl Isocyanide, $H_3C−C≡C−N≡C$, $D_3C−C≡C−N≡C$: High Resolution Infrared Spectrum of Prop-1-ynyl Isocyanide, Chem. – Eur. J. 6 (2000) 3377–3385. doi:10.1002/1521-3765(20000915)6:18<3377::AID-CHEM3377>3.0.CO;2-1.

[136] G.S. Reddy, L. Mandell, J.H. Goldstein, Synthesis and Proton Magnetic Resonance Spectrum of Propargyl Cyanide, J. Am. Chem. Soc. 83 (1961) 4729–4731. doi:10.1021/ja01484a009.

[137] A.V. Golovin, V.V. Takhistov, Thermochemistry of organic and heteroorganic species. Part XII. Mono- and disubstituted acetylenes and ethynyl free radicals. New electronegativity scale, J. Mol. Struct. 701 (2004) 57–91. doi:10.1016/j.molstruc.2004.01.022.

[138] S. Rayne, K. Forest, Thermochemistry of mono- and disubstituted acetylenes and polyynes at the Gaussian-4 level of theory, Comput. Theor. Chem. 970 (2011) 15–22. doi:10.1016/j.comptc.2011.05.018.

[139] E. Haruki, Y. Hirai, E. Imoto, Syntheses of Some Substituted Heterocyclic Compounds from Propargyl Cyanide and Methylpropargyl Cyanide, Bull. Chem. Soc. Jpn. 41 (1968) 267–267. doi:10.1246/bcsj.41.267.

[140] A. Bouchy, J. Demaison, G. Roussy, J. Barriol, Microwave spectrum of cyanoallene, J. Mol. Struct. 18 (1973) 211–217. doi:10.1016/0022-2860(73)85223-8.

[141] H. Møllendal, S. Samdal, A. Matrane, J.-C. Guillemin, Synthesis, Microwave Spectrum, and Dipole Moment of Allenylisocyanide ($H_2C═C═CHNC$), a Compound of Potential Astrochemical Interest, J. Phys. Chem. A. 115 (2011) 7978–7983. doi:10.1021/jp204296n.

[142] A. Benidar, D. Bégué, F. Richter, C. Pouchan, M. Lahcini, J.-C. Guillemin, Gas-Phase Infrared Spectra of Three Compounds of Astrochemical Interest: Vinyl, Allenyl, and Propargyl Isocyanides, ChemPhysChem. 16 (2015) 848–854. doi:10.1002/cphc.201402712.

[143] V. Moliner, J. Andrés, A. Arnau, E. Silla, I. Tuñón, Rotational constants and dipole moments of interstellar polyynes: a comparative MP2 and density functional (BP86) study, Chem. Phys. 206 (1996) 57–61. doi:10.1016/0301-0104(96)00007-9.

[144] M.M. Montero-Campillo, O. Mó, M. Yáñez, A. Benidar, C. Rouxel, N. Kerisit, Y. Trolez, J.-C. Guillemin, Gas-Phase Infrared Spectroscopy of Substituted Cyanobutadiynes: Roles of the Bromine Atom and Methyl Group as Substituents, ChemPhysChem. 17 (2016) 1018–1024. doi:10.1002/cphc.201501153.

[145] A.J. Alexander, H.W. Kroto, M. Maier, D.R.M. Walton, The microwave spectra of symmetric top polyacetylenes, J. Mol. Spectrosc. 70 (1978) 84–94. doi:10.1016/0022-2852(78)90011-5.

[146] W. Chen, J.-U. Grabow, M.J. Travers, M.R. Munrow, S.E. Novick, M.C. McCarthy, P. Thaddeus, Microwave Spectra of the Methylcyanopolyynes $CH_3(CC)_nCN$, n= 2, 3, 4, 5, J. Mol. Spectrosc. 192 (1998) 1–11. doi:10.1006/jmsp.1998.7665.

[147] F. Bohlmann, H.-J. Mannhardt, Polyacetylenverbindungen, XVIII. Mitteil.: Über die Lichtabsorption von Polyin-Carbonsäurenitrilen, Chem. Ber. 89 (1956) 2268–2272. doi:10.1002/cber.19560891009.

[148] A. Arnau, I. Tuñón, J. Andrés, E. Silla, Theoretical rotational constants of MeC_nN species, Chem. Phys. Lett. 166 (1990) 54–56. doi:10.1016/0009-2614(90)87049-W.
[149] M.C. McCarthy, W. Chen, M.J. Travers, P. Thaddeus, Microwave Spectra of 11 Polyyne Carbon Chains, Astrophys. J. Suppl. Ser. 129 (2000) 611. doi:10.1086/313428.
[150] N. Kerisit, L. Toupet, Y. Trolez, J.-C. Guillemin, Methylcyanobutadiyne: Synthesis, X-ray Structure and Photochemistry; Towards an Explanation of Its Formation in the Interstellar Medium, Chem. – Eur. J. 19 (2013) 17683–17686. doi:10.1002/chem.201303377.
[151] M. Grutter, M. Wyss, J.P. Maier, Electronic absorption spectra of $C_{2n}H^-$,$C_{2n-1}N^-$ (n=4–7), and $C_{2n-1}N$ (n=3–7) chains in neon matrices, J. Chem. Phys. 110 (1999) 1492–1496. doi:10.1063/1.478022.
[152] E.C. Stanca-Kaposta, F. Schwaneberg, M.R. Fagiani, T. Wende, F. Hagemann, A. Wünschmann, L. Wöste, K.R. Asmis, Infrared Photodissociation Spectroscopy of $C_{2n+1}N^-$ Anions with n = 1 – 5, Z. Für Phys. Chem. 228 (2014) 351–367. doi:10.1515/zpch-2014-0507.
[153] T.A. Yen, E. Garand, A.T. Shreve, D.M. Neumark, Anion photoelectron spectroscopy of C_3N^- and C_5N^-, J. Phys. Chem. A. 114 (2010) 3215–3220. doi:10.1021/jp9093996.
[154] J. Žabka, I. Ndiaye, C. Alcaraz, C. Romanzin, M. Polášek, Experimental and theoretical study of the mechanism of formation of astrochemically important $C_{2n+1}N^-$ anions via ion/molecule reactions, Int. J. Mass Spectrom. 367 (2014) 1–9. doi:10.1016/j.ijms.2014.04.008.
[155] C. Romanzin, E. Louarn, J. Lemaire, J. Žabka, M. Polášek, J.-C. Guillemin, C. Alcaraz, An experimental study of the reactivity of CN^- and C_3N^- anions with cyanoacetylene (HC_3N), Icarus. 268 (2016) 242–252. doi:10.1016/j.icarus.2015.12.001.
[156] A. Coupeaud, R. Kołos, I. Couturier-Tamburelli, J.P. Aycard, N. Piétri, Photochemical Synthesis of the Cyanodiacetylene HC_5N: A Cryogenic Matrix Experiment, J. Phys. Chem. A. 110 (2006) 2371–2377. doi:10.1021/jp055582r.
[157] I. Couturier-Tamburelli, N. Piétri, C. Crépin, M. Turowski, J.-C. Guillemin, R. Kołos, Synthesis and spectroscopy of cyanotriacetylene (HC_7N) in solid argon, J. Chem. Phys. 140 (2014) 044329. doi:10.1063/1.4861038.
[158] R.I. Kaiser, Experimental Investigation on the Formation of Carbon-Bearing Molecules in the Interstellar Medium via Neutral−Neutral Reactions, Chem. Rev. 102 (2002) 1309–1358. doi:10.1021/cr970004v.
[159] I.W.M. Smith, Reactions at Very Low Temperatures: Gas Kinetics at a New Frontier, Angew. Chem. Int. Ed. 45 (2006) 2842–2861. doi:10.1002/anie.200502747.
[160] S. Douin, M. Gronowski, N. Lamarre, V.-T. Phung, S. Boyé-Péronne, C. Crépin, R. Kołos, Cavity Ring Down Spectroscopy Measurements for High-Overtone Vibrational Bands of HC_3N, J. Phys. Chem. A. 119 (2015) 9494–9505. doi:10.1021/acs.jpca.5b05884.
[161] C. Delpech, J.C. Guillemin, P. Paillous, M. Khlifi, P. Bruston, F. Raulin, Infrared spectra of triacetylene in the 4000-220 cm^{-1} region: Absolute band intensity and implications for the atmosphere of Titan, Spectrochim. Acta Part Mol. Spectrosc. 50 (1994) 1095–1100. doi:10.1016/0584-8539(94)80031-6.
[162] F. Shindo, Y. Bénilan, P. Chaquin, J.-C. Guillemin, A. Jolly, F. Raulin, IR Spectrum of C_8H_2: Integrated Band Intensities and Some Observational Implications, J. Mol. Spectrosc. 210 (2001) 191–195. doi:10.1006/jmsp.2001.8459.
[163] G.N. Lewis, D. Lipkin, Reversible Photochemical Processes in Rigid Media: The Dissociation of Organic Molecules into Radicals and Ions, J. Am. Chem. Soc. 64 (1942) 2801–2808. doi:10.1021/ja01264a025.
[164] E. Whittle, D.A. Dows, G.C. Pimentel, Matrix Isolation Method for the Experimental Study of Unstable Species, J. Chem. Phys. 22 (1954) 1943–1943. doi:10.1063/1.1739957.
[165] R.N. Perutz, Chapter 6. Matrix isolation, Annu. Rep. Prog. Chem., Sect. C: Phys. Chem. 82 (1985) 157–191. doi:10.1039/PC9858200157.
[166] D.E. Jennings, K. Fox, Rotational temperatures of cyanodiacetylene in Sagittarius B2, TMC-1, and IRC +10216, Astrophys. J. 254 (1982) 111–115. doi:10.1086/159712.
[167] I.R. Dunkin, Matrix Isolation Techniques. A Practical Approach, Oxford University Press, New York, 1998. https://global.oup.com/academic/product/matrix-isolation-techniques-9780198558637 (accessed January 3, 2017).
[168] L. Khriachtchev, Physics and Chemistry at Low Temperatures, Pan Stanford Publishing, 2011.
[169] J.E.D. Davies, The effect of phase and pressure changes on vibrational spectra, J. Mol. Struct. 10 (1971) 1–30. doi:10.1016/0022-2860(71)87057-6.
[170] M. Ito, Raman Spectra of Polycrystalline Methylene Halides, J. Chem. Phys. 42 (1965) 391–394. doi:10.1063/1.1695704.
[171] J.R. Ferraro, S.S. Mitra, C. Postmus, The far infrared spectra of solids under high pressure (33–100 μ), Inorg. Nucl. Chem. Lett. 2 (1966) 269–275. doi:10.1016/0020-1650(66)80059-4.

[172] M.A. Morgan, G.C. Pimentel, The external heavy atom effect: photophysics of (dimethylamino)benzonitrile in cryogenic rare gas matrixes, J. Phys. Chem. 93 (1989) 3056–3062. doi:10.1021/j100345a037.
[173] N. Lamarre, C. Falvo, C. Alcaraz, B. Cunha de Miranda, S. Douin, A. Flütsch, C. Romanzin, J.-C. Guillemin, S. Boyé-Péronne, B. Gans, Photoionization spectroscopy of CH_3C_3N in the vacuum-ultraviolet range, J. Mol. Spectrosc. (2015). doi:10.1016/j.jms.2015.03.005.
[174] A. Chrostowska, A. Matrane, D. Maki, S. Khayar, H. Ushiki, A. Graciaa, L. Belachemi, J.-C. Guillemin, Are Unsaturated Isocyanides so Different from the Corresponding Nitriles?, ChemPhysChem. 13 (2012) 226–236. doi:10.1002/cphc.201100672.
[175] Y. Trolez, J.-C. Guillemin, Synthesis and Characterization of 2,4-Pentadiynenitrile—A Key Compound in Space Science, Angew. Chem. Int. Ed. 44 (2005) 7224–7226. doi:10.1002/anie.200502122.
[176] M. Khlifi, P. Paillous, C. Delpech, M. Nishio, P. Bruston, F. Raulin, Absolute IR band intensities of diacetylene in the 250 - 4300 cm^{-1} region: implications for Titan's atmosphere., J. Mol. Spectrosc. 174 (1995) 116–122. doi:10.1006/jmsp.1995.1273.
[177] Cryocooler Principle of Operation | ARS. http://www.arscryo.com/tech-notes/cryocooler-principle-of-operation.html (accessed January 28, 2017).
[178] Guide for Infrared Spectroscopy. http://www.ccmr.cornell.edu/wp-content/uploads/sites/2/2015/11/GuideforInfraredspectroscopy.pdf (accessed January 29, 2017).
[179] Quartz Crystal (SiO2) Optical Material. https://www.crystran.co.uk/optical-materials/quartz-crystal-sio2 (accessed January 29, 2017).
[180] A. Gutiérrez Quintanilla, PhD Thesis. Molecules and complexes with hydrogen bond: solvation and photoreactivity in cryogenic matrices, 2016.
[181] R.G. Parr, Y. Weitao, Density-Functional Theory of Atoms and Molecules, Oxford University Press, 1989.
[182] A.D. Becke, Density-functional thermochemistry. III. The role of exact exchange, J. Chem. Phys. 98 (1993) 5648–5652. doi:10.1063/1.464913.
[183] C. Lee, W. Yang, R.G. Parr, Development of the Colle-Salvetti correlation-energy formula into a functional of the electron density, Phys. Rev. B. 37 (1988) 785–789. doi:10.1103/PhysRevB.37.785.
[184] J.P. Perdew, J.A. Chevary, S.H. Vosko, K.A. Jackson, M.R. Pederson, D.J. Singh, C. Fiolhais, Atoms, molecules, solids, and surfaces: Applications of the generalized gradient approximation for exchange and correlation, Phys. Rev. B. 46 (1992) 6671–6687. doi:10.1103/PhysRevB.46.6671.
[185] J.P. Perdew, J.A. Chevary, S.H. Vosko, K.A. Jackson, M.R. Pederson, D.J. Singh, C. Fiolhais, Erratum: Atoms, molecules, solids, and surfaces: Applications of the generalized gradient approximation for exchange and correlation, Phys. Rev. B. 48 (1993) 4978–4978. doi:10.1103/PhysRevB.48.4978.2.
[186] T.H.J. Dunning, Gaussian basis sets for use in correlated molecular calculations. I. The atoms boron through neon and hydrogen, J. Chem. Phys. 90 (1989) 1007–1023. doi:10.1063/1.456153.
[187] D.E. Woon, T.H. Dunning Jr., Gaussian basis sets for use in correlated molecular calculations. III. The atoms aluminum through argon, J. Chem. Phys. 98 (1993) 1358–1371. doi:10.1063/1.464303.
[188] M. Gronowski, R. Kołos, Isomers of cyanodiacetylene: Predictions for the rotational, infrared and Raman spectroscopy, J. Mol. Struct. 834–836 (2007) 102–108. doi:10.1016/j.molstruc.2006.10.003.
[189] M. Gronowski, PhD Thesis. "Teoria i eksperyment w badaniach spektroskopii wybranych nitryli o znaczeniu astrochemicznym oraz cząsteczek pokrewnych," Instytut Chemii Fizycznej PAN, Warsaw, 2011.
[190] T. Yanai, D.P. Tew, N.C. Handy, A new hybrid exchange–correlation functional using the Coulomb-attenuating method (CAM-B3LYP), Chem. Phys. Lett. 393 (2004) 51–57. doi:10.1016/j.cplett.2004.06.011.
[191] A long-range-corrected time-dependent density functional theory, J. Chem. Phys. 120 (2004) 8425–8433. doi:10.1063/1.1688752.
[192] M. Gronowski, unpublished results, private communication, (2013-2017).
[193] T. Custer, **U. Szczepaniak**, M. Gronowski, E. Fabisiewicz, I. Couturier-Tamburelli, R. Kołos, Density Functional Exploration of C_4H_3N Isomers, J. Phys. Chem. A. 120 (2016) 5928–5938. doi:10.1021/acs.jpca.6b03922.
[194] M.J. Frisch, G.W. Trucks, H.B. Schlegel, G.E. Scuseria, M.A. Robb, J.R. Cheeseman, G. Scalmani, V. Barone, B. Mennucci, G.A. Petersson, Gaussian 09, Gaussian, Inc., Wallingford CT, 2009., n.d.
[195] B.P. BOTSCHWINA, M. HORN, K.M. OSWALD, R., Coupled cluster calculations for HC_7N, HC_7NH^+ and C_7N, molecules of interest to astrochemistry, Mol. Phys. 92 (1997) 381–392. doi:10.1080/002689797170112.

[196] **U. Szczepaniak**, M. Turowski, T. Custer, M. Gronowski, N. Kerisit, Y. Trolez, R. Kołos, Infrared and Raman Spectroscopy of Methylcyanodiacetylene (CH_3C_5N), ChemPhysChem 17 (2016) 3047–3054. doi:10.1002/cphc.201600437.
[197] M. Turowski, **U. Szczepaniak**, T. Custer, M. Gronowski, R. Kołos, Electronic Spectroscopy of Methylcyanodiacetylene (CH_3C_5N), ChemPhysChem 17 (2016) 4068–4078. doi:10.1002/cphc.201600949.
[198] T. Custer, unpublished results, private communication, (2013-2017).
[199] N. Piétri, private communication, (2016).
[200] R. Kołos, J.C. Dobrowolski, HCNCC – the possible isomer of cyanoacetylene, Chem. Phys. Lett. 369 (2003) 75–79. doi:10.1016/S0009-2614(02)01982-6.
[201] T. Shimanouchi, Tables of Molecular Vibrational Frequencies, National Bureau of Standards, 1972.
[202] N.F. Henfrey, B.A. Thrush, A high-resolution study of the ν7 band of propyne, J. Mol. Spectrosc. 113 (1985) 426–450. doi:10.1016/0022-2852(85)90280-2.
[203] C. Crépin, private communication, (2012-2017).
[204] R. Hattori, E. Suzuki, K. Shimizu, FTIR studies of the CH_3CN–BF_3 complex in solid Ar, N_2, and Xe: Matrix effects on vibrational spectra, J. Mol. Struct. 750 (2005) 123–134. doi:10.1016/j.molstruc.2005.04.016.
[205] N. Gupta, Dispersion of Phonons in Ideal Crystals, Aust. J. Phys. 22 (1969) 471–480.
[206] H.-J. Haink, M. Jungen, Excited states of the polyacetylenes. Analysis of the near ultraviolet spectra of diacetylene and triacetylene, Chem. Phys. Lett. 61 (1979) 319–322. doi:10.1016/0009-2614(79)80652-1.
[207] F.A. Miller, R.B. Hannan Jr., The ultraviolet absorption spectrum of dicyanoacetylene, Spectrochim. Acta. 12 (1958) 321–331. doi:10.1016/0371-1951(58)80058-2.
[208] H.D. McSwiney Jr., J.A. Merritt, 3100-Å Electronic Absorption of Dicyanodiacetylene, J. Chem. Phys. 52 (1970) 5184–5186. doi:10.1063/1.1672758.
[209] M.W. Roberts, J.M. Thomas, Surface and Defect Properties of Solids, The Royal Society of Chemistry, 1972. doi:10.1039/9781847556943.
[210] A. Galli, P. Harteck, R.R. Reeves, Preliminary study of the photochemistry of propyne with 2062-A. iodine line, J. Phys. Chem. 71 (1967) 2719–2721. doi:10.1021/j100867a050.
[211] L.J. Stief, V.J. De Carlo, W.A. Payne, Photolysis of Propyne at 1470 Å, J. Chem. Phys. 54 (1971) 1913. doi:10.1063/1.1675118.
[212] M.E. Jacox, D.E. Milligan, Matrix isolation study of the vacuum ultraviolet photolysis of allene and methylacetylene. Vibrational and electronic spectra of the species C_3, C_3H, C_3H_2, and C_3H_3, Chem. Phys. 4 (1974) 45–61. doi:10.1016/0301-0104(74)80047-9.
[213] K. Alnama, S. Boyé-Péronne, S. Douin, F. Innocenti, J. O'Reilly, A.-L. Roche, N. Shafizadeh, L. Zuin, D. Gauyacq, Photolysis of allene and propyne in the 7–30eV region probed by the visible fluorescence of their fragments, J. Chem. Phys. 126 (2007) 044304. doi:10.1063/1.2430707.
[214] D.B. Atkinson, J.W. Hudgens, Rate Coefficients for the Propargyl Radical Self-Reaction and Oxygen Addition Reaction Measured Using Ultraviolet Cavity Ring-down Spectroscopy, J. Phys. Chem. A. 103 (1999) 4242–4252. doi:10.1021/jp990468s.
[215] J.D. DeSain, C.A. Taatjes, Infrared Laser Absorption Measurements of the Kinetics of Propargyl Radical Self-Reaction and the 193 nm Photolysis of Propyne, J. Phys. Chem. A. 107 (2003) 4843–4850. doi:10.1021/jp034047t.
[216] A. Fahr, A.H. Laufer, UV-Absorption Spectra of the Radical Transients Generated from the 193-nm Photolysis of Allene, Propyne, and 2-Butyne, J. Phys. Chem. A. 109 (2005) 2534–2539. doi:10.1021/jp0406058.
[217] M. Turowski, PhD Thesis. "Niskotemperaturowe badania fotochemii i spektroskopii cyjanoacetylenów o znaczeniu astrofizycznym," Instytut Chemii Fizycznej PAN, Warsaw, 2012.
[218] F. Cataldo, Monocyanopolyynes from a carbon arc in ammonia: about the relative abundance of polyynes series formed in a carbon arc and those detected in the circumstellar shells of AGB stars, Int. J. Astrobiol. 5 (2006) 37–45. doi:10.1017/S1473550406002837.
[219] V.I. Baranov, L.A. Gribov, B.K. Novosadov, Calculation of vibronic spectra of polyatomic molecules in the Franck—Condon and Herzberg—Teller approximations, J. Mol. Struct. 70 (1981) 1–29. doi:10.1016/0022-2860(81)80089-0.
[220] V.I. Baranov, L.A. Gribov, Calculation of vibronic spectra of polyatomic molecules in the Franck—Condon and Herzberg—Teller approximations, J. Mol. Struct. 70 (1981) 31–47. doi:10.1016/0022-2860(81)80090-7.
[221] B.D. Anderson, C.M. Gordon, The Laser Synthesis of Linear Polyynes: The Particle in a Box Revisited, J. Chem. Educ. 85 (2008) 1279. doi:10.1021/ed085p1279.
[222] M. Turowski, unpublished results, private communication, (2013).

[223] F. Cataldo, Polyynes: a new class of carbon allotropes. About the formation of dicyanopolyynes from an electric arc between graphite electrodes in liquid nitrogen, Polyhedron. 23 (2004) 1889–1896. doi:10.1016/j.poly.2004.04.024.
[224] M. Turowski, C. Crépin, I. Couturier-Tamburelli, N. Piétri, R. Kołos, Low-temperature phosphorescence of dicyanoacetylene in rare gas solids, Low Temp. Phys. 38 (2012) 723–726. doi:10.1063/1.4745884.
[225] P. Botschwina, R. Oswald, Carbon chains of type $C_{2n+1}N^-$ (n=2–6): A theoretical study of potential interstellar anions, J. Chem. Phys. 129 (2008) 044305. doi:10.1063/1.2949093.
[226] J.P. Maier, Electronic Spectroscopy of Carbon Chains, J. Phys. Chem. A. 102 (1998) 3462–3469. doi:10.1021/jp9807219.
[227] G.N. Lewis, M. Calvin, The Color of Organic Substances., Chem. Rev. 25 (1939) 273–328. doi:10.1021/cr60081a004.
[228] R. Kołos, private communication, unpublished results, (2012-2017).
[229] N. Piétri, A. Coupeaud, J.-P. Aycard, I. Couturier-Tamburelli, Cyanoacetylenic complexes as pre-reactional species leading to the HC_7N synthesis. Part I: Experimental and theoretical identification of the HC3N:C4H2 complexes, Chem. Phys. 358 (2009) 7–12. doi:10.1016/j.chemphys.2008.11.027.
[230] I. Couturier-Tamburelli, B. Sessouma, A. Coupeaud, J.-P. Aycard, N. Piétri, Cyanoacetylenic complexes as pre-reactional species leading to the HC7N synthesis. Part II: Experimental and theoretical identifications of the HC_5N:C_2H_2 complex, Chem. Phys. 358 (2009) 13–20. doi:10.1016/j.chemphys.2008.11.020.
[231] A.J. Al-Edhari, C. Ceccarelli, C. Kahane, S. Viti, N. Balucani, E. Caux, A. Faure, B. Lefloch, F. Lique, E. Mendoza, D. Quenard, L. Wiesenfeld, History of the solar-type protostar IRAS 16293–2422 as told by the cyanopolyynes, Astron. Astrophys. 597 (2017) A40. doi:10.1051/0004-6361/201629506.
[232] A. Penzkofer, Phosphorescence quantum yield determination with time-gated fluorimeter and Tb(III)-acetylacetonate as luminescence reference, Chem. Phys. 415 (2013) 173–178. doi:10.1016/j.chemphys.2013.01.017.

APPENDIX 1. New bands of cyanodiacetylene phosphorescence

HC_5N was used as one of the precursor molecules for photochemical synthesis of long polyynic chains (Chapter 4). During the spectroscopic characterization of samples, HC_5N phosphorescence was observed. While this phosphorescence was studied earlier [91], a number of new bands were detected during our experiments. Several vibrational modes exhibit prominent progressions suggesting a strong vibronic coupling in this molecule.

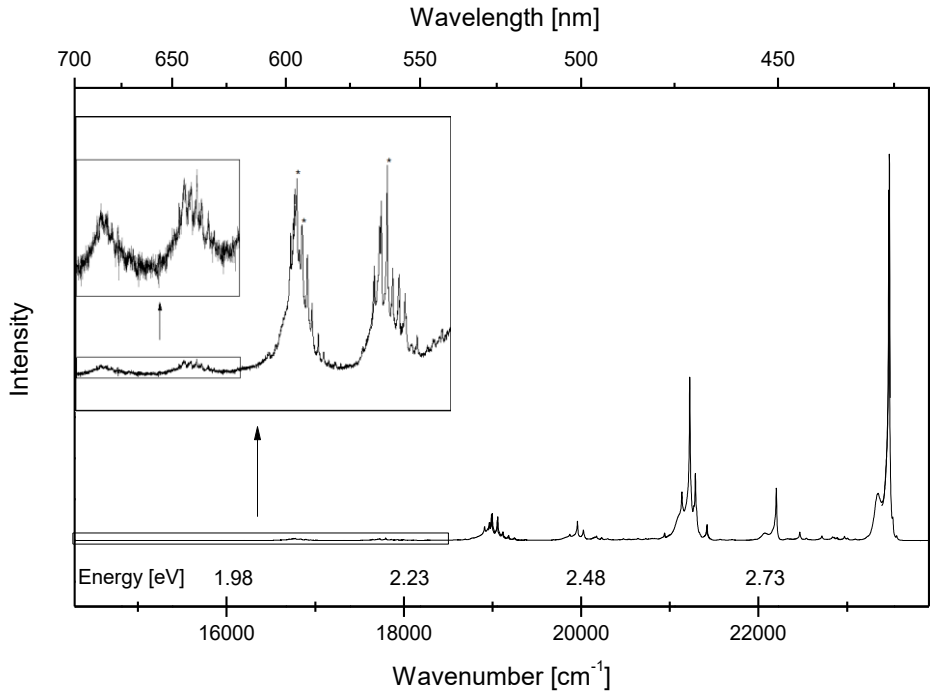

Figure 52. HC_5N phosphorescence observed from $Kr/HC_5N/CH_3C_2H$, excited with 284.8 nm (35 112 cm^{-1}, 4.35 eV). Inset marks the new bands, whose details are seen in Figure 53.

The phosphorescence spectrum of HC_5N (generated from a $Kr/CH_3C_2H/HC_5N$ sample mixture, Figure 52) is characterized by several distinct groups of bands. These 'packets' (spaced by 1000-1200 cm^{-1}) formed two principal vibronic progressions, each of them with spacing of 2000-2200 cm^{-1}. They are governed by the modes ν_2 (strong), ν_3 (strong), ν_4 (medium), and $2\nu_5$ (strong). These modes combine with other modes and, as new combinations appear, the vibronic pattern observed within consecutive packets is not necessarily conserved. There are also bands separated from the main progression by approximately 1200 cm^{-1} and which come from the combination with $2\nu_7$. The assignment of these new bands was greatly facilitated using previously published vibronic patterns (or lack thereof) and combination mode wavenumbers [91].

The two newly detected packets of bands (weak or very weak when compared to the previously reported, higher wavenumber groups) are shown in more detail in Figure 53, while their positions and assignments are listed in Table 35. The band positions might be of use for anharmonic constants calculations.

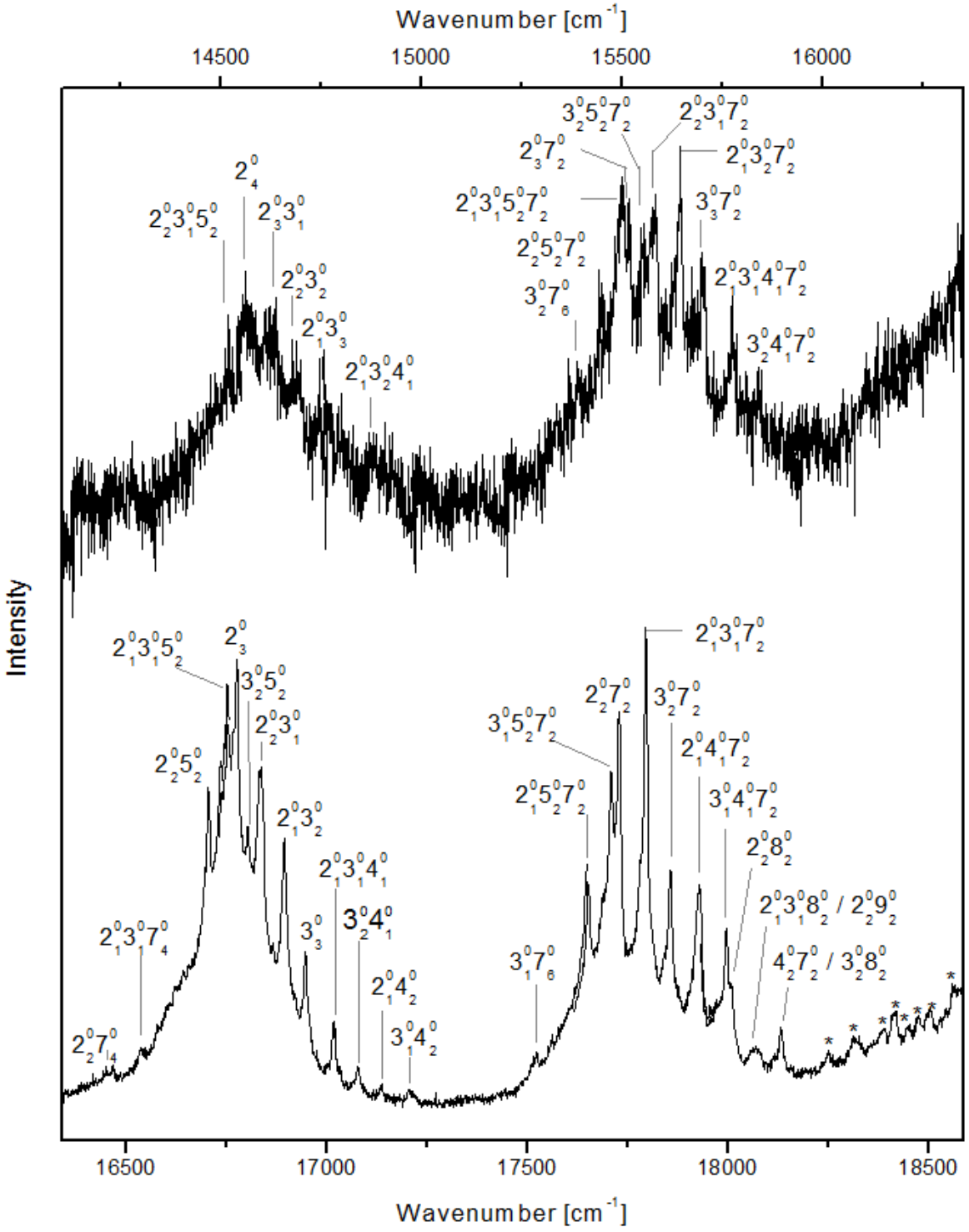

Figure 53. Part of HC_5N phosphorescence spectrum with assignment of the peaks. Note two different scales for upper and lower panel.

Table 35. Newly detected HC_5N phosphorescence bands, observed from the $Kr/HC_5N/CH_3C_2H$ sample. Thick lines separate each packet. Two last packets are characterized by much lower S/N, thus the positions are less certain. Relative wavenumber in relation to $\tilde{a} - \tilde{X}$ origin at 23 476 cm^{-1}.

Wavelength [nm]	Wavenumber [cm^{-1}]	Relative wavenumber [cm^{-1}]	Assignment
507.9	19 687	3 789	7^0_6
538.8	18 560	4 916	$2^0_1 3^0_1 8^0_1$
540.4	18 505	4 971	$2^0_2 8^0_1$
541.3	18 475	5 001	$3^0_1 5^0_2 8^0_1$ / $3^0_2 7^0_1$
542.0	18 449	5 027	7^0_8 / $2^0_1 3^0_1 8^0_1 11^0_1$
543.0	18 415	5 061	$2^0_1 5^0_2 8^0_1$ / $2^0_1 3^0_1 7^0_1$
543.8	18 388	5 088	$2^0_2 8^0_1 11^0_1$
545.9	18 319	5 157	$2^0_1 3^0_1 8^0_1 10^0_1$
548.0	18 249	5 227	$3^0_1 4^0_1 8^0_2$ / $2^0_1 4^0_1 9^0_2$ / $2^0_2 8^0_1 10^0_1$
551.5	18 133	5 343	$4^0_2 7^0_2$ [a] /$3^0_2 8^0_2$
553.4	18 070	5 406	$2^0_1 3^0_1 8^0_2$ / $2^0_2 9^0_2$
555.3	18 008	5 468	$2^0_2 8^0_2$
555.7	17 997	5 479	$3^0_1 4^0_1 7^0_2$
557.8	17 928	5 548	$2^0_1 4^0_1 7^0_2$
560.0	17 857	5 619	$3^0_2 7^0_2$
561.9	17 796	5 680	$2^0_1 3^0_1 7^0_2$
564.1	17 729	5 747	$2^0_2 7^0_2$
564.7	17 709	5 767	$3^0_1 5^0_2 7^0_2$
566.6	17 651	5 825	$2^0_1 5^0_2 7^0_2$
570.7	17 522	5 954	$3^0_1 7^0_6$
581.3	17 204	6 272	$3^0_1 4^0_2$
583.5	17 137	6 339	$2^0_1 4^0_2$
585.6	17 076	6 400	$3^0_2 4^0_1$
587.6	17 017	6 459	$2^0_1 3^0_1 4^0_1$
590.1	16 947	6 529	3^0_3
591.9	16 894	6 582	$2^0_1 3^0_2$
594.0	16 834	6 642	$2^0_2 3^0_1$
595.1	16 803	6 673	$3^0_2 5^0_2$
596.1	16 777	6 699	2^0_3
596.9	16 754	6 722	$2^0_1 3^0_1 5^0_2$
598.6	16 705	6 771	$2^0_2 5^0_2$
604.8	16 536	6 940	$2^0_1 3^0_1 7^0_4$ [a]
607.9	16 451	7 025	$2^0_2 7^0_4$
631.2	15 842	7 634	$3^0_2 4^0_1 7^0_2$
633.9	15 776	7 700	$2^0_1 3^0_1 4^0_1 7^0_2$
637.0	15 699	7 777	$3^0_3 7^0_2$
639.2	15 644	7 832	$2^0_1 3^0_2 7^0_2$
641.7	15 584	7 892	$2^0_2 3^0_1 7^0_2$
643.0	15 553	7 923	$3^0_2 5^0_2 7^0_2$
644.4	15 519	7 957	$2^0_3 7^0_2$
645.2	15 499	7 977	$2^0_1 3^0_1 5^0_2 7^0_2$
647.3	15 449	8 027	$2^0_2 5^0_2 7^0_2$
649.8	15 389	8 087	$3^0_2 7^0_6$ [b]
672.0	14 880	8 596	$2^0_1 3^0_2 4^0_1$
677.7	14 757	8 719	$2^0_1 3^0_3$
680.8	14 688	8 788	$2^0_2 3^0_2$
683.9	14 622	8 854	$2^0_3 3^0_1$ [c]
686.7	14 563	8 913	2^0_4
688.8	14 517	8 959	$2^0_2 3^0_1 5^0_2$

[a] Tentative.

[b] Tentative, as $2^0_1 7^0_6$ is not observed (and no atypical anharmonicity was expected based on Refs. [90] and [91]).

[c] Possibly overlapping the $3^0_3 5^0_2$ band.

To additionally confirm the attribution of the more intense packets of bands to HC_5N, measurements of phosphorescence lifetime were carried out. Similar measurements were precluded for the weaker bands as the signal to noise was too large. The lifetime was measured for phosphorescence detected at 425.8 nm (undoubtedly coming from HC_5N), 561.6 nm, 593.4 nm and 595.6 nm, yielding the lifetimes of 54 ms, 54 ms, 52 ms and 51 ms, respectively. These lifetimes are similar to the value of "*ca.* 40 ms" reported in Turowski *et al*. [91].

APPENDIX 2. The vibrational modes of interesting molecules

This appendix gathers together visualizations of vibrations in the ground and select excited electronic states of the molecules of interest. The symmetry of the vibrational modes refers to the ground electronic states. Respective modes in excited singlet electronic states share common pattern of atom displacements.

Table 36. HC_7N vibrations in the ground and select excited states [192], wavenumbers ($\bar{\nu}$) in cm^{-1}.

Mode	State $\bar{\nu}$	Visualization
	σ symmetry	
ν_1	$\tilde{X}$ 3324	
	$\tilde{B}$ 3316	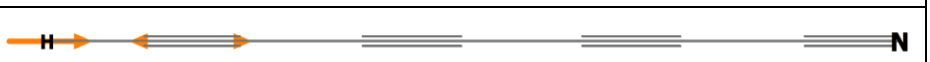
	$\tilde{E}$ 3290	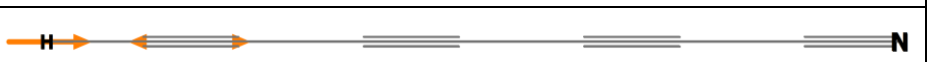
ν_2	$\tilde{X}$ 2253	
	$\tilde{B}$ 2033	
	$\tilde{E}$ 2172	
ν_3	$\tilde{X}$ 2197	
	$\tilde{B}$ 2117	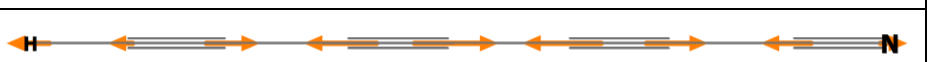
	$\tilde{E}$ 2073	
ν_4	$\tilde{X}$ 2154	
	$\tilde{B}$ 1907	
	$\tilde{E}$ 1949	
ν_5	$\tilde{X}$ 2049	
	$\tilde{B}$ 1819	
	$\tilde{E}$ 1855	
ν_6	$\tilde{X}$ 1295	
	$\tilde{B}$ 1393	
	$\tilde{E}$ 1252	
ν_7	$\tilde{X}$ 902	
	$\tilde{B}$ 926	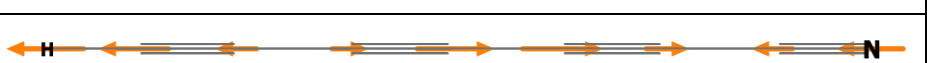
	$\tilde{E}$ 884	

ν_8	$\tilde{X}$ 464	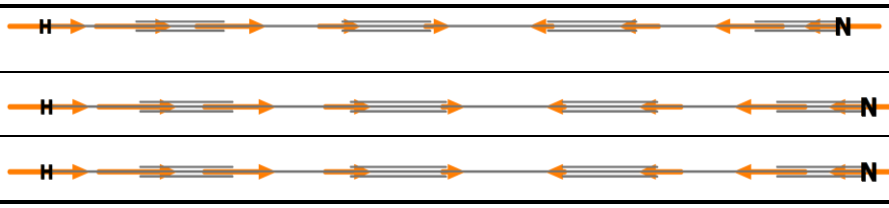
	$\tilde{B}$ 477	
	$\tilde{E}$ 456	
π symmetry		
ν_9	$\tilde{X}$ 643	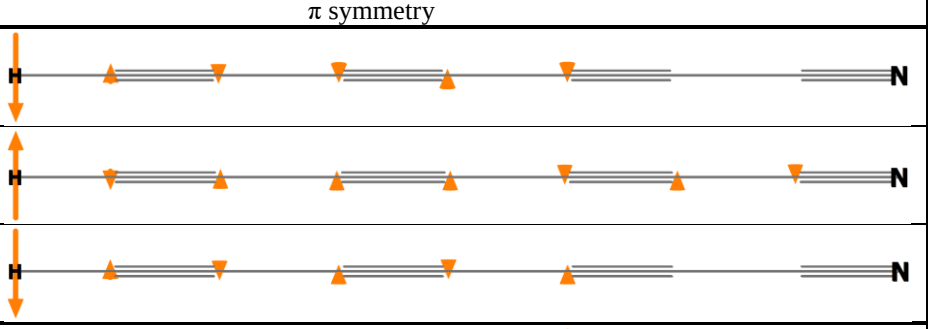
	$\tilde{B}$ 522	
	$\tilde{E}$ 541	
ν_{10}	$\tilde{X}$ 602	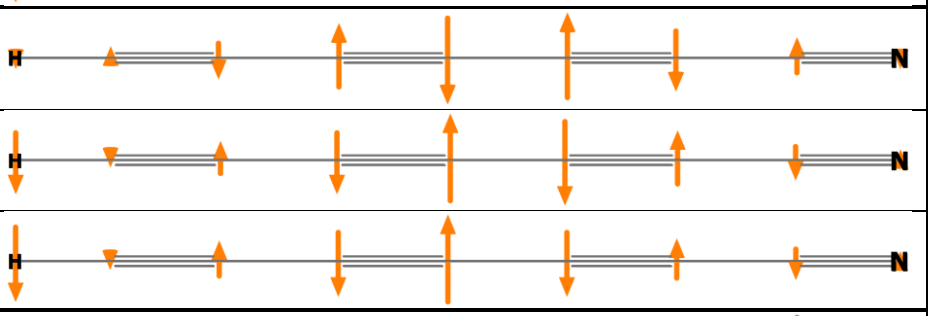
	$\tilde{B}$ 553	
	$\tilde{E}$ 517	
ν_{11}	$\tilde{X}$ 523	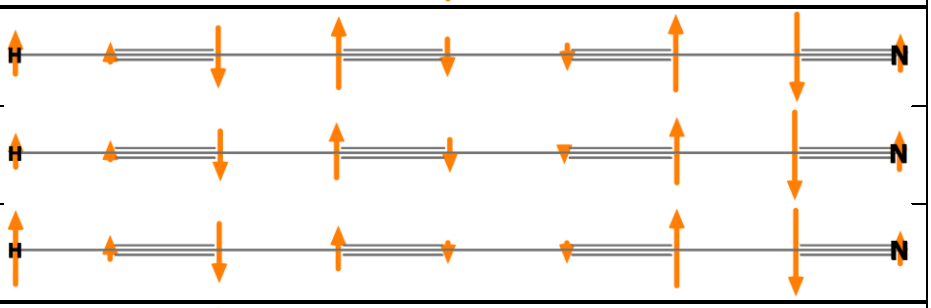
	$\tilde{B}$ 483	
	$\tilde{E}$ 434	
ν_{12}	$\tilde{X}$ 461	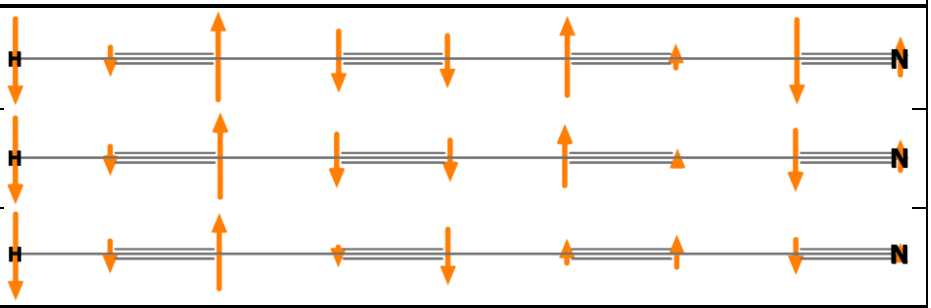
	$\tilde{B}$ 434	
	$\tilde{E}$ 412	
ν_{13}	$\tilde{X}$ 287	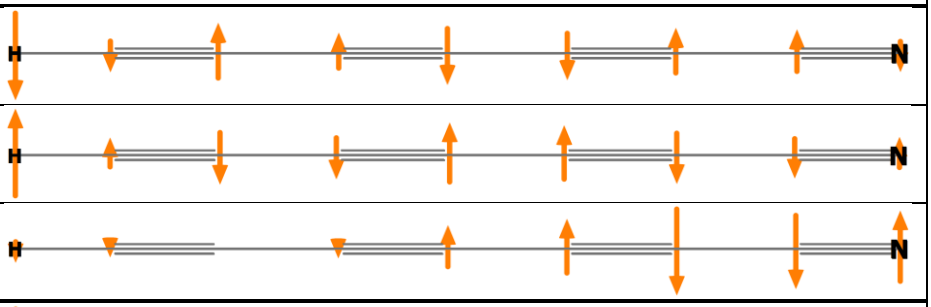
	$\tilde{B}$ 290	
	$\tilde{E}$ 211	
ν_{14}	$\tilde{X}$ 162	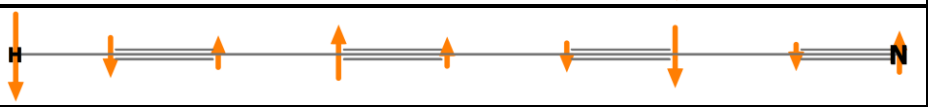

	$\tilde{B}$ 153	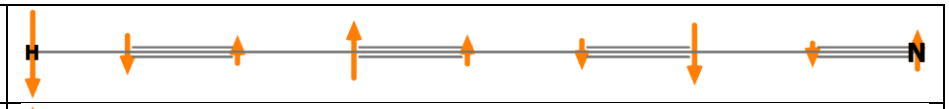
	$\tilde{E}$ 71	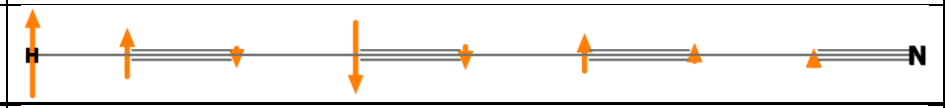
ν_{15}	$\tilde{X}$ 61	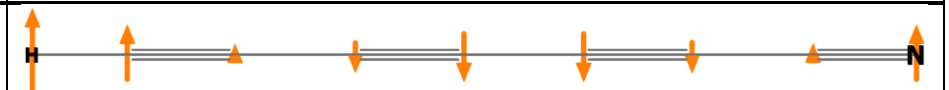
	$\tilde{B}$ 60	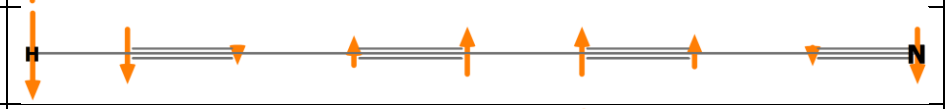
	$\tilde{E}$ 41	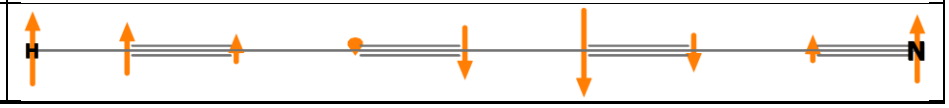

Table 37. CH_3C_7N vibrations in the ground and select excited states [192], wavenumbers ($\bar{\nu}$) in cm^{-1}.

Mode	State $\bar{\nu}$	Visualization
	a_1 symmetry	
ν_1	$\tilde{X}$ 2910	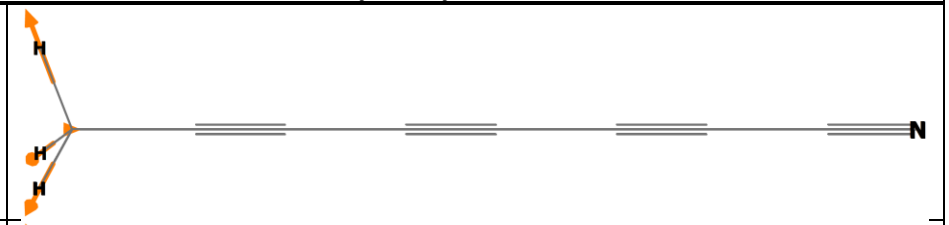
	$\tilde{E}$ 2841	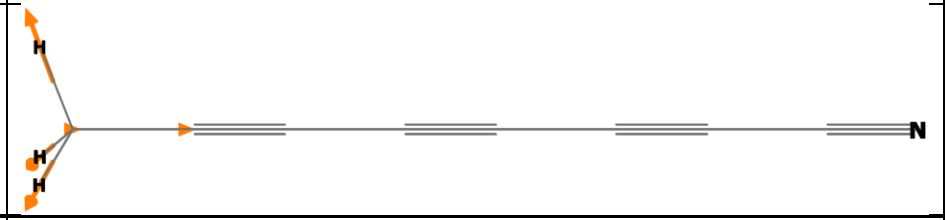
ν_2	$\tilde{X}$ 2260	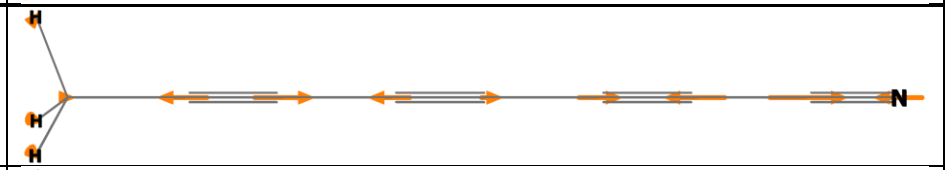
	$\tilde{E}$ 2180	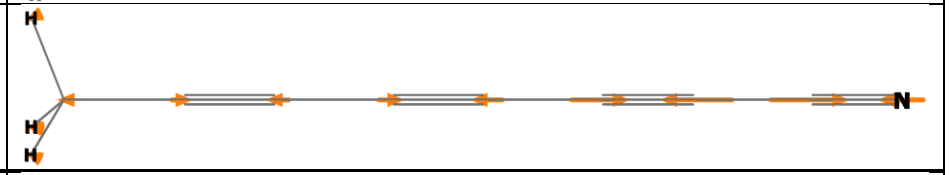
ν_3	$\tilde{X}$ 2208	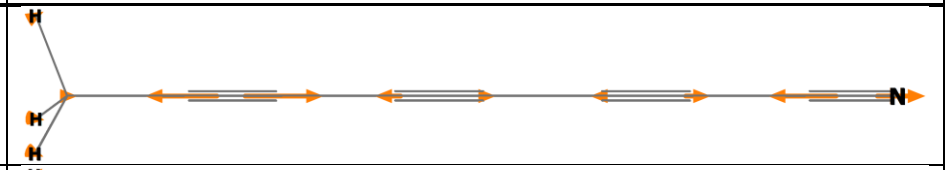
	$\tilde{E}$ 2132	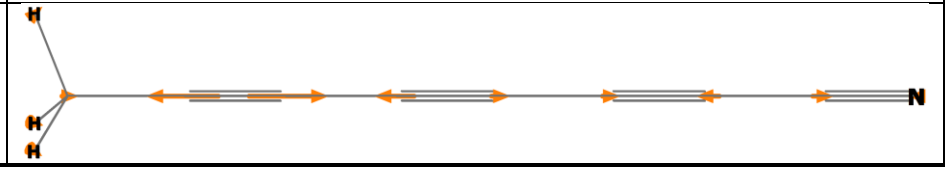

ν_4	$\tilde{X}$ 2187	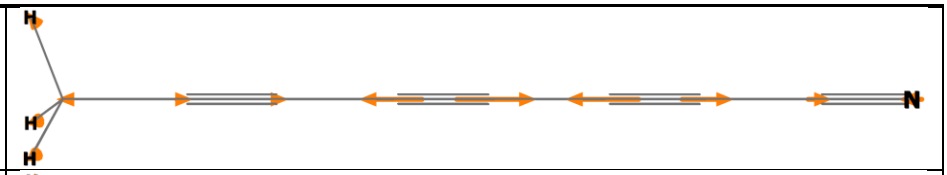
	$\tilde{E}$ 1969	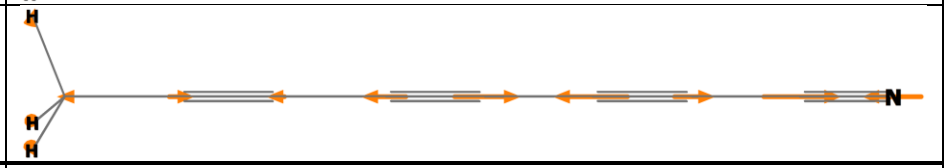
ν_5	$\tilde{X}$ 2093	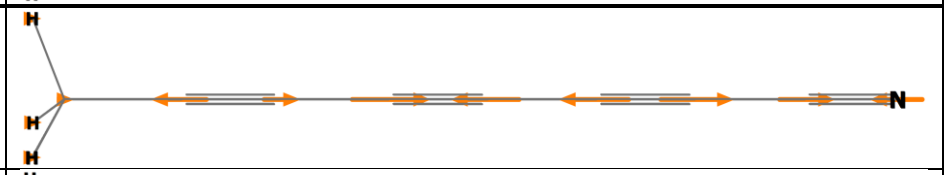
	$\tilde{E}$ 1917	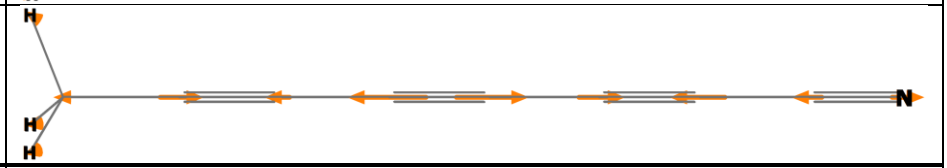
ν_6	$\tilde{X}$ 1364	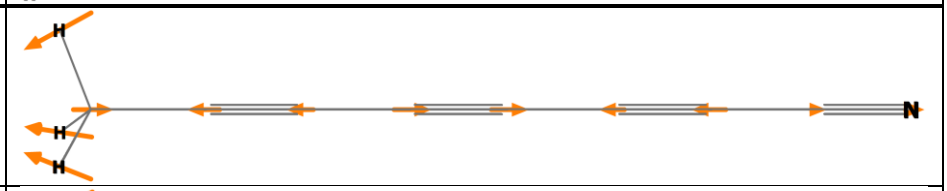
	$\tilde{E}$ 1323	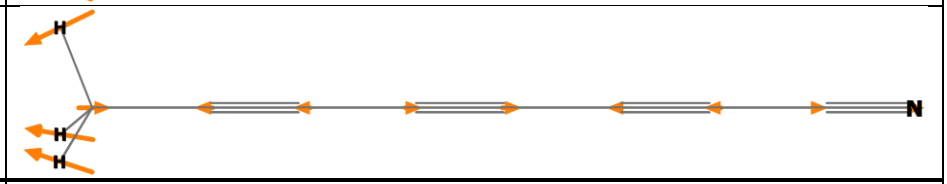
ν_7	$\tilde{X}$ 1333	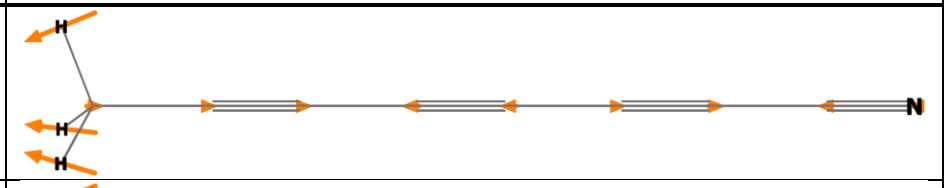
	$\tilde{E}$ 1295	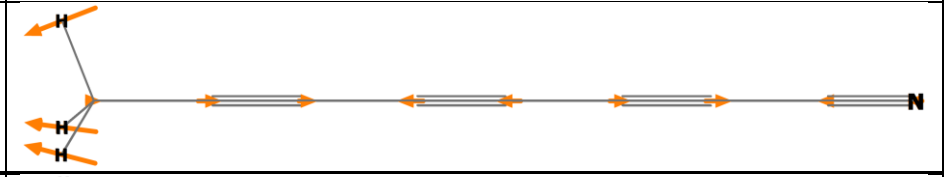
ν_8	$\tilde{X}$ 1066	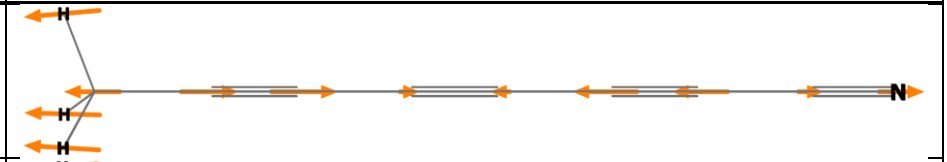
	$\tilde{E}$ 1061	
ν_9	$\tilde{X}$ 758	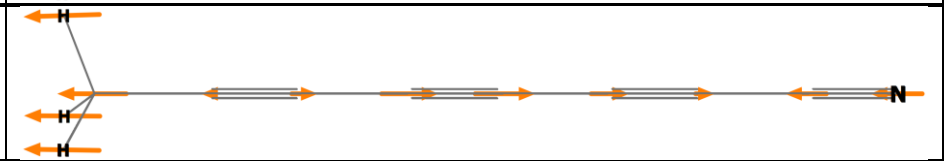

	$\tilde{E}$ 745	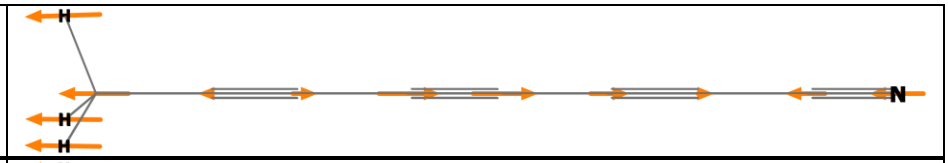
ν_{10}	$\tilde{X}$ 402	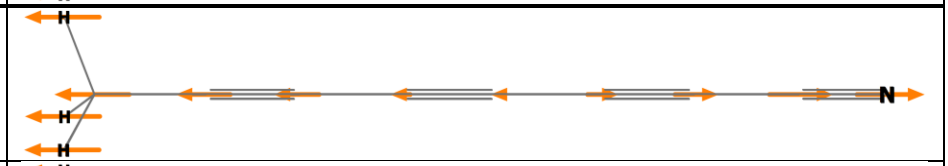
	$\tilde{E}$ 395	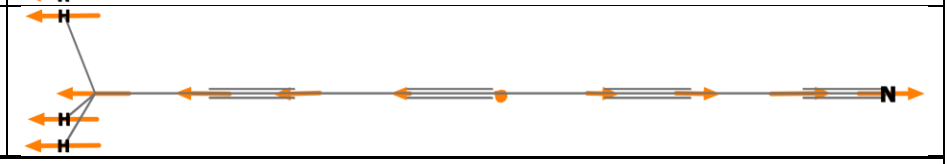
e symmetry		
ν_{11}	$\tilde{X}$ 2976	
	$\tilde{E}$ 2894	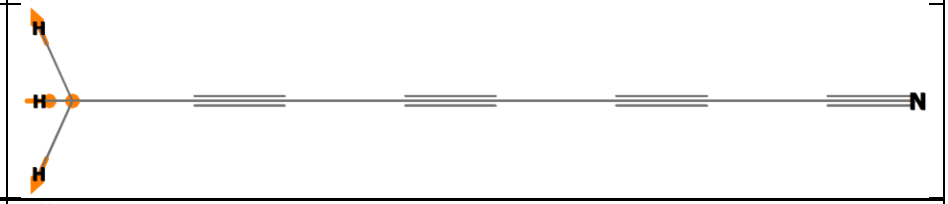
ν_{12}	$\tilde{X}$ 1398	
	$\tilde{E}$ 1352	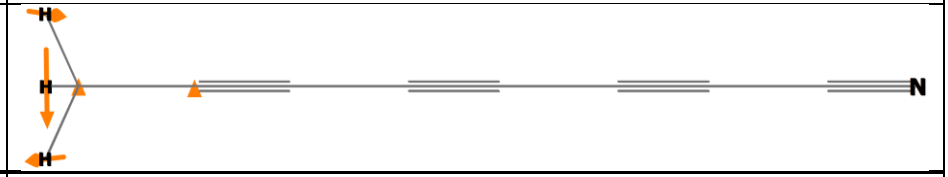
ν_{13}	$\tilde{X}$ 991	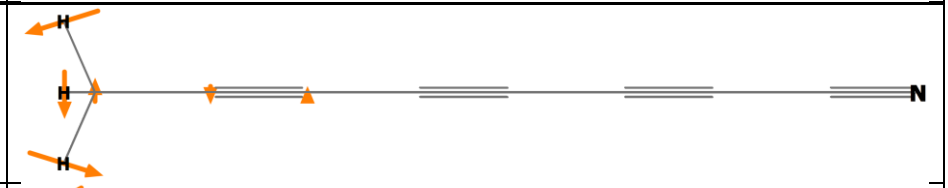
	$\tilde{E}$ 953	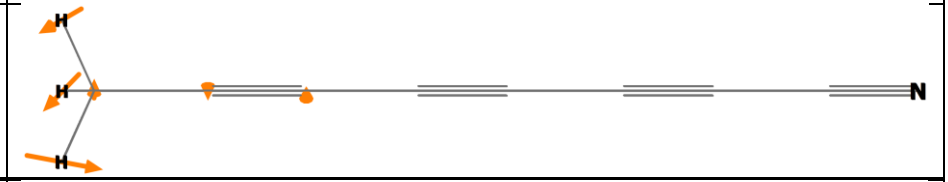
ν_{14}	$\tilde{X}$ 574	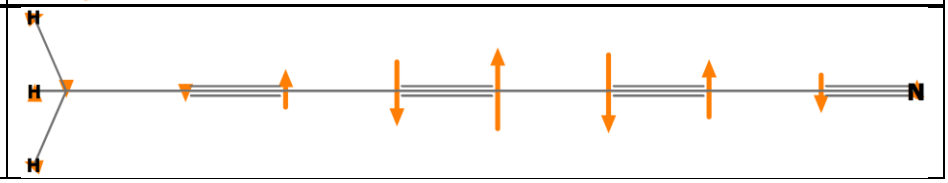

	$\tilde{E}$ 490	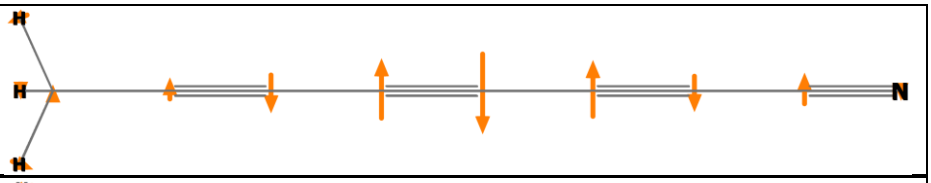
ν_{15}	$\tilde{X}$ 518	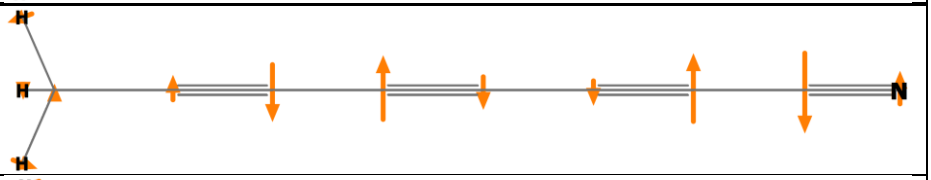
	$\tilde{E}$ 437	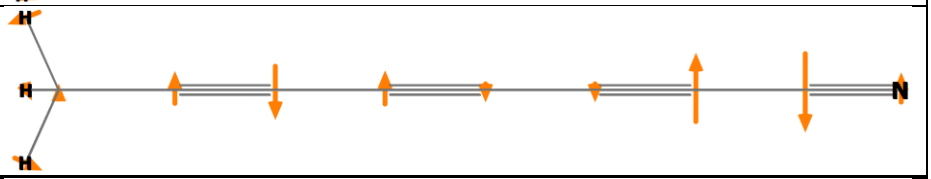
ν_{16}	$\tilde{X}$ 463	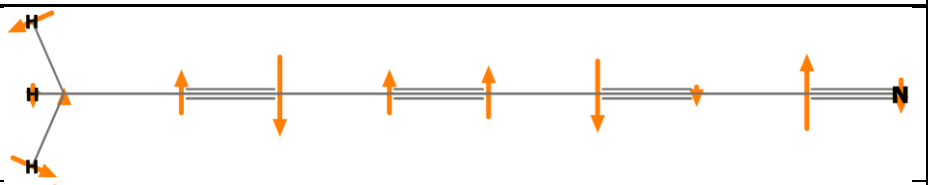
	$\tilde{E}$ 417	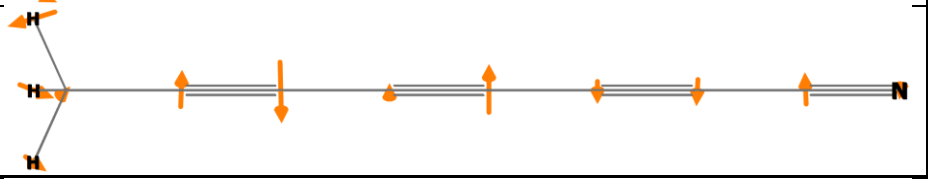
ν_{17}	$\tilde{X}$ 340	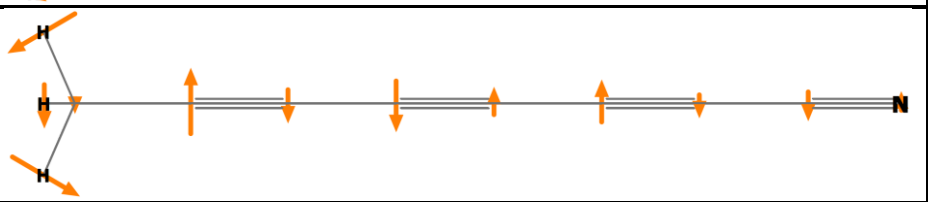
	$\tilde{E}$ 193	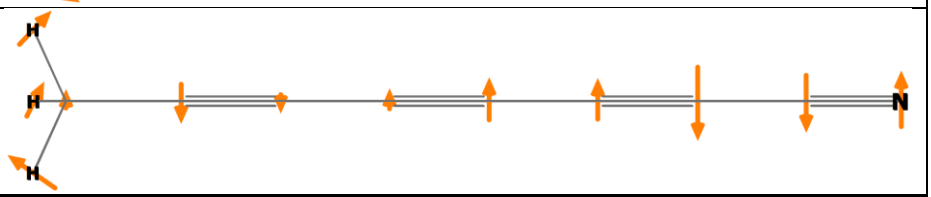
ν_{18}	$\tilde{X}$ 226	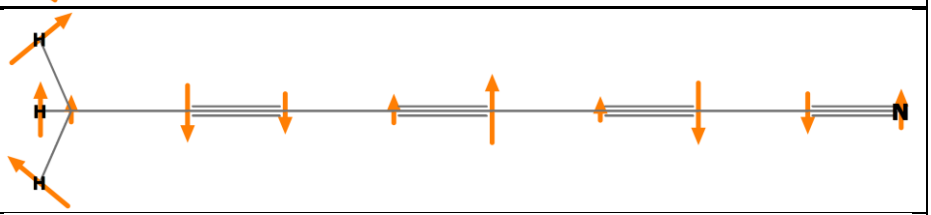
	$\tilde{E}$ 212	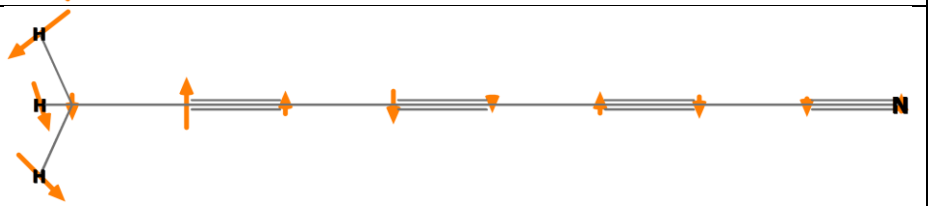
ν_{19}	$\tilde{X}$ 124	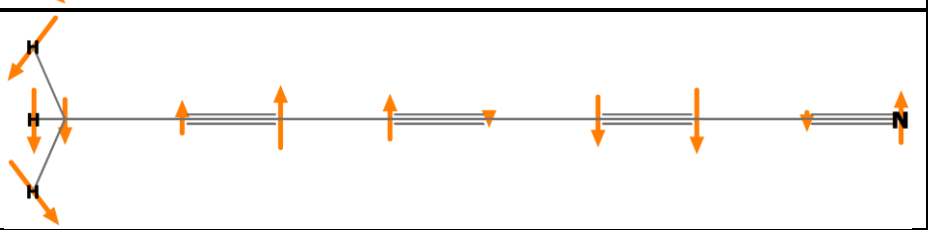

	$\tilde{E}$ 57	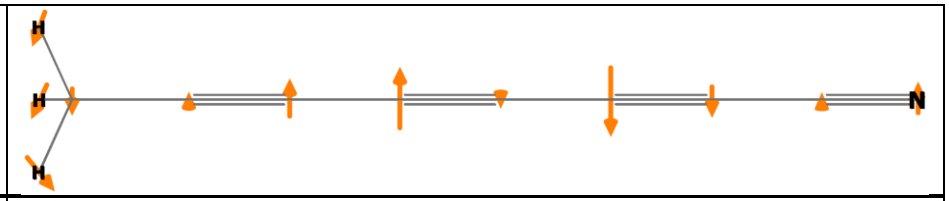
ν_{20}	$\tilde{X}$ 47	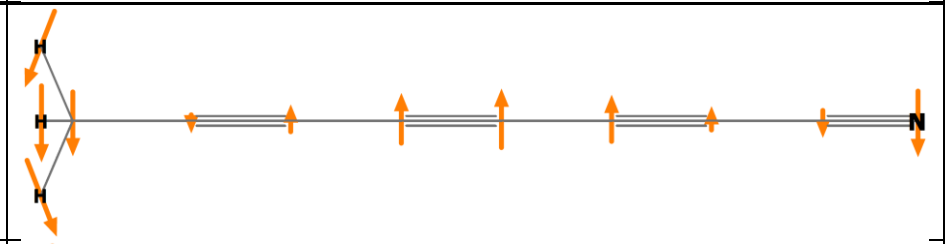
	$\tilde{E}$ 39	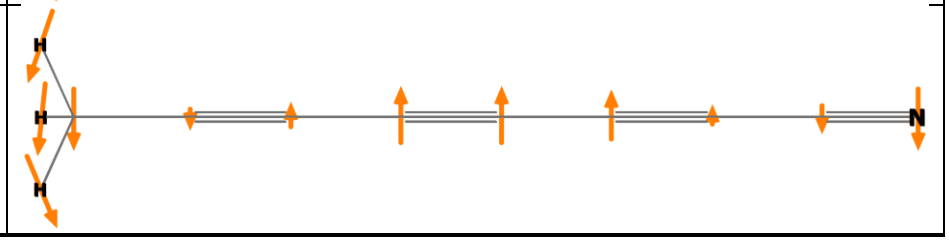

Table 38. HC_9N vibrations in the ground and select excited states [192], wavenumbers ($\bar{\nu}$) in cm^{-1}.

Mode	State $\bar{\nu}$	Visualization
	σ symmetry	
ν_1	$\tilde{X}$ 3324	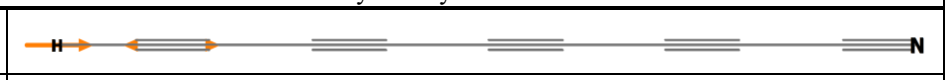
	$\tilde{B}$ 3318	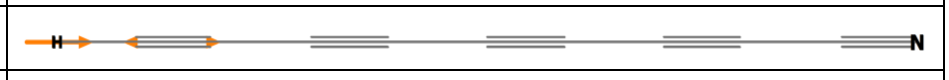
	$\tilde{E}$ 3298	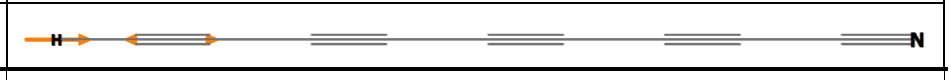
ν_2	$\tilde{X}$ 2250	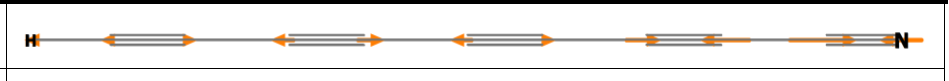
	$\tilde{B}$ 2098	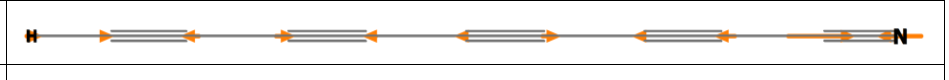
	$\tilde{E}$ 2150	
ν_3	$\tilde{X}$ 2201	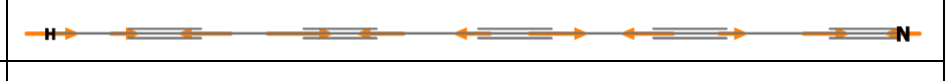
	$\tilde{B}$ 2059	
	$\tilde{E}$ 2059	
ν_4	$\tilde{X}$ 2146	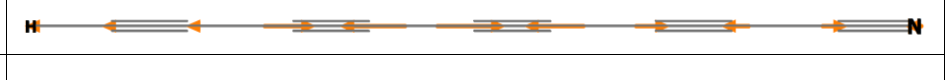
	$\tilde{B}$ 2000	
	$\tilde{E}$ 2033	
ν_5	$\tilde{X}$ 2122	
	$\tilde{B}$ 1900	
	$\tilde{E}$ 1956	

ν_6	$\tilde{X}$ 2037	
	$\tilde{B}$ 1848	
	$\tilde{E}$ 1893	
ν_7	$\tilde{X}$ 1369	
	$\tilde{B}$ 1479	
	$\tilde{E}$ 1346	
ν_8	$\tilde{X}$ 1074	
	$\tilde{B}$ 1106	
	$\tilde{E}$ 1071	
ν_9	$\tilde{X}$ 736	
	$\tilde{B}$ 741	
	$\tilde{E}$ 730	
ν_{10}	$\tilde{X}$ 376	
	$\tilde{B}$ 386	
	$\tilde{E}$ 374	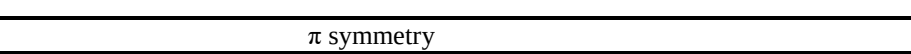
π symmetry		
ν_{11}	$\tilde{X}$ 764	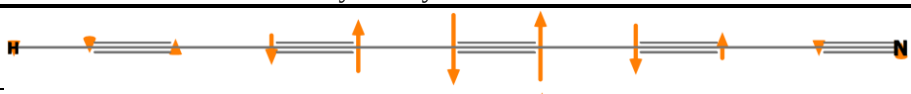
	$\tilde{B}$ 754	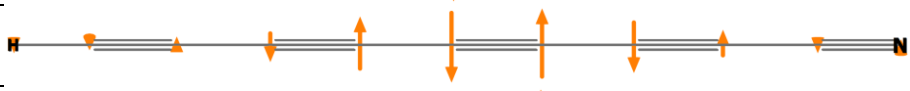
	$\tilde{E}$ 712	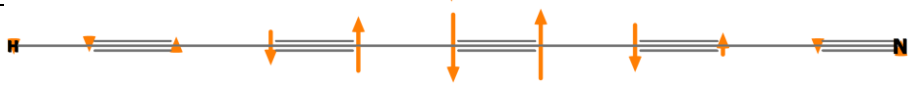
ν_{12}	$\tilde{X}$ 640	
	$\tilde{B}$ 559	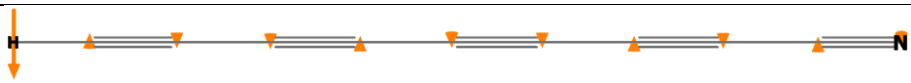
	$\tilde{E}$ 562	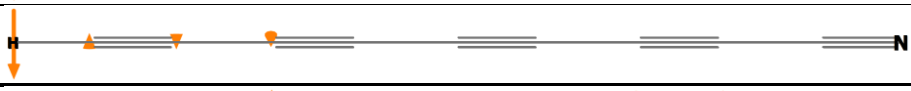
ν_{13}	$\tilde{X}$ 578	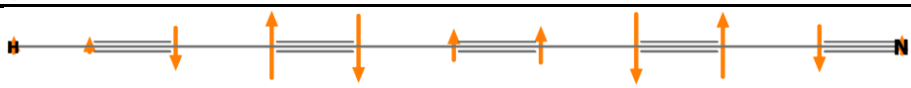
	$\tilde{B}$ 547	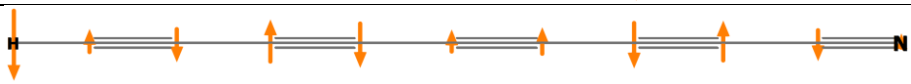
	$\tilde{E}$ 519	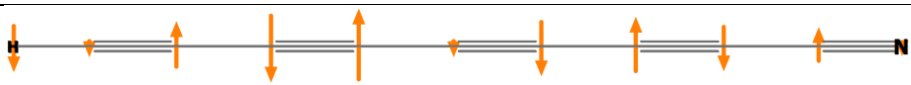
ν_{14}	$\tilde{X}$ 511	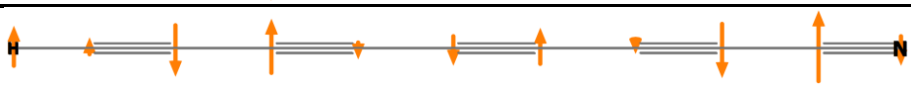

	$\tilde{B}$ 486	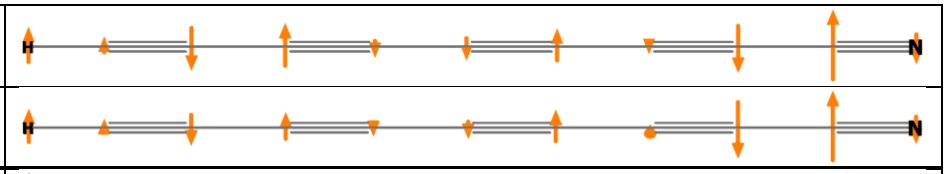
	$\tilde{E}$ 458	
ν_{15}	$\tilde{X}$ 451	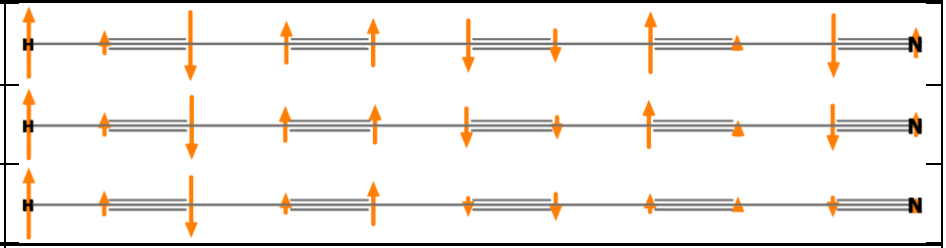
	$\tilde{B}$ 432	
	$\tilde{E}$ 419	
ν_{16}	$\tilde{X}$ 301	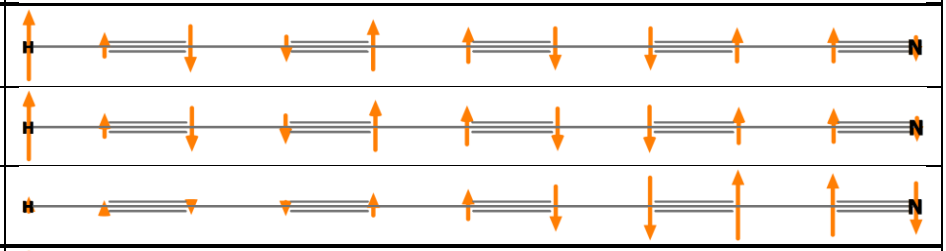
	$\tilde{B}$ 309	
	$\tilde{E}$ 253	
ν_{17}	$\tilde{X}$ 198	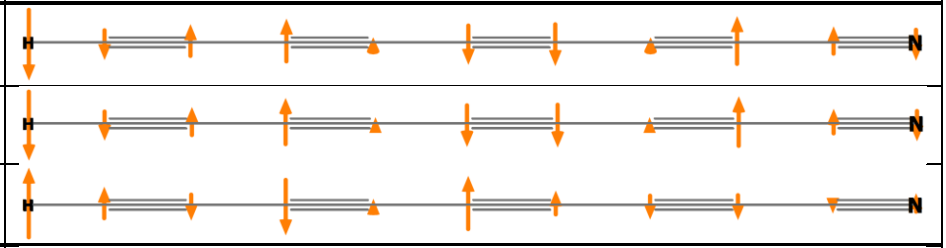
	$\tilde{B}$ 191	
	$\tilde{E}$ 147	
ν_{18}	$\tilde{X}$ 107	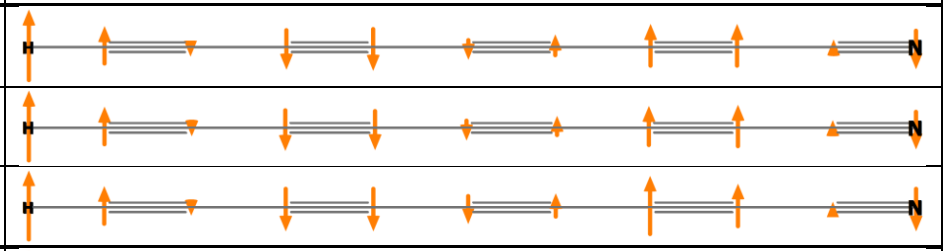
	$\tilde{B}$ 105	
	$\tilde{E}$ 88	
ν_{19}	$\tilde{X}$ 40	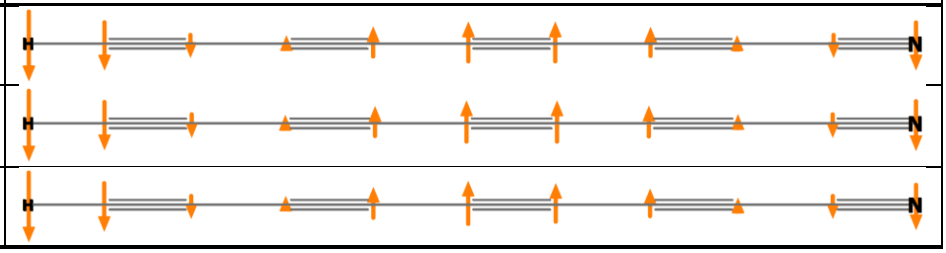
	$\tilde{B}$ 39	
	$\tilde{E}$ 35	

Table 39. $C_{10}N_2$ vibrations in the ground and select excited states [192], wavenumbers ($\tilde{\nu}$) in cm^{-1}.

Mode	State $\tilde{\nu}$	Visualization
	σ_g symmetry	
ν_1	$\tilde{X}$ 2254	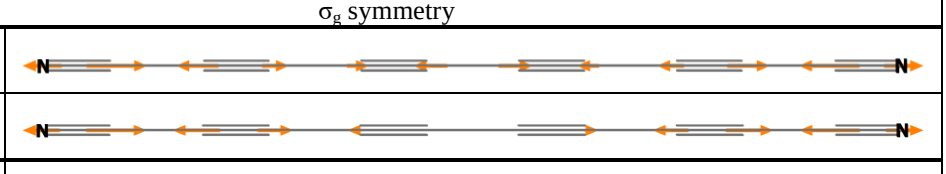
	$\tilde{H}$ 2194	
ν_2	$\tilde{X}$ 2140	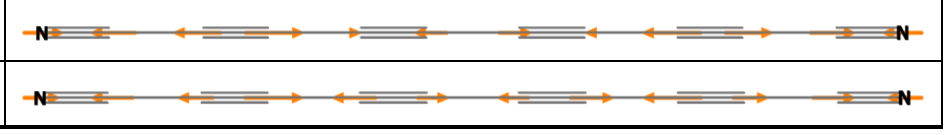
	$\tilde{H}$ 2067	

ν_3	$\tilde{X}$ 2115	
	$\tilde{H}$ 2017	
ν_4	$\tilde{X}$ 1414	
	$\tilde{H}$ 1431	
ν_5	$\tilde{X}$ 908	
	$\tilde{H}$ 911	
ν_6	$\tilde{X}$ 314	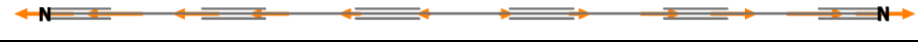
	$\tilde{H}$ 315	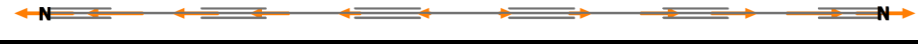
σ_u symmetry		
ν_7	$\tilde{X}$ 2241	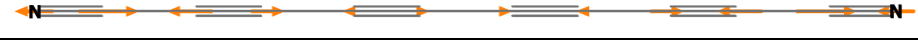
	$\tilde{H}$ 2174	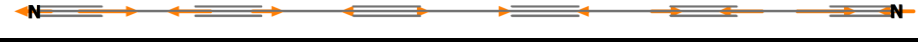
ν_8	$\tilde{X}$ 2199	
	$\tilde{H}$ 2096	
ν_9	$\tilde{X}$ 2061	
	$\tilde{H}$ 1941	
ν_{10}	$\tilde{X}$ 1180	
	$\tilde{H}$ 1190	
ν_{11}	$\tilde{X}$ 617	
	$\tilde{H}$ 621	
π_g symmetry		
ν_{12}	$\tilde{X}$ 554	
	$\tilde{H}$ 509	
ν_{13}	$\tilde{X}$ 512	
	$\tilde{H}$ 462	
ν_{14}	$\tilde{X}$ 437	
	$\tilde{H}$ 392	
ν_{15}	$\tilde{X}$ 222	
	$\tilde{H}$ 210	

ν_{16}	$\tilde{X}$ 75	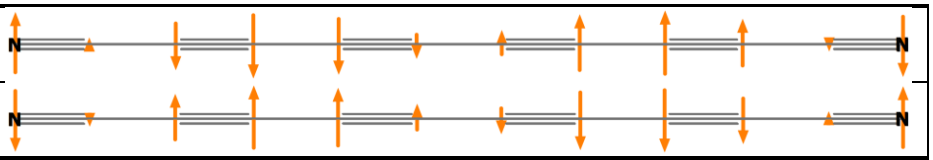
	$\tilde{H}$ 75	
π_u symmetry		
ν_{17}	$\tilde{X}$ 561	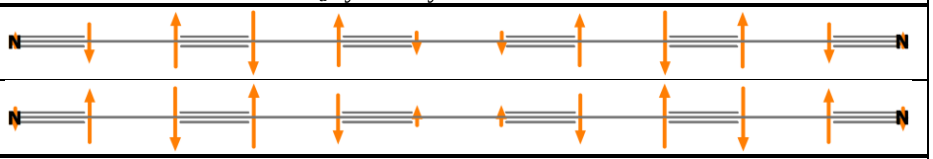
	$\tilde{H}$ 515	
ν_{18}	$\tilde{X}$ 492	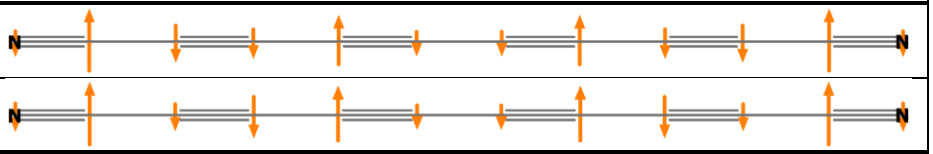
	$\tilde{H}$ 455	
ν_{19}	$\tilde{X}$ 308	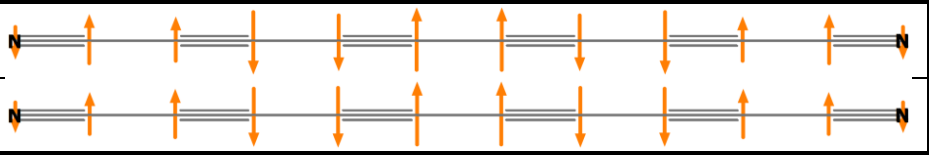
	$\tilde{H}$ 288	
ν_{20}	$\tilde{X}$ 142	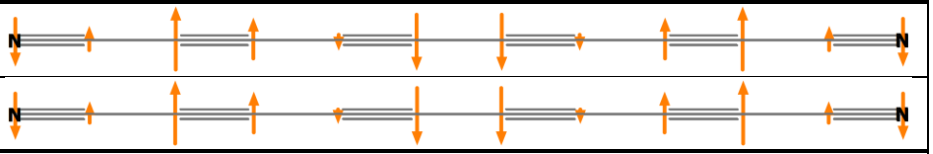
	$\tilde{H}$ 139	
ν_{21}	$\tilde{X}$ 28	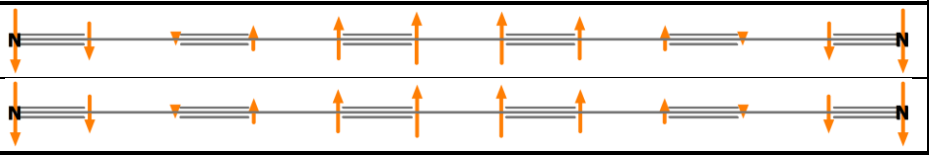
	$\tilde{H}$ 30	

LIST OF FIGURES

LIST OF TABLES

STRESZCZENIE (ABSTRACT IN POLISH)

Rozprawa dotyczy spektroskopii i fotochemii niektórych cząsteczek z rodziny cyjanoacetylenu stanowiących przedmiot zainteresowania astrochemii.

Badania dotyczą cząsteczek mających potwierdzone lub postulowane znaczenie dla chemii międzygwiazdowej, jak również chemii atmosfer planetarnych. Biorąc pod uwagę ich rozpowszechnienie w przestrzeni kosmicznej, w szczególności wewnątrz gigantycznych międzygwiazdowych obłoków gazu i pyłu, cząsteczki chemiczne mające jednocześnie grupę nitrylową –CN i jedno lub więcej wielokrotnych wiązań CC przyciągają szczególną uwagę. Rodzina cząsteczek, na którą składają się monocyjanopoliyny (H-(CC)$_n$-CN) jest przedstawicielem tej grupy. Cząsteczki o $n = 2$, 3 i 4 zostały odkryte w kosmosie. Ten projekt skupia się na takich cząsteczkach, oraz na cząsteczkach podobnych lub pochodnych, jak związki metylowane, np. metylocyjanoacetylen (H_3C-CC-CN) i jego różne izomery, a także metylocyjanodiacetylen, największy metylocyjanopoliyn zaobserwowany w przestrzeni międzygwiazdowej.

Dla większości omawianych próbek została wykorzystana kriogeniczna izolacja matrycowa w gazach szlachetnych. Matryce z gazu szlachetnego stanowią obojętne środowisko, przezroczyste w zakresie spektralnym UV-Vis-IR. Są również odpowiednim medium do badań nietrwałych indywiduów chemicznych, takich jak długie łańcuchy lub aniony badane w tej pracy.

Część badanych molekuł, w tym metylocyjanoacetylen (CH_3C_3N) i niektóre z jego izomerów, metylocyjanodiacetylen (CH_3C_5N) oraz cyjanodiacetylen (HC_5N), dostępne były na drodze preparatywnej syntezy organochemicznej. Pozostałe zostały otrzymane jako produkty reakcji fotochemicznych przeprowadzanych głównie w zestalonym kryptonie, z wykorzystaniem techniki stymulowanego ultrafioletem kriogenicznego wydłużania łańcuchów węglowo-azotowych. Podejście to pozwoliło na otrzymanie HC_9N w reakcji $C_4H_2 + HC_5N$, a także na otrzymanie $C_{10}N_2$ w reakcjach $C_4H_2 + HC_5N$ lub $HC_5N + HC_5N$. Metoda ta została dalej rozszerzona na syntezę cząsteczek metylowanych i doprowadziła do tworzenia CH_3C_5N z $CH_3C_2H + HC_3N$ oraz CH_3C_7N z $CH_3C_2H + HC_5N$. Ponadto, w eksperymentach fotochemicznych z matrycami kriogenicznymi zawierającymi HC_5N, wykryto HC_7N oraz anion C_5N^-. Zaproponowany został ogólny schemat wydłużania badanych łańcuchów.

Stymulowana ultrafioletem fotoliza CH_3C_3N w zestalonym argonie doprowadziła do formowania się dwóch jego izomerów: cyjanku allenylu oraz cyjanku propargilu, których obecność wśród produktów fotolizy została stwierdzona na podstawie zmierzonych widm IR tych cząsteczek oraz dostępnych przewidywań teoretycznych. Procesy fotochemiczne prowadzące do ich powstania zostały opisane jako konwersja cząsteczki wyjściowej w cyjanek propargilu, z cyjankiem allenylu jako produktem pośrednim.

Kompleksowe zbadanie właściwości spektroskopowych gazowego, stałego oraz izolowanego w matrycach kriogenicznych CH_3C_5N zostało przeprowadzone z użyciem spektroskopii absorpcyjnej w podczerwieni, spektroskopii Ramana oraz spektroskopii elektronowej (zarówno absorpcji w zakresie UV-Vis jak i luminescencji). Uzupełniony został opis znanej już fosforescencji cząsteczki HC_5N.

Wspomniane wyżej detekcje produktów fotochemicznego wydłużania łańcuchów nie byłyby możliwe, gdyby nie silna fosforescencja CH_3C_5N, CH_3C_7N, HC_9N, $C_{10}N_2$ oraz C_5N^-, zauważona tu po raz pierwszy. Przeanalizowana została struktura wibronowa tej emisji, jak również struktura ujawniająca się w widmach wzbudzenia fosforescencji. Pozwoliło to na scharakteryzowanie obserwowanych stanów elektronowych.

Podobieństwa, prawidłowości i istotne różnice znalezione dla szeregów homologicznych $HC_{2n+1}N$, $NC_{2n}N$ i $CH_3C_{2n+1}N$ zostały przedyskutowane ze zwróceniem szczególnej uwagi na spektroskopowe reguły wyboru, strukturę wibronową, energie przejść elektronowych i czasy zaniku fosforescencji. Dla każdego z badanych szeregów, długość fali towarzysząca przejściu *0-0* systemu $\tilde{a} - \tilde{X}$ była liniowo zależna od długości nienasyconego szkieletu węglowo-azotowego. Ekstrapolacja otrzymanych wyników pozwala na przybliżenie odpowiednich długości fali dla jeszcze niepoznanych cyjanopoliynów.

RÉSUMÉ (ABSTRACT IN FRENCH)

Ce travail est consacré à la caractérisation spectroscopique et aux études photochimiques de plusieurs molécules d'intérêt astrochimique appartenant à la famille du cyanoacétylène.

Les études portent sur des molécules ayant une importance certaine (ou présumée) dans la chimie inter- et circumstellaire, ainsi que dans la chimie des atmosphères planétaires. Etant donné leur abondance dans l'espace, notamment à l'intérieur des gigantesques nuages de gaz et de poussières interstellaires, les composés chimiques contenant à la fois un groupement nitrile -CN et une ou plusieurs liaisons CC multiples attirent une attention toute particulière. La famille de molécules que constituent les monocyanopolyynes (H-$(CC)_n$-CN) appartient à ce groupe de composés et les représentants à n = 2, 3, et 4 ont déjà été détectés dans l'espace. Le projet est centré sur des molécules proches ou dérivées, telles que les molécules méthylées comme le méthylcyanoacétylène (H_3C-CC-CN) et ses différents isomères, ainsi que le méthylcyanodiacétylène (H_3C-CC-CC-CN), le plus grand méthylcyanopolyyne observé dans le milieu interstellaire.

La technique d'isolation en matrice cryogénique de gaz rare a été utilisée pour la préparation de la plupart des échantillons. Les matrices de gaz rare forment un milieu non-réactif et transparent dans la région spectrale UV-Vis-IR. Elles sont aussi adaptées aux études d'espèces instables, comme les chaînes longues ou les anions, étudiés dans ce travail.

Certaines des molécules étudiées, comprenant CH_3C_3N (et certains de ses isomères), CH_3C_5N et HC_5N, étaient disponibles *via* une synthèse organique. D'autres sont obtenues comme produits de réactions photochimiques, principalement en matrice de Kr où la technique d'élongation des chaînes cyano-carbonées insaturées induite par irradiation UV a été utilisée pour produire des espèces plus longues. Cette approche a conduit avec succès à la production de HC_9N, à partir de C_4H_2 + HC_5N, et de $C_{10}N_2$, à partir soit de C_4H_2 + HC_5N soit de HC_5N + HC_5N. La méthode a pu être étendue à la synthèse de composés méthylés avec la formation de CH_3C_5N à partir de CH_3C_2H + HC_3N et de CH_3C_7N à partir de CH_3C_2H + HC_5N. De plus, les expériences photochimiques sur les matrices contenant HC_5N ont conduit à la détection de HC_7N et de l'anion C_5N^-. Un mécanisme général décrivant les processus d'élongation des chaînes a été formulé.

La photolyse UV du CH_3C_3N isolé en Ar solide a conduit à la formation de deux isomères (CH_2CCHCN et $CHCCH_2CN$) identifiés sur la base des spectres d'absorption IR des molécules pures et des prédictions théoriques disponibles. Les processus photochimiques en jeu peuvent être décrits par un passage de la molécule précurseur au cyanure de propargyle, avec la formation du cyanure d'allényle en intermédiaire.

Une caractérisation spectroscopique approfondie du CH_3C_5N en phase gazeuse, solide, ou isolé dans une matrice cryogénique a été réalisée avec l'utilisation combinée de l'absorption IR, de la spectroscopie Raman, de l'absorption électronique et de la luminescence

électronique. La phosphorescence de la molécule parente HC_5N a été revue et plusieurs nouvelles attributions spectrales ont été obtenues.

La détection de CH_3C_5N, CH_3C_7N, HC_9N, $C_{10}N_2$ et C_5N^-, suite aux expériences d'allongement des chaînes induite par UV, n'a été possible que grâce à leur forte phosphorescence électronique, observée ici pour la première fois. La structure vibronique de leur émission et de leur excitation a été analysée, permettant la caractérisation de plusieurs états électroniques.

Les similarités, différences et structures présentes dans les règles de sélection, les écarts vibroniques, les énergies des transitions électroniques et les durées de vie de phosphorescence ont été examinées pour les séries homologues $HC_{2n+1}N$, $NC_{2n}N$ et $CH_3C_{2n+1}N$. Au sein de chacune de ces séries, les longueurs d'onde de l'origine des transitions $\tilde{a} - \tilde{X}$ se trouvent être corrélées linéairement avec les longueurs du squelette des chaînes cyano-carbonées insaturées. L'extrapolation des résultats obtenus permet d'estimer la longueur d'onde de l'origine $\tilde{a} - \tilde{X}$ pour les cyanopolyynes actuellement inexplorés.

Title : Spectroscopy and photochemistry of astrophysically relevant molecules of the cyanoacetylene family

Keywords: spectroscopy, photochemistry, molecules of astrophysical interest, cyanopolyynes, cryogenic matrices

Abstract : **S**everal astrochemically interesting molecules of the cyanoacetylene family have been characterized spectroscopically. Photochemical studies involving these molecules have also been performed. The cryogenic rare-gas matrix isolation technique was employed for the preparation of most of the samples. The studied molecules were: CH_3C_3N (and some of its isomers), CH_3C_5N, HC_5N – all available *via* preparative organic chemical synthesis, as well as those that appeared as the products of photochemical reactions run mostly in solid Kr: HC_9N, starting from $C_4H_2 + HC_5N$, and $C_{10}N_2$, starting from either $C_4H_2 + HC_5N$ or $HC_5N + HC_5N$. The method was further extended to the synthesis of methylated compounds with formation of CH_3C_5N from $CH_3C_2H + HC_3N$, and CH_3C_7N from $CH_3C_2H + HC_5N$. In addition, photochemical experiments using HC_5N-containing matrices led to the detection of HC_7N and of the C_5N^- anion. A general scheme describing the chain elongation processes was formulated. Similarities or differences in selection rules, vibronic spacings, electronic transition energies, and phosphorescence decay times were examined for the homologous series $HC_{2n+1}N$, $NC_{2n}N$ and $CH_3C_{2n+1}N$.

Tytuł : Spektroskopia i fotochemia cząsteczek o znaczeniu astrofizycznym należących do rodziny cyjanoacetylenów

Słowa kluczowe : spektroskopia, fotochemia, cząsteczki o znaczeniu astrofizycznym, cyanopoliyny, matryce kriogeniczne

Streszczenie : Scharakteryzowana została spektroskopia i fotochemia niektórych cząsteczek o znaczeniu astrofizycznym z rodziny cyjanoacetylenów. Dla większości omawianych próbek została wykorzystana kriogeniczna izolacja matrycowa w gazach szlachetnych. Do badanych molekuł zaliczają się: CH_3C_3N (i niektóre z jego izomerów), CH_3C_5N, HC_5N – wszystkie dostępne na drodze preparatywnej syntezy organochemicznej, jak również te otrzymane jako produkty reakcji fotochemicznych przeprowadzanych głównie w zestalonym kryptonie: HC_9N w reakcji $C_4H_2 + HC_5N$ oraz $C_{10}N_2$ w reakcjach $C_4H_2 + HC_5N$ lub $HC_5N + HC_5N$. Metoda ta została dalej rozszerzona na syntezę cząsteczek metylowanych i doprowadziła do tworzenia CH_3C_5N z $CH_3C_2H + HC_3N$ oraz CH_3C_7N z $CH_3C_2H + HC_5N$. Ponadto, w eksperymentach fotochemicznych z matrycami kriogenicznymi zawierającymi HC_5N wykryto HC_7N oraz anion C_5N^-. Zaproponowany został ogólny schemat wydłużania badanych łańcuchów. Podobieństwa i różnice znalezione dla szeregów homologicznych $HC_{2n+1}N$, $NC_{2n}N$ i $CH_3C_{2n+1}N$ zostały przedyskutowane ze zwróceniem szczególnej uwagi na spektroskopowe reguły wyboru, strukturę wibronową, energie przejść elektronowych i czasy zaniku fosforescencji.

Titre : Spectroscopie et photochimie des molécules d'intérêt astrophysique de la famille des cyanopolyynes

Mots clés : spectroscopie, photochimie, molécules d’intérêt astrophysique, cyanopolyynes, matrices cryogéniques

Résumé : Plusieurs molécules d’intérêt astrochimique appartenant à la famille du cyanoacétylène ont été caractérisées spectroscopiquement. Des études photochimiques ont également été menées sur ces molécules. La technique d’isolation en matrice cryogénique de gaz rare a été utilisée pour la préparation de la plupart des échantillons. Des molécules étudiées étaient : CH_3C_3N (et certains de ses isomères), CH_3C_5N, HC_5N – toutes disponibles *via* une synthèse organique, ainsi que celles obtenues comme produits de réactions photochimiques, principalement en matrice de Kr : HC_9N, à partir de $C_4H_2 + HC_5N$, et de $C_{10}N_2$, à partir soit de $C_4H_2 + HC_5N$ soit de $HC_5N + HC_5N$. La méthode a pu être étendue à la synthèse de composés méthylés avec la formation de CH_3C_5N à partir de $CH_3C_2H + HC_3N$ et de CH_3C_7N à partir de $CH_3C_2H + HC_5N$. De plus, les expériences photochimiques sur les matrices contenant HC_5N ont conduit à la détection de HC_7N et de l'anion C_5N^-. Un mécanisme général décrivant les processus d'élongation des chaînes a été formulé. Les similarités ou différences présentes dans les règles de sélection, les écarts vibroniques, les énergies des transitions électroniques et les durées de vie de phosphorescence ont été examinées pour les séries homologues $HC_{2n+1}N$, $NC_{2n}N$ et $CH_3C_{2n+1}N$.